

**EVALUATION OF THE EFFECT OF CONTACT BETWEEN RISERS AND  
GUIDE FRAMES ON OFFSHORE SPAR PLATFORM MOTIONS**

A Dissertation

by

BON-JUN KOO

Submitted to the Office of Graduate Studies of  
Texas A&M University  
in partial fulfillment of the requirements for the degree of

DOCTOR OF PHILOSOPHY

August 2003

Major Subject: Ocean Engineering

**EVALUATION OF THE EFFECT OF CONTACT BETWEEN RISERS AND  
GUIDE FRAMES ON OFFSHORE SPAR PLATFORM MOTIONS**

A Dissertation

by

BON-JUN KOO

Submitted to Texas A&M University  
in partial fulfillment of the requirements  
for the degree of

DOCTOR OF PHILOSOPHY

Approved as to style and content by:

---

Robert E. Randall  
(Co-Chair of Committee)

---

Moo-Hyun Kim  
(Co-Chair of Committee)

---

Cheung Hun Kim  
(Member)

---

Robert H. Stewart  
(Member)

---

Paul N. Roschke  
(Head of Department)

August 2003

Major Subject: Ocean Engineering

## ABSTRACT

Evaluation of the Effect of Contact between Risers and Guide Frames on  
Offshore Spar Platform Motions. (August 2003)

Bon-Jun Koo, B.S.; M.S., Inha University

Co-Chairs of Advisory Committee: Dr. Robert E. Randall

Dr. Moo-Hyun Kim

A computer program is developed for the dynamic analysis of a spar platform coupled with mooring lines and risers in waves, winds, and currents. The new multi-contact analysis program is developed for the nonlinear multi-contact coupling between vertical risers and guide frames inside of the spar moon-pool. The program extends capability of the current coupled dynamic analysis program, WINPOST, by adding the capability of analyzing riser effects caused by the contact forces and moments from buoyancy-cans inside the spar moon-pool on the global spar motions. The gap between the buoyancy can and riser guide frames are modeled using three different types of nonlinear gap springs. The new riser model also considers the Coulomb damping between the buoyancy-cans and riser guide frames, and it also calculates the impact force on risers for use in fatigue analysis.

The spar platform generally uses vertical risers with dry trees. However, as the water depth increases, the size of the buoyancy-can increases, and it makes installation more difficult. The pneumatic riser support system does not use buoyancy-cans and is an alternative solution to the buoyancy-can approach. The dynamic characteristics of pneumatic riser support system are studied by using the newly developed numerical

analysis program.

The damped Mathieu instability diagram for the damped Mathieu's equation is developed. Due to spar heave and pitch coupling, Mathieu's instability may become excited in long period waves. In the numerical analysis program, pitch and roll hydrostatic stiffness are recalculated for heave motion in every time step to check Mathieu's instability for the spar platform. Simplified vortex-induced vibration effects on the spar platform are considered in newly developed numerical analysis program, and the results are systematically compared with those of the original program WINPOST.

The results in this paper show that the buoyancy-can effect significantly reduces the spar pitch motion, and the Coulomb damping effect also significantly reduces the spar heave motion. The buoyancy-can effect also plays an important role in Mathieu instability. The results also show that a pneumatic riser support system increases the spar heave motion and payload.

## ACKNOWLEDGMENTS

I would like to express my sincere gratitude to my advisor Dr. Robert E. Randall for his inspiration, encouragement, and guidance during my whole study. I also would like to express special thanks to my co-advisor Dr. M. H. Kim for his continuous encouragement and guidance during my research. I would like to thank Dr. Zhihuang Ran for sharing with me his valuable knowledge and experience in the numerical modeling of mooring lines and coupled floating body analysis. Special thanks are extended to Dr. C. H. Kim and Dr. R. H. Stewart for serving as members of my graduate committee.

I would like to express my appreciation to my parents, Dr. Ja-heung Koo and Dr. In-duck Park, for their continuous support and inspiration throughout my life. Finally, I would like to express special thanks to my lovely wife, Ji-hee Kim, for her support and encouragement during my study.

## TABLE OF CONTENTS

	Page
ABSTRACT .....	iii
ACKNOWLEDGMENTS .....	v
TABLE OF CONTENTS.....	vi
LIST OF FIGURES .....	ix
LIST OF TABLES .....	xvii
CHAPTER	
I INTRODUCTION.....	1
1.1 General .....	1
1.2 Literature Review .....	8
1.3 Objective and Scope .....	12
1.4 Organization .....	14
II DYNAMICS OF THE FLOATING PLATFORM.....	16
2.1 Introduction .....	16
2.2 Wave Theory .....	16
2.3 Wave and Current Loads on Structures .....	20
2.3.1 Diffraction and Radiation Theory.....	20
2.3.2 First-and Second-order Boundary Value Problem.....	22
2.3.3 First-Order Hydrodynamic Force and Moment.....	27
2.3.4 Second-Order Hydrodynamic Force and Moment .....	31
2.3.5 Time Domain Expression for Wave Loads.....	33
2.3.6 Morison's Equation and Lift Force on a Column Based Body .....	35
2.4 Time Domain Solution of the Platform .....	37
2.5 Mathieu Instability of the Spar Platform .....	40
2.5.1 Mathieu Equation .....	40
2.5.2 Heave/Pitch Coupled Equation for Classical Spar Platform .....	44
III DYNAMICS OF MOORING LINES AND RISERS .....	46
3.1 Introduction .....	46
3.2 Slender Rod Theory .....	48
3.3 Finite Element Model .....	52
3.4 Formulation of Static Problem .....	56

CHAPTER	Page
3.5 Formulation for Dynamic Problem – Time Domain Integration.....	60
3.6 Modeling of the Seafloor.....	64
<b>IV INTEGRATED MODELING OF PLATFORM AND MOORING/RISER.....</b>	<b>66</b>
4.1 Introduction .....	66
4.2 Spring Coupling between the Platform and Mooring Lines.....	68
4.3 Damper Connection between the Platform and Mooring Lines.....	73
4.4 Multi-Contact Coupling between the Spar Platform and Risers .....	74
4.4.1 Connected Spring Model.....	75
4.4.2 Piecewise-Linear Gap-Contact Spring Model.....	76
4.4.3 Piecewise-Quadratic Gap-contact Spring Model .....	78
4.4.4 Cubic Spring Approximation.....	79
4.5 Alternative Riser Support System Modeling.....	81
4.6 Coulomb Damping between the Platform and Risers .....	82
4.7 Coupled Global Matrix.....	83
<b>V CASE STUDY 1: BUOYANCY-CAN EFFECT ON SPAR PLATFORM.....</b>	<b>86</b>
5.1 Introduction .....	86
5.2 Description of the Spar Platform, Mooring System, and Risers .....	87
5.3 Description of Case Study and Design Environmental Conditions.....	91
5.4 Results and Analysis.....	95
5.4.1 Static Offset and Free Decay Simulation .....	95
5.4.2 100-year Hurricane Simulations.....	109
5.4.3 Comparison with Existing Experimental Data.....	122
<b>VI CASE STUDY 2: ALTERNATIVE RISER SUPPORT SYSTEM .....</b>	<b>126</b>
6.1 Introduction .....	126
6.2 Description of the Spar Platform, Mooring System and Risers .....	126
6.3 Description of Case Study and Design Environmental Conditions.....	128
6.4 Results .....	129
6.4.1 Free Decay Simulation .....	129
6.4.2 100-year Hurricane Simulation .....	136
<b>VII CASE STUDY 3: MATHIEU’S INSTABILITY .....</b>	<b>148</b>
7.1 Introduction .....	148
7.2 Description of the Spar Platform, Mooring System and Risers .....	149
7.3 Description of Case Study and Environmental Conditions.....	149
7.4 Results and Analysis.....	151
7.4.1 Free Decay Simulation .....	151
7.4.2 Mathieu’s Instability in Regular Waves.....	156

CHAPTER	Page
7.4.3 Mathieu Instability in Swell Condition .....	176
VIII CASE STUDY 4: LOOP CURRENT SIMULATION .....	186
8.1 Introduction .....	186
8.2 Description of Case study and Design Environmental Conditions .....	188
8.3 Results and Analysis.....	190
IX SUMMARY, CONCLUSIONS AND RECOMMENDATIONS .....	202
9.1 Dynamics of a Spar Platform with Buoyancy-Can .....	202
9.2 Dynamics of a Spar Platform with Pneumatic Riser Support System.....	204
9.3 Mathieu’s Instability in Spar Platform .....	205
9.4 Vortex Induced Vibration on Spar Hull .....	206
9.5 Recommendations and Future Studies .....	207
REFERENCES .....	209
APPENDIX A.....	215
APPENDIX B.....	220
VITA .....	226



## LIST OF FIGURES

FIGURE	Page
1.1 Platform cost comparison, Gulf of Mexico (Günther et al, 1988).....	1
1.2 Example Pictures of classical spar (left) and truss spar (right) (Courtesy, J. Ray McDermott).....	3
1.3 Schematic drawing of spar riser system with buoyancy-can.....	6
1.4 Pneumatic Riser Support System (Courtesy, Aker Maritime).....	7
2.1 Stability diagram for damped Mathieu’s equation. ....	43
3.1 Coordinate system for slender rod.....	48
4.1 Connected spring model. ....	75
4.2 Piecewise linear gap spring model. ....	77
4.3 Piecewise quadratic gap-contact spring model.....	78
4.4 Cubic spring approximation model .....	80
4.5 Schematic drawing of pneumatic riser support cylinder. ....	81
4.6 Schematic Drawing of Coulomb Damping. ....	83
4.7 Coupled global matrix (1-mooring with 6-element, 1-riser with 4 multi-contact coupling 6-element).....	84
5.1 The illustration of the spar platform and mooring/riser configuration (not to scale). ....	87
5.2 Schematic drawing of a spar riser system. ....	90
5.3 Spring constant for multi-contact model. ....	93
5.4 Spring constant for multi-contact model after the gap. ....	93
5.5 Environmental direction of 100-year hurricane condition. ....	95
5.6 Platform surge static offset curve (CASE B).....	96

5.7	Most loaded line tension (CASE B).....	96
5.8	Least loaded line tension curve (CASE B).....	96
5.9	Surge free decay motion time series.....	99
5.10	Surge free decay motion spectrum. ....	99
5.11	Surge free decay motion time series.....	100
5.12	Contact force on the spar platform at keel (from production riser No.23).....	100
5.13	Nodal reaction force on riser (production riser No.23, node 11).....	100
5.14	Surge free decay simulation time series. ....	101
5.15	Contact force on the spar platform at keel (from production riser No.23).....	101
5.16	Nodal reaction force on riser (production riser No.23, node 11).....	101
5.17	Surge free decay simulation time series. ....	102
5.18	Contact force on the spar platform at keel (from production riser No.23).....	102
5.19	Nodal reaction force on riser (production riser No.23, node 11).....	102
5.20	Heave free decay simulation results.....	104
5.21	Heave free decay motion spectrum. ....	104
5.22	Heave free decay simulation time series (CASE C).....	105
5.23	Coulomb damping force on the spar platform at keel (drilling riser).....	105
5.24	Horizontal contact force on the spar platform at keel (drilling riser).....	105
5.25	Pitch free decay simulation time series. ....	107
5.26	Pitch free decay motion spectrum. ....	107
5.27	Pitch free decay simulation time series. ....	108
5.28	Contact moment on the spar platform at keel (from production riser # 23).....	108
5.29	100-year Gulf of Mexico hurricane wind velocity spectrum. ....	110

FIGURE	Page
5.30 100-year Gulf of Mexico hurricane wave spectrum.....	111
5.31 100-year hurricane wave elevation time series. ....	111
5.32 Surge response time series (CASE A). ....	113
5.33 Surge response time series (CASE B). ....	113
5.34 Surge response time series (CASE D). ....	113
5.35 Comparison of the surge response spectrum (CASE A, CASE B, and CASE D). ....	114
5.36 Heave response time series (CASE B). ....	115
5.37 Heave response time series (CASE C). ....	115
5.38 Comparison of heave response spectrum (CASE B and CASE C). ....	115
5.39 Pitch response time series (CASE A). ....	117
5.40 Pitch response time series (CASE B). ....	117
5.41 Comparison of the pitch response spectrum (CASE A and CASE B). ....	118
5.42 Most loaded mooring line top tension time series (CASE A). ....	120
5.43 Most loaded mooring line top tension time series (CASE C). ....	120
5.44 Most loaded line top tension spectrum (CASE A and CASE C). ....	120
5.45 Comparison of the nodal reaction force spectrum for production riser # 23 (CASE C and CASE D, node # 11). ....	121
5.46 Comparison the of nodal reaction force spectrum for production riser # 23 (CASE C and CASE E, node # 11). ....	121
6.1 The illustration of the spar platform and mooring/riser configuration (not to scale). ....	127
6.2 Surge free decay time series. ....	131
6.3 Surge free decay spectrum.....	131

FIGURE	Page
6.4 Heave free decay time series. ....	132
6.5 Heave free decay spectrum. ....	132
6.6 Drilling riser top tension time series (CASE A). ....	133
6.7 Drilling riser top tension time series (CASE B). ....	133
6.8 Production riser top tension time series (CASE A). ....	134
6.9 Production riser top tension time series (CASE B). ....	134
6.10 Pitch free decay time series. ....	135
6.11 Pitch free decay spectrum. ....	135
6.12 100-year hurricane wave spectrum. ....	138
6.13 100-year hurricane wave time series. ....	138
6.14 100-year hurricane wind velocity spectrum. ....	138
6.15 Surge response time series (CASE A). ....	139
6.16 Surge response time series (CASE B). ....	139
6.17 Surge response spectrum. ....	139
6.18 Heave response time series (CASE A). ....	140
6.19 Heave response time series (CASE B). ....	140
6.20 Heave response Spectrum. ....	140
6.21 Pitch response time series (CASE A). ....	141
6.22 Pitch response time series (CASE B). ....	141
6.23 Pitch response spectrum. ....	141
6.24 Drilling riser top tension time series (CASE A). ....	142
6.25 Drilling riser top tension time series (CASE B). ....	142

FIGURE	Page
6.26 Drilling riser top tension spectrum (CASE A). .....	143
6.27 Drilling riser top tension spectrum (CASE B). .....	143
6.28 Production riser top tension time series (CASE A). .....	144
6.29 Production riser top tension time series (CASE B). .....	144
6.30 Production riser top tension spectrum with pneumatic cylinder (CASE A). .....	145
6.31 Production riser top tension spectrum with buoyancy-can (CASE B). .....	145
6.32 Most loaded line top tension time series (CASE A). .....	146
6.33 Most loaded line top tension time series (CASE B). .....	146
6.34 Most loaded line top tension spectrum. ....	146
7.1 Pitch free decay simulation time series (CASE A, CASE B, and CASE C). .....	153
7.2 Pitch free decay simulation spectrum (CASE A, CASE B, and CASE C). .....	153
7.3 Pitch free decay simulation time series (CASE D and CASE E). .....	154
7.4 Pitch free decay simulation spectrum (CASE D and CASE E). .....	154
7.5 Heave free decay time series. ....	155
7.6 Heave free decay spectrum. ....	155
7.7 Spar heave and pitch motions in RW-A (CASE A: $T_p = 26$ sec, amp. = 6.0 m). .....	159
7.8 Heave/Pitch response time series (1000 sec – 4000 sec). .....	160
7.9 Spar heave and pitch motions without time varying pitch hydrostatic restoring coefficient (CASE A: $T_p = 26$ sec, amp. = 6.0 m). .....	161
7.10 Spar heave and pitch motions (CASE B: $T_p = 26$ sec, amp. = 6.0 m). .....	162
7.11 Spar heave and pitch motions (CASE C: $T_p = 26$ sec, amp. = 6.0 m). .....	163
7.12 Spar heave and pitch motions (CASE D: $T_p = 26$ sec, amp. = 7.0 m). .....	164
7.13 Spar heave and pitch motions (CASE E: $T_p = 26$ sec, amp. = 7.0 m). .....	165

FIGURE	Page
7.14 Spar heave and pitch motions (CASE B: $T_p = 27.8$ sec, amp. = 1.5 m).....	169
7.15 Spar heave and pitch motions (CASE C: $T_p = 27.8$ sec, amp. = 1.5 m).....	170
7.16 Spar heave and pitch motions (CASE C: $T_p = 27.8$ sec, amp. = 2.0 m).....	171
7.17 Spar heave and pitch motions (CASE D: $T_p = 27.8$ sec, amp. = 7.0 m).....	172
7.18 Heave/Pitch response time series (1000 sec – 5000 sec). ....	173
7.19 Spar heave and pitch motions (CASE E: $T_p = 27.8$ sec, amp. = 7.0 m).....	174
7.20 Spar heave and pitch motions (CASE E: $T_p = 22.7$ sec, amp. = 7.0 m).....	175
7.21 Wave spectrum for Swell – A. ....	177
7.22 Wave time series for Swell – A. ....	177
7.23 Wave spectrum for Swell – B. ....	178
7.24 Wave time series for Swell – B. ....	178
7.25 Surge response time series ( $H_s = 2.5$ m, $T_p = 23$ sec, $\gamma = 6.0$ ).....	179
7.26 Surge response spectrum ( $H_s = 2.5$ m, $T_p = 23$ sec, $\gamma = 6.0$ ).....	179
7.27 Heave response time series ( $H_s = 2.5$ m, $T_p = 23$ sec, $\gamma = 6.0$ ).....	180
7.28 Heave response spectrum ( $H_s = 2.5$ m, $T_p = 23$ sec, $\gamma = 6.0$ ).....	180
7.29 Pitch response time series ( $H_s = 2.5$ m, $T_p = 23$ sec, $\gamma = 6.0$ ).....	181
7.30 Pitch response spectrum ( $H_s = 2.5$ m, $T_p = 23$ sec, $\gamma = 6.0$ ).....	181
7.31 Surge response time series ( $H_s = 1.7$ m, $T_p = 25$ sec, $\gamma = 6.0$ ).....	182
7.32 Surge response spectrum ( $H_s = 1.7$ m, $T_p = 25$ sec, $\gamma = 6.0$ ).....	182
7.33 Heave response time series ( $H_s = 1.7$ m, $T_p = 25$ sec, $\gamma = 6.0$ ).....	183
7.34 Heave response spectrum ( $H_s = 1.7$ m, $T_p = 25$ sec, $\gamma = 6.0$ ).....	183
7.35 Pitch response time series ( $H_s = 1.7$ m, $T_p = 25$ sec, $\gamma = 6.0$ ).....	184

FIGURE	Page
7.36 Pitch response spectrum ( $H_s = 1.7$ m, $T_p = 25$ sec, $\gamma = 6.0$ ).....	184
8.1 Loop current for the Gulf of Mexico (Gyory et al., 2001).....	187
8.2 Environmental direction of loop current condition.....	189
8.3 Loop current and 100-yr hurricane current profile.....	189
8.4 Loop current condition wind velocity spectrum.....	191
8.5 Loop current condition wave spectrum.....	191
8.6 Loop current condition wave time series.....	191
8.7 Surge response time series (CASE A, $C_L = 0.0$ ).....	192
8.8 Surge response time series (CASE B, $St = 0.23$ , $C_L = 0.4$ ).....	192
8.9 Surge response time series (CASE C, $St = 0.153$ , $C_L = 0.4$ ).....	192
8.10 Comparison of surge response spectrum ( $\blacksquare$ shows the peak from experiment).....	193
8.11 Heave response time series (CASE A, $C_L = 0.0$ ).....	194
8.12 Heave response time series (CASE B, $St = 0.23$ , $C_L = 0.4$ ).....	194
8.13 Heave response time series (CASE C, $St = 0.153$ , $C_L = 0.4$ ).....	194
8.14 Comparison of heave response spectrum.....	195
8.15 Pitch response time series (CASE A, $C_L = 0.0$ ).....	196
8.16 Pitch response time series (CASE B, $St = 0.23$ , $C_L = 0.4$ ).....	196
8.17 Pitch response time series (CASE C, $St = 0.153$ , $C_L = 0.4$ ).....	196
8.18 Comparison of Pitch response spectrum.....	197
8.19 Mooring top tension time series (CASE A, $C_L = 0.0$ ).....	200
8.20 Mooring top tension time series (CASE B, $St = 0.23$ , $C_L = 0.4$ ).....	200
8.21 Mooring top tension time series (CASE C, $St = 0.153$ , $C_L = 0.4$ ).....	200

FIGURE	Page
8.22 Comparison of top tension spectrum. ....	201



## LIST OF TABLES

TABLE	Page
5.1 Principle particulars of the spar platform. ....	88
5.2 Spar mooring system configuration.....	89
5.3 Spar mooring characteristics. ....	89
5.4 Riser System Characteristics. ....	89
5.5 Summary of conditions for fully modeled spar case studies. ....	92
5.6 Surge free decay simulation results. ....	103
5.7 Heave free decay simulation results. ....	106
5.8 Pitch free decay simulation results. ....	109
5.9 Comparison of the statistics of surge response (Hurricane Condition). ....	112
5.10 Comparison of statistics of heave response (Hurricane Condition). ....	116
5.11 Comparison of the statistics of pitch response (Hurricane Condition). ....	118
5.12 Comparison of statistics of mooring tension. ....	119
5.13 Comparison of riser horizontal nodal reaction force at keel (production riser # 23, node # 11). ....	122
5.14 Natural periods comparison. ....	123
5.15 Spar surge response comparison. ....	124
5.16 Spar heave response comparison. ....	124
5.17 Spar pitch response comparison. ....	124
5.18 Comparison of pitch motion reduction. ....	125
6.1 Pretension from mooring lines and risers. ....	128
6.2 Summary of the spar platform used in case study. ....	129

TABLE	Page
6.3 Summary of free decay simulation.....	130
6.4 Summary of 100-year hurricane condition statistics (CASE A). ....	137
6.5 Summary of 100-year hurricane condition statistics (CASE B). ....	137
6.6 Summary of drilling riser top tension statistics.....	143
6.7 Summary of drilling riser top tension statistics.....	145
6.8 Summary of most loaded line top tension statistics. ....	147
7.1 Drag coefficient of the spar platform. ....	149
7.2 Summary of the spar platform used in case study. ....	151
7.3 Regular wave condition.....	151
7.4 Swell environment condition.....	151
7.5 Pitch motion natural periods and damping ratios. ....	154
7.6 Heave motion natural periods and damping ratio.....	155
7.7 Comparison of the statistics (Regular wave simulation A). ....	158
7.8 Comparison of the statistics (Regular wave simulation A). ....	158
7.9 Comparison of statistics (Regular wave simulation B). ....	168
7.10 Comparison of statistics (Regular wave simulation B and C).....	168
7.11 Summary of swell condition A statistics.....	185
7.12 Summary of swell condition B statistics. ....	185
8.1 Summary of loop current condition statistics (CASE A). ....	198
8.2 Summary of loop current condition statistics (CASE B). ....	198
8.3 Summary of loop current condition statistics (CASE C). ....	198
8.4 Summary of statistics of most loaded line top tension statistics. ....	199

## CHAPTER I

### INTRODUCTION

#### 1.1. General

As the search for oil and gas progresses into deep waters (>610 m (2000 ft)), it is expected that pile-supported platforms will not be used. The maximum water depth generally considered for fixed platforms is 366 m (1,200 ft) – 457 m (1,500 ft) primarily due to the cost of fabrication and installation constraints. A comparison of the relative cost trends for pile supported platforms, compliant towers, and tension leg platforms for the Gulf of Mexico, is shown in Fig. 1.1.

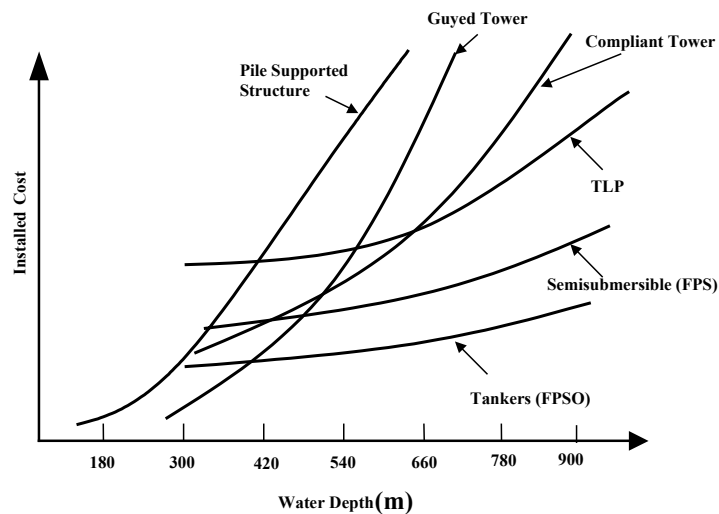


**Fig. 1.1. Platform cost comparison, Gulf of Mexico (Günther et al, 1988).**

---

This dissertation follows the style and format of the Journal of Ocean Engineering

However, new types of platforms such as tension leg platform (TLP), semisubmersible (FPS), floating production storage and offloading (FPSO) and spar offer promise of extending platform capability significantly into deeper water. These are loosely identified as compliant structures or floating structures, which are designed to move with the forces of wind, wave, and current, and are restrained with a mooring system rather than rigidly resist them.

After the middle of the 1990's, oil and gas fields progressed into deep water 914 m (3000 ft) – 3048 m (10,000 ft). For this range of water depth, classical spar, truss spar, semisubmersible and FPSO are common concepts used for developing oil and gas fields.

The spar platform has been considered as a competitive alternative for deep water oil and gas field development. Among the various hull types of a spar, the classical spar and the truss spar are the most attractive concepts for deep and ultra deep water production platforms. Fig. 1.2 shows a classical spar production platform and a truss spar production platform.

The classical spar production platform is a large circular cylinder with constant cross section and with a draft of approximately 198 m (650 ft). The idea behind this concept, or rather what is justifying the use of this enormous hull, is that due to the large draft the heave and pitch motion response of the platform is small enough to permit installation of rigid risers with dry trees.

The truss spar production platform is the latest developed concept that replaces the cylindrical lower section of a classical spar with an open truss structure that includes heave plates. One of the principle advantages of the truss spar is lower unit fabrication cost than the bottom section of a classical spar. The truss section of the truss spar decreases the hull

construction costs by 20% to 40% (Magee et al., 2000). The idea behind this concept is that the truss spar is relatively transparent to the ambient current, resulting in considerably less surge offset and mooring requirement, and the series of heave plates of truss spar are designed to reduce heave motion by increasing the added mass and hydrodynamic damping. The truss spar also has less vortex-induced vibration compared with classical spar.



**Fig. 1.2. Example Pictures of classical spar (left) and truss spar (right) (Courtesy, J. Ray McDermott).**

One of the advantages of the spar platform (classical and truss spar) is its natural frequency is not near the peak frequency of the dominant wave energy. However, wave and wind loads can excite large amplitude resonant motion and tension responses in mooring lines, most notably due to second order low-frequency effects. The contribution of the second order loads to the motions and tensions plays an important role in the platform design. Thus, dynamic analysis based on a reliable technique should be used for analyzing

spar production platform. The relevant theory and comparisons are summarized in Ran et al. (1995), Mekha et al. (1995), Cao and Zhang (1996), Kim et al. (1997), and Ran and Kim (1997). In offshore industry, the design of riser and mooring lines has mostly been based on either uncoupled quasi-static analysis (model mooring and riser as massless linear or nonlinear spring, calculate hull responses, and estimate the mooring tension from static-mooring load) or semi-coupled dynamic analysis (model mooring and riser as massless linear or nonlinear spring, calculated motions at the fairlead, and run line dynamics program for each mooring line). As the water depth greatly increases, more inertia and damping effects can come from mooring lines and risers. Under this circumstance, uncoupled analysis methods may lead to inaccurate results. The reliability of those uncoupled or semi-coupled approximation methods have been checked against model test data. However, the existing wave basin has depth limitation and the riser and mooring lines have to be truncated in the scale model testing thus not representing the actual contributions of mooring lines and riser. Thus, a reliable coupled dynamic analysis of the floating platform systems is more and more important with increasing water depth. Time domain coupled analysis methods of floating platform and mooring lines have been reported by many researchers (Paulling and Webster, 1986, Kim et al., 1994, Kim et al., 1997 and 2001, Ma et al., 2000, and Gupta et al., 2000). Paulling and Webster (1998) and Kim et al. (1994) conducted coupled analysis for TLP response. Gupta et al. (2000) showed coupled analysis in spar design. Ma et al. (2000) showed coupled analysis in both spar and TLP. In particular, Ran and Kim (1997) developed a very efficient 3-D hull/mooring/riser coupled dynamics program “WINPOST” based on a global-coordinate-based finite element methods (FEM), which was originally introduced by Garrett (1982).

The WINPOST is a time-domain program for the hull/mooring/riser coupled static/dynamic analysis of compliant offshore structures. In WINPOST, the platform is assumed to be a rigid body under going motion in waves, winds, and currents, and linear translational/rotational springs and linear translational dampers model the connections between the platform and the mooring lines and risers. The classical spar platform, which is the target structure in this research, generally uses rigid vertical riser systems. The vertical riser system is generally supported by a freely floating buoyancy-can near the top of the riser and it passes through a series of riser guide frames. Fig. 1.3 shows the general configuration of the spar buoyancy-can supported vertical riser system for a spar platform.

In the previous WINPOST model, the riser system includes a buoyancy-can is modeled as truncated simplified elements. The risers are modeled up to the spar keel and the buoyancy-cans effects are approximately induced in the hull restoring coefficient matrix (Tahar et al., 2002). The truncated riser model with approximated buoyancy-can connection cannot accurately model the interaction and gap effects between risers and support guide frames inside of the spar moon-pool. The truncated riser system also ignores the Coulomb friction between risers and support guide frames. Thus, the truncated riser system ignores additional restoring force and coulomb damping effects from interaction between risers and support guide frames, and this model overestimates the global spar motion. Thus, in the first part of this study, contact forces between the riser buoyancy-cans and riser support guide frames are modeled. In the new multi-contact model, the risers are modeled as an elastic rod extended through the moon-pool, and the series of guide frames are modeled as a horizontal spring with a large spring constant, thus the additional restoring force and moment from interaction between buoyancy-cans and guide frames on

the global spar motion are considered. The properties of the riser inside spar hull and buoyancy-cans including buoyancy are accurately modeled and the gap between the buoyancy can and riser guide frames are also modeled using four different types of spring connections. The new multi-contact riser model also considers the coulomb friction between the buoyancy-cans and riser guide frames. For simplification, the additional excitation on risers from moon-pool sloshing and riser-riser interactions are not considered in this study.

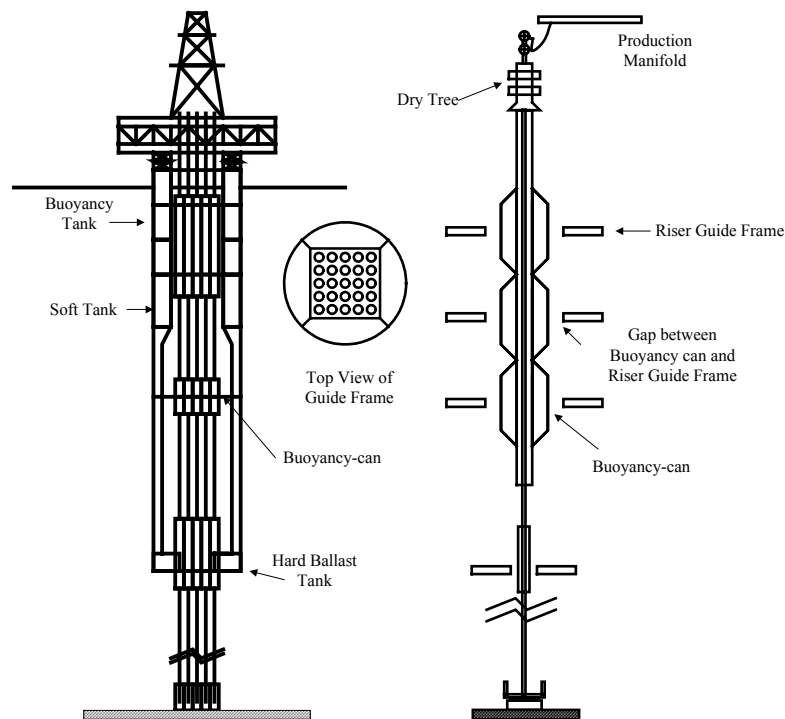


**Fig. 1.3. Schematic drawing of spar riser system with buoyancy-can.**

As the water depth of oil and gas fields is getting deeper, the length of the risers must increase, and the required buoyant force to support the rigid riser system must increase. Due to large buoyant force, the size of the buoyancy-can is large, and it makes installation



difficult, particularly from a safety standpoint. The alternative concept for riser support system is pneumatic cylinders. The function of pneumatic cylinder is to maintain the riser tension. Fig. 1.4 shows the pneumatic riser support system. In the second part of the study, the risers inside of the spar are fully modeled with pneumatic cylinders, and the results are compared with buoyancy-can supported model. The results may help to understand the alternate riser support system.

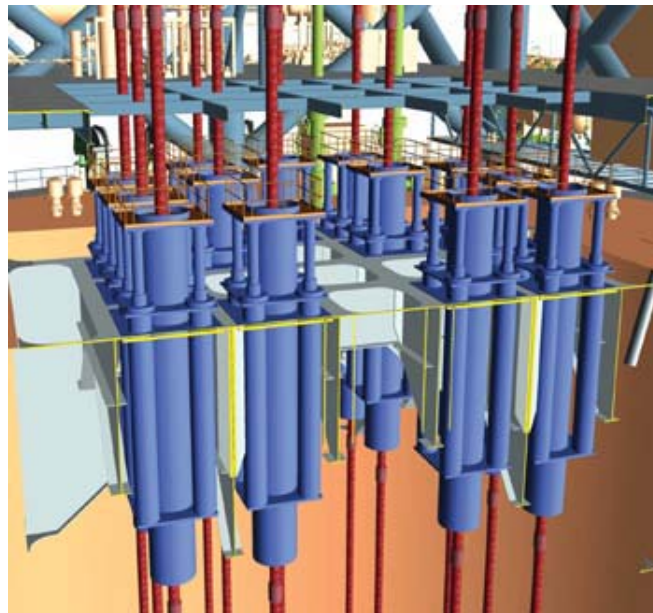


**Fig. 1.4. Pneumatic Riser Support System (Courtesy, Aker Maritime).**

In the third part of the study, the Mathieu's instability for the spar platform is checked by Mathieu instability diagram. The Mathieu instability diagram is generated by the Mathieu equation with Hill's infinite determinant methods (Jordan and Smith, 1977). Mathieu instability arises when there is a harmonic variation in the coefficients of a second order nonlinear difference equation. In the spar platform, it is well known that the pitch

motion is coupled with heave motion. The pitch restoring coefficient can be represented by a function of the displaced volume and the metacentric height. Due to heave motion, the displaced volume and the metacentric height of the spar platform are changed and this heave/pitch coupling can be represented by Mathieu's equation. In this part of the study, the Mathieu type instability for the spar platform is checked under long period regular wave environment as well as the West Africa and North Sea swell condition.

In the last part of the study, the simplified vortex induced vibration effects on the spar platform are considered. Vortex induced vibration effect is not significant in the hurricane condition, but is very important in the loop current condition. WINPOST uses piece-wise linear current velocity profile. Under this situation, the spar hull has single vortex shedding frequency at each depth. Thus, the vortex-induced vibration can be approximated as a sinusoidal force in the lift direction on the spar hull. The loop current condition in Gulf of Mexico is considered in this part of the study.

## **1.2. Literature Review**

The research interest on the spar platform has evolved during the 1990's. A number of investigators have studied separately several aspects of the spar platform coupled motion analysis with mooring lines and risers. The existing literature has shown the importance of coupled analysis and the various nonlinear effects in the calculation of the spar motion analysis.

Besides the coupled motion analysis of the spar platform, various studies were completed to investigate the wave structure interaction. Mekha et al. (1995, 1996) and

Johnson et al. (1996) performed time domain analyses for the spar platform in regular and irregular waves using Morison's equation. Their studies illustrated the importance of the different nonlinear effects. Weggel and Roesset (1996a, 1996b) did similar work using 2<sup>nd</sup> order diffraction theory implementing WAMIT (Lee, 1995), TFPOP (Ude et al. 1996), as well as an approximation by Donley and Spanos (1990). Zhang et al. (1995), Cao and Zhang (1996) used the Hybrid Wave Model (HWM) for irregular wave up to 2<sup>nd</sup> order and demonstrated the importance of accurate wave-kinematics in predicting the nonlinear response of the spar platform. Ran et al. (1995) used diffraction theory and boundary elements (as in WAMIT) to study the behavior of the spar platform in the time domain using 2<sup>nd</sup> order forces.

The development of an equation of motions for elastic rods and its computational analysis using finite difference method and finite element method was initiated by Nordgren (1974) and Garret (1982). Garret (1982) developed a finite element model of inextensible elastic principle stiffness. Using generalized coordinates, the model permits large deflections and finite rotation and accounts for the tension variation along its length. Chen et al. (2001) developed equation of motion of elastic rods based on large strain assumption. Ran and Kim (1997) and Kim et al. (2001a, 2001b) completed several coupled-dynamic analyses, and they did some studies on spars and TLPs using a very efficient program, WINPOST. A comparison between time- and frequency-domain analysis was also investigated by Ran et al. (1999). The time-domain analysis can simulate the nonlinear effect without linearization and generally produces large wave-frequency and slowly varying responses and mooring tension better than the frequency-domain analysis.

Prislin et al. (1999) discusses the full-scale measurement of the Oryx Neptune Spar

platform performance, and they discussed measured and predicted Neptune Spar motions during two storms during September 1998, hurricanes Earle and Georges. The measurement results show that the Neptune Spar motions are lower than predicted by physical model test and analytical tools. A possible reason for the difference is that the buoyancy-can effects in the spar moon-pool have been ignored in the experiment and analysis. Gupta et al. (2000) shows buoyancy-can effects on the global spar motions analysis. However they use three different programs to simulate the buoyancy-can effects, and thus the analysis processes are very complicated. In Tahar et al. (2002), the interaction effects between risers and riser guide frames are modeled as a simple inverted pendulum model as well as more rigorous riser modeling through riser guides inside the moon-pool. The interaction between risers and riser guide frames are modeled by Tahar et al. (2002), as horizontal springs with large stiffness to restrict the horizontal motion of the risers while allowing them to move freely in vertical direction. Zhang and Zou (2002) also considered the risers and riser guide frames effect on the global spar motion. Tahar et al. (2002) and Zhang and Zou (2002) results clearly show the buoyancy-can effect reduces the global spar motion, particularly in pitch. However, in the actual system the interaction between riser buoyancy-can and riser guide frame is gap contact. The horizontal connected spring ignores the gap contact effect between riser and riser guide frame. In the previous studies (Gupta et al. (2000), Tahar et al. (2002), and Zhang and Zou (2002)) did not consider the gap effects on the global spar motion as well as the buoyancy-can. The contact-induced force between riser and riser guide frame also adds Coulomb damping to spar motions in vertical direction. Gupta et al. (2000) and Zhang and Zou (2002) consider Coulomb damping effects in their study. Gupta et al. (2000) clearly showed that the Coulomb

damping reduces the spar heave motion, but results from Zhang and Zou (2002) showed that the Coulomb damping do not change heave motion significantly.

The pitch and heave coupling can be represented by a damped Mathieu's equation. Haslum and Faltinsen (1999) checked the Mathieu's instability in pitch motion combined with extreme amplitude heave resonance using a model test and simplified calculations. They showed a stability diagram for Mathieu's equation without considering pitch damping effects. Rho et al. (2002) also checked Mathieu's instability by model test and numerical calculation. They performed model tests for a spar platform with a moon-pool, helical strakes, and damping plates to see the effect of each case. Their studies show that the additional damping from heave plates and helical strake reduce the heave motion and experimentally confirmed the heave/pitch coupled non-linear motion for spar platforms. However, Haslum and Faltinsen (1999) and Rho et al. (2002) experiment did not considered hull/mooring/riser coupling effects. In their experiment, the spar model has very small KB (i.e. distance between buoyancy center and keel). The real spar platform has large KB (=164m). The location of the buoyancy tank in the real spar platform is located in upper part of the spar hull and the lower part of the hull is a hollow cylinder without a bottom. Thus, the center of buoyancy of the spar platform is located in upper one-third part of the spar hull, and it increases the metacentric height. Zhang et al. (2002) extended their studies to include pitch damping effects and developed a damped Mathieu's stability diagram for Mathieu's equation.

### 1.3. Objective and Scope

Despite the considerable amount of analytical and experimental studies conducted on the spar platform, there is still a need to compare and correlate the results obtained by various approaches. The main objectives of this study are to investigate the differences and increase the accuracy of the coupled analysis to predict for the global spar platform motions. As mentioned in section 1.2, the first part of this study discusses about buoyancy-can effects on the global spar motions. The newly developed numerical analysis program includes:

- multi-contact coupling effect for modeling the buoyancy-can effects on the global spar motions.
- a series of guide frames are modeled by four different spring connections (i.e. connected spring, piecewise-linear gap-contact spring, piecewise-quadratic gap-contact spring, and cubic spring) to evaluate the gap contact effects on the global spar motions as well as the buoyancy-cans
- Coulomb friction effects are modeled between buoyancy-cans and riser guide frames to evaluate the Coulomb damping effects on the global spar motions.

To capture the buoyancy-can effects (i.e. multi-contact coupling between buoyancy-can and guide frames which includes gap boundary condition and Coulomb friction) on the global spar motion, four comparison studies are conducted as follows:

- extended riser model (i.e. consider buoyancy-can effects) versus truncated riser model.
- four different guide frame models (i.e. connected spring, piecewise-linear

gap-contact spring, piecewise-quadratic gap-contact spring, and cubic spring) are compared case by case.

- Coulomb damping effects versus without Coulomb damping effects.
- compare the results with existing experimental and simulation results.

From these comparison studies, the newly developed numerical analysis program that includes buoyancy-can effects will be verified.

In the second part of this study, an alternative riser support system (i.e. pneumatic cylinder) is modeled in the newly developed numerical analysis program. The comparison study is conducted between buoyancy-can riser support system and pneumatic riser support system. Their different dynamic characteristics are extensively studied, and the feasibility of the pneumatic riser support system is discussed in this part of study.

In the third part of this study, the Mathieu's instability for a spar platform is discussed. In the newly developed numerical analysis program, the pitch/roll hydrostatic coefficients are recalculated for heave motion at each time step. As mentioned in section 1.2, the pitch damping effects on the Mathieu instability are extensively studied by following procedure:

- develop damped Mathieu stability diagram
- regular wave simulations are conducted for a spar platform without mooring lines and risers with different spar hull CD (drag coefficient) values
- regular wave simulations are conducted for a spar platform with mooring lines and risers

Based on the regular wave simulation results, the Mathieu instability in the swell wave condition is checked.

In the last part of this study, the vortex-induced vibration (VIV) effects on a spar

platform are studied. In the newly developed numerical program, the VIV is modeled as a harmonic lift force. The comparison study between with- and without-VIV effects are conducted for loop current condition in Gulf of Mexico, and a parametric study is conducted to evaluate the effect of different Strouhal number and lift coefficients.

#### **1.4. Organization**

In Chapter II, the dynamics of a floating platform are discussed. The linear and nonlinear wave kinematics theory as well as first- and second-order hydrodynamic forces and moments are explained in the first part of the Chapter II. The theoretical formulation and numerical implementation in the time domain for a spar platform are discussed in the second part of the Chapter II. The simplified vortex induced vibration effect on the spar platform is discussed in the third part of the Chapter II. The fourth part of the Chapter II discusses the Mathieu's instability problem for the spar platform.

In Chapter III, the dynamics of the mooring lines and risers are explained. The finite element modeling for mooring lines and risers in static and time-domain analysis are described.

In Chapter IV, the integrated modeling of the floating platform and mooring/riser system is discussed. The static and dynamic formulations of a single point spring-damper connection between the platform and mooring lines are discussed in the first part of this Chapter. In the second part, the static and dynamic formulations of multi-contact coupling between riser/buoyancy-can and riser guide frame are discussed with four different guide frame models (i.e. connected spring model, piece-wise linear gap spring model, piece-wise



quadratic gap spring model and cubic spring approximation model). In the third part, dynamic formulation of Coulomb damping between riser/buoyancy-can and guide frame is explained. In the last part of this chapter, the formulation for pneumatic cylinder riser support system is explained.

In Chapter V, a series of free decay simulations and 100-year hurricane simulations are conducted to check the buoyancy-can effects (i.e. multi-contact riser and Coulomb damping) on the spar platform. In the free decay simulations, the natural periods and the damping ratios of the newly developed models are obtained, and the results are systematically compared. The 100-year hurricane simulations show dynamic analysis of a spar platform in non-collinear wind, wave, and current condition. In the 100-year hurricane simulations, the buoyancy-can effects are clearly shown by a rational comparison of each case.

In Chapter VII, Mathieu's instability is checked for a spar platform. The parametric study is performed based on newly generated damped Mathieu's diagram. In this chapter, simulations are conducted by regular wave as well as swell condition. In the simulation, the uncoupled spar (without mooring/riser) and fully coupled spar (with mooring/riser) are compared to show the hull/mooring/riser coupling effects on suppressing the Mathieu's instability. In Chapter VIII, the loop current condition is conducted to show the vortex induced vibration effect on the global spar motion. Finally, the findings and possible extensions are summarized in Chapter IX.

## CHAPTER II

### DYNAMICS OF THE FLOATING PLATFORM

#### 2.1. Introduction

The wave loads and dynamic response of the floating structure are reviewed in this chapter. Linear and second order wave theories are reviewed first, then first- and second-order potential forces on the floating structures are reviewed. Finally, the dynamics of a floating structure are discussed. In this chapter, the heave and pitch coupling by time varying restoring coefficients for floating structures are presented. Discussion is presented as necessary and more detailed theory should be referred to the references.

#### 2.2. Wave Theory

The derivation of the linear wave theory is start with establishing and solving boundary value problems with linearized kinematics and dynamic free surface boundary conditions. The second-order Stokes wave theory is extended from the linear wave theory by perturbation of linearized boundary conditions up to second order. Both wave theories are based on irrotational motion, incompressible fluid, and continuous flow assumptions. Ignorance of the viscous effects, the boundary value problem can be expressed by velocity potential function  $\Phi(x,y,z)$ . From the velocity potential function, the velocity vectors and pressure in the fluid domain can be expressed by

$$\mathbf{u} = \frac{\partial\Phi}{\partial x}, \quad \mathbf{v} = \frac{\partial\Phi}{\partial y}, \quad \mathbf{w} = \frac{\partial\Phi}{\partial z} \quad (2.1)$$

$$p = -\rho g z - \rho \frac{\partial\Phi}{\partial t} - \frac{1}{2} (\Phi_x^2 + \Phi_y^2 + \Phi_z^2) \quad (2.2)$$

where  $u$ ,  $v$ ,  $w$  represent particle velocity vectors with respect to  $x$ -,  $y$ -, and  $z$ - axis in Cartesian coordinate system. The coordinate system is defined as origin is at mean water level,  $z$  is positive upward and the origin of the  $x$  and  $y$  axis are on the water surface following the right hand rule. The pressure  $p$  in the fluid filed in the equation (2.2) is comes from Bernoulli equation.  $\rho$  and  $g$  represent fluid density and gravitational accelerations.

Based on irrotational motion, incompressible fluid, and continuous flow assumptions boundary conditions must satisfy the Laplace equation:

$$\nabla^2\Phi = 0 \quad (2.3)$$

To solve the Laplace equation, the proper boundary condition in the domain should be defined. The common boundary conditions for ocean water wave problem are described in following equations.

Bottom boundary condition:

$$\frac{\partial\Phi}{\partial z} = 0 \quad \text{at } z = -d \quad (2.4)$$

where  $-d$  is water depth. This boundary condition is from flat bottom with impermissible assumption of the ocean bottom. At the free surface, the wave is governed by kinematics and dynamic free surface boundary conditions.

Free surface boundary condition:

1) kinematics free surface boundary condition

$$\frac{\partial \eta}{\partial t} + u \frac{\partial \eta}{\partial x} + v \frac{\partial \eta}{\partial y} - \frac{\partial \Phi}{\partial t} = 0 \quad \text{at } z = \eta \quad (2.5)$$

2) dynamic free surface boundary condition

$$\rho \frac{\partial \Phi}{\partial t} + \frac{1}{2} (\Phi_x^2 + \Phi_y^2 + \Phi_z^2) + \rho g z = 0 \quad \text{at } z = \eta \quad (2.6)$$

where  $\eta(x, y, t)$  represent free surface elevation as function of spatial and time. The kinematics boundary conditions states that the particle on the free surface at one instant of time will continue to stay on the free surface and the dynamics boundary condition is based on the assumption that the pressure at the free surface is constant and equal to atmospheric pressure. Due to nonlinear terms in free surface boundary condition and additional nonlinearity, the exact solution for the velocity potential in the Laplace equation with the described boundary conditions difficult to obtain. The most popular approach to solve this problem is small amplitude wave theory with perturbation methods. From small amplitude wave theory, the approximated solution of the certain order of accuracy can be obtained. As mentioned before, the linear wave theory uses linearized boundary condition, which considers first order only. The second order wave theory considers up to second order terms from the perturbation. Thus, the obtained velocity potential from second order theory includes the first order solution as well. The following equations show the first- and second-order velocity potentials and wave elevations.

First-order velocity potential:

$$\Phi^{(1)} = \text{Re} \left[ -\frac{igA}{\omega} \frac{\cosh k(z+d)}{\cosh kd} e^{i(kx \cos \theta + ky \sin \theta - \omega t)} \right] \quad (2.7)$$

Second-order velocity potential:

$$\Phi^{(2)} = \text{Re} \left[ -\frac{3}{8} \omega A^2 \frac{\cosh 2k(z+d)}{\sinh^4 kd} e^{i(2kx \cos \theta + 2ky \sin \theta - 2\omega t)} \right] \quad (2.8)$$

First-order free surface elevation:

$$\eta^{(1)} = A \cos(kx \cos \theta + ky \sin \theta - \omega t) \quad (2.9)$$

Second-order free surface elevation:

$$\eta^{(2)} = A^2 \frac{\cosh kd}{\sinh^3 kd} \cos(2kx \cos \theta + 2ky \sin \theta - 2\omega t) \quad (2.10)$$

where  $\theta$  is the incident wave angle,  $A$  is the wave amplitude,  $\omega$  is the wave frequency, and  $k$  is the wave number.

In the real ocean, the waves are random and irregular. A fully developed wave condition can be modeled as energy spectra described ensemble of regular wave trains combining in the random phases. Especially wind-driven wave height can be approximated by Rayleigh distribution. Several different wave spectra used in ocean engineering design of offshore facilities. Three of these spectra include the Pierson- Moskowitz, JONSWAP (Joint North Sea Wave Project), and ITTC (International Towing Tank Conference). To describe the wave energy distribution based on the wind velocity, significant wave height and peak wave period.

The random wave time series from a given wave spectrum  $S(\omega)$  can be generated by superposition of a large number of linear wave component with random phases

$$\eta(x, t) = \sum_{i=1}^N A_i \cos(k_i x + \omega_i t + \varepsilon_i) = \text{Re} \left[ \sum_{i=1}^N A_i e^{i(k_i x - \omega_i t + \varepsilon_i)} \right] \quad (2.11)$$

where  $A_i = \sqrt{2S(\omega_i)\Delta\omega}$ ,  $N$  and  $\Delta\omega$  are the number of wave components and interval of frequency division, and  $\varepsilon_i$  is a random phase angle. To avoid the increase of wave components for long simulation, equation (2.11) can be modified as

$$\eta(x, t) = \text{Re} \left[ \sum_{i=1}^N A_i e^{i(k_i x - \omega'_i t + \varepsilon_i)} \right] \quad (2.12)$$

where  $\omega'_i = \omega_i + \delta\omega_i$  and  $\delta\omega_i$  is random perturbation number uniformly distributed between  $-\Delta\omega/2$  and  $\Delta\omega/2$ . The random wave velocity and acceleration can be obtained in a similar manner.

### 2.3. Wave and Current Loads on Structures

In deep water, the platform is usually a large-displacement floating structure (e.g. TLP, classical spar, and tanker based FPSO) and due to the large volume and water plane area, most of offshore structures are in the diffraction regime. Therefore, The diffraction theory is the most appropriate methods to predict the wave load on the offshore platform. On the other for structure with slender member (e.g. truss member on spar) the Morison's equation is also widely used. Thus, in this section, both the diffraction theory and Morison's equation are discussed.

#### 2.3.1. Diffraction and Radiation Theory

In this section, the boundary value problem for the interactions of incident waves with a large three-dimensional body is reviewed. As mentioned before, the hydrodynamic

coefficient and the wave exciting force and moment on large floating structures can be obtained using three dimensional first- and second- order diffraction theory. As mentioned in section 2.2, the incident wave velocity potential ( $\Phi_I$ ) satisfy the Laplace equation, bottom boundary condition and free surface boundary condition (e.g. equation (2.3), (2.4), (2.5), and (2.6)). When a three-dimensional body interacts with incident waves in the fluid domain, two more velocity potentials occur during the interaction. The first additional velocity potential is the diffraction potential ( $\Phi_D$ ), which represents the scattered wave due to presence of the body. The second additional velocity potential is the radiation potential ( $\Phi_R$ ), which represents the waves generated by the body motion in calm water. To solve the fluid body interaction, two more boundary conditions must added. The first additional boundary condition is called the body boundary condition, which represents body surface with normal vector  $\mathbf{n}$ , and the second additional boundary condition, is called the Sommerfeld radiation condition, which represents the decay and vanish of the diffraction and radiation potential at the great distance from the structure. Therefore, the total velocity potential up to second order can be written as:

$$\Phi = \sum_{n=1}^2 \varepsilon^n \Phi^{(n)} = \sum_{n=1}^2 \varepsilon^n (\Phi_I^{(n)} + \Phi_D^{(n)} + \Phi_R^{(n)}) \quad (2.13)$$

where  $\varepsilon$  is a non-dimensional perturbation parameter that is equal to the wave stiffness. In the first order, the diffraction potential,  $\Phi_D^{(1)}$ , represents the scattered wave due to the presence of the fixed body, and the radiation potential,  $\Phi_R^{(1)}$ , represents the radiated wave due to the first order body motion in the calm water. In the second order,  $\Phi_D^{(2)}$  represents the combined diffracted potential due to the presence of the second order incident wave as well as the forcing due to all the quadratic contributions of the first order quantities on the free surface and on the body (i.e. a second order problem for a body either fixed or

undergoing first order motion only). The radiation potential,  $\Phi_R^{(2)}$ , represents the out going wave due to the second order motions only in calm water. Therefore,  $\Phi_I^{(2)}$  and  $\Phi_D^{(2)}$  give the total excitation force on the second order body motions, and  $\Phi_R^{(2)}$  is identical to that of a first order problem but at the respective sum and difference frequency. The following equations show the body surface boundary condition and Sommerfield radiation condition.

Body boundary condition:

$$\frac{\partial \Phi}{\partial n} = V_n \quad \text{on body surface} \quad (2.14)$$

where  $V_n$  is the normal velocity of the body at its surface

Sommerfield radiation condition:

$$\lim_{r \rightarrow \infty} \sqrt{r} \left( \frac{\partial \phi_{D,R}}{\partial r} \pm ik \phi_{D,R} \right) = 0 \quad (2.15)$$

where  $r$  is the radial distance from the center of the body.

### 2.3.2. First-and Second-order Boundary Value Problem

As mentioned in section 2.3.1., a body interacting with incoming monochromatic incident waves can be analyzed as a first-order boundary value problem. The total potential solution is written as:

$$\begin{aligned} \Phi^{(1)} &= \left( \Phi_I^{(1)} + \Phi_D^{(1)} + \Phi_R^{(1)} \right) \\ &= \text{Re} \left\{ \left[ \phi_I^{(1)}(x, y, z) + \phi_D^{(1)}(x, y, z) + \phi_R^{(1)}(x, y, z) \right] e^{-i\omega t} \right\} \end{aligned} \quad (2.16)$$

The incident wave potential from  $x, y \rightarrow \infty$  is given from linear wave theory and rewritten again:



$$\phi_1^{(1)} = \text{Re} \left[ -\frac{igA}{\omega} \frac{\cosh k(z+d)}{\cosh kd} e^{i(kx \cos \theta + ky \sin \theta - \omega t)} \right] \quad (2.17)$$

The boundary value problems for the first-order diffraction and radiation potentials are defined as:

$$\nabla^2 \phi_{D,R}^{(1)} = 0 \quad \text{in the fluid } (z < 0) \quad (2.18)$$

$$\left( -\omega^2 + g \frac{\partial}{\partial z} \right) \phi_{D,R}^{(1)} = 0 \quad \text{on the free surface } (z = 0) \quad (2.19)$$

$$\frac{\partial \phi_{D,R}^{(1)}}{\partial z} = 0 \quad \text{on the bottom } (z = -d) \quad (2.20)$$

$$\frac{\partial \phi_D^{(1)}}{\partial \mathbf{n}} = \frac{\partial \phi_1^{(1)}}{\partial \mathbf{n}} \quad \text{on the body surface} \quad (2.21)$$

$$\frac{\partial \phi_R^{(1)}}{\partial \mathbf{n}} = -i\omega \mathbf{n} \cdot (\boldsymbol{\xi}^{(1)} + \boldsymbol{\alpha}^{(1)} \times \mathbf{r}) \quad \text{on the body surface} \quad (2.22)$$

$$\lim_{r \rightarrow \infty} \sqrt{r} \left( \frac{\partial}{\partial r} \pm ik \right) \phi_{D,R}^{(1)} = 0 \quad \text{at far field} \quad (2.23)$$

where  $\mathbf{r}$  is the position vector on the body surface,  $\mathbf{n} = (n_x, n_y, n_z)$  is the outward unit normal vector on the body surface. The first-order motion of the body in the translational ( $\boldsymbol{\Xi}^{(1)}$ ) and rotational ( $\boldsymbol{\alpha}^{(1)}$ ) directions can be written as:

$$\boldsymbol{\Xi}^{(1)} = \text{Re} \{ \boldsymbol{\xi}^{(1)} e^{-i\omega t} \} \quad \boldsymbol{\xi}^{(1)} = \{ \xi_1^{(1)}, \xi_2^{(1)}, \xi_3^{(1)} \} \quad (2.24)$$

$$\boldsymbol{\alpha}^{(1)} = \text{Re} \{ \boldsymbol{\alpha}^{(1)} e^{-i\omega t} \} \quad \boldsymbol{\alpha}^{(1)} = \{ \alpha_1^{(1)}, \alpha_2^{(1)}, \alpha_3^{(1)} \} \quad (2.25)$$

where subscript 1,2 and 3 represent translational (surge, sway and heave) and rotational (roll, pitch and yaw) modes with respect to the x-, y-, and z-axis, respectively. To simplify the notation of motion, the first order six-degree of freedom can be rewritten as:

$$\zeta_i = \xi_i^{(1)} \quad \text{for } i = 1,2,3 \quad (2.26)$$

$$\zeta_i = \alpha_{i-3}^{(1)} \quad \text{for } i = 1,2,3 \quad (2.27)$$

The radiation potentials in terms of the velocity potential of the rigid body motion ( $\phi_i^{(1)}$ ) can be written as:

$$\phi_R^{(1)} = \sum_{i=1}^6 \zeta_i \phi_i^{(1)} \quad (2.28)$$

where  $\phi_i^{(1)}$  represents the velocity potential of the rigid body motion with unit amplitude in the  $i$ -th mode in the absence of incident waves. These potentials must satisfy the free surface boundary condition, bottom boundary condition, far field radiation boundary condition, and the body boundary condition. Substituting  $\phi_i^{(1)}$  into equation (2.22), the body boundary condition can be re-written as:

$$\frac{\partial \phi_i^{(1)}}{\partial n} = n_i \quad (2.29)$$

$$\frac{\partial \phi_i^{(1)}}{\partial n} = (\mathbf{r} \times \mathbf{n})_{i-3} \quad (2.30)$$

on the body surface( $S_B$ ).

Since the decomposition of the total potential is not unique, the diffraction potential ( $\phi_D^{(2)}$ ) and the radiation potential ( $\phi_R^{(2)}$ ) are defined as mentioned in section 2.3.1. In the presence of two plane incident waves of frequency  $\omega_i$  and  $\omega_j$  the second order potential can be written as

$$\Phi^{(2)}(x, t) = \text{Re} \sum_{j=1}^2 \sum_{i=1}^2 \left\{ \phi_i^-(x) e^{-i\omega^- t} + \phi_i^+(x) e^{-i\omega^+ t} \right\} \quad (2.31)$$

where  $\omega^- = \omega_j - \omega_i$  and  $\omega^+ = \omega_j + \omega_i$ . The sum- and difference-frequency of the second-order incident wave potentials can be written as:

$$\phi_i^+ = \frac{1}{2} (\gamma_{ji}^+ + \gamma_{ij}^+) \frac{\cosh k^+(z+d)}{\cosh k^+ h} e^{ik^+ x} \quad (2.32)$$

where  $\gamma_{ji}^+ = \frac{-igA_j k_j^2 (1 - \tanh^2 k_j h) - 2k_j k_i (1 + \tanh k_j h \tanh k_i h)}{2\omega_j v^+ - k^+ \tanh k^+ h}$  and

$$\phi_1^- = \frac{1}{2} (\gamma_{ji}^- + \gamma_{ij}^{-*}) \frac{\cosh k^- (z+d)}{\cosh k^- h} e^{ik^- x} \quad (2.33)$$

where  $\gamma_{ji}^- = \frac{-igA_j^* k_j^2 (1 - \tanh^2 k_j h) - 2k_j k_i (1 + \tanh k_j h \tanh k_i h)}{2\omega_j v^- - k^- \tanh k^- h}$ , superscript \* represents

complex conjugate, and  $v^\pm = \frac{\omega^{\pm 2}}{g}$ ,  $k^\pm = k_j \pm k_i$ .

The boundary value problem governing the second-order diffraction potential  $\phi_D^\pm$  is

$$\nabla^2 \phi_D^\pm = 0 \quad \text{in the fluid } (z < 0) \quad (2.34)$$

$$\left( -\omega^{\pm 2} + g \frac{\partial}{\partial z} \right) \phi_D^\pm = Q^\pm \quad \text{on the free surface } (z = 0) \quad (2.35)$$

$$\frac{\partial \phi_D^\pm}{\partial z} = 0 \quad \text{on the bottom } (z = -d) \quad (2.36)$$

$$\frac{\partial \phi_D^{(1)}}{\partial n} = \frac{\partial \phi_1^{(1)}}{\partial n} + B^\pm \quad \text{on the body surface} \quad (2.37)$$

$$\text{far field boundary condition} \quad (2.38)$$

The sum- and difference-frequency free-surface forcing terms in equation (2.35) can be written as:

$$Q^+ = \frac{1}{2} (q_{ji}^+ + q_{ij}^+) \quad (2.39)$$

$$Q^- = \frac{1}{2} (q_{ji}^- + q_{ij}^{-*}) \quad (2.40)$$

where

$$q_{ji}^+ = \frac{-i\omega}{2g} \phi_1^{(1)} \left( -\omega_j^2 \frac{\partial \phi_j^{(1)}}{\partial z} + g \frac{\partial^2 \phi_j^{(1)}}{\partial z^2} \right) + i\omega_1 \nabla \phi_j^{(1)} \cdot \nabla \phi_1^{(1)} - q_{ij}^+ \quad (2.41)$$

$$q_{jl}^- = \frac{i\omega}{2g} \phi_1^{(1)*} \left( -\omega_j^2 \frac{\partial \phi_j^{(1)}}{\partial z} + g \frac{\partial^2 \phi_j^{(1)}}{\partial z^2} \right) + i\omega_1 \nabla \phi_j^{(1)} \cdot \nabla \phi_1^{(1)*} - q_{ljl}^- \quad (2.42)$$

The sum- and difference-frequency body-surface forcing terms in equation (2.37) can be written as:

$$B^+ = \frac{1}{2} (b_{jl}^+ + b_{lj}^+) \quad (2.43)$$

$$B^- = \frac{1}{2} (b_{jl}^- + b_{lj}^{-*}) \quad (2.44)$$

where

$$b_{jl}^+ = -\frac{1}{2} \mathbf{n} \cdot (\zeta_1^{(1)} \cdot \nabla) \nabla \phi_j^{(1)} \quad (2.45)$$

$$b_{jl}^- = \frac{1}{2} \mathbf{n} \cdot (\zeta_1^{(1)*} \cdot \nabla) \nabla \phi_j^{(1)} \quad (2.46)$$

The radiation boundary condition equation (2.38) for second-order diffraction potential  $\phi_D^\pm$  is more complicated than that of the first-order. The  $\phi_D^\pm$  needs to be decomposed into a homogeneous solution and a particular solution, satisfying respectively the homogeneous and inhomogeneous free-surface boundary conditions and jointly the inhomogeneous body-boundary conditions. The homogeneous potential has far-field behavior of a free propagating wave, and the particular potential is governed by that of the free surface forcing,  $Q^\pm$ . The detailed explanations of the radiation boundary condition are available in Kim and Yue (1990).

The second-order radiation,  $\phi_R^\pm$ , satisfies the boundary value problems similar to the first-order radiation body boundary condition in equation (2.22). As mentioned before, the second order radiation potential involves only the first- and second- order potentials. Therefore, the solutions for the  $\phi_R^\pm$  for the second-order hydrodynamic coefficients are

identical to that of the first-order radiation problem at sum- and difference frequencies.

### 2.3.3. First-Order Hydrodynamic Force and Moment

The first-order forces and moments acting on a floating body as well as the free-surface elevations can be obtained directly from first-order diffraction and radiation potential. The first-order total pressure can be defined as:

$$\mathbf{P}^{(1)} = -\rho \left( \frac{\partial \Phi^{(1)}}{\partial t} + g z \right) \quad (2.47)$$

The six components of the force and moment vectors are directly obtained by integration of the pressure over the instantaneous wetted body surface ( $S_B$ ) or can be decomposed into three components.

$$\begin{aligned} \mathbf{F}^{(1)} &= \mathbf{F}_{HS}^{(1)} + \mathbf{F}_R^{(1)} + \mathbf{F}_{EX}^{(1)} \\ &= -\rho g \iint_{s_0} z n_j dS \\ &\quad - \rho \operatorname{Re} \sum_{j=1}^6 i \omega \zeta_j e^{-i \omega t} \iint_{s_0} \phi_j n_j dS \quad \text{for } j = 1 \text{ to } 6 \quad (2.48) \\ &\quad - \rho \operatorname{Re} i \omega A e^{-i \omega t} \iint_{s_0} (\phi_I + \phi_D) n_j dS \end{aligned}$$

where  $(n_1, n_2, n_3) = \mathbf{n}$  and  $(n_4, n_5, n_6) = \mathbf{r} \times \mathbf{n}$ . The first term on the left side of equation (2.58) represents hydrostatic restoring component ( $\mathbf{F}_{HS}^{(1)}$ ), the second term represents the radiation component ( $\mathbf{F}_R^{(1)}$ ), and the last term represents the linear wave exciting component ( $\mathbf{F}_{EX}^{(1)}$ ).

The hydrostatic restoring forces, ( $\mathbf{F}_{HS}^{(1)}$ ), are induced by the hydrostatic pressure

change (and wetted surface change in the calm water) due to the motion of the body. The matrix of the hydrostatic and gravitational restoring coefficients can be listed as follows:

$$K_{33} = \rho g A_w \quad (2.49)$$

$$K_{34} = K_{43} = \rho g A_w y_f \quad (2.50)$$

$$K_{35} = K_{53} = -\rho g A_w x_f \quad (2.51)$$

$$K_{44} = \rho g (S_{22} + \nabla z_b) - mgz_b \quad (2.52)$$

$$K_{45} = K_{54} - \rho g S_{12} \quad (2.53)$$

$$K_{46} = -\rho g \nabla x_b + mgx_g \quad (2.54)$$

$$K_{55} = \rho g (S_{11} + \nabla z_b) - mgz_b \quad (2.55)$$

$$K_{56} = -\rho g \nabla y_b + mgy_g \quad (2.56)$$

where  $\nabla$  is the mean body wetted volume,  $A_w$  is the water plane area,  $x_f$ , and  $y_f$  are the locations of the center of the flotation in the horizontal plane,  $x_g$ ,  $y_g$ , and  $z_g$  the location of the center of the gravity, and  $x_b$ ,  $y_b$ , and  $z_b$  are the location of the center of the gravity, and

$$S_{11} = \iint_{S_B} x^2 dS \quad (2.57)$$

$$S_{22} = \iint_{S_B} y^2 dS \quad (2.58)$$

$$S_{33} = \iint_{S_B} z^2 dS \quad (2.59)$$

The matrix form of hydrostatic coefficients with respect to water plane area can be shown as follows

$$\mathbf{K}_{ij} = \begin{bmatrix} 0 & 0 & 0 & 0 & 0 & 0 \\ 0 & 0 & 0 & 0 & 0 & 0 \\ 0 & 0 & \rho g A_w & 0 & \rho g A_w \overline{FG} & 0 \\ 0 & 0 & 0 & \rho g \nabla \overline{GM}_T & 0 & 0 \\ 0 & 0 & \rho g A_w \overline{FG} & 0 & \rho g \nabla \overline{GM}_L & 0 \\ 0 & 0 & 0 & 0 & 0 & 0 \end{bmatrix} \quad (2.60)$$

where

$\overline{FG}$  = horizontal distance between center of gravity and center of flotation

$\nabla$  = displaced volume (in calm water)

$\overline{GM}_T$  = metacentric height in the transverse direction (in calm water)

$\overline{GM}_L$  = metacentric height in the longitudinal direction (in calm water)

Therefore, hydrostatic forces can be written as:

$$\mathbf{F}_{HS}^{(1)} = -[\mathbf{K}]\{\zeta^{(1)}\} \quad (2.61)$$

The radiation component,  $(\mathbf{F}_R^{(1)})$ , in equation (2.48) comes from the first-order motion of the rigid body. Therefore, this term corresponds to the added mass and damping coefficient of the rigid body. The six components of the radiation forces and moments can be written in the matrix form as

$$\mathbf{F}_R^{(1)} = \text{Re}([\mathbf{f}]\{\zeta^{(1)}\}) \quad (2.62)$$

where

$$f_{ij} = -\rho \iint_{S_b} \frac{\partial \phi_i}{\partial n} \phi_j dS \quad (2.63)$$

The coefficients  $f_{ij}$  are complex as a result of the free surface condition, and the real and imaginary parts depend on the frequency  $\omega$ . Therefore, the coefficients take the form

$$f_{ij} = -\omega^2 M_{ij}^a - i\omega C_{ij} \quad (2.64)$$

Therefore, the equation (2.62) can be re-written as

$$\mathbf{F}_R^{(1)} = \text{Re} \left( [\mathbf{M}^a] \{\ddot{\zeta}^{(1)}\} + [\mathbf{C}] \{\dot{\zeta}^{(1)}\} \right) \quad (2.65)$$

where,  $\mathbf{M}^a$  represents the added mass coefficient matrix, and  $\mathbf{C}$  as the potential damping coefficients.

The last term in the right hand side of the equation (2.48) is related to the linear wave exciting forces and moments that are proportional to the incident wave amplitude.

$$\mathbf{F}_{EX}^{(1)} = \text{Re} \left\{ -\rho A e^{-i\omega t} \iint_{S_0} (\phi_I + \phi_D) \frac{\partial \phi_j}{\partial \mathbf{n}} dS \right\} \quad (2.66)$$

The exciting force from a unit amplitude incident wave is called as linear force transfer functions (LTF). LTF defines the relation between the wave elevation and the first-order diffraction forces on the body. The first-order motions follow from the equation of motions and in the absence of external forces it can be expressed as

$$\begin{aligned} \mathbf{M} \frac{\partial^2}{\partial t^2} (\boldsymbol{\Xi}^{(1)} + \boldsymbol{\alpha}^{(1)} \times \mathbf{r}_G) &= \mathbf{F}_{HS}^{(1)} + \mathbf{F}_R^{(1)} + \mathbf{F}_{EX}^{(1)} \\ [\mathbf{M}] \{\ddot{\zeta}^{(1)}\} &= -[\mathbf{K}] \{\zeta^{(1)}\} - ([\mathbf{M}^a] \{\ddot{\zeta}^{(1)}\} + [\mathbf{C}] \{\dot{\zeta}^{(1)}\}) + \mathbf{F}_{EX} \end{aligned} \quad (2.67)$$

where  $\mathbf{M}$  is  $6 \times 6$  body mass matrix that can be defined as

$$M_{ij} = \begin{bmatrix} m & 0 & 0 & 0 & mz_G & -my_G \\ 0 & m & 0 & -mz_G & 0 & mx_G \\ 0 & 0 & m & my_G & -mx_G & 0 \\ 0 & -mz_G & my_G & I_{11} & I_{12} & I_{13} \\ mz_G & 0 & -mx_G & I_{21} & I_{22} & I_{23} \\ -my_G & mx_G & 0 & I_{31} & I_{32} & I_{33} \end{bmatrix} \quad (2.68)$$

where  $m$  is the body mass and  $I_{ij}$  is the moment of inertia defined as



$$m = \iiint_{V_B} \rho_B dV \quad (2.69)$$

$$I_{ij} = \iiint_{V_B} \rho_B [x \cdot x \delta_{ij} - x_i \cdot x_j] dV \quad (2.70)$$

where  $\nabla$  denotes the body volume and  $\delta_{ij}$  is the Kronecker delta function.

### 2.3.4. Second-Order Hydrodynamic Force and Moment

The second-order forces and moments acting on the floating body can be obtained directly from second-order diffraction and radiation potential. The second-order total pressure can be obtained as:

$$P^{(2)} = -\rho \frac{\partial \Phi^{(2)}}{\partial t} - \frac{1}{2} \rho (\nabla \Phi^{(1)})^2 \quad (2.71)$$

In the presence of bichromatic waves, equation (2.81) can be re-written as:

$$P^{(2)} = \text{Re} \left[ A_j A_l p_{jl}^+ e^{-i\omega^+ t} + A_j A_l^* p_{jl}^- e^{-i\omega^- t} \right] \quad (2.72)$$

where  $p_{jl}^\pm$  is defined as the sum and difference frequency quadratic transfer functions for the pressure. The complete second-order pressure generally includes two separate contributions: (1) the quadratic products of the first order potentials ( $p_q$ ), and (2) the second order potential itself ( $p_p$ ). These two components can be expressed as

$$p_{jl}^\pm = p_{qjl}^\pm + p_{pjl}^\pm \quad (2.73)$$

$$p_{qjl}^+ = \left[ -\frac{1}{4} \rho_0 \nabla \phi_j^{(1)} \cdot \nabla \phi_l^{(1)} \right] / A_j A_l \quad (2.74)$$

$$p_{qjl}^- = \left[ -\frac{1}{4} \rho_0 \nabla \phi_j^{(1)} \cdot \nabla \phi_l^{(1)*} \right] / A_j A_l^* \quad (2.75)$$

$$p_{pjl}^\pm = \frac{1}{2} \rho_0 i \omega^\pm \phi^\pm / (A_j A_l, A_j A_l^*) \quad (2.76)$$

From the hydrodynamic pressure, the second-order wave forces and moments on a body can be obtained by direct integration of the hydrodynamic pressure over the instantaneous wetted body surface,  $S_B$ . The second-order forces and moments can be divided into four different components:

$$\mathbf{F}^{(2)} = \mathbf{F}_{HS}^{(2)} + \mathbf{F}_R^{(2)} + \mathbf{F}_p^{(2)} + \mathbf{F}_q^{(2)} \quad (2.77)$$

where  $\mathbf{F}_q^{(2)}$  represents the contribution from the quadratic product of first-order,  $\mathbf{F}_p^{(2)}$  is the second-order potential,  $\mathbf{F}_R^{(2)}$  is the second-order radiation potential, and the second-order hydrostatic coefficient  $\mathbf{F}_{HS}^{(2)}$ . The each second-order force and moment can be written as:

$$\mathbf{F}_p^{(2)} = -\rho \iint_{S_B} \frac{\partial \Phi}{\partial t} \mathbf{n} dS \quad (2.78)$$

$$\begin{aligned} \mathbf{F}_R^{(2)} = & -\rho \iint_{S_B} \left[ \frac{1}{2} (\nabla \Phi^{(1)})^2 + (\boldsymbol{\Xi}^{(1)} + \boldsymbol{\alpha}^{(1)} \times \mathbf{r}) \frac{\partial}{\partial t} (\nabla \Phi^{(1)}) \right] \mathbf{n} dS \\ & + \frac{1}{2} \rho g \int_{WL} \left[ \eta_r^{(1)} - (\xi_3^{(1)} + y \alpha_1^{(1)} - x \alpha_2^{(1)}) \right] \mathbf{N} dl + \boldsymbol{\alpha}^{(1)} \times \mathbf{F}^{(1)} \\ & - \rho g A_w \left[ \alpha_2^{(1)} (x_f \alpha_1^{(1)} - y_f \alpha_2^{(1)}) \right] \mathbf{k} \end{aligned} \quad (2.79)$$

where  $\mathbf{N} = \mathbf{n} / (1 - n_3^2)^{\frac{1}{2}}$ ,  $\mathbf{k}$  is the unit vector in the z-direction, and  $\eta_r^{(1)}$  is the relative wave height. The second order force from radiation and hydrostatics are similar to that of the first-order force. The wave damping and added mass at the sum- and difference-frequency can be obtained from first-order solutions, and the hydrostatic restoring coefficients are identical to that of the first-order. In the presence of bichromatic waves, the second-order wave exciting forces can be defined as

$$\mathbf{F}_{EX}^{(2)} = \text{Re} \sum_{j=1}^2 \sum_{l=1}^2 \left[ A_j A_l f_{jl}^+ e^{-i\omega^+ t} + A_j A_l^* f_{jl}^- e^{-i\omega^- t} \right] \quad (2.80)$$

$$\mathbf{f}_{jl}^{\pm} = \mathbf{f}_{qjl}^{\pm} + \mathbf{f}_{pj1}^{\pm} \quad (2.81)$$

where  $\mathbf{f}_{jl}^{\pm}$  is defined as the complete sum- and difference-frequency exciting force quadratic transfer functions (QTF). For fixed bodies, the QTF can be written as:

$$\mathbf{f}_{qjl}^{+} = \left[ -\frac{\rho}{4} \iint_{S_B} (\nabla \phi_j^{(1)} \cdot \nabla \phi_l^{(1)}) ndS - \frac{\rho \omega_j \omega_l}{4} \int_{WL} \phi_j^{(1)} \cdot \phi_l^{(1)} N dl \right] / A_j A_l \quad (2.82)$$

$$\mathbf{f}_{qjl}^{-} = \left[ -\frac{\rho}{4} \iint_{S_B} (\nabla \phi_j^{(1)} \cdot \nabla \phi_l^{(1)*}) ndS - \frac{\rho \omega_j \omega_l}{4} \int_{WL} \phi_j^{(1)} \cdot \phi_l^{(1)*} N dl \right] / A_j A_l^* \quad (2.83)$$

$$\mathbf{f}_{pj1}^{\pm} = \left[ \rho i \omega^{\pm} \iint_{S_B} (\phi_1^{\pm} + \phi_D^{\pm}) ndS \right] / (A_j A_l, A_j A_l^*) \quad (2.84)$$

### 2.3.5. Time Domain Expression for Wave Loads

In the previous section, the wave forces from potential theory were discussed. From previous section, the linear wave forces are calculated at the specified wave frequency, and the second order sum and difference frequency force are obtained from the interactions of the bichromatic waves. However, in the real ocean, the waves are random or irregular. In this section, the extension of monochromatic and bichromatic waves to the time domain random wave is discussed. The linear and second-order hydrodynamic forces on the body due to stationary Gaussian random seas can in general be expressed as a two-term Volterra series in time domain:

$$F^{(1)}(t) + F^{(2)}(t) = \int_{-\infty}^{\infty} h_1(\tau) \eta(t-\tau) d\tau + \int_{-\infty}^{\infty} \int_{-\infty}^{\infty} h_2(\tau_1 \tau_2) \eta(t-\tau_1) \eta(t-\tau_2) d\tau_1 d\tau_2 \quad (2.85)$$

where  $h_1(\tau)$  and  $h_2(\tau_1 \tau_2)$  are the linear and quadratic impulse response functions

respectively. Recall that the wave elevations can be expressed as a sum of frequency components, and the equation (2.85) can be rewritten in the equivalent form in linear and bi-frequency domain. For unidirectional wave exciting forces with N wave components it can be expressed as:

$$F_1^{(1)}(t) = \text{Re} \left[ \sum_{j=1}^N A_j L(\omega_j) e^{i\omega_j t} \right] \quad (2.86)$$

$$F_1^{(2)}(t) = \text{Re} \left[ \sum_{j=1}^N \sum_{l=1}^N A_j A_l^* D(\omega_j - \omega_l) e^{i(\omega_j - \omega_l)t} + \sum_{j=1}^N \sum_{l=1}^N A_j A_l S(\omega_j + \omega_l) e^{i(\omega_j + \omega_l)t} \right] \quad (2.87)$$

where \* represents complex conjugate of the quantities.  $L(\omega_j)$  is linear force transfer functions (LTF),  $D(\omega_j - \omega_l)$  and  $S(\omega_j + \omega_l)$  are difference- and sum-frequency forces quadratic transfer function (QTF) respectively. The first- and second-order force from radiation potential can be written as equation (2.88) in time domain:

$$F_R = -m(\infty)\ddot{\zeta} - \int_{-\infty}^t R(t-\tau)\dot{\zeta}d\tau \quad (2.88)$$

where the convolution integral represents the memory effects of the wave force on the platform from the waves generated by platform motion prior to time t.  $R(t)$  is called the retardation function and is related to the frequency domain solution of the radiation. The formulation for  $R(t)$  is shown as:

$$R(t) = \frac{2}{\pi} \int_0^{\infty} C(\omega) \frac{\sin \omega t}{\omega} d\omega \quad (2.89)$$

where  $C(\omega)$  is the wave damping coefficients at frequency  $\omega$  which is defined in equation (2.65). The term,  $m(\infty)$  in the equation (2.88) is the added mass of the body at the infinite frequency. The formulation for infinite added mass coefficients can be written as:

$$m(\infty) = m^a(\omega) - \int_0^{\infty} R(t) \cos \omega t dt \quad (2.90)$$

where  $m^a(\omega)$  is the added mass at frequency  $\omega$ . From previous derivations, the total wave force can be obtained by the summation of incident wave force, added mass, and radiation damping force

$$F_T = F_I + F_C + \tilde{F}_R \quad (2.91)$$

where  $F_T = F^{(1)} + F^{(2)}$  is the total wave exciting force,  $F_I = F_I^{(1)} + F_I^{(2)}$  is the summation of the equation (2.86) and (2.87),  $F_C$  and  $\tilde{F}_R$  are from equation second term and first term in the equation (2.88), respectively. The following formulations represent the energy spectra of the linear wave force, difference- and sum-frequency wave forces. These energy spectra can be obtained from equation (2.86) and (2.87) using by Fourier transform

$$S_F^{(1)}(\omega) = S_{\eta}(\omega) |L(\omega)|^2 \quad (2.92)$$

$$S_F^{(2)-}(\omega) = 8 \int_0^{\omega} |D(\mu, \omega - \mu)|^2 S_{\eta}(\mu) S_{\eta}(\omega - \mu) d\mu \quad (2.93)$$

$$S_F^{(2)+}(\omega) = 8 \int_0^{\omega/2} \left| S\left(\frac{\omega}{2} + \mu, \frac{\omega}{2} - \mu\right) \right|^2 S_{\eta}\left(\frac{\omega}{2} + \mu\right) S_{\eta}\left(\frac{\omega}{2} - \mu\right) d\mu \quad (2.94)$$

where  $S_{\eta}(\omega)$  is wave spectrum,  $S_F^{(1)}(\omega)$  is linear wave spectrum,  $S_F^{(2)-}(\omega)$  and  $S_F^{(2)+}(\omega)$  is the second-order sum- and difference-frequency wave force spectrum, respectively.

### 2.3.6. Morison's Equation and Lift Force on a Column Based Body

Viscous flow phenomena are of importance in several related wave and current loads

on offshore structures. For slender cylindrical members of a floating platform, where the diameter of the member is small compared to the wave length, the diffraction effect is usually negligible and the viscous effect becomes significant. For those members, the Morison's equation is commonly used for evaluating the wave load as well as current loads. Morison et al. (1950) proposed an equation for a fixed cylindrical body. However, Morison's equation can be modified in the case of floating cylindrical structure as follow:

$$F_n = C_m \rho \frac{\pi D^2}{4} \dot{u}_n - C_a \rho \frac{\pi D^2}{4} \ddot{x}_n + \frac{1}{2} \rho C_d (u_n - \dot{x}_n) |u_n - \dot{x}_n| \quad (2.95)$$

where  $F_n$  represents Morison's force,  $C_m (= 1 + C_a)$  represents inertia coefficient,  $C_a$  represents added mass coefficient, and  $C_d$  represents the drag coefficient.  $\dot{u}_n$  and  $u_n$  are the fluid acceleration and velocity normal to the body, and  $\ddot{x}_n$  and  $\dot{x}_n$  are normal acceleration and velocity of the structure. Equation (2.95) shows that the total force,  $F_n$ , is composed of inertia and viscous force terms. The first two terms on the right hand side of equation (2.95) show the inertia force including the Froude-Krylov force and added mass force. The last term in equation (2.95) represents the drag force in the relative velocity form. This relative-velocity form indicates that the drag force contributes to both the exciting force and damping force on the body. Another important viscous effect on the offshore floating structure is vortex-induced vibration. When a column based floating structure (i.e. classical spar) is exposed to strong current (i.e. Loop Currents). The pressure difference around a bluff body in current may cause flow separation. Due to the velocity difference between the outermost boundary layers and innermost boundary layer and if the velocity of flow is large enough, this causes the boundary layers to roll into the rear wake and form periodic vortices. The interaction of the structure with these vortices causes the structure to vibrate transverse to the flow direction, and this phenomenon is called as

vortex-induced vibration. The frequency of vortex shedding can be found by the Strouhal number that is function of Reynolds number and body geometry. In the numerical simulation called WINPOST, the currents are modeled as steady and unidirectional. In this case, the vortex-induced vibration can be modeled as a simple harmonic excitation force in the drag and lift direction, (Faltinsen, 1990). Based on unidirectional and steady current assumption, vortex-induced vibration can be approximated as follows:

$$F_L(t) = \frac{1}{2} \rho C_L U_\infty^2 D \cos(2\pi f_v t + \alpha) \quad (2.96)$$

where  $F_L$  is lift force on the structure,  $C_L$  is lift coefficient,  $U_\infty$  is incident steady current velocity from far upstream,  $f_v$  is Strouhal frequency, and  $\alpha$  is phase angle. In this study, the diameter of the classical spar platform hull is comparable to the wave length and thus diffraction theory is used to predict the wave force on the spar hull. However, when the viscous effect can not be neglected (as in the case of current and damping for the drag force in slow drift motion, and additional excitation force from vortex-induced vibration from strong current), the drag force term in Morison's equation and lift force are combined with the potential theory to determines the wave and current forces on the column based platforms.

#### 2.4. Time Domain Solution of the Platform

From conservation of momentum in the Newton's second law, the equilibrium of the inertia force and external force can be expressed as:

$$\mathbf{m} \frac{d^2 \mathbf{x}_G}{dt^2} = \mathbf{f} \quad (2.97)$$

$$\mathbf{I} \frac{d\boldsymbol{\varphi}}{dt} + \boldsymbol{\varphi} \times (\mathbf{I}\boldsymbol{\varphi}) = \mathbf{m}\mathbf{o} \quad (2.98)$$

where  $\mathbf{m}$  represents the body mass of floating platform,  $x_G$  represents body fixed coordinate with respect to the center of gravity of the floating structure,  $\mathbf{f}$  represents external force in equation (2.97).  $\mathbf{I}$  represents moment of inertia,  $\boldsymbol{\varphi}$  represents angular velocity,  $\mathbf{m}\mathbf{o}$  represents external moments in equation (2.98). The bold letters represent matrix and vector. In angular momentum equation (2.98), the second term in the left hand side is nonlinear, and the relation between the angular velocity and the Euler angles which define the body rotation are also nonlinear. These nonlinearities introduce complexity in solving the motion equations, especially in the frequency domain. If the rotation angle is assumed to be small, then equations (2.97) and (2.98) can be written as linear equations:

$$\mathbf{M}\ddot{\boldsymbol{\zeta}} = \mathbf{F}(t) \quad (2.99)$$

where  $\mathbf{M}$  represents  $6 \times 6$  body mass matrix which shown in equation (2.78),  $\ddot{\boldsymbol{\zeta}}$  represents body acceleration, and  $\mathbf{F}(t)$  represents the external force and moment vector. In the time domain, equation (2.99) can be expressed as follows:

$$\left[ \mathbf{M} + \mathbf{M}^a(\infty) \right] \ddot{\boldsymbol{\zeta}} + \mathbf{K}\dot{\boldsymbol{\zeta}} = \mathbf{F}_1(t) + \mathbf{F}_C(t, \dot{\boldsymbol{\zeta}}) + \mathbf{F}_N(t, \dot{\boldsymbol{\zeta}}) \quad (2.100)$$

where  $\mathbf{M}^a(\infty)$  is added mass as shown in equation (2.90),  $\mathbf{F}_1(t)$  is first- and second-order wave exciting force on the platform, and  $\mathbf{F}_C(t, \dot{\boldsymbol{\zeta}})$  represents radiation damping force as follows:

$$\mathbf{F}_C(t, \dot{\boldsymbol{\zeta}}) = \int_{-\infty}^t \mathbf{R}(t-\tau) \dot{\boldsymbol{\zeta}} d\tau \quad (2.101)$$

The last term in right hand side of the equation (2.100),  $\mathbf{F}_N(t, \dot{\boldsymbol{\zeta}})$ , represents an additional force from the Morison equation (and lift force for column based floating structure). There



are many numerical integration methods developed to solve the second-order differential equations. In this study, the Adams-Moulton method, which has a second-order accuracy, is used. To solve the equation (2.100) with Adams-Moulton method, equation (2.100) is first changed to two first order differential equations:

$$\overline{\mathbf{M}}\dot{\xi} = \mathbf{F}_I(t) + \mathbf{F}_C(t, \dot{\xi}) + \mathbf{F}_N(t, \dot{\xi}) - \mathbf{K}\xi \quad (2.102)$$

$$\dot{\xi} = \xi \quad (2.103)$$

where  $\overline{\mathbf{M}} = \mathbf{M} + \mathbf{M}^\infty$ . In the second step, performs time integration for equation (2.102) and (2.103) in  $t^{(n)}$  to  $t^{(n+1)}$  interval, then obtain following equations.

$$\overline{\mathbf{M}}\xi^{(n+1)} = \overline{\mathbf{M}}\xi^{(n)} + \int_{t^{(n)}}^{t^{(n+1)}} (\mathbf{F}_I + \mathbf{F}_C + \mathbf{F}_N) dt + \int_{t^{(n)}}^{t^{(n+1)}} -\mathbf{K}\xi dt \quad (2.104)$$

$$\xi^{(n+1)} = \xi^{(n)} + \int_{t^{(n)}}^{t^{(n+1)}} \xi dt \quad (2.105)$$

In the third step, applying the Adams–Moulton scheme  $\left( \int_{t^{(n)}}^{t^{(n+1)}} x dt = \frac{\Delta t}{2} [x^{(n)} + x^{(n+1)}] \right)$ , and rearranging the equations make the equation (2.104) and (2.105) yields the following linear algebraic equation with unknown quantities  $\xi^{(n+1)}$  and  $\zeta^{(n+1)}$ :

$$\begin{aligned} \overline{\mathbf{M}}\xi^{(n+1)} = \overline{\mathbf{M}}\xi^{(n)} + \frac{\Delta t}{2} (\mathbf{F}_I^{(n+1)} + \mathbf{F}_I^{(n)} + \mathbf{F}_C^{(n+1)} + \mathbf{F}_C^{(n)} + \mathbf{F}_N^{(n+1)} + \mathbf{F}_N^{(n)}) \\ - \frac{\Delta t}{2} \mathbf{K} (\xi^{(n+1)} + \xi^{(n)}) \end{aligned} \quad (2.106)$$

$$\xi^{(n+1)} = \frac{2}{\Delta t} (\zeta^{(n+1)} - \zeta^{(n)}) - \xi^{(n)} \quad (2.107)$$

However, due to convolution integral and drag force are functions of the unknown platform velocity at (n+1) time step. To avoid an iterative process to compute  $\mathbf{F}_C^{(n+1)}$  and  $\mathbf{F}_N^{(n+1)}$ , the Adams-Bashforth scheme is used. The following equations show the Adams-Bashforth scheme for the nonlinear terms:

$$\int_{t^{(n)}}^{t^{(n+1)}} \mathbf{F}_C dt = \frac{\Delta t}{2} (3\mathbf{F}_C^{(n)} - \mathbf{F}_C^{(n-1)}) \quad \text{and} = \Delta t \mathbf{F}_C^{(0)} \quad \text{for } n = 0 \quad (2.108)$$

$$\int_{t^{(n)}}^{t^{(n+1)}} \mathbf{F}_N dt = \frac{\Delta t}{2} (3\mathbf{F}_N^{(n)} - \mathbf{F}_N^{(n-1)}) \quad \text{and} = \Delta t \mathbf{F}_N^{(0)} \quad \text{for } n = 0 \quad (2.109)$$

From the above procedure, the final form of the integration equation can be obtained by combining the equation (2.106), (2.107), (2.108), and (2.109).

$$\left[ \frac{4}{\Delta t^2} \overline{\mathbf{M}} + \mathbf{K} \right] = \frac{4}{\Delta t^2} \overline{\mathbf{M}} \xi^{(n)} + (\mathbf{F}_I^{(n+1)} + \mathbf{F}_I^{(n)}) + (3\mathbf{F}_C^{(n)} + \mathbf{F}_C^{(n-1)}) + (3\mathbf{F}_N^{(n)} + \mathbf{F}_N^{(n-1)}) - 2\mathbf{K}\zeta^{(n)} + 2\mathbf{F}_0 \quad (2.110)$$

where

$$\Delta \zeta = \zeta^{(n+1)} - \zeta^{(n)} \quad (2.111)$$

and  $\mathbf{F}_0$  represents the net buoyancy force on the platform for balancing the system. From equation (2.110),  $\Delta \zeta$  can be obtained, then  $\xi^{(n+1)}$  and  $\zeta^{(n+1)}$  are obtained from (2.107) and (2.111), and these values are used in the right hand side of the equation (2.110) for the next time step. To avoid numerical instability in the Adams-Bashforth scheme, the smaller time interval ( $\Delta t$ ) is needed. However, due to the strong nonlinearity in the mooring line, much smaller time interval is required to solve the equation when the mooring lines and risers are included. Therefore, the time interval for simulation is governed by the mooring analysis, which is small enough for platform dynamic analysis.

## 2.5. Mathieu Instability of the Spar Platform

### 2.5.1. Mathieu Equation

The Mathieu equation is a special case of Hill's equation. Hill's equation is a linear equation with a periodic coefficient. The standard form for Hill's equation is as follows:

$$\ddot{x} + (\alpha + p(t))x = 0 \quad (2.112)$$

When  $p(t)$  is periodic, then it is known as Hill's equation. For the special case  $p(t) = \beta \cos t$ ,

$$\ddot{x} + (\alpha + \beta \cos t)x = 0 \quad (2.113)$$

it is referred to the undamped Mathieu's equation. A general damped Mathieu's equation is shown as follows:

$$\ddot{x} + c\dot{x} + (\alpha + \beta \cos t)x = 0 \quad (2.114)$$

This kind of nonlinear ordinary equation cannot be solved explicitly. However, by fixing the damping coefficient, zeros of infinite determinants can be found by specifying  $\alpha$  (or  $\beta$ ) and searching for the corresponding  $\beta$  (or  $\alpha$ ) that gives a set of results sufficiently close to zero. Two methods are available to find the parameter values for parametric plane. The first is using the perturbation method and the second is using Hill's infinite determinants method. Using Hill's infinite determinants, the parametric curves can be obtained by the complex Fourier series. The first periodic solution of period  $2\pi$  is as follow:

$$x(t) = \sum_{n=-\infty}^{\infty} s_n e^{int} \quad (2.115)$$

After substituting equation (2.115) into the damped Mathieu's equation, equation (2.113), the solution for all  $t$  is:

$$\sum_{n=-\infty}^{\infty} e^{int} \left\{ \frac{1}{2} \beta s_{n+1} + (\alpha + inc - n^2) s_n + \frac{1}{2} \beta s_{n-1} \right\} = 0 \quad (2.116)$$

This can be satisfied only if the coefficients are all zero:

$$\frac{1}{2} \beta s_{n+1} + (\alpha + inc - n^2) s_n + \frac{1}{2} \beta s_{n-1} = 0, \quad n = 0, \pm 1, \pm 2, \dots \quad (2.117)$$

This infinite set of homogeneous equations for  $\{s_n\}$  has non-zero solutions if the infinite determinant formed by the coefficients is zero, when  $\alpha \neq n^2$  for any  $n$ . The infinite

determinant is formed as:

$$\begin{vmatrix} \cdot & \cdot & \cdot & \cdot & \cdot & \cdot \\ \cdot & \gamma_1 & 1 & \gamma_1 & 0 & 0 \\ \cdot & 0 & \gamma_0 & 1 & \gamma_0 & 0 \\ \cdot & 0 & 0 & \gamma_1 & 1 & \gamma_1 \\ \cdot & \cdot & \cdot & \cdot & \cdot & \cdot \end{vmatrix} = 0 \quad (2.118)$$

where

$$\gamma_n = \beta/2(\alpha + inc - n^2), \quad n = 0, 1, 2, \dots \quad (2.119)$$

To find the second periodic solution of period  $4\pi$  is as followed

$$x(t) = \sum_{n=-\infty}^{\infty} s_n e^{\frac{1}{2}int} \quad (2.120)$$

After substituting equation (2.115) into damped Mathieu's equation, equation (2.114), the solution for all  $t$  is represented as:

$$\sum_{n=-\infty}^{\infty} e^{int} \left\{ \frac{1}{2}\beta s_{n+2} + \left(\alpha + \frac{1}{2}inc - \frac{1}{4}n^2\right)s_n + \frac{1}{2}\beta s_{n-2} \right\} = 0 \quad (2.121)$$

This can be satisfied only if the coefficients are all zero:

$$\frac{1}{2}\beta s_{n+2} + \left(\alpha + \frac{1}{2}inc - \frac{1}{4}n^2\right)s_n + \frac{1}{2}\beta s_{n-2} = 0, \quad n = 0, \pm 1, \pm 2, \dots \quad (2.122)$$

This infinite set of homogeneous equations for  $\{s_n\}$  has non-zero solutions if the infinite determinant formed by the coefficients is zero; when  $\alpha \neq n^2$  for any  $n$ . The infinite determinant is formed as:

$$\begin{vmatrix} \cdot & \cdot & \cdot & \cdot & \cdot & \cdot \\ \cdot & \gamma_2 & 1 & \gamma_2 & 0 & 0 \\ \cdot & 0 & \gamma_1 & 1 & \gamma_1 & 0 \\ \cdot & 0 & 0 & \gamma_1 & 1 & \gamma_1 \\ \cdot & 0 & 0 & 0 & \gamma_2 & 1 \\ \cdot & \cdot & \cdot & \cdot & \cdot & \cdot \end{vmatrix} = 0 \quad (2.123)$$

where

$$\gamma_{2n+1} = \beta / 2 \left( \alpha + \frac{1}{2} i(2n+1)c - \frac{1}{4} (2n+1)^2 \right), \quad n = 0, 1, 2, \dots \quad (2.124)$$

The parametric plane generated by Hill's infinite determinant method is shown in Fig. 2.1. The Fig. 2.1 shows that the second unstable region is more influenced by the damping effect than the principal unstable region, and the damped Mathieu diagram also shows that when the damping is added to the system, the unstable regions separate from the  $\alpha$ -axis. This means that the unstable region is reduced when damping is added to the system. However, when the principal unstable region is less influenced by damping, the principal unstable region should be examined carefully.

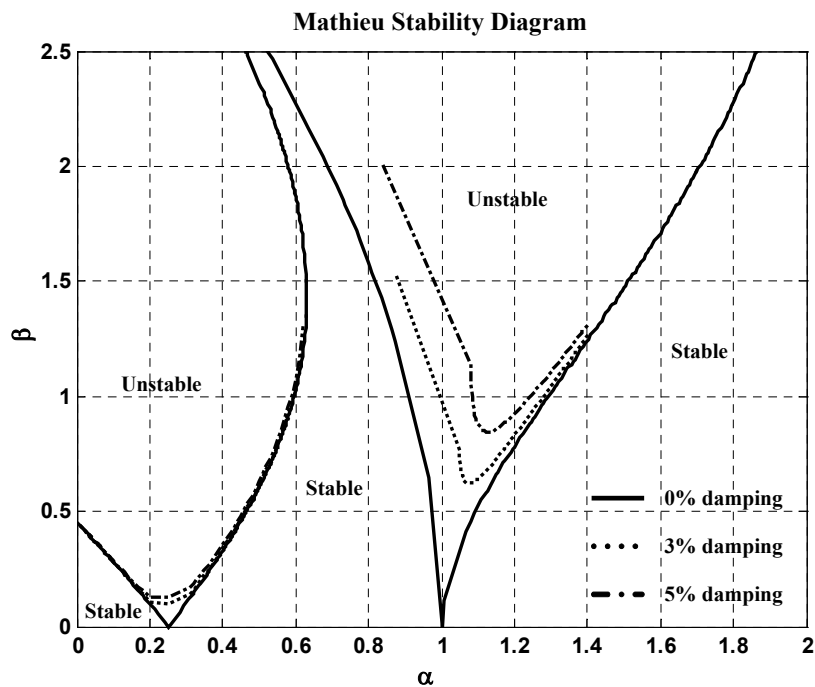


**Fig. 2.1. Stability diagram for damped Mathieu's equation.**

### 2.5.2. Heave/Pitch Coupled Equation for Classical Spar Platform

For a spar, the pitch restoring stiffness  $K_{55}$  is a function of displaced volume and Metacentric height  $\overline{GM}$ , represented by  $\rho g \nabla \overline{GM}$  in still water. When the spar has heave motion and the heave amplitude is assumed as  $\zeta_3$ , then the metacentric height and displaced volume are changed with heave motion. The metacentric height and displaced volume can be obtained by following equation:

$$\overline{GM}_{\text{new}} = \overline{GM} - \frac{1}{2} \zeta_3(t) \quad (2.125)$$

$$\nabla_{\text{new}} = \nabla - A_w \zeta_3(t) \quad (2.126)$$

where  $A_w$  is the spar water plane area. Based on a new metacentric height and displaced volume, the new pitch restoring stiffness,  $K_{55\text{new}}$ , can be calculated as follow:

$$K_{55\text{new}} = \rho g \nabla_{\text{new}} \overline{GM}_{\text{new}} = K_{55} - \frac{1}{2} \rho g (\nabla + 2A_w \overline{GM}) \zeta_3 + \frac{1}{2} \rho g A_w \zeta_3^2 \quad (2.127)$$

Equation (2.127) clearly shows heave/pitch coupling and also shows time dependence of pitch stiffness. For simplicity, the heave motion is assumed as a one-term harmonic,  $\zeta_3(t) = \zeta_3 \cos \omega t$ , where  $\omega$  is heave motion frequency. Thus, the pitch motion can be written as:

$$(I_{55} + A_{55}) \ddot{\zeta}_5(t) + C_{55} \dot{\zeta}_5(t) + \rho g \nabla (\overline{GM} - \frac{1}{2} \zeta_3 \cos \omega t) \zeta_5(t) = 0 \quad (2.128)$$

where  $I_{55}$  and  $A_{55}$  are the pitch moment of inertia and the added pitch moment of inertia.  $\zeta_5$  and  $\zeta_3$  are pitch and heave motion respectively. Based on the new pitch equation of motion the parameter in the Mathieu's equation can be defined as follows:

$$\alpha = \frac{\rho g \nabla GM}{(I_{55} + A_{55}) \omega^2} = \frac{\omega_5^2}{\omega^2} \quad (2.129)$$

$$\beta = \frac{0.5 \rho g \nabla \zeta_3}{(I_{55} + A_{55}) \omega^2} \quad (2.130)$$

$$c = \frac{C_{55}}{(I_{55} + A_{55}) \omega} \quad (2.131)$$

where,  $\omega_5$  is pitch natural frequency. However, in the time domain platform motion, equation (2.127) is used for  $K_{44\text{new}}$  and  $K_{55\text{new}}$  in Mathieu's instability investigation. The resultant formulation for pitch equation of motion in the time domain simulation can be expressed as:

$$(I_{55} + A_{55}) \ddot{\zeta}_5(t) + C_{55} \dot{\zeta}_5(t) + \rho g \nabla_{\text{new}} (GM - \frac{1}{2} \zeta_3(t)) \zeta_5(t) = 0 \quad (2.132)$$

## CHAPTER III

### DYNAMICS OF MOORING LINES AND RISERS

#### 3.1. Introduction

In the previous Chapter II, the hydrodynamic loads and motions of a floating platform are reviewed. In this chapter, the theoretical and numerical formulations of the static and dynamic analysis of mooring lines and risers are discussed.

The function of the mooring system is to keep the floating platform in the position over the reservoir. For station keeping purposes, there are two kinds of mooring systems, which are single-leg and multi-leg mooring systems. The most common concept in deepwater oil field is a multi-leg mooring system, which is more reliable compared to the single point mooring system. The multi-leg mooring systems can be categorized by their shape as: catenary system, semi-taut, taut system, and vertical tension tendons. The catenary and taut mooring systems generally use chain-wire-chain or chain-polyester-chain mooring combination. The semisubmersible, spar platform, and tanker based FPSO generally use these two kinds of mooring system for their station keeping. Due to the large footprint of the catenary spread mooring line, semi-taut or taut mooring lines are more common in the very deep water oil field. Vertical tension leg tendons that are generally made of steel pipes, have been used in Tension Leg Platform (TLP) to improve the heave, pitch and roll responses. Due to weight of tendons and installation costs, the TLP concept generally is considered to have a depth limitation (beyond 1300 meter).



To import and export oil and gas in the offshore field, risers are another important sub system of the floating platform. There are two kinds of riser systems commonly used in the offshore field. The first one is the steel vertical riser system which is used for a classical spar or truss spar platform. The advantage of a steel vertical riser is that a dry tree system can be used which does not need sub-sea operation. The other one is flexible riser, which can be arranged in catenary shapes. The advantage of the flexible riser system is that it is able to operate with much larger platform motion compared with steel vertical riser system. Although the main functions of the riser system are to transport oil and gas as well as drilling, the riser system also gives additional contribution to the station keeping performance of the offshore platform. For example, the vertical riser system in classical spar platform reduces heave and pitch responses, and the steel catenary riser reduces the translational motion of the floating platform.

In the theoretical and numerical view, both the mooring line and riser can be treated as slender rods or cables. Therefore, the analysis of the mooring lines and risers has been developed based on the slender rod theory. Due to large displacement and small strain, the geometric nonlinearity is dominant in mooring lines and risers. To consider the hydrodynamic force on the line as well as the strain and stress with geometric nonlinearity of the line, the beam theory combined with updated Lagrangian methods are used in this study, which is derived by Nordgen (1974) and Garret (1982). In this study, three-dimensional elastic rod theory, which is extended to include line stretching, are chosen to model the mooring lines and risers. The advantage of the slender rod theory is that the governing equation is developed in a single global coordinate system. In the numerical modeling scheme, the static and dynamic behavior (characteristics) of the lines are

modeled as a weak formulation based on the Galerkin methods in order to apply the Finite Element Method. Most of derivation and numerical schemes were developed by Ran (2000), and therefore, the derivation and the notation in this study follow Ran (2000).

### 3.2. Slender Rod Theory

In the slender rod theory, the deformed state of the rod can be expressed in terms of the position of the center line of the rod in the space curve  $\mathbf{r}(s,t)$ , as illustrated in Fig. 3.1.

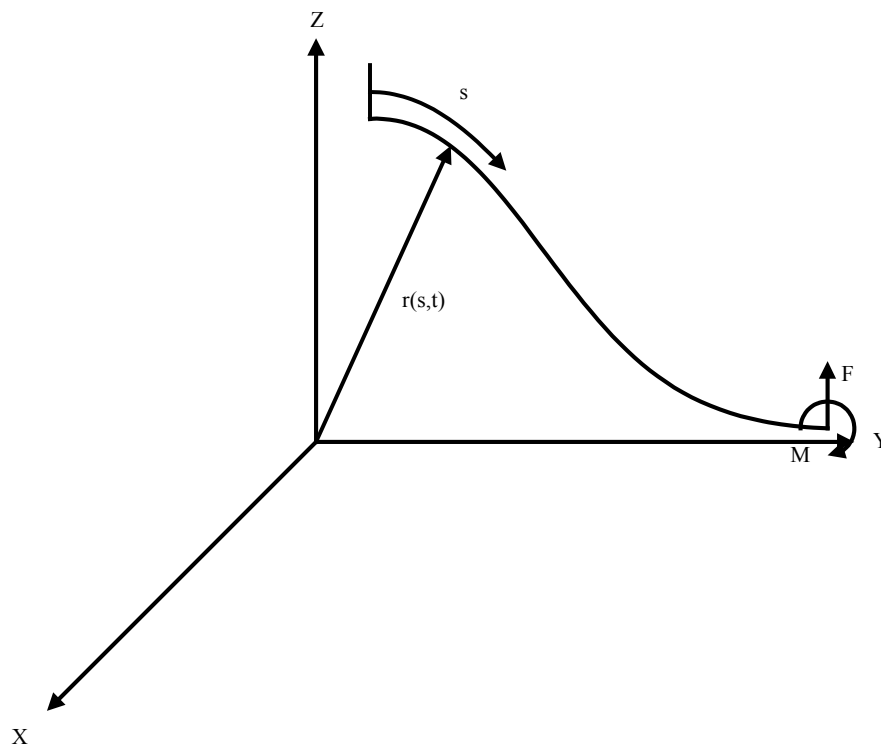


**Fig. 3.1. Coordinate system for slender rod.**

The space curve is defined by the position vector  $\mathbf{r}$  that is a function of the arc-length  $s$  (measured along the curve) and time  $t$ . If the rod is assumed as inextensible, which means the arc length  $s$  is not changed after deformation. The unit tangent vector to the space curve is  $\mathbf{r}'$ , and the principle normal vector is  $\mathbf{r}''$ . The bi-normal is directed along  $\mathbf{r}' \times \mathbf{r}''$ , where the prime denotes the differential with respect to arc-length. The internal state of stress at a point on the rod can be described by the resultant force  $\mathbf{F}$  and moment  $\mathbf{M}$  acting along the center line. The equilibrium of the linear force and moment for a segment of rod with unit arc-length leads to the following equation of motion:

$$\mathbf{F}' + \mathbf{q} = \rho \ddot{\mathbf{r}} \quad (3.1)$$

$$\mathbf{M}' + \mathbf{r}' \times \mathbf{F}' + \mathbf{m} = \mathbf{0} \quad (3.2)$$

where  $\mathbf{F}'$  : resultant force acting along the centerline

$\mathbf{M}'$  : resultant moment acting along the centerline

$\mathbf{q}$  : applied force per unit length

$\rho$  : mass of the rod per unit length

$\mathbf{m}$  : applied moment per unit length

For an elastic rod with equal principle stiffness, the bending moment is proportional to curvature and is directed along the bi-normal. Thus the resultant moment  $\mathbf{M}$  can be expressed as:

$$\mathbf{M}' = \mathbf{r}' \times EI\mathbf{r}'' + H\mathbf{r}' \quad (3.3)$$

where  $EI$  is the bending stiffness and  $H$  is the torque. Substituting the equation (3.3) into equation (3.2) then:

$$\mathbf{r}' \times \left[ (EI\mathbf{r}'')' + \mathbf{F} \right] + H'\mathbf{r}' + H\mathbf{r}'' + \mathbf{m} = \mathbf{0} \quad (3.4)$$

and the scalar product of the above equation with  $\mathbf{r}'$  yields:

$$\mathbf{H}' + \mathbf{m} \cdot \mathbf{r}' = \mathbf{0} \quad (3.5)$$

If there is no distributed torsional moment  $\mathbf{m} \cdot \mathbf{r}'$ , it is shown from the above equation that the torque  $\mathbf{H}$  is independent of arc lengths. Due to the circular cross section of the line element, there is no distributed torsional motion from the hydrodynamic forces. In addition, the torque in the lines is usually small, and thus it can be neglected. Therefore, both  $\mathbf{H}$  and  $\mathbf{m}$  are assumed to be zero. Thus, equation (3.5) can be rewritten as:

$$\mathbf{r}' \times \left[ (\mathbf{E}I\mathbf{r}'')' + \mathbf{F} \right] = \mathbf{0} \quad (3.6)$$

Using a scalar function  $\lambda(s, t)$ , equation (3.6) can be written as follows:

$$\mathbf{F} = -(\mathbf{E}I\mathbf{r}'')' + \lambda\mathbf{r}' \quad (3.7)$$

The scalar product of equation (3.7) with  $\mathbf{r}'$  results in:

$$\lambda = \mathbf{F} \cdot \mathbf{r}' - (\mathbf{E}I\mathbf{r}'')' \cdot \mathbf{r}' \quad (3.8)$$

or

$$\lambda = T - EI\kappa^2 \quad (3.9)$$

where  $T$  is the tension and  $\kappa$  is the curvature of the line. Combining equation (3.7) and (3.1), the equation of the rod can be established:

$$-(\mathbf{E}I\mathbf{r}'')'' + (\lambda\mathbf{r}')' + \mathbf{q} = \rho\ddot{\mathbf{r}} \quad (3.10)$$

In addition,  $\mathbf{r}$  must satisfy the inextensibility condition:

$$\mathbf{r}' \cdot \mathbf{r}' = 1 \quad (3.11)$$

If the rod is considered stretchable and the stretch is linear and small, the above inextensibility condition can be approximated by:

$$\frac{1}{2}(\mathbf{r}' \cdot \mathbf{r}' - 1) = \frac{T}{AE} \approx \frac{\lambda}{AE} \quad (3.12)$$

The scalar function  $\lambda(s, t)$  is also called a Lagrangian multiplier since it appears as a

result of the assumption of the inextensibility. The dependent variables  $\lambda(s, t)$  and  $\mathbf{r}(s, t)$  can be determined by using equation (3.10) and (3.11) or (3.12) with initial conditions, boundary conditions, and applied force  $\mathbf{q}$ . In most offshore applications, the applied force on the rod (mooring line, riser and tendon) comes from the hydrostatic and hydrodynamic force from the surrounding fluid, and the gravity force of the rod itself. Therefore, the external force equation can be written as:

$$\mathbf{q} = \mathbf{w} + \mathbf{F}^s + \mathbf{F}^d \quad (3.13)$$

where  $\mathbf{w}$  represents the weight of the rod per unit length,  $\mathbf{F}^s$  is the hydrostatic force on the rod per unit length, and  $\mathbf{F}^d$  is the hydrodynamic load per unit length. The hydrostatic force can be written as follows:

$$\mathbf{F}^s = \mathbf{B} - (\mathbf{P} \mathbf{r}')' \quad (3.14)$$

where  $\mathbf{B}$  is the buoyant force of the rod per unit length (assume the cross sections are subjected to the hydrostatic pressure), and the  $P$ , which is scalar, is the hydrostatic pressure at the point  $\mathbf{r}$  on the rod.

Morison's formula is used to compute the hydrodynamic force on the rod:

$$\begin{aligned} \mathbf{F}^d &= -C_A \ddot{\mathbf{r}}^n + C_M \dot{\mathbf{V}}^n + C_D |\mathbf{V}^n - \dot{\mathbf{r}}^n| (\mathbf{V}^n - \dot{\mathbf{r}}^n) \\ &= -C_A \ddot{\mathbf{r}}^n + \overline{\mathbf{F}}^d \end{aligned} \quad (3.15)$$

where  $C_A$  is the added mass coefficient (added mass per unit length),  $C_M$  is the inertia coefficient (inertia force per unit length per unit normal acceleration),  $C_D$  is the drag coefficient (drag force per unit length per unit normal velocity).  $\mathbf{V}^n$  and  $\dot{\mathbf{V}}^n$  are fluid velocity and acceleration normal to the rod centerline. The normal fluid velocity and acceleration can be obtained from the total fluid velocity and the tangent vector of the line:

$$\mathbf{V}^n = (\mathbf{V} - \dot{\mathbf{r}}) - [(\mathbf{V} - \dot{\mathbf{r}}) \cdot \mathbf{r}'] \mathbf{r}' \quad (3.16)$$

$$\dot{\mathbf{V}}^n = \dot{\mathbf{V}} - (\mathbf{V} \cdot \dot{\mathbf{r}}) \cdot \mathbf{r}' \quad (3.17)$$

where  $\dot{\mathbf{V}}$  and  $\mathbf{V}$  are the total water particle acceleration and velocity at the center line of the rod assuming the fluid field is undisturbed by the existence of the rod. In equation (3.15),  $\dot{\mathbf{r}}^n$  and  $\mathbf{r}'^n$  are the components of the rod acceleration and velocity normal to its centerline and can be obtained from the following equation:

$$\dot{\mathbf{r}}^n = \dot{\mathbf{r}} - (\dot{\mathbf{r}} \cdot \mathbf{r}') \mathbf{r}' \quad (3.18)$$

$$\mathbf{r}'^n = \mathbf{r}' - (\mathbf{r}' \cdot \mathbf{r}') \mathbf{r}' \quad (3.19)$$

Combining equation (3.13), (3.14) and (3.15) with (3.10), the equation of the rod with its weight, hydrostatic and hydrodynamic forces in water becomes:

$$\rho \ddot{\mathbf{r}} + C_a \rho_w \dot{\mathbf{r}}^n + (EI \mathbf{r}''')' - (\tilde{\lambda} \mathbf{r}')' = \tilde{\mathbf{w}} + \bar{\mathbf{F}}^d \quad (3.20)$$

where

$$\tilde{\lambda} = T + P - EI \kappa^2 = \tilde{T} - EI \kappa^2 \quad (3.21)$$

$$\tilde{\mathbf{w}} = \mathbf{w} + \mathbf{B} \quad (3.22)$$

$$\tilde{T} = T + P \quad (3.23)$$

and  $\tilde{\mathbf{w}}$  and  $\tilde{T}$  represent effective weight and effective tension respectively. Finally equation (3.20) with equation (3.11) or (3.12), the static or dynamic governing equation of the slender rod in water is established.

### 3.3. Finite Element Model

Since the governing equation is nonlinear, it is difficult to solve the equation by analytically. Therefore, the finite element method is used to transform the differential

equations into a series of algebraic equations through an integral statement. For convenience, the governing equations (3.20) and (3.12) are written in subscript notation:

$$-\rho\ddot{r}_i - C_a\rho_w\ddot{r}_i^n - (EI r_i'')'' + (\tilde{\lambda} r_i')' + \tilde{w}_i + \bar{F}_i^d = 0 \quad (3.24)$$

and

$$\frac{1}{2}(r_i' \cdot r_i' - 1) - \frac{\lambda}{AE} = 0 \quad (3.25)$$

where the subscripts range from 1 to 2 for the 2 dimensional problem and from 1 to 3 for the 3 dimensional problem. Repeating of the subscripts in the same equation means summation over the subscripts' range.

In the finite element method, the line is discretized into elements with finite length and the algebraic equations are developed in the element level. The unknown variable  $r_i(s, t)$ ,  $\lambda(s, t)$  can be approximated as:

$$r_i(s, t) = A_i(s)U_{ii}(t) \quad (3.26)$$

$$\lambda(s, t) = P_m(s)\lambda_m(t) \quad (3.27)$$

where,  $0 \leq s \leq L$ ,  $A_i(s)$  and  $P_m(s)$  are interpolation functions, and  $U_{ii}(t)$  and  $\lambda_m(t)$  are the unknown coefficients. By introducing shape functions for the solution, the weak formulations for applying the finite element method technique are written by multiplying the weight function:

$$\int_0^L \delta r_i \left[ -\rho\ddot{r}_i - C_a\rho_w\ddot{r}_i^n - (EI r_i'')'' + (\tilde{\lambda} r_i')' + \tilde{w}_i + \bar{F}_i^d \right] ds = 0 \quad (3.28)$$

$$\int_0^L \delta \lambda \left[ \frac{1}{2}(r_i' \cdot r_i' - 1) - \frac{\lambda}{AE} \right] ds = 0 \quad (3.29)$$

The following cubic shape functions for  $A_i(s)$  and quadratic shape function for  $P_m(s)$  are used for the basis of the relation of  $\delta r_i = A_i \delta U_{ii}(t)$  and  $\delta \lambda = P_m \lambda \delta_m$  such as equation (3.28) and (3.29):

$$\begin{aligned}
A_1 &= 1 - 3\xi^2 + 2\xi^3 \\
A_2 &= L(\xi - 2\xi^2 + \xi^3) \\
A_3 &= 3\xi^2 - 2\xi^3 \\
A_4 &= L(-\xi^2 + \xi^3)
\end{aligned} \tag{3.30}$$

$$\begin{aligned}
P_1 &= 1 - 3\xi^2 + 2\xi^3 \\
P_2 &= 4\xi(1 - \xi) \\
P_3 &= \xi(2\xi - 1)
\end{aligned} \tag{3.31}$$

where  $\xi = \frac{s}{L}$

$$\begin{aligned}
U_{i1} &= r_i(0, t), & U_{i2} &= r_i'(0, t) \\
U_{i3} &= r_i(L, t), & U_{i4} &= r_i'(L, t)
\end{aligned} \tag{3.32}$$

$$\lambda_1 = \lambda(0, t), \quad \lambda_2 = \lambda\left(\frac{L}{2}, t\right), \quad \lambda_3 = \lambda(L, t) \tag{3.33}$$

Thus, the equation (3.30) and (3.31) can be written as follows:

$$\int_0^L \delta r_i (\rho \ddot{r}_i - C_a \rho_w \ddot{r}_i^n) ds = \int_0^L (\rho \ddot{r}_i - C_a \rho_w \ddot{r}_i^n) A_1 \delta U_{i1} ds \tag{3.34}$$

$$\begin{aligned}
\int_0^L \delta r_i (EI r_i'') ds &= \int_0^L (EI r_i'') A_1 \delta U_{i1} ds \\
&= \left[ (EI r_i'') A_1 \Big|_0^L - EI r_i'' A_1 \Big|_0^L + \int_0^L EIA_1' r_i'' ds \right] \delta U_{i1}
\end{aligned} \tag{3.35}$$

$$\begin{aligned}
\int_0^L \delta r_i (\tilde{\lambda} r_i') ds &= \int_0^L (\tilde{\lambda} r_i') A_1 \delta U_{i1} ds \\
&= \left[ (\tilde{\lambda} r_i' A_1) \Big|_0^L + \int_0^L \tilde{\lambda} r_i' A_1' ds \right] \delta U_{i1}
\end{aligned} \tag{3.36}$$

$$\int_0^L \delta r_i [\tilde{w}_i + \bar{F}_i^d] ds = \left[ \int_0^L (\tilde{w}_i + \bar{F}_i^d) A_1 ds \right] \delta U_{i1} \tag{3.37}$$

$$\int_0^L \delta \lambda \left[ \frac{1}{2} (r_i' \cdot r_i' - 1) - \frac{\lambda}{AE} \right] ds = \int_0^L P_m \left[ \frac{1}{2} (r_i' \cdot r_i' - 1) - \frac{\lambda}{AE} \right] ds \delta \lambda_m \tag{3.38}$$

If equations (3.34) to (3.37) are assembled and the term of  $\delta U_{i1}$  is canceled out on both sides of the above equations, the following equation is obtained:



$$\begin{aligned}
& \int_0^L \left\{ A_1 (\rho \ddot{r}_i - C_a \rho_w \ddot{r}_i^n) + EIA_1 r'' + \tilde{\lambda} r'_1 A'_1 - A_1 (\tilde{w}_i + \bar{F}_i^d) \right\} ds \\
& = EIr_1'' A_1' \Big|_0^L + \left[ \tilde{\lambda} r'_1 + (EIr_1'')' \right] A_1 \Big|_0^L
\end{aligned} \tag{3.39}$$

The same procedures are applied for equation (3.38) and  $\delta\lambda_m$  is removed from both side of the equation (3.38), and the final form of the equation (3.38) is:

$$\int_0^L P_m \left[ \frac{1}{2} (r'_r \cdot r'_r - 1) - \frac{\lambda}{AE} \right] ds = 0 \tag{3.40}$$

Thus, the unknown quantities that need to be determined are the position vector and tangent vectors at the two end nodes of the elements and the scalar  $\lambda$ . The  $\lambda$  represents the line tension at the end nodes and the midpoint. By combining equations (3.19), (3.26) and (3.27) with (3.39) The equation of motion for the element can be written as follows:

$$(M_{ijkl} + M_{ijkl}^a) \ddot{U}_{jk} + (K_{ijkl}^1 + \lambda_n K_{nijlk}^2) U_{jk} - F_{il} = 0 \tag{3.41}$$

where

$$M_{ijkl} \ddot{U}_{jk} = \int_0^L \rho A_1 \ddot{r}_i ds = \int_0^L \rho A_1 A_k \delta_{ij} ds \ddot{U}_{jk} \tag{3.42}$$

$$\begin{aligned}
M_{ijkl}^a \ddot{U}_{jk} &= \int_0^L A_1 (C_A \ddot{r}_i^n) ds \\
&= C_A \left[ \int_0^L A_1 A_k \delta_{ij} ds - \int_0^L (A_1 A_k A'_s A'_t) U_{it} U_{js} \delta_{ij} ds \right] \ddot{U}_{jk}
\end{aligned} \tag{3.43}$$

$$K_{ijkl}^1 U_{jk} = \int_0^L EIA_1 r''_i ds = \int_0^L EIA_1'' A_k \delta_{ij} ds U_{jk} \tag{3.44}$$

$$K_{ijkl}^2 U_{jk} = \int_0^L \tilde{\lambda} A_1 r'_i ds = \tilde{\lambda}_n \int_0^L P_n A_1 A'_k \delta_{ij} ds U_{jk} \tag{3.45}$$

$$F_{il} = \int_0^L (\tilde{w}_i + \bar{F}_i^d) A_1 ds \tag{3.46}$$

and  $\delta_{ij}$  is the Kronecker Delta function. The resultant forces and moments are not included in this equation, since these forces and moments canceled with the neighboring element during the assembly of the element equation to satisfy the compatibility between

two elements.  $M_{ijkl}$  in equation (3.42) represents the mass term and  $M_{ijkl}^a$  in equation (3.43) represents the added mass. In equation (3.44) and (3.45), there are two stiffness terms.  $K_{ijkl}^1$  is the material stiffness that comes from the bending stiffness  $EI$ , and  $K_{ijkl}^2$  is the stiffness from tension and the curvature of the rod. For the two dimensional problem,  $i, j = 1, 2$  and for the three dimensional problem,  $i, j = 1, 2, 3$  and the subscript  $l, k, s, t = 1, 2, 3, 4$ . The equation (3.40) can be written as:

$$G_m = A_{mil}U_{kl}U_{ki} - B_m - C_{mn}\lambda_n = 0 \quad (3.47)$$

where

$$A_{mil}U_{jl}U_{jk} = \int_0^L P_m \frac{1}{2} r'_r r'_r ds = \frac{1}{2} \int_0^L P_m A'_l A'_k ds U_{jl} U_{jk} \quad (3.48)$$

$$B_m = \frac{1}{2} \int_0^L P_m ds \quad (3.49)$$

$$C_{mn} = \int_0^L P_m \frac{\lambda}{AE} ds = \frac{1}{AE} \int_0^L \lambda_n P_m P_n ds \quad (3.50)$$

From equations (3.41) and (3.47), each element has 12 second-order ordinary differential equations and 3 algebraic equations (3-dimensional problem). All these equations are nonlinear and the force vector,  $F_{il}$ , is also a nonlinear function of the unknowns because the wave force varies with the line position. In the next two sections, the numerical treatment for these nonlinear equations is discussed.

### 3.4. Formulation of Static Problem

In previous section, the equation of motion is derived and expended by finite element method. As mentioned in section 3.3, the numerical treatment of the nonlinear governing equation is discussed in this section and the next section. To analyze the dynamic problem,

first the static equilibriums should be obtained. Therefore, in this section, the static problem is discussed. If the inertia term in equation (3.41) is removed, then the governing equation becomes the static equilibrium equation and it also becomes a nonlinear algebraic equation:

$$\mathbf{R}_{il} = 0 \quad (3.51)$$

$$\mathbf{G}_m = 0 \quad (3.52)$$

where,

$$\mathbf{R}_{il} = (\mathbf{K}_{ijlk}^1 + \lambda_n \mathbf{K}_{nijlk}^2) \mathbf{U}_{jk} - \mathbf{F}_{il} \quad (3.53)$$

and  $\mathbf{F}_{il}$  is a static forcing term from the gravity force, drag force from the steady current and other applied static forces on the line. To solve the nonlinear equations, the Newton-Raphson's iterative method is used. Using the Taylor series expansion, the equation (3.51) and (3.52) can be expressed as follow:

$$\mathbf{R}_{il}^{(n+1)} = \mathbf{R}_{il}^{(n)} + \frac{\partial \mathbf{R}_{il}}{\partial \mathbf{U}_{jk}} (\Delta \mathbf{U}_{jk}) + \frac{\partial \mathbf{R}_{il}}{\partial \lambda_n} (\Delta \lambda_n) \quad (3.54)$$

$$\mathbf{G}_m^{(n+1)} = \mathbf{G}_m^{(n)} + \frac{\partial \mathbf{G}_m}{\partial \mathbf{U}_{jk}} (\Delta \mathbf{U}_{jk}) + \frac{\partial \mathbf{G}_m}{\partial \lambda_n} (\Delta \lambda_n) \quad (3.55)$$

where

$$\frac{\partial \mathbf{R}_{il}}{\partial \mathbf{U}_{jk}} = \mathbf{K}_{ijlk}^1 + \lambda_n \mathbf{K}_{nijlk}^2 \quad (3.56)$$

$$\frac{\partial \mathbf{R}_{il}}{\partial \lambda_n} = \mathbf{K}_{nijlk}^2 \quad (3.57)$$

$$\frac{\partial \mathbf{G}_m}{\partial \mathbf{U}_{jk}} = 2\mathbf{A}_{mkl} \mathbf{U}_{jk} \quad (3.58)$$

$$\frac{\partial \mathbf{G}_m}{\partial \lambda_n} = -\mathbf{C}_{mn} \quad (3.59)$$

and re-arrange the terms,

$$(\mathbf{K}_{ijlk}^1 + \lambda_n \mathbf{K}_{nijlk}^2) \Delta \mathbf{U}_{jk} + (\mathbf{K}_{nijlk}^2 \mathbf{U}_{jl}) \Delta \lambda_n = -\mathbf{R}_{il}^{(n)} \quad (3.60)$$

$$(2A_{mkl}U_{jl})\Delta U_{jk} + (-C_{mn})\Delta\lambda_n = -G_m^{(n)} \quad (3.61)$$

from equation (3.60) and (3.61), the equation can be expressed by matrix form as follows:

$$\begin{bmatrix} K_{ijkl}^{t0(n)} & K_{iln}^{t1(n)} \\ D_{mjk}^{t0(n)} & D_{mn}^{t1(n)} \end{bmatrix} \begin{Bmatrix} \Delta U_{jk} \\ \Delta\lambda_n \end{Bmatrix} = \begin{Bmatrix} -R_{il}^{(n)} \\ -G_m^{(n)} \end{Bmatrix} \quad (3.62)$$

where,

$$K_{ijkl}^{t0(n)} = K_{ijkl}^1 + \lambda_n^{(n)} K_{nijlk}^2 \quad (3.63)$$

$$K_{iln}^{t1(n)} = K_{nijlk}^2 U_{jk}^{(n)} = \left( \int_0^L P_n A'_l A'_k ds \right) U_{jk}^{(n)} \quad (3.64)$$

$$D_{mjk}^{t0(n)} = A_{mkp} U_{jp}^{(n)} = \left( \int_0^L P_m A'_k A'_p ds \right) U_{jp}^{(n)} \quad (3.65)$$

$$D_{mn}^{t1(n)} = -C_{mn} = -\frac{1}{AE} \int_0^L P_m P_n ds \quad (3.66)$$

$$R_{il}^{(n)} = (K_{ijkl}^1 + \lambda_n K_{nijlk}^2) U_{jk}^{(n)} - F_{il} \quad (3.67)$$

$$G_m^{(n)} = A_{mil} U_{kl}^{(n)} U_{ki}^{(n)} - B_m - C_{mn} \lambda_n^{(n)} = 0 \quad (3.68)$$

After renumbering, the equation (3.26) can be written in the form:

$$\mathbf{K}^{(n)} (\Delta \mathbf{y}) = \mathbf{F}^{(n)} \quad (3.69)$$

where  $U_{jk}$  and  $\lambda_n$  form the vector  $\mathbf{y}$

$$\mathbf{y}^T = [U_{11} \ U_{12} \ U_{21} \ U_{22} \ U_{31} \ U_{32} \ \lambda_1 \ \lambda_2 \ U_{13} \ U_{14} \ U_{23} \ U_{24} \ U_{33} \ U_{34} \ \lambda_3] \quad (3.70)$$

the force vector is as follows:

$$\mathbf{F}^T = [-R_{11} -R_{12} -R_{21} -R_{22} -R_{31} -R_{32} -G_1 -G_2 -R_{13} -R_{14} -R_{23} -R_{24} -R_{33} -R_{34} \ G_3] \quad (3.71)$$

and  $\mathbf{K}$  represents stiffness matrix

$$\mathbf{y}^{(n+1)} = \mathbf{y}^{(n)} + \Delta \mathbf{y} \quad (3.72)$$

In every iterative step, the stiffness and the force vector are recalculated to solve for  $\Delta \mathbf{y}$ .

Because one element has 15 algebraic equation, the bend width of the stiffness matrix is 15, and total number of equations for one rod is  $(N+1) \times 8 - 1$ , where N is number of elements in a rod. From right hand side of the equation (3.39), the force vector can be written as:

$$\mathbf{F}^r = \begin{bmatrix} -\left[\lambda r_1' + (\mathbf{B}r_1'')'\right] A_1 \Big|_{s=0} \\ \left[\mathbf{E}I r_1''\right] A_1' \Big|_{s=0} \\ -\left[\lambda r_2' + (\mathbf{B}r_2'')'\right] A_1 \Big|_{s=0} \\ \left[\mathbf{E}I r_2''\right] A_2' \Big|_{s=0} \\ -\left[\lambda r_3' + (\mathbf{B}r_3'')'\right] A_1 \Big|_{s=0} \\ \left[\mathbf{E}I r_3''\right] A_3' \Big|_{s=0} \\ 0 \\ 0 \\ \left[\lambda r_1' + (\mathbf{B}r_1'')'\right] A_1 \Big|_{s=L} \\ -\left[\mathbf{E}I r_1''\right] A_1' \Big|_{s=L} \\ \left[\lambda r_2' + (\mathbf{B}r_2'')'\right] A_1 \Big|_{s=L} \\ -\left[\mathbf{E}I r_2''\right] A_2' \Big|_{s=L} \\ \left[\lambda r_3' + (\mathbf{B}r_3'')'\right] A_1 \Big|_{s=L} \\ \left[\mathbf{E}I r_3''\right] A_1' \Big|_{s=L} \\ 0 \end{bmatrix} = \begin{bmatrix} -N_1^{[1]} \\ -L_1^{[1]} \\ -N_2^{[1]} \\ -L_2^{[1]} \\ -N_3^{[1]} \\ -L_3^{[1]} \\ 0 \\ 0 \\ -N_1^{[2]} \\ -L_1^{[2]} \\ -N_2^{[2]} \\ -L_2^{[2]} \\ -N_3^{[2]} \\ -L_3^{[2]} \\ 0 \end{bmatrix} \quad (3.73)$$

where the superscript [1] represents the first end of the element ( $s = 0$ ) and [2] represents the second end ( $s = L$ ).  $\mathbf{N} = \{N_1, N_2, N_3\}^T$  represents the nodal resultant force and  $\mathbf{L} = \{L_1, L_2, L_3\}^T$  represents the nodal resultant moment  $\mathbf{M} (\mathbf{M} = \mathbf{L} \times \mathbf{r}')$ . Therefore, after solving the variables U and  $\lambda$  (at iteration  $n+1$ ), the resultant force at the end nodes of an element can be obtained from force vector  $\mathbf{F}^r$

$$\mathbf{F}^r = -\mathbf{F}^{(n+1)} \quad (3.74)$$

### 3.5. Formulation for Dynamic Problem – Time Domain Integration

The dynamic equation of motion (3.41), and the stretch condition (3.47) can be rearrange as follows:

$$\widehat{M}_{ijkl} \ddot{U}_{jk} = -\left(K_{ijkl}^1 + \lambda_n K_{nijlk}^2\right) U_{jk} + F_{il} = \widehat{F}_{il} \quad (3.75)$$

$$G_m = A_{mil} U_{kl} U_{ki} - B_m - C_{mn} \lambda_n = 0 \quad (3.76)$$

where,

$$\widehat{M}_{ijkl} = M_{ijkl} + M_{ijkl}^a \quad (3.77)$$

$$\widehat{F}_{il} = -F_{il}^1 - F_{il}^2 + F_{il} \quad (3.78)$$

$$F_{il}^1 = K_{ijkl}^1 U_{jk} \quad (3.79)$$

$$F_{il}^2 = \lambda_n K_{nijlk}^2 U_{jk} \quad (3.80)$$

The equation (3.77) is a second order differential equation and (3.76) is algebraic equation with no time derivatives of the variables. To establish the time integration numerical scheme, equation (3.77) is split into two first order differential equations:

$$\widehat{M}_{ijkl} \dot{V}_{jk} = \widehat{F}_{il} \quad (3.81)$$

$$\dot{U}_{jk} = V_{jk} \quad (3.82)$$

Integrating the above two equations from time  $t^{(n)}$  (at  $n^{\text{th}}$  time step) to  $t^{(n+1)}$  (at  $n+1^{\text{th}}$  time step) the equation can be written as:

$$\int_{t^{(n)}}^{t^{(n+1)}} \widehat{M}_{ijkl} \dot{V}_{jk} dt = \int_{t^{(n)}}^{t^{(n+1)}} \widehat{F}_{il} dt \quad (3.83)$$

$$\int_{t^{(n)}}^{t^{(n+1)}} \dot{U}_{jk} dt = \int_{t^{(n)}}^{t^{(n+1)}} V_{jk} dt \quad (3.84)$$

Because  $\widehat{M}_{ijk}$  includes the added mass, the mass term is not constant, and it varies with line position, which means it is a function of time. By approximating the time varying  $\widehat{M}_{ijk}$  in time interval  $\Delta t(t^{(n+1)} - t^{(n)})$  to be a constant  $\widehat{M}_{ijk}^{(n+\frac{1}{2})}$ , which is the mass at  $t^{(n)} + \frac{\Delta t}{2}$ , then the integration in equation (3.83) can be simplified as follows with second order accuracy as:

$$\widehat{M}_{ijk}^{(n+\frac{1}{2})} \dot{V}_{jk}^{(n+1)} + \widehat{M}_{ijk}^{(n+\frac{1}{2})} \dot{V}_{jk}^{(n)} = \int_{t^{(n)}}^{t^{(n+1)}} \widehat{F}_{il} dt \quad (3.85)$$

The  $V_{jk}^{(n+1)}$  of the equation (3.84) can be obtained as follows using trapezoidal methods:

$$U_{jk}^{(n+1)} = U_{jk}^{(n)} + \frac{\Delta t}{2} (V_{jk}^{(n+1)} + V_{jk}^{(n)}) \quad (3.86)$$

Re-arranging equation (3.85) and (3.86), the equation becomes:

$$\frac{4}{\Delta t^2} \widehat{M}_{ijk}^{(n+\frac{1}{2})} \Delta U_{jk} = \frac{4}{\Delta t^2} \widehat{M}_{ijk}^{(n+\frac{1}{2})} V_{jk}^{(n)} + \frac{2}{\Delta t} \int_{t^{(n)}}^{t^{(n+1)}} \widehat{F}_{il} dt \quad (3.87)$$

$$V_{jk}^{(n+1)} = \frac{2}{\Delta t} (\Delta U_{jk}) - V_{jk}^{(n)} \quad (3.88)$$

where

$$\Delta U_{jk}^{(n+1)} = U_{jk}^{(n+1)} - U_{jk}^{(n)} = \frac{\Delta t}{2} (V_{jk}^{(n+1)} + V_{jk}^{(n)}) \quad (3.89)$$

and the integral term in equation (3.85) can be written as:

$$\int_{t^{(n)}}^{t^{(n+1)}} \widehat{F}_{il} dt = - \int_{t^{(n)}}^{t^{(n+1)}} F_{il}^1 dt - \int_{t^{(n)}}^{t^{(n+1)}} F_{il}^2 dt + \int_{t^{(n)}}^{t^{(n+1)}} F_{il} dt \quad (3.90)$$

For the first and second terms at the right hand side, applying trapezoidal rules, then

$$\begin{aligned} \int_{t^{(n)}}^{t^{(n+1)}} F_{il}^1 dt &= \frac{\Delta t}{2} (F_{il}^{1(n+1)} + F_{il}^{1(n)}) \\ &= \frac{\Delta t}{2} [K_{ijk}^1 \Delta U_{jk} + 2K_{ijk}^1 U_{jk}^{(n)}] \end{aligned} \quad (3.91)$$

$$\begin{aligned}
\int_{t^{(n)}}^{t^{(n+1)}} F_{il}^2 dt &= \frac{\Delta t}{2} (F_{il}^{2(n+1)} + F_{il}^{2(n)}) \\
&= \frac{\Delta t}{2} \left[ \lambda_n^{(n+1)} K_{nijlk}^2 U_{jk}^{(n+1)} + \lambda_n^{(n)} K_{nijlk}^2 U_{jk}^{(n)} \right] \\
&\approx \frac{\Delta t}{2} \left[ \lambda_n^{(n+\frac{1}{2})} K_{nijlk}^2 U_{jk}^{(n+1)} + \lambda_n^{(n+\frac{1}{2})} K_{nijlk}^2 U_{jk}^{(n)} \right] \\
&= \frac{\Delta t}{2} \left[ 2\lambda_n^{(n+\frac{1}{2})} K_{nijlk}^2 U_{jk}^{(n)} + 2K_{nijlk}^2 U_{jk}^{(n)} \Delta\lambda_n + \lambda_n^{(n-\frac{1}{2})} K_{nijlk}^2 \Delta U_{jk} \right]
\end{aligned} \tag{3.92}$$

where  $\Delta\lambda_n = \lambda_n^{(n+\frac{1}{2})} - \lambda_n^{(n-\frac{1}{2})}$ . The third term in equation (3.90) includes the applied force  $F_{il}$  which is from gravity and hydrodynamic forces. The gravity force is independent of time, but the hydrodynamic force from Morison equation is unknown at time step (n+1) since the force is function of the unknown rod position and velocity. Therefore, the Adams-Bashforth explicit scheme is used for the integration:

$$\int_{t^{(n)}}^{t^{(n+1)}} F_{il}^2 dt = \begin{cases} \Delta t F_{il}^{(0)} & \text{for step 1} \\ \frac{\Delta t}{2} (3F_{il}^{(n)} + F_{il}^{(n-1)}) & \text{for other step} \end{cases} \tag{3.93}$$

Using the above equations, the time integration equation (3.85) can be obtained as follows:

$$\begin{aligned}
&\left[ \frac{4}{\Delta t^2} \widehat{M}_{ijlk}^{(n+\frac{1}{2})} + K_{ijlk}^1 + \lambda_n^{(n-\frac{1}{2})} K_{nijlk}^2 \right] \Delta U_{jk} + 2K_{nijlk}^2 U_{jk}^{(n)} \Delta\lambda_n \\
&= \frac{4}{\Delta t^2} \widehat{M}_{ijlk}^{(n+\frac{1}{2})} V_{jk}^{(n)} + (3F_{il}^{(n)} - F_{il}^{(n-1)}) - 2K_{ijlk}^1 U_{jk}^{(n)} - 2\lambda_n^{(n+\frac{1}{2})} K_{nijlk}^2 U_{jk}^{(n)}
\end{aligned} \tag{3.94}$$

Using Adams-Bashforth method can approximate the time varying mass:

$$\widehat{M}_{ijlk}^{(n+\frac{1}{2})} = \frac{1}{2} (3\widehat{M}_{ijlk}^{(n)} - \widehat{M}_{ijlk}^{(n-1)}) \tag{3.95}$$

For the stretch condition (equation (3.76)), the time marching can be obtained by Taylor expansion



$$\begin{aligned}
0 &= 2G_m^{(n+1)} \approx 2G_m^{(n)} + 2 \frac{\partial G_m}{\partial U_{jk}} \Delta U_{jk} + 2 \frac{\partial G_m}{\partial \lambda_n} \Delta \lambda_n \\
&= 2G_m^{(n)} + 2K_{mijkl}^2 U_{il} \Delta U_{jk} - 2C_{mn} \Delta \lambda_n \\
&= 2G_m^{(n)} + \widehat{D}_{mjk}^{t0(n)} \Delta U_{jk} - 2\widehat{D}_{mn}^{t1(n)} \Delta \lambda_n
\end{aligned} \tag{3.96}$$

Using equation (3.95) and (3.96), the equation of motion and the stretch condition can be re-written as follows:

$$\widehat{K}_{ijkl}^{t0(n)} \Delta U_{jk} + \widehat{K}_{lin}^{t1(n)} \Delta \lambda_n = -\widehat{R}_{il} \tag{3.97}$$

$$\widehat{D}_{mjk}^{t0(n)} \Delta U_{jk} + \widehat{D}_{mn}^{t1(n)} \Delta \lambda_n = -\widehat{G}_m \tag{3.98}$$

where

$$\widehat{K}_{ijkl}^{t0(n)} = \frac{2}{\Delta t^2} \left( 3\widehat{M}_{ijkl}^{(n)} - \widehat{M}_{ijkl}^{(n-1)} \right) + K_{ijkl}^1 + \lambda_n^{(n-\frac{1}{2})} K_{nijlk}^2 \tag{3.99}$$

$$\widehat{K}_{lin}^{t1(n)} = 2K_{nijlk}^2 U_{jk}^{(n)} \tag{3.100}$$

$$\widehat{D}_{mjk}^{t0(n)} = 2K_{nijlk}^2 U_{jk}^{(n)} \tag{3.101}$$

$$\widehat{D}_{mn}^{t1(n)} = -2C_{mn} = 2D_{mn}^{t1(n)} \tag{3.102}$$

$$\begin{aligned}
\widehat{R}_{il} &= \frac{2}{\Delta t^2} \left( 3\widehat{M}_{ijkl}^{(n)} - \widehat{M}_{ijkl}^{(n-1)} \right) + \left( 3F_{il}^{(n)} - F_{il}^{(n-1)} \right) \\
&\quad - 2K_{ijkl}^1 U_{jk}^{(n)} - 2\lambda_n^{(n+\frac{1}{2})} K_{nijlk}^2 U_{jk}^{(n)}
\end{aligned} \tag{3.103}$$

$$\widehat{G}_m^{(n)} = 2G_m^{(n)} \tag{3.104}$$

The resultant forms of the equation (3.97) and (3.98) are similar to the static problem.

The equation of motion in matrix form can be written as follows:

$$\widehat{\mathbf{K}}^{(n)} (\Delta \mathbf{y}) = \widehat{\mathbf{F}}^{(n)} \quad \text{at time step } n \tag{3.105}$$

$$\mathbf{F}^r = -\widehat{\mathbf{F}}^{(n+1)} \tag{3.106}$$

Using Adams-Moulton with Adams-Bashforth scheme, the numerical methods in this study,

mixed implicit and explicit scheme is used to avoid iterative methods in time domain problem.

### 3.6. Modeling of the Seafloor

For the catenary mooring system, a portion of a mooring line near the anchor usually lies on the seabed. The interaction between steel catenary riser and the seafloor is also very important in the riser design. Due to this reason, the interaction between mooring line (or riser) and seafloor is modeled. In the numerical modeling, the horizontal friction between line and seafloor are neglected. However, in vertical direction, the seafloor is modeled as elastic foundation, and the dynamic bottom boundary conditions are shown in following equations:

$$f_1 = 0, \quad f_2 = 0, \quad f_3 = \begin{cases} c(r_3 - D)^2 & \text{for } r_3 - D < 0 \\ 0 & \text{for } r_3 - D \geq 0 \end{cases} \quad (3.107)$$

where  $D$  represents the water depth or vertical distance between the seafloor and the origin of the coordinate, and  $r_3$  is the  $z$ -component of the line position vector. Include seafloor interaction, the equation of motion is re-written as follows:

$$\left( M_{ijkl} + M_{ijkl}^a \right) \ddot{U}_{jk} + \left( K_{ijkl}^1 + \lambda_n K_{nijlk}^2 \right) U_{jk} = F_{il} + F_{il}^f \quad (3.108)$$

where

$$F_{il}^f = \begin{cases} \int_0^L A_1 \delta_{i3} c(r_3 - D)^2 & \text{for } r_3 - D < 0 \\ 0 & \text{for } r_3 - D \geq 0 \end{cases} \quad (3.109)$$

$$= \begin{cases} \int_0^L A_1 \delta_{i3} c(\delta_{i3} A_k U_{jk} - D)^2 & \text{for } r_3 - D < 0 \\ 0 & \text{for } r_3 - D \geq 0 \end{cases}$$

and,

$$\delta_{i3} = \begin{cases} 1 & \text{for } i=3 \\ 0 & \text{otherwise} \end{cases} \quad (\text{Kronecker Delta}) \quad (3.110)$$

In the static analysis, the stiffness matrix is modified as follows:

$$\begin{aligned} \mathbf{K}_{ijkl}^3 &= \frac{\partial F_{il}^f}{\partial U_{jk}} \\ &= \begin{cases} \int_0^L 2A_1 \delta_{i3} c \delta_{j3} A_k (\delta_{m3} A_n U_{mn}^{(n)} - D)^2 & \text{for } r_3 - D < 0 \\ 0 & \text{for } r_3 - D \geq 0 \end{cases} \end{aligned} \quad (3.111)$$

The additional stiffness  $\mathbf{K}_{ijkl}^3$  from seafloor is added to  $\mathbf{K}_{ijkl}^{t0}$ . In the time domain analysis using the trapezoidal rule, the stiffness matrix modified as follows:

$$\begin{aligned} \int_{t^{(n)}}^{t^{(n+1)}} F_{il}^f dt &= \frac{\Delta t}{2} (F_{il}^{f(n+1)} + F_{il}^{f(n)}) \\ &= \frac{\Delta t}{2} [\mathbf{K}_{ijkl}^3 \Delta U_{jk} + 2F_{il}^{f(n)}] \end{aligned} \quad (3.112)$$

The equation of motion include seafloor effects finally written as follows:

$$\begin{aligned} &\left[ \frac{4}{\Delta t^2} \widehat{\mathbf{M}}_{ijkl}^{(n+\frac{1}{2})} + \mathbf{K}_{ijkl}^1 + \lambda_n^{(n-\frac{1}{2})} \mathbf{K}_{nijlk}^2 \right] \Delta U_{jk} + 2\mathbf{K}_{nijlk}^2 U_{jk}^{(n)} \Delta \lambda_n \\ &= \frac{4}{\Delta t^2} \widehat{\mathbf{M}}_{ijkl}^{(n+\frac{1}{2})} V_{jk}^{(n)} + (3F_{il}^{(n)} - F_{il}^{(n-1)} + 2F_{il}^{f(n)}) - 2\mathbf{K}_{ijkl}^1 U_{jk}^{(n)} - 2\lambda_n^{(n+\frac{1}{2})} \mathbf{K}_{nijlk}^2 U_{jk}^{(n)} \end{aligned} \quad (3.113)$$

## CHAPTER IV

# INTEGRATED MODELING OF PLATFORM AND MOORING/RISER

### 4.1. Introduction

In this chapter, the coupling between platform and mooring line (or riser) is discussed. In most cases, the boundary conditions applied to mooring lines are the constraints at the two ends of the line: the upper end of the lines are connected to the floating platform and is forced to move with the platform, and the lower end are connected to structures such as anchors and templates at the seafloor. As discussed in Chapter II, the floating platform is modeled as a rigid body with motion in six degrees of freedom. The motion of the platform gives the dynamic boundary condition at the upper end of the mooring lines. On the other hand, the mooring lines give the additional restoring force to the floating platform. The types of connection between the mooring lines and the floating platform can be modeled using combinations of translational springs and rotational springs. Another type of connection is to use a viscous damper, which is intended to subdue the high frequency resonance of the tensioned lines, such as the tendon of a TLP.

In deep water, the inertia effect as well as hydrodynamic force from mooring lines and risers cannot be neglected in analyzing a floating platform. Due to this reason, the coupled analysis of floating platforms with mooring lines and risers is important. Ran (2000) has developed a mathematical formulation of these coupling effects. Therefore, in the first part

of this chapter, the single point coupling model is reviewed.

The single point coupling model can analyze the mooring lines and a steel catenary riser system. However, the rigid vertical riser system for a spar platform cannot be modeled correctly with the single point coupling model. In the second part of this chapter, the newly developed multi-contact coupling with a nonlinear gap boundary condition is discussed. The spar platform (classical spar and truss spar), which is the target structure in this research, uses a vertical rigid riser system with a dry tree. The vertical riser system is generally supported by freely floating buoyancy-can (e.g. classical spar and truss spar platform) or hydraulic/pneumatic cylinder (e.g. TLP). The previous numerical model in WINPOST, the riser system includes a buoyancy-can and it is modeled as truncated simplified elements. The risers are modeled up to keel and the buoyancy-cans are modeled as the top tension of each riser. The truncated riser model ignores the interaction between risers and support guide frames inside of the spar moon-pool. Thus, the truncated riser system ignores the additional restoring force and Coulomb damping effect caused by the interaction between risers and support guide frames, and consequently, the model results overestimate the spar hull motion. In Tahar, Ran and Kim (2002), the interaction effects between risers and riser guide frames are modeled as a simple inverted pendulum model as well as more rigorous riser modeling through riser guides inside the moon-pool. Tahar, Ran and Kim (2002), the interaction between risers and riser guide frames are modeled as horizontal springs with large stiffness to restrict the horizontal motion of the risers while allowing them to move freely in vertical direction. In the actual system the interaction between the riser and riser guide frame is called gap-contact. The horizontal connected spring ignores the gap-contact effect between riser and riser guide frame. The contact-

induced force between riser and riser guide frame also rise to gives Coulomb (frictional) damping to spar heave motion. Thus, in this chapter, the mathematical formulations for the interactions between risers and riser guide frames are developed by using four different types of spring connections (e.g. connected spring, piecewise linear gap spring, piecewise quadratic gap spring and cubic spring approximation). The mathematical formulation for Coulomb damping between risers and riser guide frames is also developed. In the last part of this chapter, the mathematical formulation for a nonlinear pneumatic vertical riser support system is developed. In this part, the nonlinear dynamic boundary condition on top of the risers is introduced. Thus, in this chapter, detailed mathematical a formulations for the interaction between a rigid vertical riser and floating platform is developed.

## 4.2. Spring Coupling between the Platform and Mooring Lines

As mentioned in Chapter III, equation (3.73) describes the nodal resultant force  $\mathbf{N} = \{N_1, N_2, N_3\}^T$  and moment  $\mathbf{L} = \{L_1, L_2, L_3\}^T$ . During the assembling the adjacent element, these force and moment are canceled out. However, the mooring lines or risers are connected to platform as well as seafloor, thus the first node and end node of the line has a dynamic boundary condition. Therefore, when the end node of line is connected to platform by linear springs or rotational springs, the resultant force and moment are equal to the force applied on the node from the spring. If a small angle assumption is valid, the forces and the moments on the end node of the line are written as:

$$\mathbf{N}_i = \mathbf{K}_i^L (\mathbf{X}_i + \mathbf{p}_i + \boldsymbol{\theta}_j \times \mathbf{p}_k - \mathbf{r}_i) \quad (4.1)$$

$$L_i = K^0 \left( \mathbf{e}_i + \theta_j \times \mathbf{e}_k - \frac{\mathbf{r}'_i}{|\mathbf{r}'_i|} \right) \quad (4.2)$$

where  $K_1^L$ ,  $K_2^L$  and  $K_3^L$  are the linear spring constant in x, y, and z direction, respectively. The terms  $X_i$  and  $\theta_i$  represent translational and rotational motion of the platform. The term  $\mathbf{p}_i$  represents the position vector of the point on the platform where the springs are attached, and  $\mathbf{r}_i$  is the position vector of the end node of the line which is attached to the rigid body by springs.  $K^0$  is the rotational spring constant, and  $\mathbf{e}_i$  is a unit vector which denotes the direction of the spring reference.  $\mathbf{r}'_i$  is the tangent to the riser centerline. For the stretch condition  $\frac{\mathbf{r}'_i}{|\mathbf{r}'_i|}$  is used to ensure the unity of the tangent. Equation (4.1) and (4.2) show the spring force can be calculated through relative displacement of attached point between platform and mooring line. As mentioned before, the end node of element attached to platform, and thus the position vector  $\mathbf{r}_i$ , and  $\mathbf{r}'_i$  can be written as:

$$\mathbf{r}_1 = U_{13}, \quad \mathbf{r}_2 = U_{23}, \quad \mathbf{r}_3 = U_{33} \quad (4.3)$$

$$\mathbf{r}'_1 = U_{14}, \quad \mathbf{r}'_2 = U_{24}, \quad \mathbf{r}'_3 = U_{34} \quad (4.4)$$

The additional restoring forces and moments from the mooring line to platform can be written as follow:

$$\mathbf{F}^L = -\mathbf{N} \quad (4.5)$$

$$\mathbf{F}^0 = 0 \quad (4.6)$$

$$\mathbf{M}^L = \mathbf{P} \times -\mathbf{N} \quad (4.7)$$

$$\mathbf{M}^0 = \mathbf{L} \times \mathbf{r}' \approx \mathbf{L} \times \mathbf{e} \quad (4.8)$$

For the convenience, the cross product term in equation (4.1) and (4.2) (i.e.  $\theta_j \times \mathbf{p}_k$ ,

$\theta_j \times e_k$ ) can be written as

$$N_i = K_i^L (X_i + p_i + \theta_j C_{ji} - r_i) \quad (4.9)$$

$$L_i = K^0 \left( e_i + \theta_j D_{ji} - \frac{r'_i}{|r'_i|} \right) \quad (4.10)$$

where

$$\mathbf{C} = \begin{bmatrix} 0 & -p_3 & p_2 \\ p_3 & 0 & -p_1 \\ -p_2 & p_1 & 0 \end{bmatrix} \quad (4.11)$$

$$\mathbf{D} = \begin{bmatrix} 0 & -e_3 & e_2 \\ e_3 & 0 & -e_1 \\ -e_2 & e_1 & 0 \end{bmatrix} \quad (4.12)$$

and using subscript notations for connector force on the rigid body as

$$F_i = -N_i \quad (4.13)$$

$$M_i = N_k C_{ki} + L_k D_{ki} \quad (4.14)$$

The connector forces and moments, equation (4.9), (4.10), (4.13), and (4.14), are included in the relative motion equations of the mooring line and the platform as external forces and moments. In the following static and dynamic analysis, derived formulation defines the coupling between the line and the platform.

In the static analysis of the mooring line and riser, the Newton's iteration method is used. Thus, the connector force at the end node connected to the spring in  $(n+1)^{\text{th}}$  iteration can be approximate from the  $(n)^{\text{th}}$  iteration.

$$N_i^{(n+1)} = N_i^{(n)} + \frac{\partial N_i}{\partial r_j} \Delta r_j + \frac{\partial N_i}{\partial X_j} \Delta X_j + \frac{\partial N_i}{\partial \theta_j} \Delta \theta_j \quad (4.15)$$

$$L_i^{(n+1)} = L_i^{(n)} + \frac{\partial L_i}{\partial r'_j} \Delta r'_j + \frac{\partial L_i}{\partial \theta_j} \Delta \theta_j \quad (4.16)$$



Similarly, the contact force on the platform at  $(n+1)^{\text{th}}$  iteration can be approximated by:

$$F_i^{(n+1)} = F_i^{(n)} + \frac{\partial F_i}{\partial r_j} \Delta r_j + \frac{\partial F_i}{\partial X_j} \Delta X_j + \frac{\partial F_i}{\partial \theta_j} \Delta \theta_j \quad (4.17)$$

$$M_i^{(n+1)} = M_i^{(n)} + \frac{\partial M_i}{\partial r_j} \Delta r_j + \frac{\partial M_i}{\partial r'_j} \Delta r'_j + \frac{\partial M_i}{\partial X_j} \Delta X_j + \frac{\partial M_i}{\partial \theta_j} \Delta \theta_j \quad (4.18)$$

The equation (4.15) and (4.16) show that the line at connected node is coupled with the unknown platform motion. The second term in the right hand side of equation is included in the equation of line element connected to the platform, and the third and the fourth terms in the equation (4.17) and (4.18) are included in the equation of the platform. The equation for line and platform are coupled by the third and fourth terms in the equation (4.15), the third term in equation (4.16), second term in the equation (4.17) and second and third terms in equation (4.18). At each iteration, the coupled algebraic equations are solved to obtain the solution of the line and the rigid body simultaneously. The iteration continues until a specific tolerance is reached.

In the time domain integration, the connector force on the line is added to the equation of the line and the equation of motion of platform and is integrated from time  $t^{(n)}$  to  $t^{(n+1)}$ :

$$\int_{t^{(n)}}^{t^{(n+1)}} N_i dt = \frac{\Delta t}{2} (N_i^{(n+1)} + N_i^{(n)}) \approx \frac{\Delta t}{2} \left( \frac{\partial N_i}{\partial r_j} \Delta r_j + \frac{\partial N_i}{\partial X_j} \Delta X_j + \frac{\partial N_i}{\partial \theta_j} \Delta \theta_j + 2N_i^{(n)} \right) \quad (4.19)$$

$$\int_{t^{(n)}}^{t^{(n+1)}} L_i dt = \frac{\Delta t}{2} (L_i^{(n+1)} + L_i^{(n)}) \approx \frac{\Delta t}{2} \left( \frac{\partial L_i}{\partial r'_j} \Delta r'_j + \frac{\partial L_i}{\partial \theta_j} \Delta \theta_j + 2L_i^{(n)} \right) \quad (4.20)$$

$$\int_{t^{(n)}}^{t^{(n+1)}} F_i dt = \frac{\Delta t}{2} (F_i^{(n+1)} + F_i^{(n)}) \approx \frac{\Delta t}{2} \left( \frac{\partial F_i}{\partial r_j} \Delta r_j + \frac{\partial F_i}{\partial X_j} \Delta X_j + \frac{\partial F_i}{\partial \theta_j} \Delta \theta_j + 2F_i^{(n)} \right) \quad (4.21)$$

$$\int_{t^{(n)}}^{t^{(n+1)}} M_i dt = \frac{\Delta t}{2} (M_i^{(n+1)} + M_i^{(n)}) \quad (4.22)$$

$$\approx \frac{\Delta t}{2} \left( \frac{\partial M_i}{\partial r_j} \Delta r_j + \frac{\partial M_i}{\partial r'_j} \Delta r'_j + \frac{\partial M_i}{\partial X_j} \Delta X_j + \frac{\partial M_i}{\partial \theta_j} \Delta \theta_j + 2M_i^{(n)} \right)$$

Like the static analysis, the coefficient in the above equations are associated with the time domain equations of the platform and the element of the line contact to the platform.

Using symbol  $K_{ij}^{AB}$  to indicate the tangential stiffness coefficient for degree of freedom B j in equation A i, terms in (4.15) through (4.22) can be shown as follow:

$$\begin{aligned} K_{ij}^{rr} &= -\frac{\partial N_i}{\partial r_j} = K_i^L \delta_{ij} & K_{ij}^{Xr} &= -\frac{\partial F_i}{\partial r_j} = K_i^L \delta_{ij} \\ K_{ij}^{rX} &= -\frac{\partial N_i}{\partial X_j} = -K_i^L \delta_{ij} & K_{ij}^{XX} &= -\frac{\partial F_i}{\partial X_j} = -K_i^L \delta_{ij} \\ K_{ij}^{r\theta} &= -\frac{\partial N_i}{\partial \theta_j} = K_i^L C_{ij} & K_{ij}^{X\theta} &= -\frac{\partial F_i}{\partial \theta_j} = -K_i^L C_{ij} \\ K_{ij}^{r'r'} &= -\frac{\partial L_i}{\partial r'_j} = K_\theta \left[ \frac{\delta_{ij}}{(r'_m r'_m)^{1/2}} - \frac{r'_i r'_j}{(r'_n r'_n)^{3/2}} \right] & K_{ij}^{\theta r} &= -\frac{\partial M_i}{\partial r_j} = K_\theta C_{ij} \\ K_{ij}^{r'\theta} &= -\frac{\partial L_i}{\partial \theta_j} = K_\theta D_{ij} & K_{ij}^{\theta r'} &= -\frac{\partial M_i}{\partial r'_j} = K_\theta D_{ij} \\ & & K_{ij}^{\theta\theta} &= -\frac{\partial M_i}{\partial \theta_j} = K_i C_{ki} C_{kj} + K_\theta D_{ki} D_{kj} \end{aligned} \quad (4.23)$$

The element tangential stiffness matrix that needed to be added into the end node of the leg is

$$\begin{bmatrix} K_{ij}^{rr} & 0 \\ 0 & K_{ij}^{r'r'} \end{bmatrix} \begin{Bmatrix} \Delta r_j \\ \Delta r'_j \end{Bmatrix} = \begin{Bmatrix} N_i \\ L_i \end{Bmatrix} \quad (4.24)$$

The element tangential stiffness matrix that needed to be added into the end node of the leg is

$$\begin{bmatrix} K_{ij}^{XX} & K_{ij}^{X\theta} \\ K_{ij}^{\theta X} & K_{ij}^{\theta\theta} \end{bmatrix} \begin{Bmatrix} \Delta X_j \\ \Delta \theta_j \end{Bmatrix} = \begin{Bmatrix} F_i \\ M_i \end{Bmatrix} \quad (4.25)$$

Finally, the coupling terms of element tangential stiffness matrix which need to be added into the global matrix are

$$\begin{bmatrix} 0 & 0 & \mathbf{K}_{ij}^{rX} & \mathbf{K}_{ij}^{r\theta} \\ 0 & 0 & 0 & \mathbf{K}_{ij}^{r'\theta} \\ \mathbf{K}_{ij}^{Xr} & 0 & 0 & 0 \\ \mathbf{K}_{ij}^{\theta r} & \mathbf{K}_{ij}^{\theta r'} & 0 & 0 \end{bmatrix} \begin{Bmatrix} \Delta \mathbf{r}_j \\ \Delta \mathbf{r}'_j \\ \Delta \mathbf{X}_j \\ \Delta \theta_j \end{Bmatrix} = \begin{Bmatrix} \mathbf{N}_i \\ \mathbf{L}_i \\ \mathbf{F}_i \\ \mathbf{M}_i \end{Bmatrix} \quad (4.26)$$

The detailed matrix formulation is shown in the last part of this chapter.

### 4.3. Damper Connection between the Platform and Mooring Lines

As mentioned before, another available connection in the dynamic problem is a viscous damper. In this study, the damper is modeled as a damping force linearly related to the relative translational velocity between the connecting point on the platform and the top node of the line. The damping force ( $\mathbf{N}^D$ ) on the connected node of the line element is:

$$\mathbf{N}_i^D = \mathbf{D}(\dot{\mathbf{X}}_i + \dot{\theta}_j \mathbf{C}_{ji} - \dot{\mathbf{r}}_i) \quad (4.27)$$

where  $\mathbf{D}$  is the viscous damping coefficient.  $\dot{\mathbf{X}}$  and  $\dot{\theta}$  are the translational and rotational velocity of the rigid body, and  $\dot{\mathbf{r}}$  is the velocity of the attached node. Matrix  $\mathbf{C}$  is identical as equation (4.11). The damping force on the rigid body is  $\mathbf{F}_i^D = -\mathbf{N}_i^D$ .

In time domain, integration is as follows:

$$\begin{aligned} \int_{t^{(n)}}^{t^{(n+1)}} \mathbf{N}_i^D dt &= \int_{t^{(n)}}^{t^{(n+1)}} \mathbf{D} d\mathbf{X}_i + \int_{t^{(n)}}^{t^{(n+1)}} \mathbf{C}_{ji} d\theta_j - \int_{t^{(n)}}^{t^{(n+1)}} \mathbf{D} d\mathbf{r}_i \\ &= (\mathbf{D}) \Delta \mathbf{X}_i + (\mathbf{C}_{ji}) \Delta \theta_j - (\mathbf{D}) \Delta \mathbf{r}_i \end{aligned} \quad (4.28)$$

$$\int_{t^{(n)}}^{t^{(n+1)}} \mathbf{N}_i^D dt = (-\mathbf{D}) \Delta \mathbf{X}_i + (\mathbf{C}_{ij}) \Delta \theta_j + (\mathbf{D}) \Delta \mathbf{r}_i \quad (4.29)$$

The coefficient in equation (4.28) and (4.29) is added to the equation of the line and the platform.

#### **4.4. Multi-Contact Coupling between the Spar Platform and Risers**

As mentioned before, the spar platform generally uses buoyancy-can supported production risers. There are several guide frames inside of the spar moon-pool, and the function of these guide frames is to support the riser horizontal direction and prevent collision. Thus, when the spar moves, the buoyancy-cans give additional moments to resist the hull pitch/roll motions and contact forces at support guide frames. The shape of buoyancy-can is circular cylinder, and the guide frame is also a round shape, and thus the contact between buoyancy-can and riser support frame can be modeled as point contact. In the numerical modeling, the point contact is modeled as a concentration force using a translational spring. Thus, the resulting contact forces affect both the motion of the riser and the motion of the spar hull. Because the spar has several guide frames; the riser and the spar have the same number of multi-contact couplings as guide frames. In equation (3.40), the first term on the right hand side is the bending moment and the second term in the right hand side is force at the node, and if there is no multi-contact coupling, these two terms canceled for internal element in global force vector to satisfy the compatibility between elements. However, when the support guide frame touches the riser, the contact force is applied to the node and the second term of equation (3.40) does not vanish from which the contact force can be calculated. The derivations of static and time domain dynamic formulation are identical to the single point coupling. However, in the global matrix

formation, the difference between single point coupling and the multi-contact coupling is the dimension of the coupling matrix. The detailed matrix formation is shown in the last section of this chapter. In this study, four different types of multi-contact coupling models are developed to include model the nonlinear gap boundary condition between riser and guide frames.

#### 4.4.1. Connected Spring Model

In this model, the guide frames are modeled as a horizontal spring with large stiffness to restrict the horizontal motion of riser, and the gap effects are ignored. Fig. 4.1 shows a schematic drawing of connected spring model.

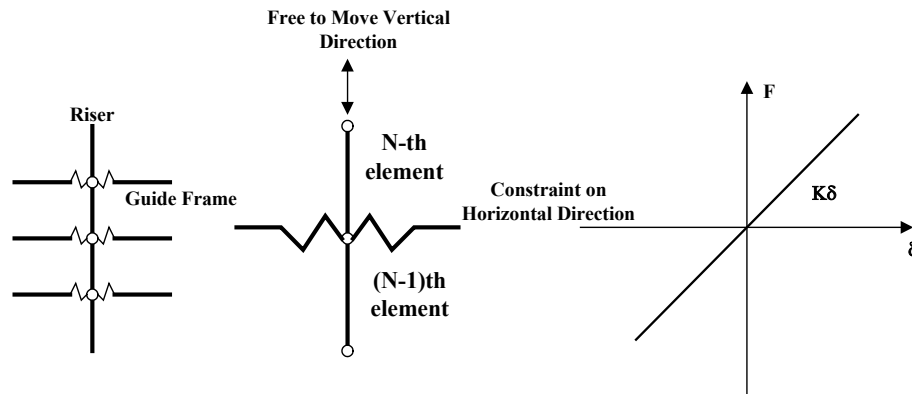


**Fig. 4.1. Connected spring model.**

The contact force between the risers and guide frames is modeled as follow;

$$N_1 = K_1^L (X_1 + p_1 + \theta_2 p_3 - \theta_3 p_2 - r_1) \quad (4.30)$$

$$N_2 = K_2^L (X_2 + p_2 + \theta_1 p_3 - \theta_3 p_1 - r_2) \quad (4.31)$$

$$N_3 = 0 \quad (4.32)$$

where  $K_1^L$  and  $K_2^L$  are stiffness in x and y direction, respectively.  $X_1$  and  $X_2$  are the translational motion of the rigid body at its origin of the body coordinate system, and  $\theta_1$ ,  $\theta_2$  and  $\theta_3$  are the angular motion of the rigid body. The terms  $p_1$ ,  $p_2$  and  $p_3$  are the position vectors (in body coordinate) of the point on the platform where the multi-contact occurs, and  $r_1$  and  $r_2$  are the nodal position of the riser which are expected to contact with guide frame. The contact forces and moments on the platform are identical to equation (4.13) and (4.14)

#### 4.4.2. Piecewise-Linear Gap-Contact Spring Model

The contact between the risers and the riser guide frames is gap-contact. In the actual riser support system, the buoyancy-cans and riser guide frames have a gap between them, and the gap makes it possible for the riser to move freely in the vertical direction. Fig. 4.2 shows the gap spring stiffness. In the gap-contact model, when the relative motion between the buoyancy-cans and riser guide frames is greater than the gap, the contact force is applied to the risers and guide frames, and the relative motion between the buoyancy-cans and the riser support frames are less than the gap, and the contact force vanishes. The gap-contact force between risers and guide frames is modeled as follows:

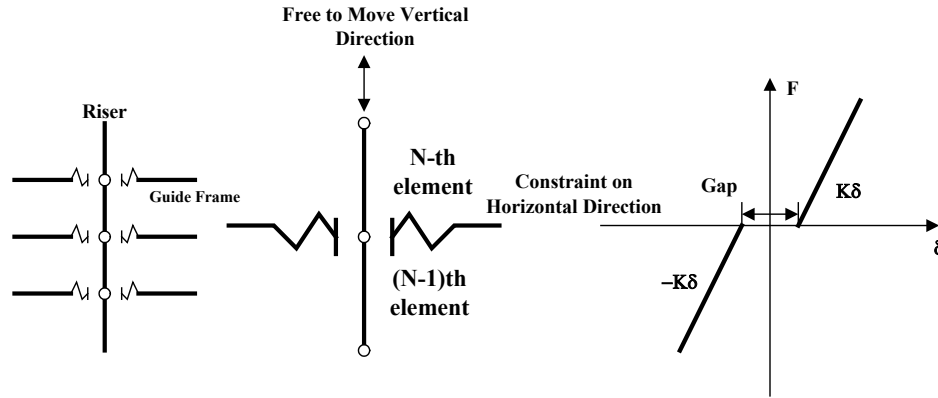


**Fig. 4.2. Piecewise linear gap spring model.**

when,  $(X_i + p_i + \theta_j \times p_j - r_i) \geq \Delta_i$  then

$$N_1 = K_1^L (X_1 + p_1 + \theta_2 p_3 - \theta_3 p_2 - r_1 - \Delta_1) \quad (4.33)$$

$$N_2 = K_2^L (X_2 + p_2 + \theta_1 p_3 - \theta_3 p_1 - r_2 - \Delta_2) \quad (4.34)$$

$$N_3 = 0 \quad (4.35)$$

when,  $-\Delta_i < (X_i + p_i + \theta_j \times p_j - r_i) < \Delta_i$  then

$$N_1 = 0 \quad (4.36)$$

$$N_2 = 0 \quad (4.37)$$

$$N_3 = 0 \quad (4.38)$$

when,  $(X_i + p_i + \theta_j \times p_j - r_i) \leq -\Delta_i$  then

$$N_1 = K_1^L (X_1 + p_1 + \theta_2 p_3 - \theta_3 p_2 - r_1 + \Delta_1) \quad (4.39)$$

$$N_2 = K_2^L (X_2 + p_2 + \theta_1 p_3 - \theta_3 p_1 - r_2 + \Delta_2) \quad (4.40)$$

$$N_3 = 0 \quad (4.41)$$

where,  $\Delta_1$  and  $\Delta_2$  are the gap distances between the risers and the riser guide frames.

The contact forces and moments on the platforms are same as shown in equation (4.13) and (4.14). In this model, the gap between buoyancy-cans and the riser guide frames is correctly modeled. However, the piecewise linear gap-contact spring model has discontinuity in the stiffness, which may cause numerical problems. In the simulation, the horizontal guide frames are modeled as horizontal spring with large stiffness, but its value may have numerical limitation at  $10e+06(N/m)$ . Due to this limitation, the next two models, piecewise-quadratic gap-spring model and cubic spring model are developed.

#### 4.4.3. Piecewise-Quadratic Gap-contact Spring Model

In this model, the gap-contact stiffness is modeled as quadratic spring. The gap-contact mechanisms are the same as a piecewise-linear gap-spring model except a quadratic spring is used. The quadratic spring can model hardening of guide frame also. The piecewise quadratic gap spring stiffness is shown in Fig. 4.3, and the formulations are as follow:

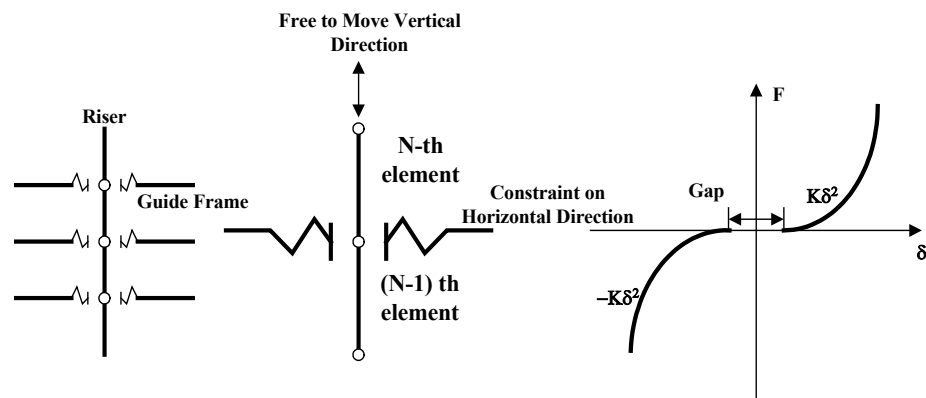


**Fig. 4.3. Piecewise quadratic gap-contact spring model.**



when,  $(X_i + p_i + \theta_j \times p_j - r_i) \geq \Delta_i$  then

$$N_1 = K_1^L (X_1 + p_1 + \theta_2 p_3 - \theta_3 p_2 - r_1 - \Delta_1)^2 \quad (4.42)$$

$$N_2 = K_2^L (X_2 + p_2 + \theta_1 p_3 - \theta_3 p_1 - r_2 - \Delta_2)^2 \quad (4.43)$$

$$N_3 = 0 \quad (4.44)$$

when,  $-\Delta_i < (X_i + p_i + \theta_j \times p_j - r_i) < \Delta_i$  then

$$N_1 = 0 \quad (4.45)$$

$$N_2 = 0 \quad (4.46)$$

$$N_3 = 0 \quad (4.47)$$

when,  $(X_i + p_i + \theta_j \times p_j - r_i) \leq -\Delta_i$  then

$$N_1 = -K_1^L (X_1 + p_1 + \theta_2 p_3 - \theta_3 p_2 - r_1 + \Delta_1)^2 \quad (4.48)$$

$$N_2 = -K_2^L (X_2 + p_2 + \theta_1 p_3 - \theta_3 p_1 - r_2 + \Delta_2)^2 \quad (4.49)$$

$$N_3 = 0 \quad (4.50)$$

In this model, the tangential stiffness of guide frame quadratically increases when the riser touches the guide frame. The continuity of slope at the beginning or the contact solves the numerical difficulty faced by the piecewise-linear gap spring model. The relative distance of the risers and riser guide frames should be checked at each time step.

#### 4.4.4. Cubic Spring Approximation

In this model, the gap-contact spring stiffness is approximated by a cubic curve. Although not exactly modeling the gap, the advantage of this model is reducing the

computation time and increasing numerical stability in the simulation. For the piecewise-linear gap-contact spring model and the piecewise-quadratic gap-contact spring model, the relative displacement and gap distance have to be checked every time steps, but the cubic spring model does not need this procedure. Fig. 4.4 shows the cubic spring approximation stiffness.

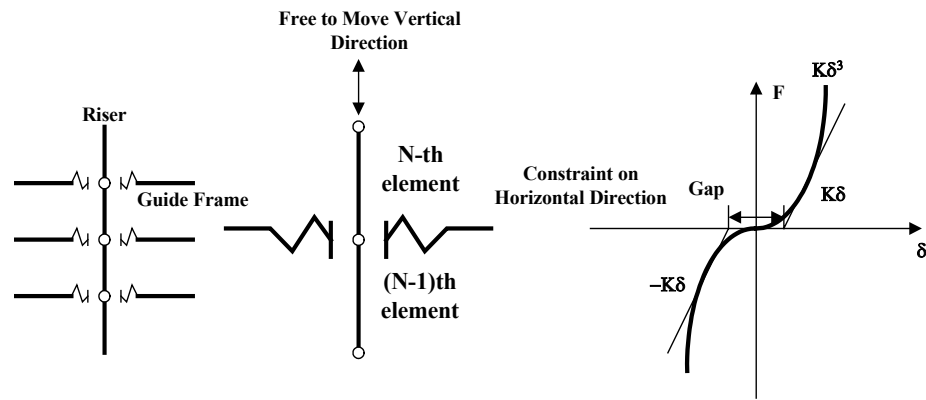


**Fig. 4.4. Cubic spring approximation model**

The formulations are as follow;

$$N_1 = K_1^L (X_1 + p_1 + \theta_2 p_3 - \theta_3 p_2 - r_1)^3 \quad (4.51)$$

$$N_2 = K_2^L (X_2 + p_2 + \theta_1 p_3 - \theta_3 p_1 - r_2)^3 \quad (4.52)$$

$$N_3 = 0 \quad (4.53)$$

The contact forces and moments on the platforms are same as equation (4.13) and (4.14).

#### 4.5. Alternative Riser Support System Modeling

The pneumatic cylinder can be modeled as ideal-gas equation. The pneumatic cylinder for each riser acts as a soft spring and gives additional restoring force to the platform motion. Fig. 4.5 shows schematic drawing of the pneumatic cylinder.

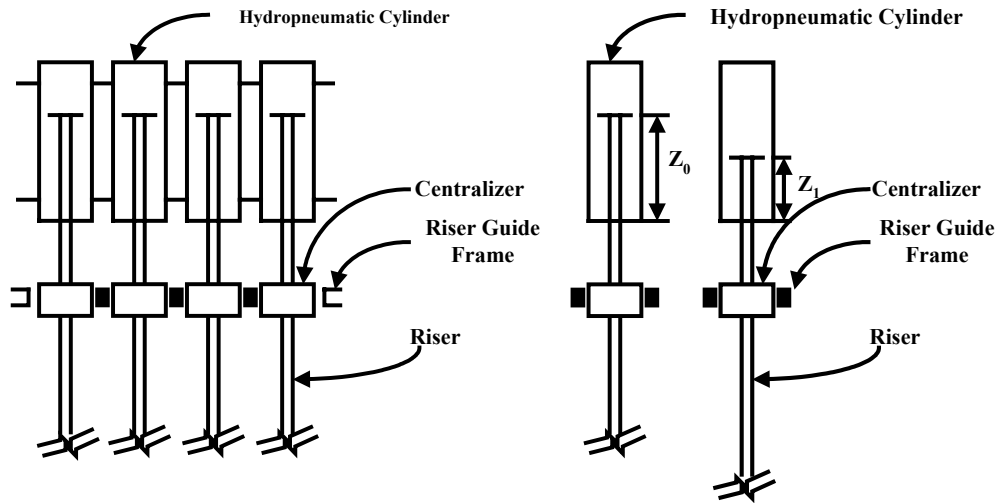


**Fig. 4.5. Schematic drawing of pneumatic riser support cylinder.**

The hydropneumatic cylinder force on the riser and the platform can be modeled as follow:

$$P_0 V_0 = P_1 V_1 \quad (4.54)$$

$$P_1 A Z_1 = P_0 A Z_0 \quad (4.55)$$

$$F_1 Z_1 = F_0 Z_0 \quad (4.56)$$

$$F_1 = F_0 \frac{Z_0}{Z_1} \quad (4.57)$$

where,  $P_0$  and  $P_1$  are the pressure,  $V_0$  and  $V_1$  are the volume inside,  $A$  is the cross sectional area of the cylinder,  $Z_0$  and  $Z_1$  are the stroke,  $F_0$  and  $F_1$  are the tension.

From equation (4.55)  $Z_1$  can be expressed as:

$$Z_1 = Z_0 - (X_3 + p_3 + \theta_1 p_2 - \theta_2 p_1 - r_3) \quad (4.58)$$

The dynamic top tension from pneumatic cylinder can be modeled as:

$$N_3 = T_0 \left( \frac{Z_0}{Z_0 - (X_3 + p_3 + \theta_1 p_2 - \theta_2 p_1 - r_3)} \right) \quad (4.59)$$

where  $T_0$  represent initial tension. The forces and moments on the platforms are same as equation (4.13) and (4.14). Due to the location of the pneumatic cylinder connection point between the end of riser and the platform, the derivations of static and time domain dynamic formulations and matrix formation are identical to the single point coupling.

#### 4.6. Coulomb Damping between the Platform and Risers

As mentioned before, when the riser contacts the guide frame, it also induces frictional damping to resist hull heave motion. This frictional damping, is commonly called Coulomb damping, and it has three different characteristics compared with viscous damping. The differences between Coulomb damping and viscous damping are; First, with Coulomb damping, the amplitude decays linearly rather than exponentially. Second, the motion under Coulomb friction comes to a complete stop, at a potentially different equilibrium position than when initially at rest. Whereas, a viscously damped system oscillates around a single equilibrium with infinitesimally small amplitude. Finally, the oscillation frequency of a system with Coulomb damping is the same as the undamped frequency, whereas viscous damping alters the frequency of oscillation (Inman, 1996). Fig. 4.6 shows the Coulomb damping model.

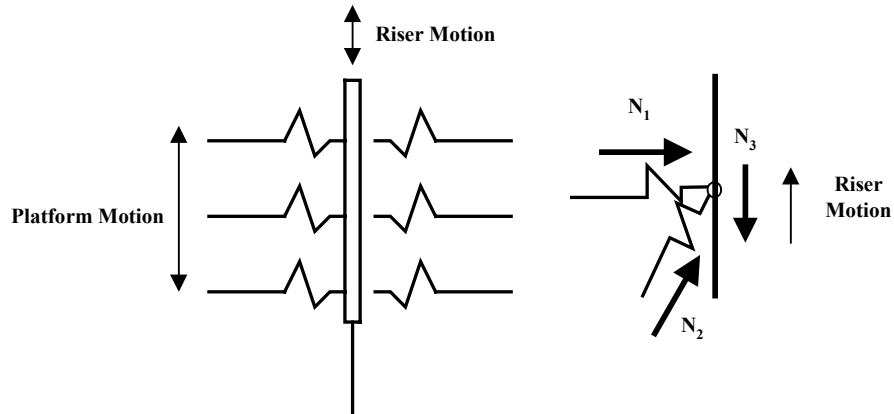


**Fig. 4.6. Schematic Drawing of Coulomb Damping.**

The coulomb damping from contact force is formulated as follow:

$$N_3 = \mu \operatorname{sgn}(\dot{X}_3 + \dot{\theta}_1 P_2 - \dot{\theta}_2 P_1 - \dot{R}_3) \sqrt{(N_1)^2 + (N_2)^2} \quad (4.60)$$

$$F_3 = -N_3 \quad (4.61)$$

where  $N_1$  and  $N_2$  are the contact force on riser in x and y direction and  $\mu$  is the coulomb damping coefficient. The force vector,  $N_3$  and  $F_3$ , are added to the force vector at the right side of the equations of the riser element and the platform. The derivations of time domain dynamic formulation are identical to the single point coupling. However, Coulomb damping effects is added to the nodes that are in contact with guide frames.

#### 4.7. Coupled Global Matrix

As mentioned before, the equation of motion of the platform can be formulated as  $6 \times 6$  stiffness (for dynamic problem inertia, damping, and stiffness) matrix with 6 rows displacement and external force vectors. For equation of mooring lines and riser also can

be formulated as  $8 \times (N+1) - 1$  rows and column stiffness matrix (for dynamic problem inertia, damping, and stiffness) with  $8 \times (N+1) - 1$  rows displacement and external force vectors for a single line. To formulate the coupling between platform and mooring lines and risers, the matrix becomes sparse due to coupling terms. For example, when one mooring line and one riser is coupled with the platform, the assembled global stiffness matrix has the following form:

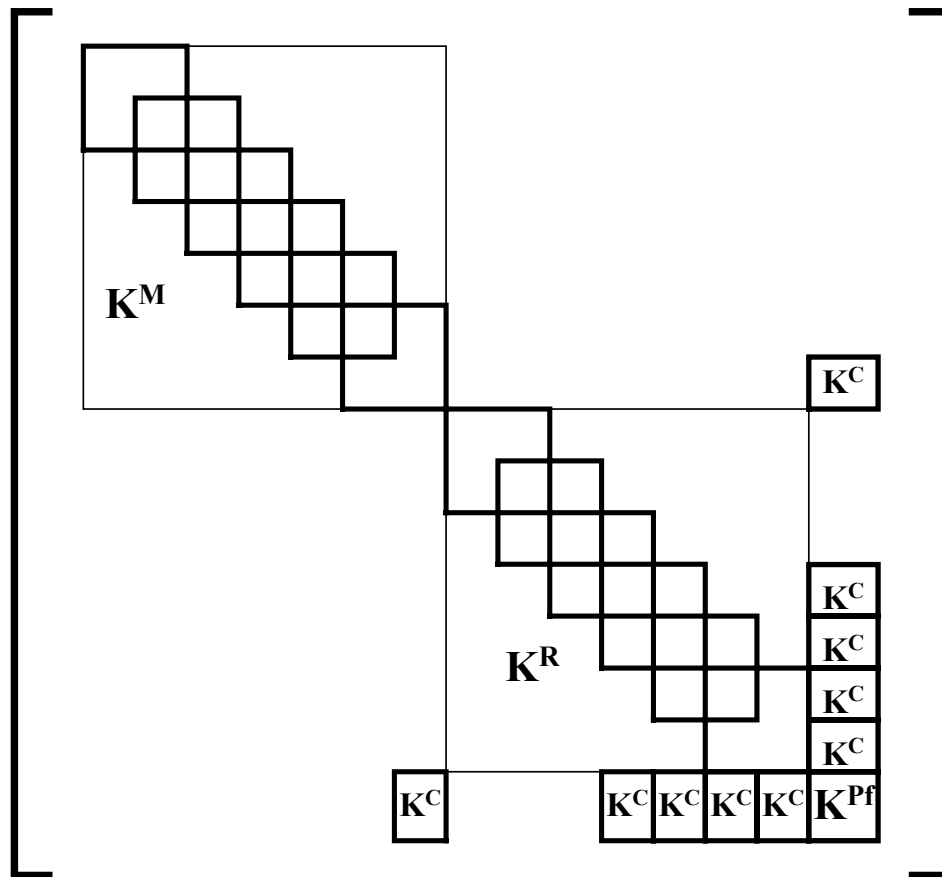


**Fig. 4.7. Coupled global matrix (1-mooring with 6-element, 1-riser with 4 multi-contact coupling 6-element).**

where  $K^M$  matrix represents the coefficient from mooring line,  $K^R$  matrix represents coefficients from riser,  $K^C$  matrix represents the coupling coefficient matrix between line and platform, and  $K^{Pf}$  matrix represents the coefficients from the platform. The global matrix clearly shows the difference between single point coupling and multi-contact coupling. Only the end of the node of mooring line connected to the platform, thus the coupling term exists in end node of the line. On the other hand, if the riser is steel vertical riser, then the riser has multiple contact points with platform, and thus the coupling coefficient matrix increases in the riser in the global matrix. As shown in Fig. 4.7, the lines are not directly coupled to each other but coupled through the platform.

## CHAPTER V

### CASE STUDY 1: BUOYANCY-CAN EFFECT ON SPAR PLATFORM

#### 5.1. Introduction

In the preceding chapters, the theory and numerical methods for the coupled dynamics of a floating structure with mooring lines and risers have been discussed. In this chapter, the buoyancy-can effects on the global spar motion are investigated. As mentioned before, the buoyancy-cans inside of spar moon-pool are ignored or simplified in previous studies. Due to ignorance of riser effects (i.e. buoyancy-can effects), the spar heave and pitch motions are over estimated in simulation as well as in experiments. In the simulations, six different spar platforms are modeled and the results are systematically compared to capture the buoyancy-can effects including the gap boundary condition as well as Coulomb damping effects. For simplification, the additional excitation on risers (i.e. buoyancy-can) from moon-pool sloshing and riser-riser interactions are not considered. The simulations are conducted for a spar platform in 914.4 m (3000 ft) water depth exposed to 100-year Gulf of Mexico hurricane condition. The simulation results are also compared with available experiment data and other simulation results. The results from this case study clearly show the buoyancy-can effects on the global spar motion.



## 5.2. Description of the Spar Platform, Mooring System, and Risers

The spar platform used in this study has length of 214.88 meters, and diameter of 37.19 meters. For the load condition, the spar has an average draft of 198.12 meters, with a total displacement of 220.74 metric ton. The hull consists of three parts: the hard tank in the upper part of the hull, the fixed ballast tank at the bottom of the hull, and the tank in the middle of the hard and the fixed ballast tank. Each tank has its own purpose. The hard tank provides buoyancy force to support the platform weight, and the fixed ballast tank provides stability. The skirt tank serves as the connection between the hard tank and fixed ballast tank. The principle particulars of the spar platform are summarized in Table 5.1 and illustrated in Fig. 5.1.

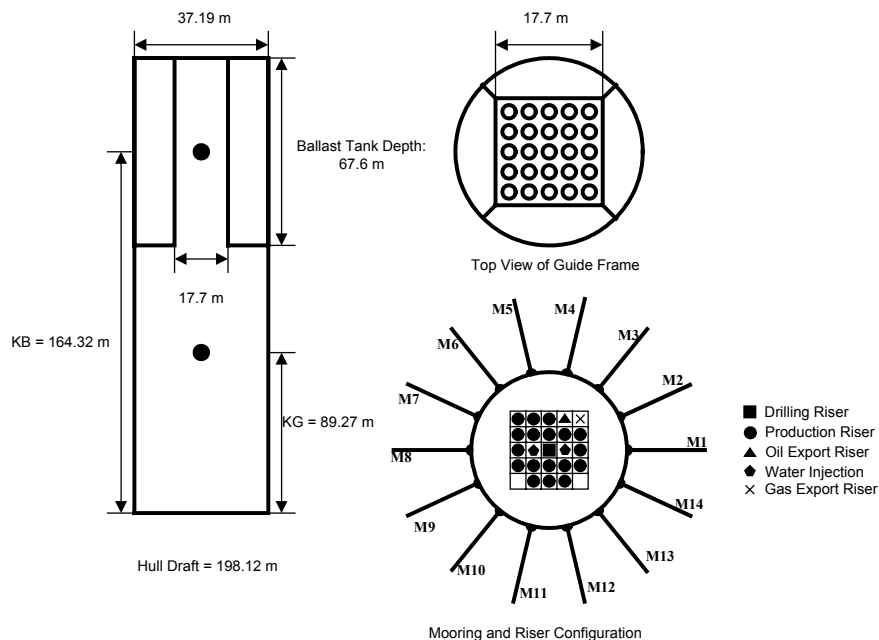


**Fig. 5.1. The illustration of the spar platform and mooring/riser configuration (not to scale).**

**Table 5.1. Principle particulars of the spar platform.**

Designation	Unit	Quantity
Length	<i>m</i>	214.88
Diameter	<i>m</i>	37.19
Draft	<i>m</i>	198.12
Hard tank depth	<i>m</i>	67.06
Well bay dimension (25 slots)	<i>m</i>	17.7 × 17.7
KB	<i>m</i>	164.59
KG	<i>m</i>	125.7
KG (based on total displacement)	<i>m</i>	89.27
Light ship weight	<i>N</i>	5.673E+08
Displacement	<i>N</i>	2.214E+09
Water weight (water in ballast tank and moon-pool)	<i>N</i>	1.564E+09
Vertical mooring tension	<i>N</i>	3.219E+07
Vertical riser tension	<i>N</i>	5.034E+07
Pitch radius of gyration	<i>m</i>	66.228
Yaw radius of gyration	<i>m</i>	12.829
Drag coefficient	-	1.5

The light ship weight means the net buoyancy, which include hull, topsides and hard tank. The total displacement means the light ship weight plus mooring lines, water in the ballast tank and moon-pool. The spar platform has 14 mooring lines and 23 risers. The arrangement of mooring lines and risers are shown in Fig. 5.1. The characteristics of mooring line and riser are summarized in Table 5.2 through Table 5.4

**Table 5.2. Spar mooring system configuration.**

Directional Spread	Omni-direction
No. Mooring Lines	14
Chain	5 – 1/4” K4 Studless Chain
Wire	5 – 3/8” Sheathed Wire

**Table 5.3. Spar mooring characteristics.**

Mooring Lines	Dry/Wet weight (N/m)	Axial Stiffness (KN)	Added mass (N/m)
5–1/4” K4 Studless Chain	370.93 / 322.71	1.328E+06	48.22
5–3/8” Sheathed Wire	99.10 / 19.79	1.628E+06	19.79

**Table 5.4. Riser System Characteristics.**

Riser	No.	Top Tension (KN) At Keel/At Top of spar	Axial Stiffness (KN)	Dry/Wet Weight (N/m)
Drilling	1	3.269E+03 / 4.167E+03	1.201E+07	595.26 / 366.17
Production	18	2.106E+03 / 2.344E+03	2.994E+06	300.61 / 195.12
Water Injection	2	1.362E+03 / 1.443E+03	1.837E+06	103.28 / 64.64
Oil Export	1	1.738E+03 / 1.872E+03	4.626E+06	296.15 / 163.16
Gas Export	1	8.870E+02 / 9.53E+02	4.626E+06	208.34 / 75.35

The schematic drawing of a buoyancy-can inside of the spar moon-pool is shown in Fig. 5.2. As mentioned before, a spar platform generally uses buoyancy-can supported production risers. There are several guide frames inside of the spar moon-pool, and the function of these guide frames is to constraint the riser horizontal motion and prevent collision of the risers. Fig. 5.2 shows the gap between buoyancy-can and guide frames.

This gap allows the riser to move freely in the vertical direction.

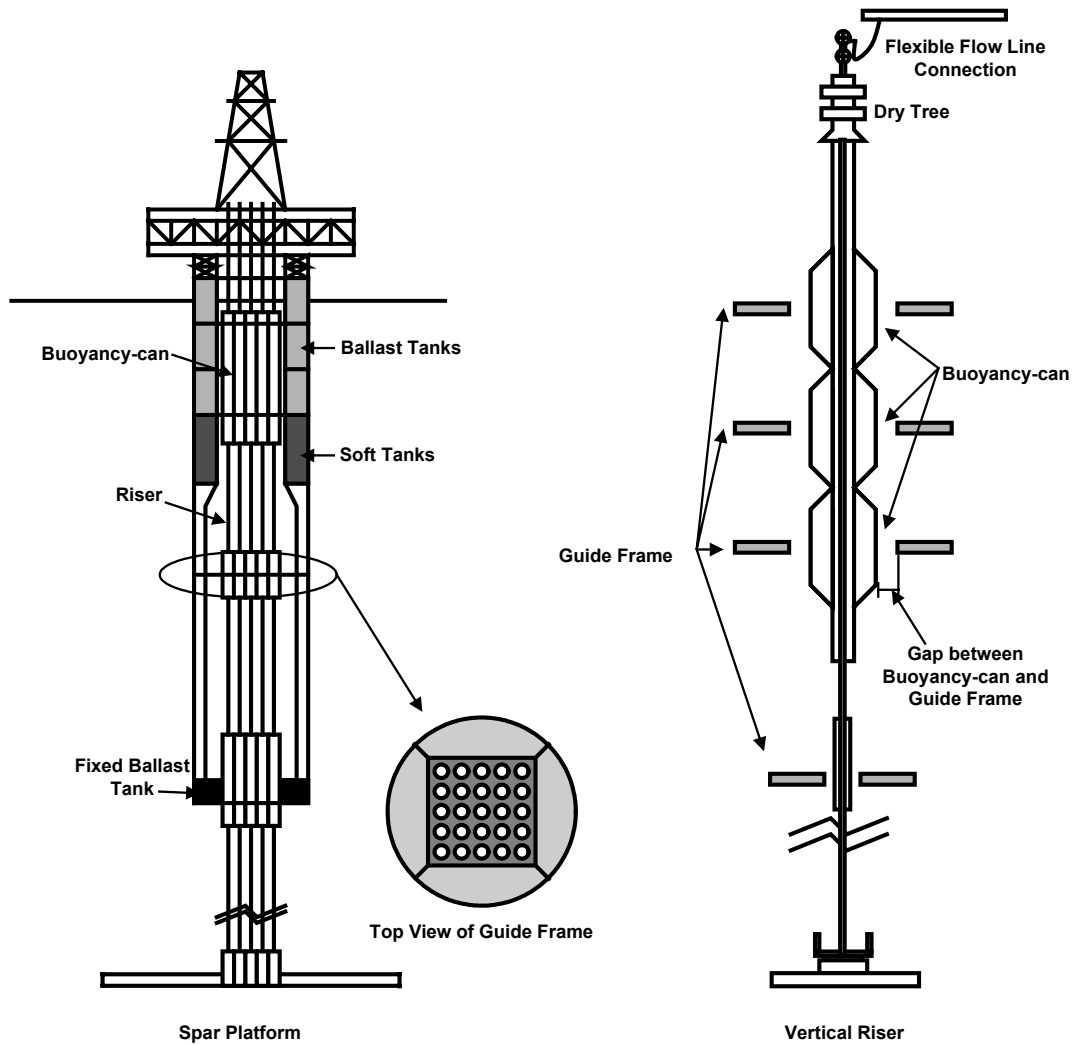


**Fig. 5.2. Schematic drawing of a spar riser system.**

### 5.3. Description of Case Study and Design Environmental Conditions

In this case study, the multiple contact between the risers and riser guide frames in the spar moon-pool are modeled five different ways as an effort to capture the different interaction effects between the buoyancy-cans and riser guide frames. In the Case A model, the risers are truncated at the spar keel and the top of the riser is supported by a constant force representing the buoyancy-cans. Therefore, the riser tension is not included in the vertical static equilibrium of the spar hull. In the Case B model, the risers are extended through moon-pool. The riser guides are modeled as horizontal spring connected to risers. The stiffness of the spring is large enough, as shown in Fig. 5.3, not allow any free horizontal motion at the location of the guide frame. Case C is similar to Case B, but the Coulomb damping between the buoyancy-cans and riser guide frames is considered. Case D is similar to Case C, but the riser guide frames are modeled as piecewise-linear gap-contact spring. This case accounts for gap effects (zero force during no contact) between risers and riser guide frames. If we apply larger spring stiffness for this model, numerical problems occur due to the discontinuity. Therefore, we applied relatively soft spring representing soft contact. Case E and Case F models are similar to the Case D, but Case E uses piecewise-quadratic gap-contact spring and Case E uses cubic springs to model the riser guide frame. Among the six cases, Case F best represents the gap effect and relatively hard contact between riser and riser guide frame. To show the gap distance effect, two different gap distances are simulated for gap spring model (Case D and Case E). The Case C, Case D, Case E and Case F models consider Coulomb damping effect. For all models, the top of the risers are supported by a constant force representing the buoyancy-cans. The

case studies are summarized in Table 5.5. Fig. 5.3 shows the spring constants for guide frame model for Case B, D, E, and F. As mentioned before, the piecewise-linear gap-contact spring model (Case D) has numerical instability problems. To avoid the numerical instability, a relatively small spring constant is used in the piecewise-linear gap-contact spring model. Due to this reason, it is hard to show the piecewise-linear gap-contact spring constant in Fig. 5.3. However, Fig. 5.4 shows the Case D spring constant after the gap-contact. To compare and verify the gap mechanism, consistent gap distance is very important. In Case D and Case E the gap distance can be given by artificially, but cubic spring model (Case F) cannot be given by artificially. Fig. 5.4 shows that Case F has stiffness between the gap distances, but the tangential stiffness of Case E between the gap distances is very small. Due to this reason, the simulation results show a similar gap effect in all three (i.e. Case D, Case E, and Case F) models.

**Table 5.5. Summary of conditions for fully modeled spar case studies.**

	Riser Model	Connection Type	Coulomb Damping
CASE A	Truncated (Up to Keel)	Connected Spring (Only at Keel)	N/A
CASE B	Fully modeled (Inside Moon-pool)	Connected Spring (Linear Spring)	N/A
CASE C	Fully modeled (Inside Moon-pool)	Connected Spring (Linear Spring)	Considered
CASE D	Fully modeled (Inside Moon-pool)	Gap Spring (Piecewise-Linear)	Considered
CASE E	Fully modeled (Inside Moon-pool)	Gap Spring (Piecewise-Quadratic)	Considered
CASE F	Fully modeled (Inside Moon-pool)	Connected Spring (Cubic Spring)	Considered

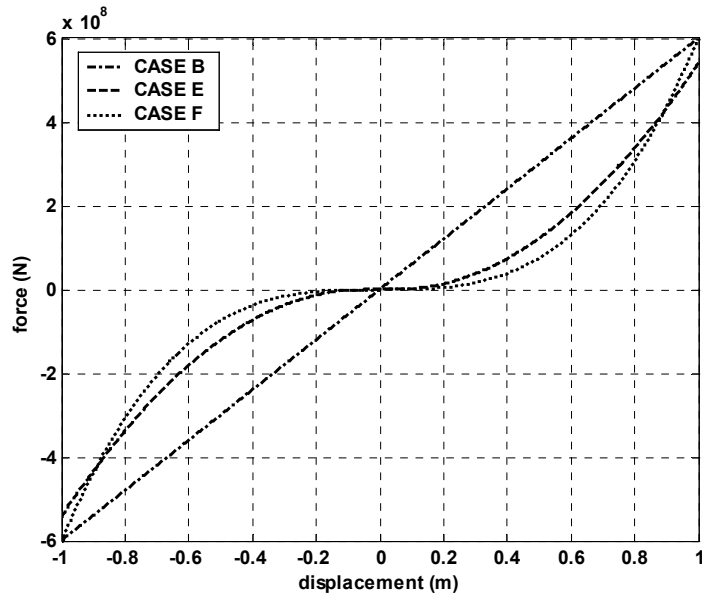


Fig. 5.3. Spring constant for multi-contact model.

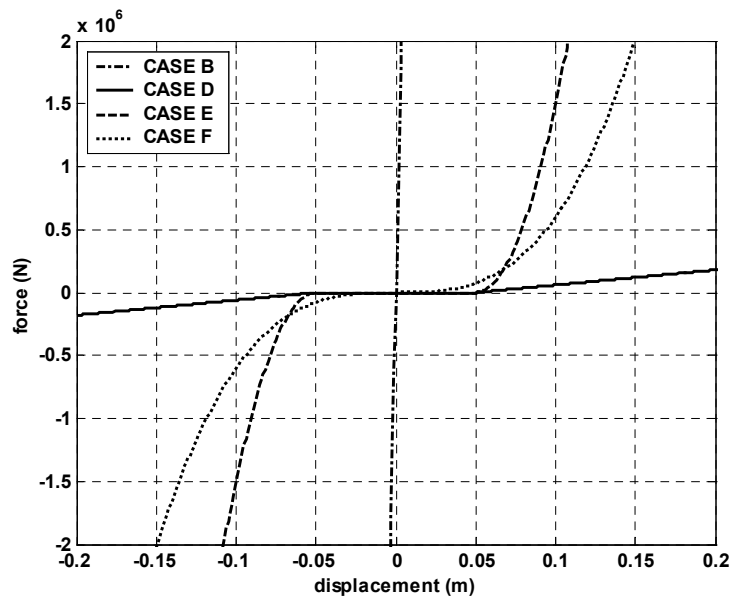
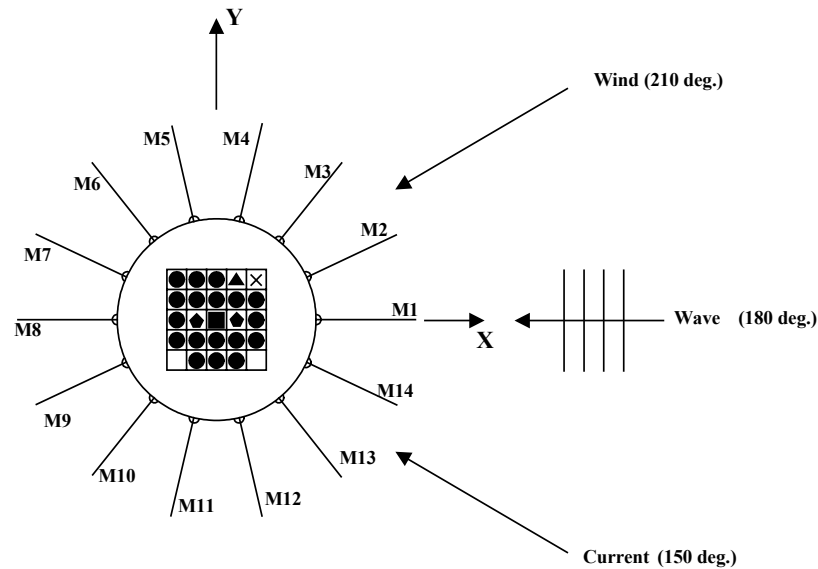


Fig. 5.4. Spring constant for multi-contact model after the gap.

As mentioned before, the 100-year hurricane condition in Gulf of Mexico is used in this case study. In the numerical modeling, the current is assumed to be steady and the irregular wave unidirectional. The wave heading is 180 degree with respect to the global axis. A JONSWAP spectrum of significant wave height,  $H_s = 12.19$  m (40.0 ft), peak periods  $T_p = 14$  sec, and overshoot parameter  $\gamma = 2.5$  was selected to present a typical 100-year hurricane in the Gulf of Mexico. The hurricane induced current flows from 30 degrees right of wave direction. The current velocity is assumed to be 1.07 m/sec from mean water level to 60.96 m (200 ft) water depths and is reduced to 0.091 m/sec at 91.44 m (300 ft) and zero at 914.4 m (3000 ft). The wind speed used is 41.1 m/sec (i.e. 1-hour averaged) at 10 m above mean water level and wind direction is 30 degrees left of wave direction. API (America Petroleum Institute) wind spectrum is used for the generation of time varying wind forces (API RP-2A WSD, 1994). Fig. 5.5 shows the environment direction of the 100-year hurricane condition in Gulf of Mexico. The time step used in time-domain hurricane condition simulation is 0.05 seconds and the total simulation time is 3 hours (216000 time steps).





**Fig. 5.5. Environmental direction of 100-year hurricane condition.**

## 5.4. Results and Analysis

### 5.4.1. Static Offset and Free Decay Simulation

The surge static offset simulation is conducted by pulling VCG (Vertical Center of Gravity) of spar in the horizontal direction in calm water. Typical results for surge static offset simulation results are shown in Fig. 5.6 through Fig. 5.8. From the static offset simulation, results show that the pretension of the mooring line is 3027 KN at the 49-degree fairlead angle. As surge offset increases, the taut-side becomes more taut and the slack-side becomes more slack resulting in less tension. Due to the mooring characteristics, the surge static-offset simulations show hardening phenomenon of the mooring line clearly.

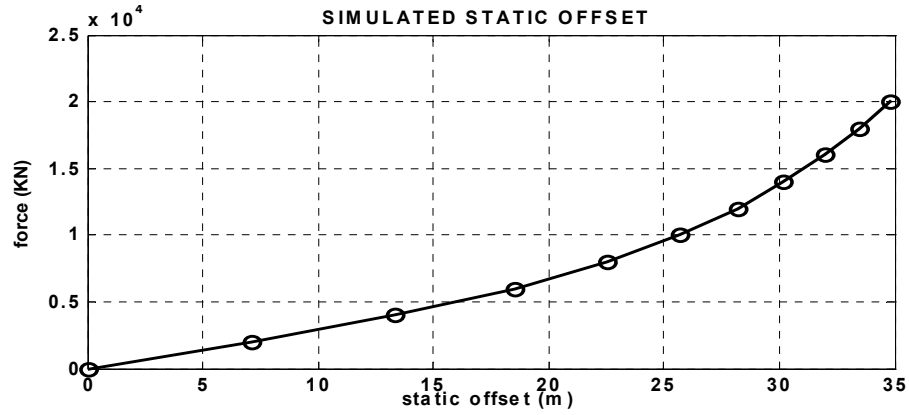


Fig. 5.6. Platform surge static offset curve (CASE B).

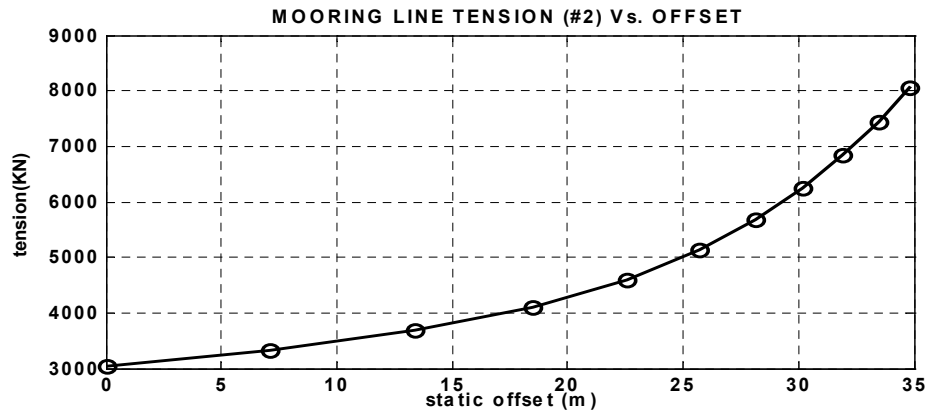


Fig. 5.7. Most loaded line tension (CASE B).

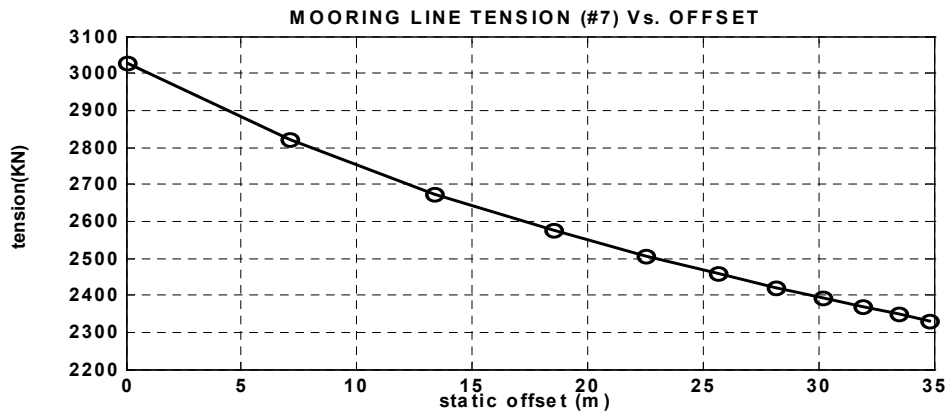


Fig. 5.8. Least loaded line tension curve (CASE B).

To evaluate the damping ratios and natural periods of the spar platform, free decay simulations are conducted for the surge, heave and pitch directions. To capture the buoyancy-can effects in the free-decay simulations, all the spar models are compared with and without riser model in surge and pitch free decay simulations. In the without riser model, all the risers are completely removed from the spar platform and only mooring lines are modeled.

The spar surge free decay simulation results are summarized in Table 5.6 and Fig. 5.9 through Fig. 5.19. Fig. 5.9 shows that the motion amplitude and period of the without-riser models are slightly larger than the truncated riser model, the riser contributes to the surge damping, however additional surge restoring force from risers decrease surge natural period. The damping contribution from riser is expected to be more important as water depth increases. The results also shows that the damping ratio from the average of the first three peaks and the first seven peaks are significantly different, which shows that the damping increase with motion amplitude. Fig. 5.11 through Fig. 5.19 shows the surge free decay motion, contact force on the spar, and the nodal reaction force on the riser. It is interesting to notice that the phase difference between the surge motion and the contact force is 180 degree. This means that the contact force direction at the keel is always opposite to the surge free decay motion. In the surge free decay motion result, Case A through Case F are virtually same and it shows that different riser modeling (e.g. buoyancy-can, gap effect and Coulomb damping) do not change the global surge motion appreciably. Fig. 5.12, Fig. 5.15, and Fig. 5.18 show the gap-contact force. When gap-contact forces are compared, there exist some discrepancy but the differences are small. Fig. 5.13, Fig. 5.16, and Fig. 5.19 show the nodal reaction force of the riser. The difference

in the nodal reaction forces of the riser can be appreciable depending on gap-contact models (Case D, Case E and Case F), and it is interesting to notice that the nodal reaction forces of the gap-contact models (Case D, Case E and Case F) have a periodic impact-like force. Its magnitude is especially amplified in the case of the piecewise-quadratic gap-contact spring. On the other hand, connected spring models (Case B and Case C) even though they have the greatest stiffness (see Fig. 5.4) do not show impact-like periodic behavior in the riser nodal reaction force. These results show that the gap between riser and riser guide frame may induce fatigue for the buoyancy-can.

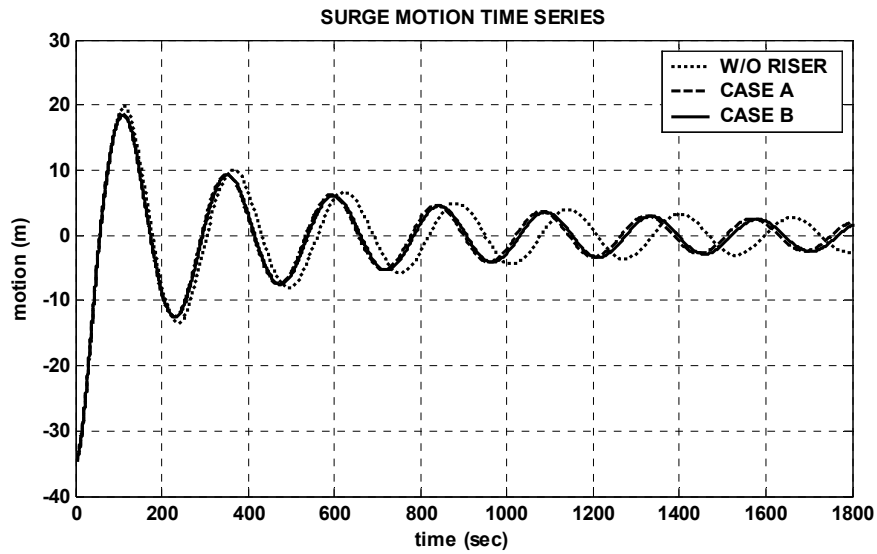


Fig. 5.9. Surge free decay motion time series.

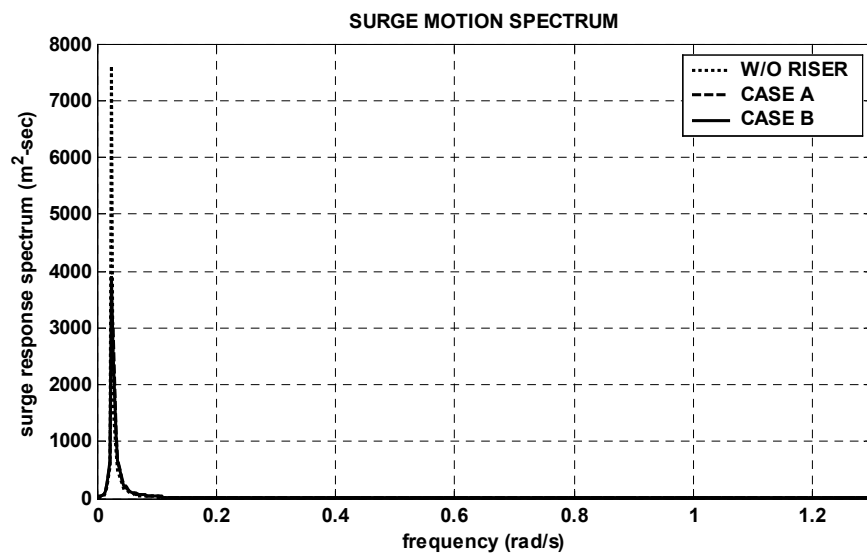


Fig. 5.10. Surge free decay motion spectrum.

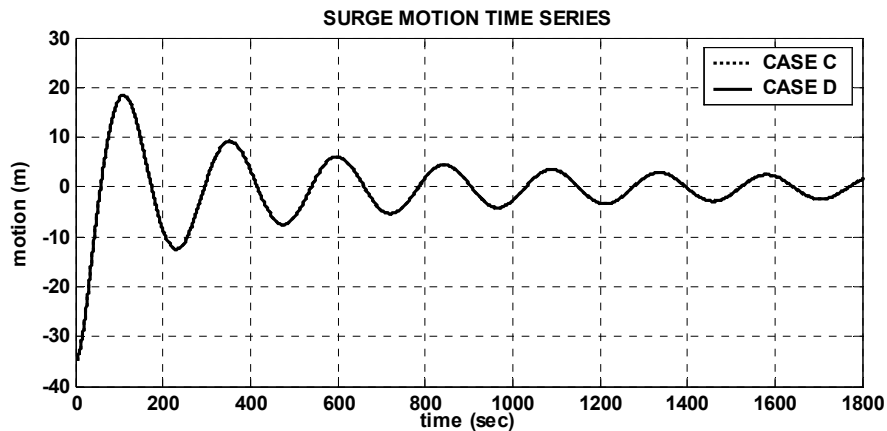


Fig. 5.11. Surge free decay motion time series.

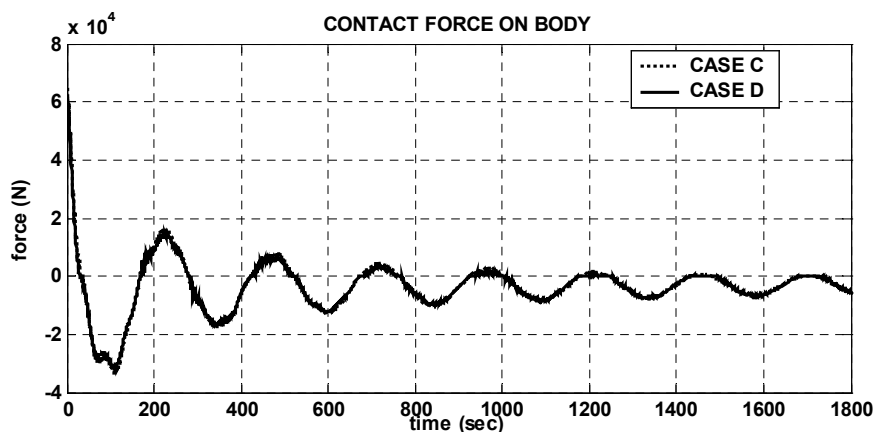


Fig. 5.12. Contact force on the spar platform at keel (from production riser No.23).

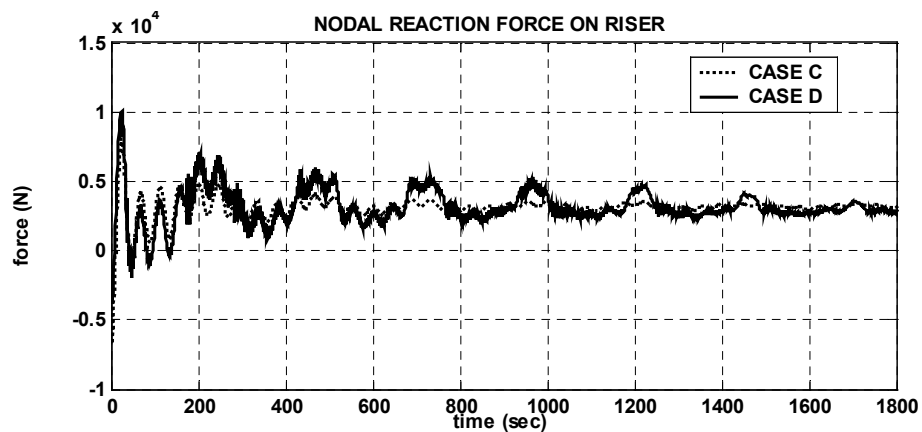


Fig. 5.13. Nodal reaction force on riser (production riser No.23, node 11).

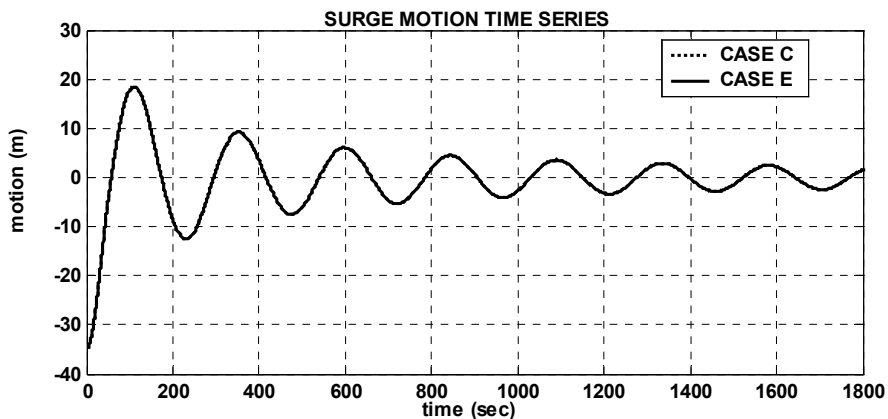


Fig. 5.14. Surge free decay simulation time series.

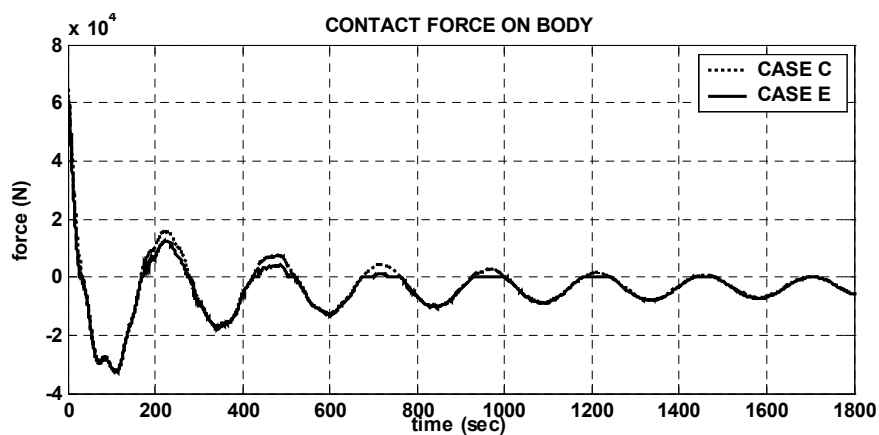


Fig. 5.15. Contact force on the spar platform at keel (from production riser No.23).

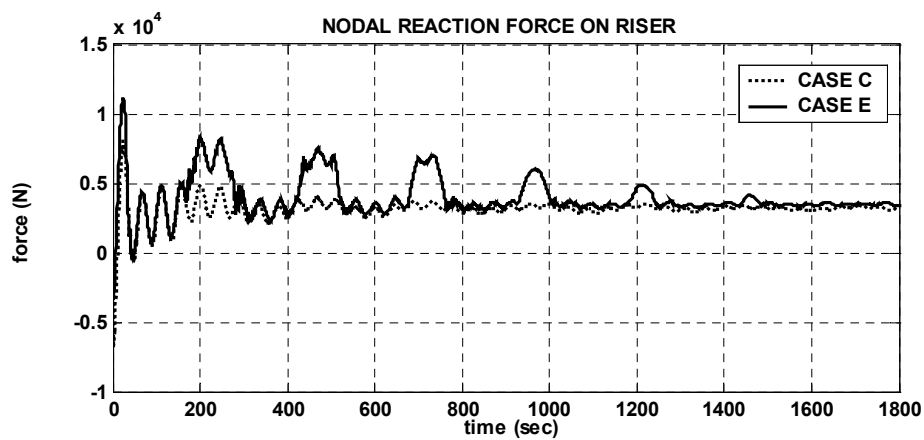


Fig. 5.16. Nodal reaction force on riser (production riser No.23, node 11).

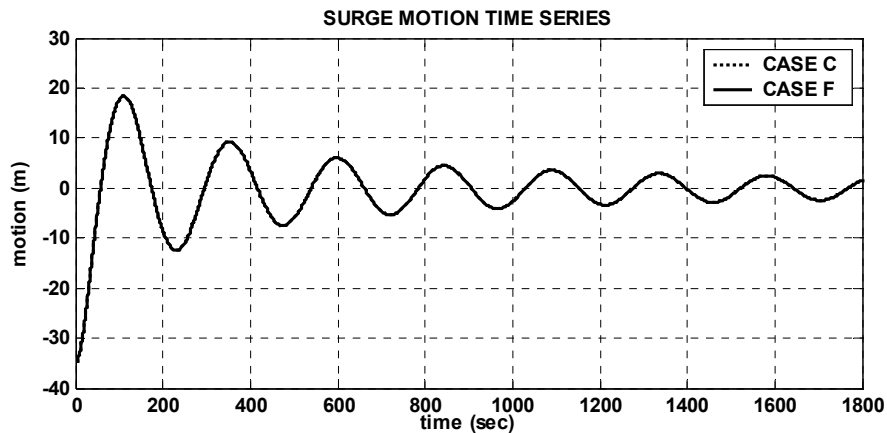


Fig. 5.17. Surge free decay simulation time series.

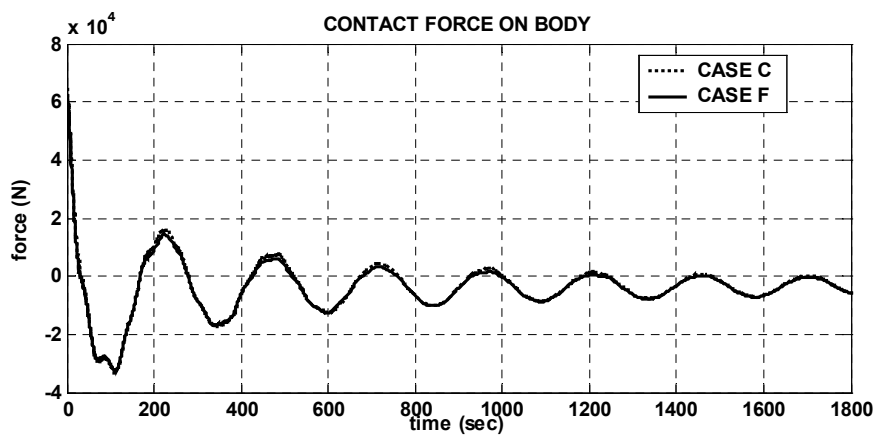


Fig. 5.18. Contact force on the spar platform at keel (from production riser No.23).

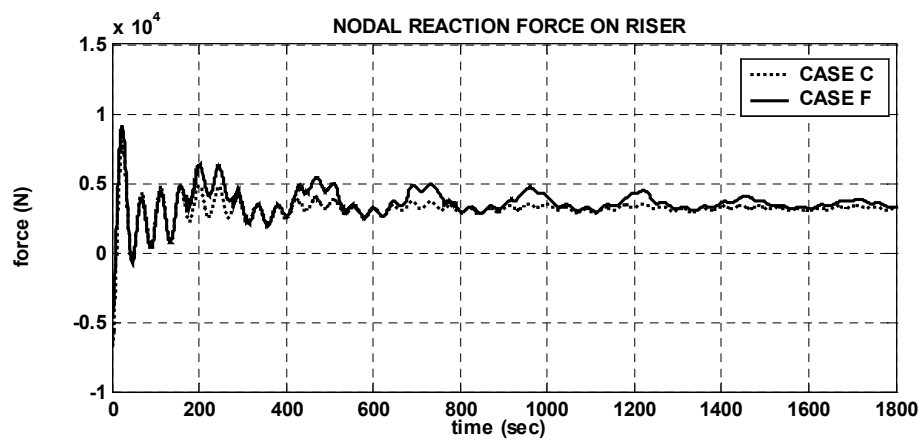


Fig. 5.19. Nodal reaction force on riser (production riser No.23, node 11).



**Table 5.6. Surge free decay simulation results.**

	$T_N$ (sec)	Damp. Ratio% (1st 3 Ave.)	Damp. Ratio% (1st 7 Ave.)
W/O Riser	257	9.5	5.8
CASE A	257	9.9	6.0
CASE B	257	9.9	6.0
CASE C	257	9.9	6.0
CASE D	257	9.9	6.0
CASE E	257	9.9	6.0
CASE F	257	9.9	6.0
<i>Note:</i> W/O = without			

To capture the Coulomb damping effects on the spar heave motion, initial offsets were given in pitch and roll directions. The simulation results are summarized in Table 5.7 and Fig. 5.20 through Fig. 5.24. In the heave free decay simulations, the Coulomb damping force between the risers and riser guide frames is clearly shown in Fig. 5.22 and Fig. 5.24. Due to additional damping from friction between the riser and riser guide frame, heave damping ratios are increased in the models, which consider Coulomb damping. As mentioned before, with Coulomb damping, amplitude decays linearly rather than exponentially, and Fig. 5.20 shows that the amplitude of heave free decay motion with Coulomb damping (Case C) decays almost linearly compare to the without Coulomb damping model (Case B). Fig. 5.21 also shows that the Coulomb damping does not alter the frequency of heave motion. Fig. 5.23 shows Coulomb damping force at the spar keel. In the Coulomb damping modeling, the Coulomb damping force is proportional to the sum of the normal force and frictional coefficient. Fig. 5.24 shows horizontal contact force and this graph shows that during the heave free decay test, the horizontal contact forces are almost constant. In the case of gap-contact models, the Coulomb friction contributes only

when riser contact with the riser-guide frames. The additional damping from coulomb damping can be changed with the horizontal force. Therefore, in the 100-year hurricane simulation, the Coulomb damping effects will be larger than free decay simulation.

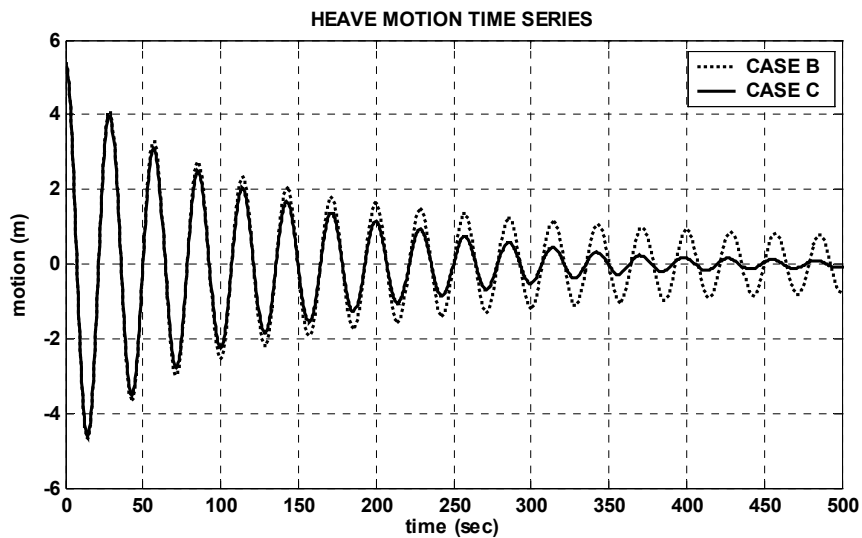


**Fig. 5.20. Heave free decay simulation results.**

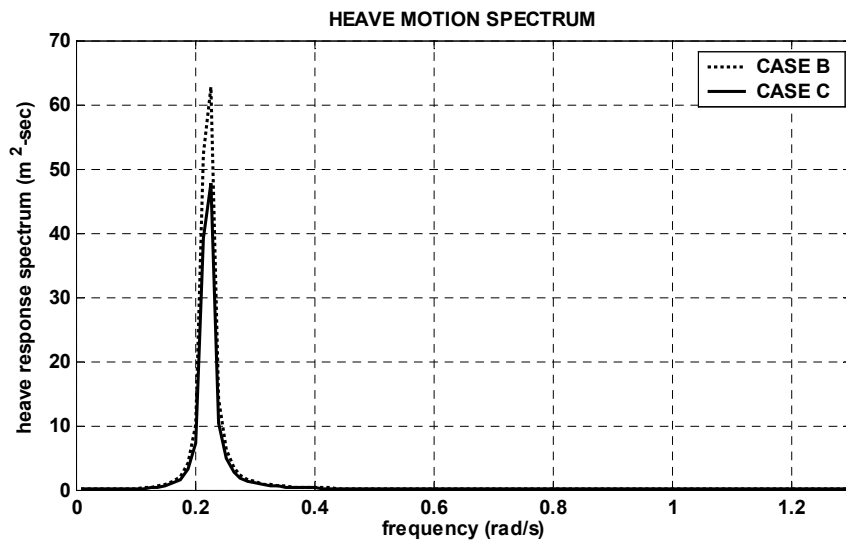


**Fig. 5.21. Heave free decay motion spectrum.**

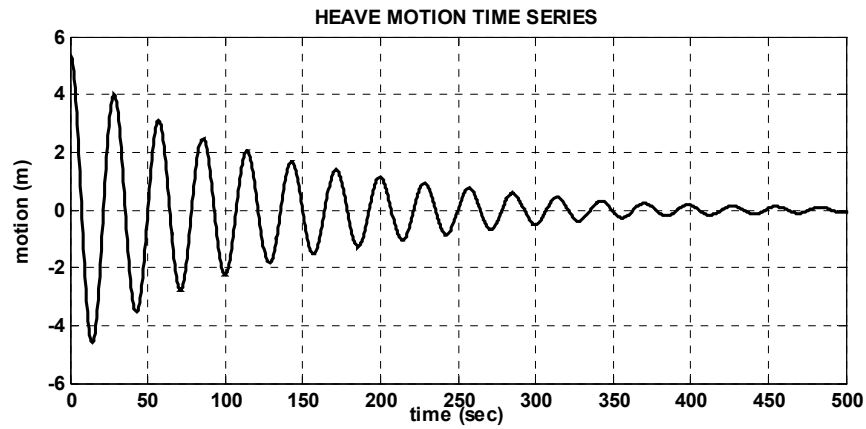


Fig. 5.22. Heave free decay simulation time series (CASE C).

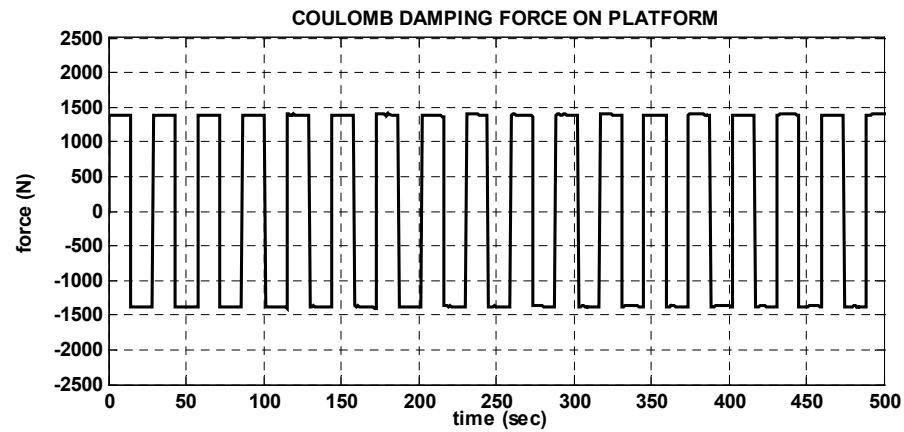


Fig. 5.23. Coulomb damping force on the spar platform at keel (drilling riser).

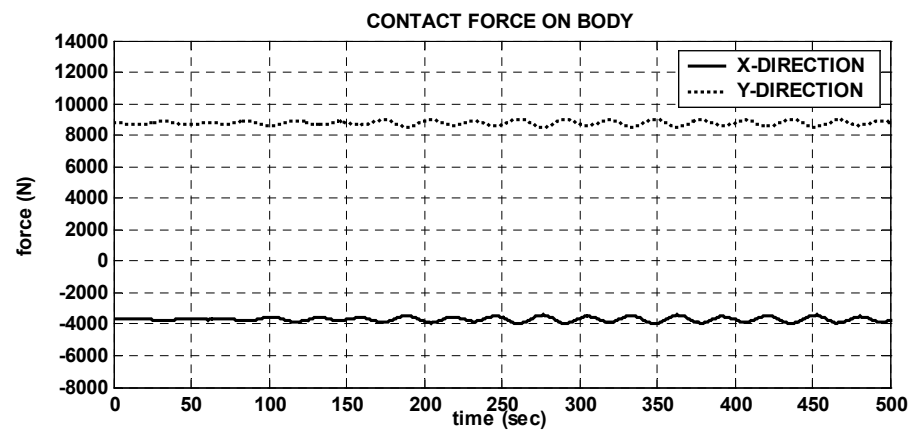


Fig. 5.24. Horizontal contact force on the spar platform at keel (drilling riser).

**Table 5.7. Heave free decay simulation results.**

	$T_N$ (sec)	Damp. Ratio% (1st 3 Ave.)	Damp. Ratio% (1st 7 Ave.)
CASE A	27.81	3.56	2.72
CASE B	27.81	3.56	2.72
CASE C	27.81	4.06	3.50
CASE D	27.81	4.00	3.37
CASE E	27.81	4.02	3.43
CASE F	27.81	4.03	3.44

The pitch free decay simulation results are summarized in Table 5.8 and Fig. 5.25 through Fig. 5.28. Table 5.8 illustrates the effects of the riser and contact models on period and damping ratio. It is also shown that the riser appreciably increases the total pitch damping. When risers are extended through the inside of the moon-pool, (Case B) the pitch natural period is shifted compared to the Case A (riser truncated at the keel). This frequency shift is due to the additional pitch restoring moment caused by the inverted pendulum effect of the buoyancy-cans. The pitch natural period difference is clearly shown in Fig. 5.26. Fig. 5.27 and Fig. 5.28 shows the pitch free decay motions and contact moments for the multi-contact model. In these figures, the contact moment induced by the contact force has a 180-degree phase difference with the pitch free decay motion. This means the pitch motion is reduced when the restoring moment is taken into account. On the other hand, different gap-spring models do not influence the pitch damping and pitch natural period. The contact moment result for the piecewise-quadratic gap-contact spring model (Case E) in Fig. 5.28 has some noise-like fluctuation but it hardly influences the global pitch motion. The noise-like fluctuation is caused by the sudden rapid increase discontinuity at the initial contact force. Fig. 5.4 shows that the piecewise-quadratic gap-contact spring model has the largest discontinuity at the point. Whereas, the continuous

cubic spring approximation model (Case F) eliminates the noise-like behavior. Thus, from a numerical view, the cubic spring approximation model is best for simulation.

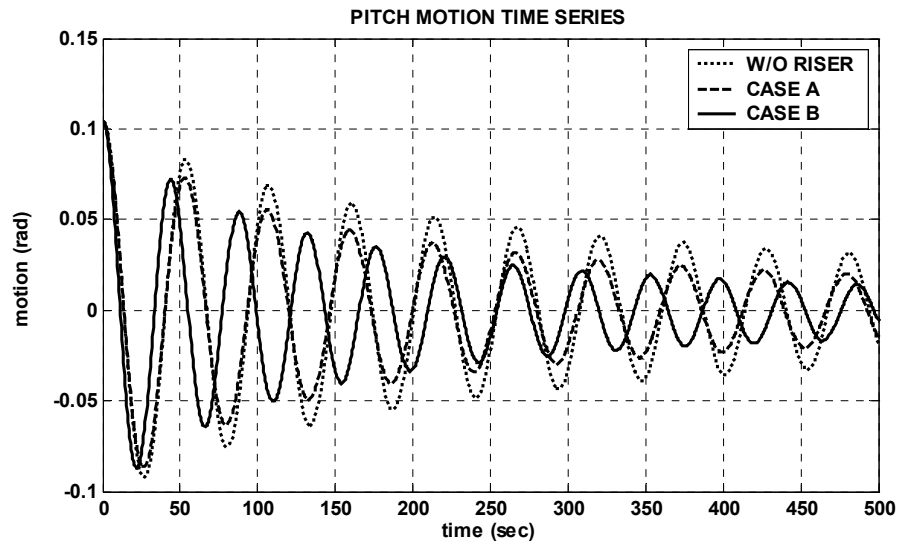


Fig. 5.25. Pitch free decay simulation time series.

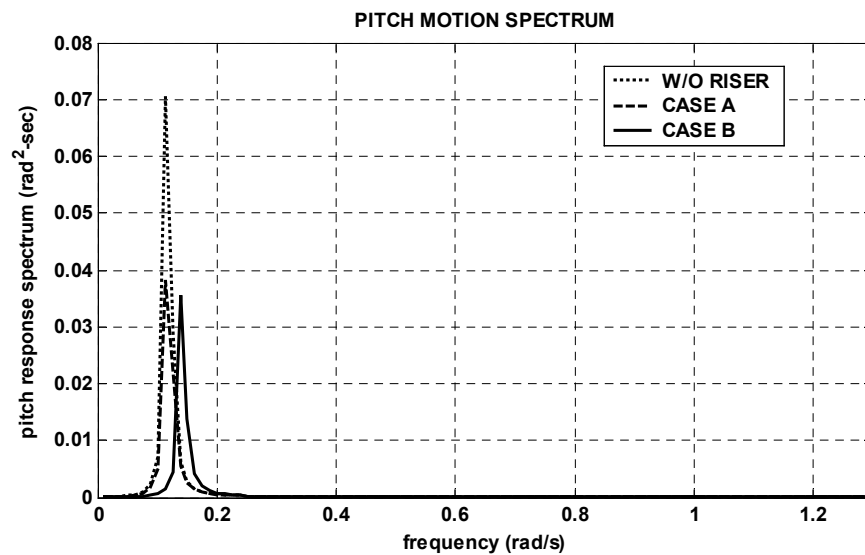


Fig. 5.26. Pitch free decay motion spectrum.

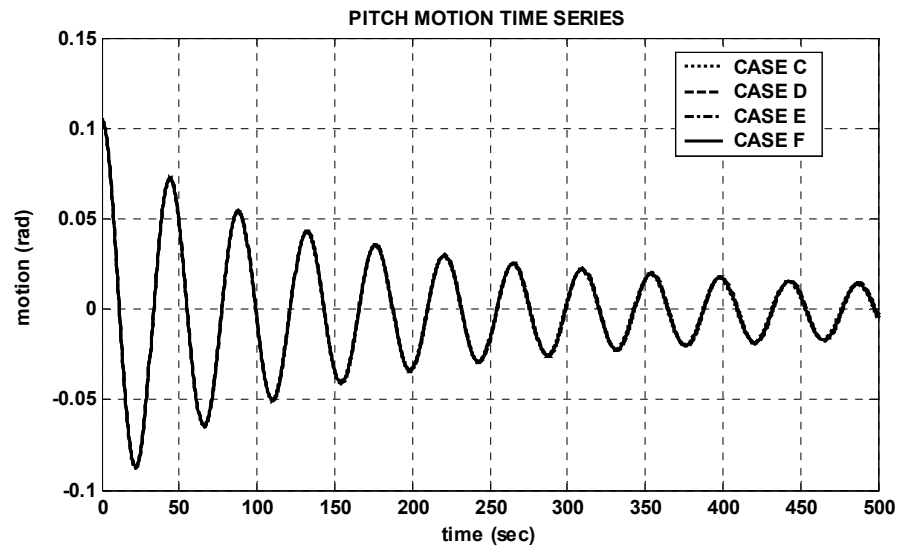


Fig. 5.27. Pitch free decay simulation time series.

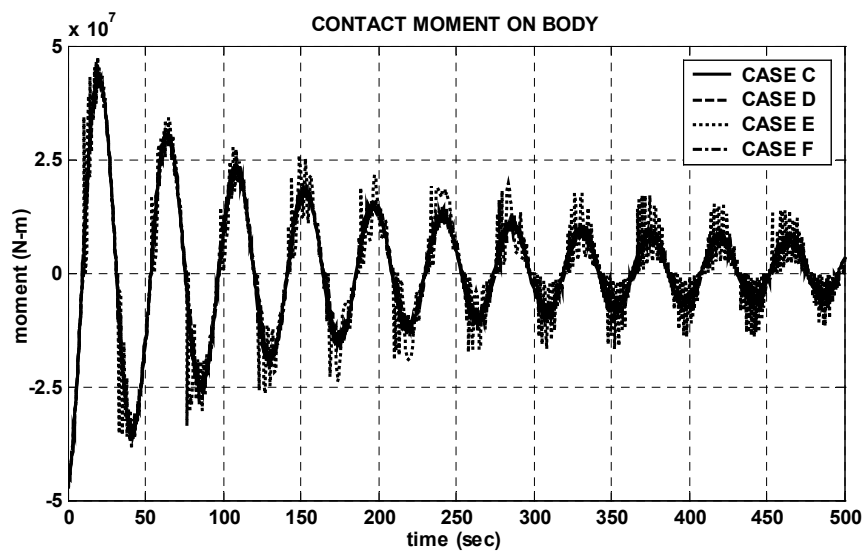


Fig. 5.28. Contact moment on the spar platform at keel (from production riser # 23).

**Table 5.8. Pitch free decay simulation results.**

	$T_N$ (sec)	Damp. Ratio% (1st 3 Ave.)	Damp. Ratio% (1st 7 Ave.)
W/O Riser	55.6	3.0	2.3
CASE A	55.6	4.5	3.3
CASE B	45.5	4.7	3.5
CASE C	45.5	4.7	3.6
CASE D	45.5	4.6	3.5
CASE E	45.5	4.7	3.5
CASE F	45.5	4.7	3.5

*Note:* W/O = without

#### 5.4.2. 100-year Hurricane Simulations

To capture the buoyancy-can and gap contact effects on the global spar motion response, in this section, the simulation results are systematically compared and summarized. Fig. 5.29, Fig. 5.30, and Fig. 5.31 show the wind velocity spectrum, the wave spectrum, and wave time series used in simulations. The JONSWAP spectrum used in this paper is as follows:

$$S(\omega) = \frac{5H_s^2\omega_p^4}{16\omega^5} (1 - 0.287 \ln \gamma) \exp \left[ -\frac{5}{4} \left( \frac{\omega_p}{\omega} \right)^4 \right] \gamma^a \quad (5.1)$$

where  $H_s$  is the significant wave height,  $\omega$  is frequency,  $\omega_p$  is the peak frequency, and  $\gamma$  is the over shooting parameter. The symbol  $a$  is defined by

$$a = \exp \left[ \frac{-(\omega - \omega_p)^2}{2\sigma^2\omega_p^2} \right] \quad (5.2)$$

where  $\sigma = 0.07$  when  $\omega < \omega_p$  and  $\sigma = 0.09$  when  $\omega > \omega_p$ .

The input wave spectrum is truncated at  $0.2 \text{ (rad/sec)} < \omega < 1.2 \text{ (rad/sec)}$  in this study,

and wind spectrum is truncated at 2 (rad/sec).

The API wind spectrum used in this paper is as follows:

$$S(\omega) = \frac{\sigma^2(z)}{2\pi f_p \left[ 1 + \frac{1.5}{2\pi f_p} \right]^{\frac{5}{3}}} \quad (5.3)$$

where  $f_p$  is average factor derived from measured spectrum and is given by

$$f_p = \frac{0.025V_w(z)}{z} \quad (5.4)$$

The symbol  $\sigma(z)$  is the standard deviation of wind speed and related to turbulence intensity.

The value of  $\sigma(z)$  at 10 meter above mean water level can be expressed as

$$\sigma(z) = 0.15 \left( \frac{z}{20} \right)^{-0.125} V_w(z) \quad (5.5)$$

where  $V_w(z)$  is the one hour mean wind speed (m/s)  $z$  meters above water level.

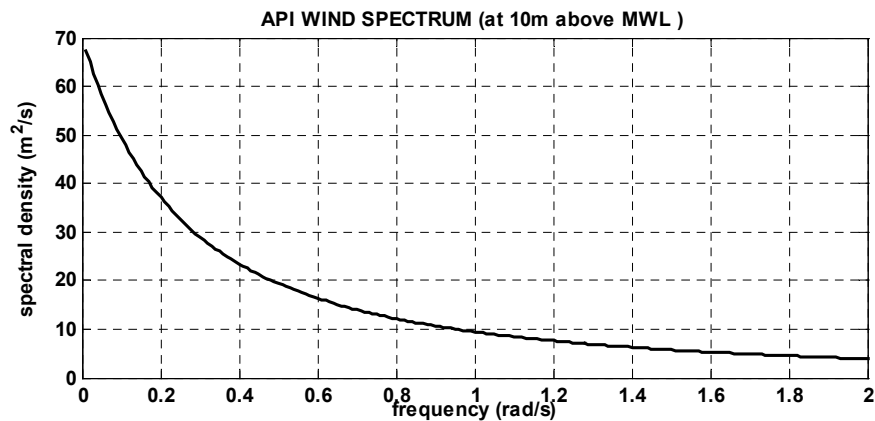


**Fig. 5.29. 100-year Gulf of Mexico hurricane wind velocity spectrum.**



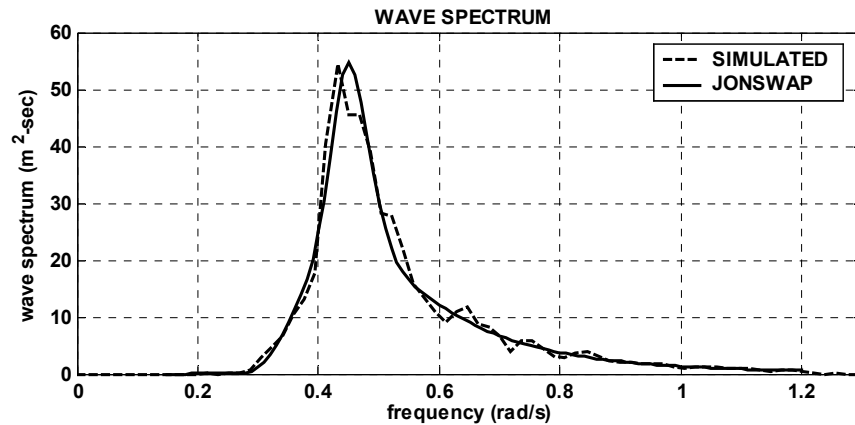


**Fig. 5.30. 100-year Gulf of Mexico hurricane wave spectrum.**

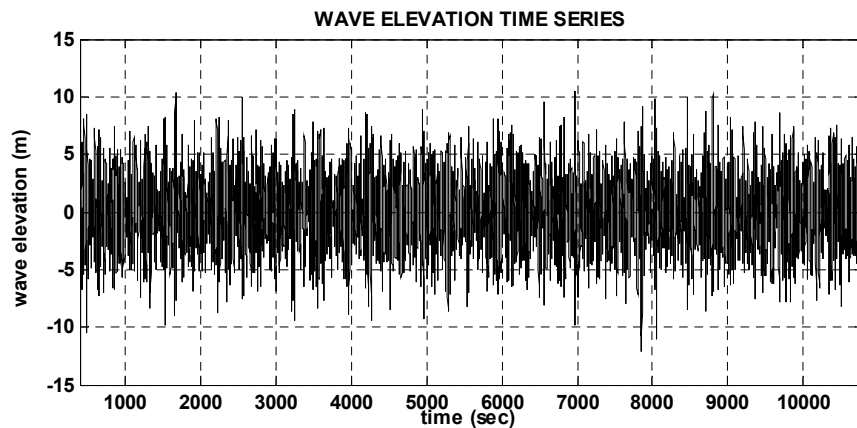


**Fig. 5.31. 100-year hurricane wave elevation time series.**

The spar surge motion responses are summarized in Table 5.9 and Fig. 5.32 through Fig. 5.35. The results show that the effects of the risers inside of the spar moon-pool do not change the spar surge motion significantly. In the station keeping view (i.e. surge and sway motion), buoyancy-can effect on the surge and sway spar motion is not important. These results are consistent with free decay simulation results. In the surge free decay simulation, the surge motions are almost identical for each case. The reason is that buoyancy-can supported riser system is not connected to the spar platform, thus buoyancy-can effects

only changes the mass of spar platform in surge and sway motion. However, the mass changes due to buoyancy-can are not large compared to total mass of the spar system. The contact force from buoyancy-can in surge and sway directions are also small compared to mooring tension. The reason is that the buoyancy-can gives vertical force on riser, therefore additional force from buoyancy-can is not enough to changes the horizontal motion of the spar platform. Due to these two reason, the spar surge response from all cases are almost identical. However, following heave and pitch motion results will clearly show the buoyancy-can effect on the spar platform. In this study, the low and wave frequencies are defined as  $\omega < 0.2$  (rad/sec) and  $0.2$  (rad/sec)  $< \omega < (1.2$  rad/sec), respectively.

**Table 5.9. Comparison of the statistics of surge response (Hurricane Condition).**

Spar Surge Motion in 100-year Hurricane Condition Gulf of Mexico					
	MEAN (m)	STD (m)	LF STD (m)	WF STD (m)	EXE (m)
CASE A	-21.969	2.015	1.913	0.634	-28.227
CASE B	-22.176	2.013	1.912	0.631	-28.413
CASE C	-22.176	2.014	1.913	0.631	-28.415
CASE D	-22.168	2.015	1.914	0.630	-28.414
CASE E	-22.173	2.015	1.914	0.630	-28.416
CASE F	-22.172	2.015	1.914	0.631	-28.415
<i>Notes:</i> STD = standard deviation; EXE = extreme; LF = low frequency; WF = wave frequency					

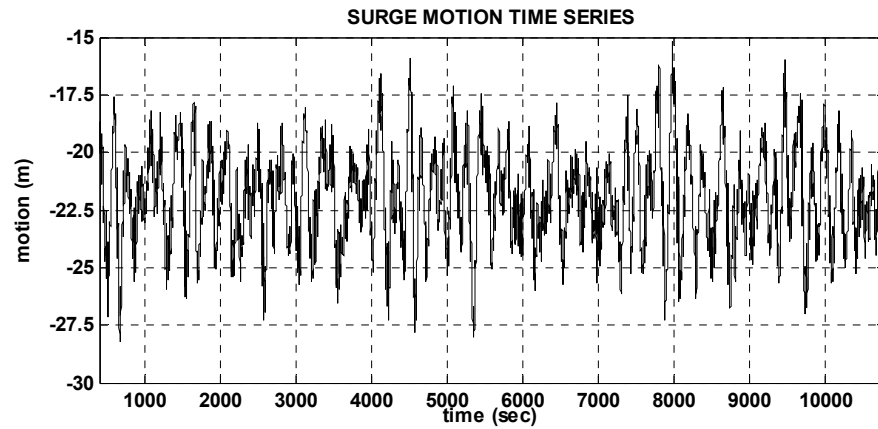


**Fig. 5.32. Surge response time series (CASE A).**

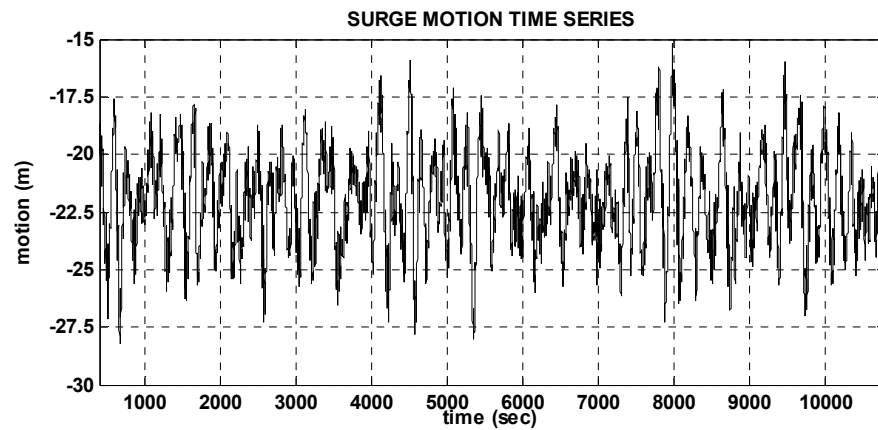


**Fig. 5.33. Surge response time series (CASE B).**

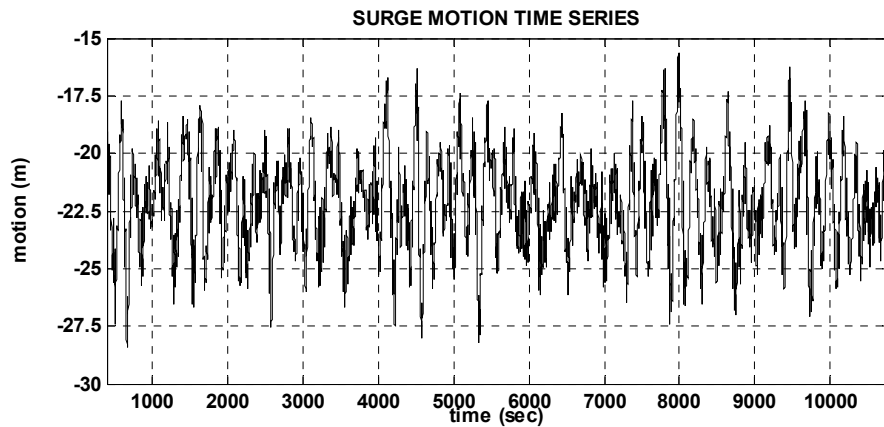


**Fig. 5.34. Surge response time series (CASE D).**

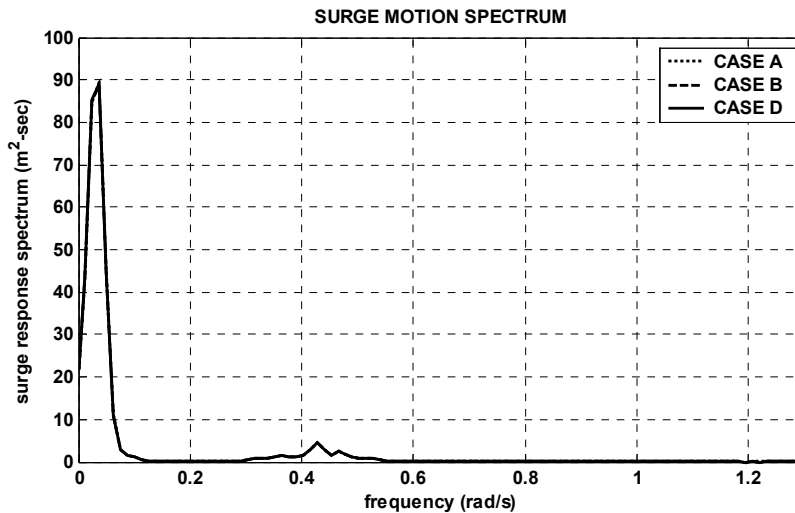


**Fig. 5.35. Comparison of the surge response spectrum (CASE A, CASE B, and CASE D).**

The spar heave motion responses are summarized in Table 5.10 and Fig. 5.36 through Fig. 5.38. In the heave motion, the results show the Coulomb damping effect. Table 5.10 shows that the heave standard deviation is reduced by 25% and maximum motion is also reduced by 12.2% for the Coulomb damping cases. Due to the large horizontal contact force from the surge and sway motion, the Coulomb damping effects are increased in the 100-year hurricane simulation. Comparison between heave free decay motion spectrum and heave response spectrum from the 100-year hurricane simulation show that the Coulomb damping is proportional to magnitude of the horizontal contact force. From the calculated standard deviation, the Coulomb damping effects reduce the heave free decay motion by 12 %, but in the 100-year hurricane conditions, the heave motion response reduced by 25%. Fig. 5.38 and Table 5.10 also show that the Coulomb damping reduces the spar heave motion in the heave natural period region (0.224 rad/sec), and it also shows that the first peak caused by the set down, is not affected by Coulomb damping.

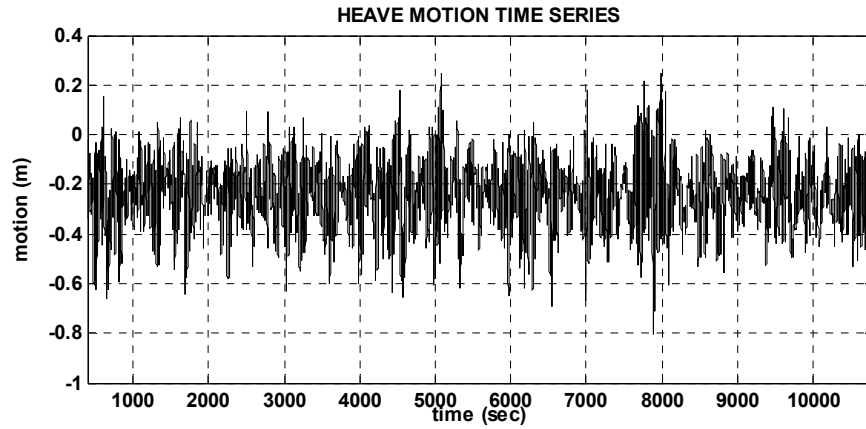


Fig. 5.36. Heave response time series (CASE B).

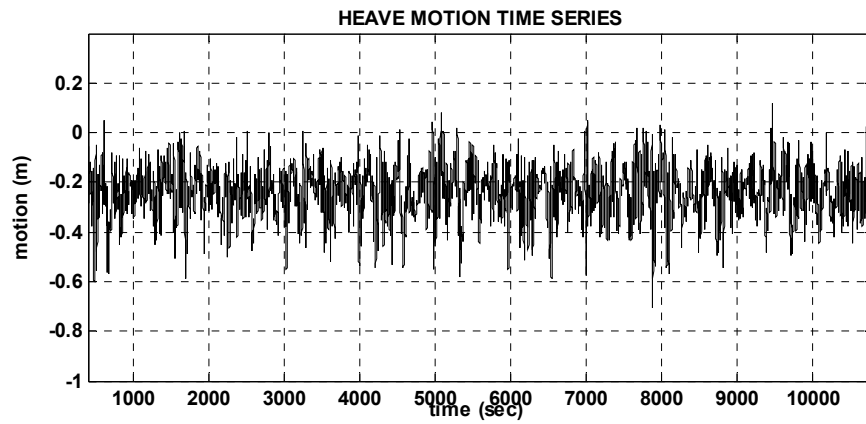


Fig. 5.37. Heave response time series (CASE C).

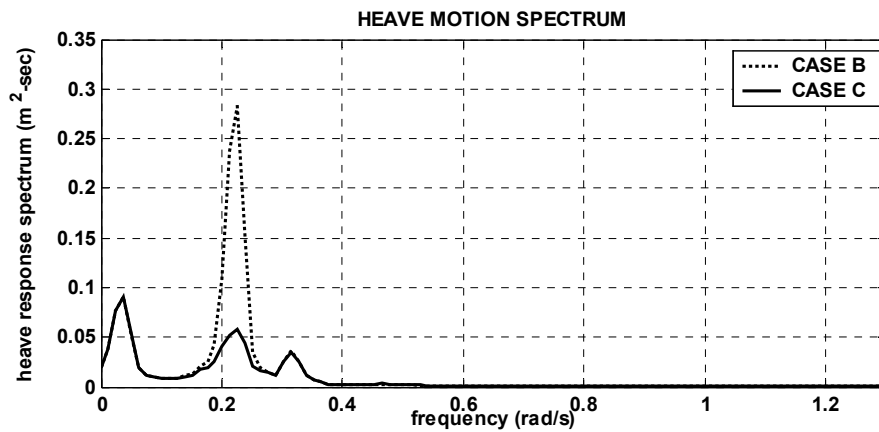


Fig. 5.38. Comparison of heave response spectrum (CASE B and CASE C).

**Table 5.10. Comparison of statistics of heave response (Hurricane Condition).**

Spar Heave Motion in 100-year Hurricane Condition Gulf of Mexico					
	MEAN (m)	STD (m)	LF STD (m)	WF STD (m)	EXE (m)
CASE A	-0.239	0.135	0.074	0.109	-0.813
CASE B	-0.240	0.135	0.073	0.109	-0.805
CASE C	-0.239	0.101	0.072	0.069	-0.707
CASE D	-0.239	0.102	0.072	0.069	-0.708
CASE E	-0.239	0.101	0.072	0.069	-0.712
CASE F	-0.239	0.102	0.072	0.070	-0.709
<i>Notes:</i> STD = standard deviation; EXE = extreme; LF = low frequency; WF = wave frequency					

The spar pitch motion responses are summarized in Table 5.11 and Fig. 5.39 through Fig. 5.41. The comparison of truncated riser (Case A) and extended riser case (Case B through Case E) clearly shows the effect of additional pitch restoring moment by buoyancy-cans and risers inside of the spar moon-pool. When the spar heels, the risers will contact the support guide frames. Then, the contact forces produce additional pitch righting moment. As a result, the mean pitch offset of fully modeled riser cases (Case B through Case F) are reduced by 29%, and the standard deviation pitch is reduced by 13% when compared with the truncated riser model (Case A) respectively. The reduction of pitch standard deviation is mainly due to the increase of pitch damping and stiffness. This means that the shift of natural frequency makes the wind loading less influential to the slowly-varying pitch responses. Interestingly, wave-frequency pitch motions are not influenced by the increase of pitch stiffness. Table 5.11 shows that the standard deviation of low-frequency pitch motion is reduced by 24% when compared to the truncated riser model. Due to the reduction in both the mean and standard deviation, the maximum pitch response in simulated hurricane conditions is reduced by 24% when compared to the truncated riser model. The results show that neglecting the buoyancy-can effects causes an overestimation

of the pitch and roll response of the spar platform.

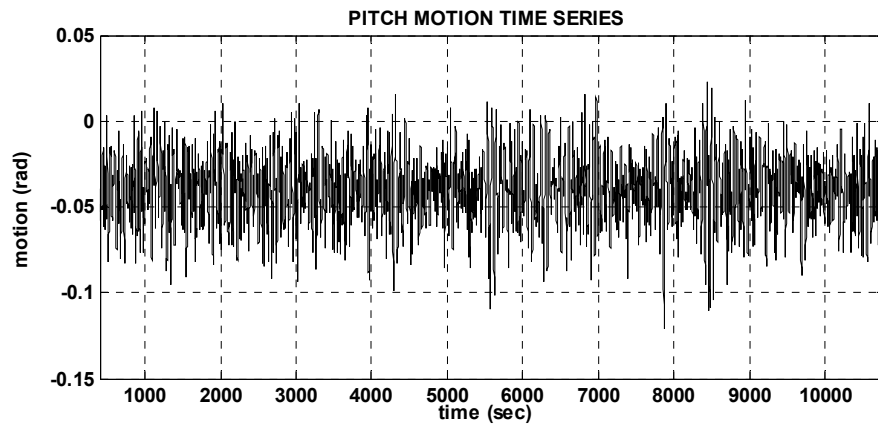


**Fig. 5.39. Pitch response time series (CASE A).**

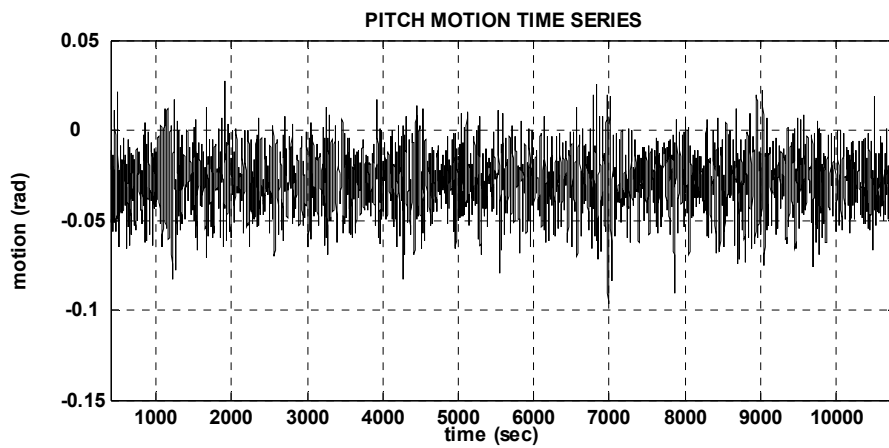


**Fig. 5.40. Pitch response time series (CASE B).**

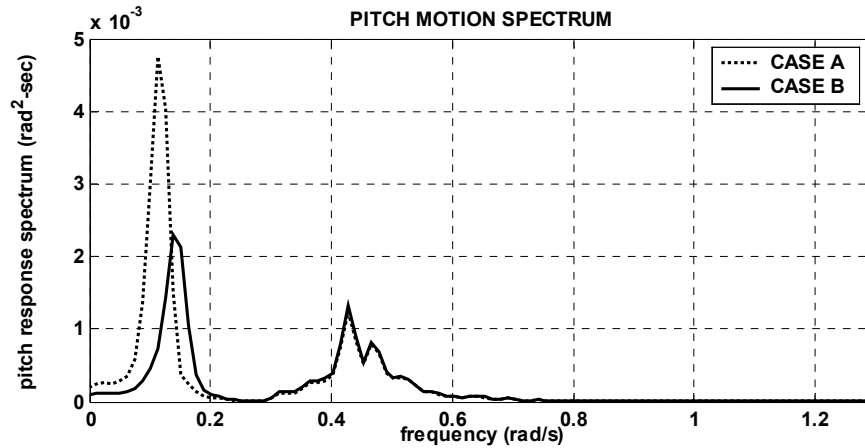


**Fig. 5.41. Comparison of the pitch response spectrum (CASE A and CASE B).**

**Table 5.11. Comparison of the statistics of pitch response (Hurricane Condition).**

Spar Pitch Motion in 100-year Hurricane Condition Gulf of Mexico					
	MEAN (deg.)	STD (deg.)	LF STD (deg.)	WF STD (deg.)	EXE (deg.)
CASE A	-2.316	1.053	0.112	0.082	-6.915
CASE B	-1.638	0.903	0.083	0.085	-5.515
CASE C	-1.638	0.902	0.083	0.085	-5.511
CASE D	-1.644	0.907	0.084	0.085	-5.533
CASE E	-1.642	0.904	0.084	0.085	-5.521
CASE F	-1.641	0.904	0.084	0.085	-5.522

*Notes:*  
 STD = standard deviation; EXE = extreme; LF = low frequency; WF = wave frequency

Table 5.12 and Fig. 5.42 through Fig. 5.44 show the most loaded mooring line top tension in the 100-year hurricane simulations. Due to almost identical surge motion between truncated riser model case (Case A) and fully modeled riser cases (Case B through Case F), the most loaded line tension is almost identical. Most of the mooring line tension is from slowly-varying surge motion, and buoyancy-can effects do not significantly change most loaded mooring line tension.



The free decay simulations and 100-year hurricane simulation results clearly show that the gap between the buoyancy-can and guide frame gives not change the spar global motions. On the other hand, the surge free decay simulation results show that the gap between the buoyancy-can and guide frame causes an impact force on buoyancy-can. To confirm the gap effect on buoyancy-can, other simulations are conducted for Case D and Case E with different gap distances. Fig. 5.45, Fig. 5.46, and Table 5.13 summarize the riser nodal reaction force comparison. The results show that the gap distance increases the standard deviation and the maximum value of the riser nodal reaction force. Therefore, reducing the gap distance reduces the impact force and also reduces the fatigue problem of buoyancy-can. The  $\Delta t$  of the contact with the piecewise-quadratic gap-contact riser, Case E, is also expected to be smaller, thus leads to larger impact.

**Table 5.12. Comparison of statistics of mooring tension.**

	CASE A	CASE B	CASE C	CASE D	CASE E	CASE F
MEAN (N)	4.95E+06	4.96E+06	4.96E+06	4.95E+06	4.96E+06	4.96E+06
STD (N)	6.02E+05	6.04E+05	6.03E+05	6.03E+05	6.03E+05	6.03E+05
EXE (N)	7.81E+06	7.68E+06	7.63E+06	7.62E+06	7.62E+06	7.62E+06
<i>Notes:</i> STD = standard deviation; EXE = extreme						

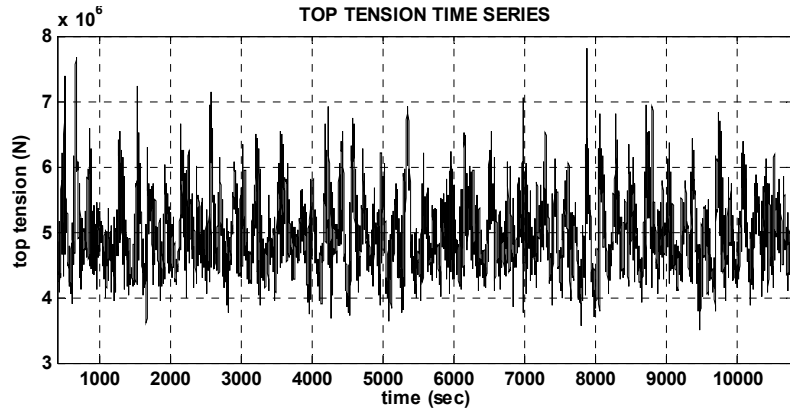


Fig. 5.42. Most loaded mooring line top tension time series (CASE A).

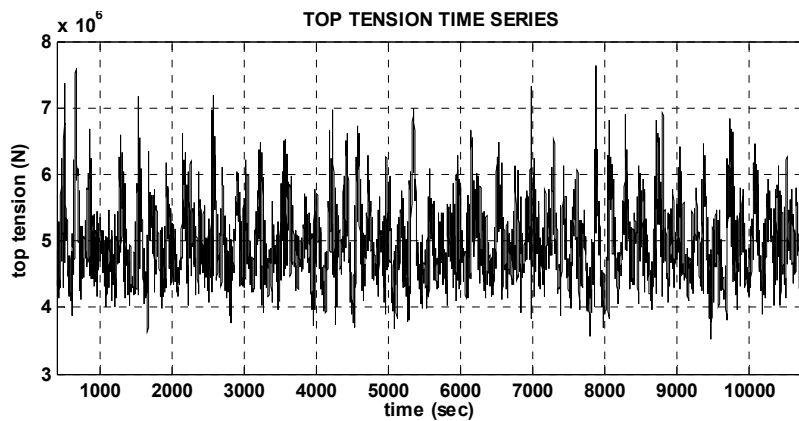


Fig. 5.43. Most loaded mooring line top tension time series (CASE C).

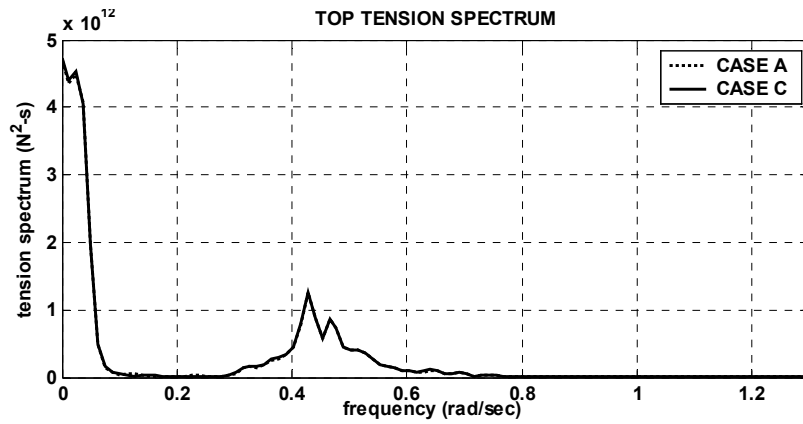
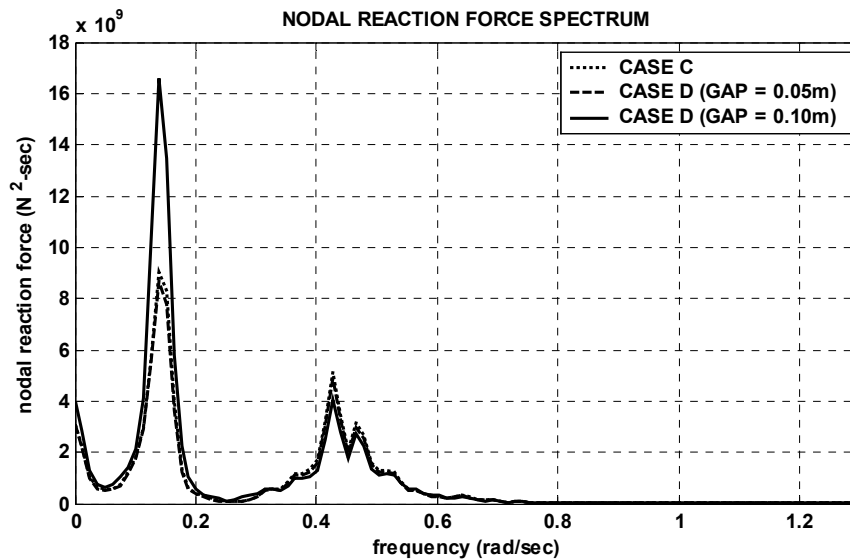
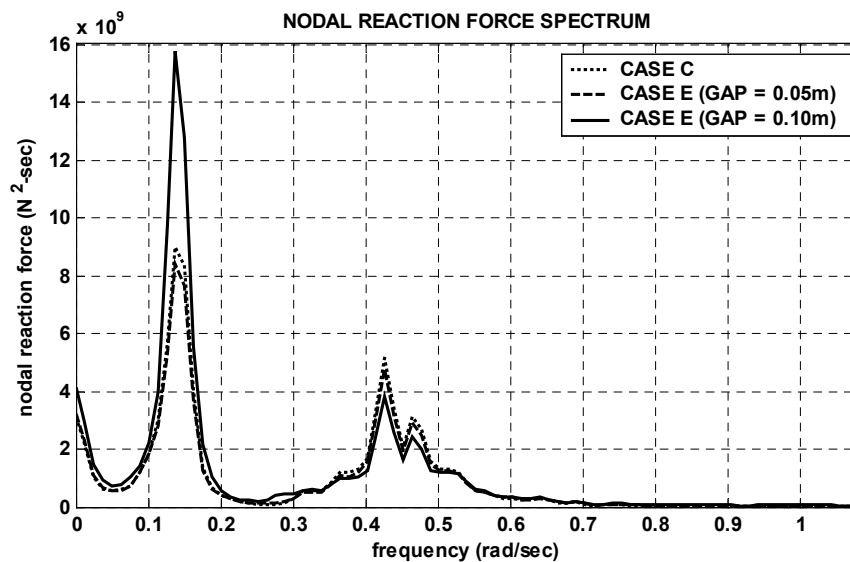


Fig. 5.44. Most loaded line top tension spectrum (CASE A and CASE C).



**Fig. 5.45. Comparison of the nodal reaction force spectrum for production riser # 23 (CASE C and CASE D, node # 11).**



**Fig. 5.46. Comparison the of nodal reaction force spectrum for production riser # 23 (CASE C and CASE E, node # 11).**

**Table 5.13. Comparison of riser horizontal nodal reaction force at keel (production riser # 23, node # 11).**

	CASE A	CASE D		CASE E	
	0.00 m	0.05m	0.10m	0.05m	0.10m
STD (N)	3.22E+04	3.18E+04	3.63E+04	3.26E+04	3.86E+04
EXE (N)	2.04E+05	2.05E+05	2.40E+05	2.26E+05	2.53E+05
<i>Notes:</i> STD = standard deviation; EXE = extreme					

### 5.4.3. Comparison with Existing Experimental Data

Zhang and Zou (2002) developed software for predicting buoyancy-can effects on the global spar motion and compare their results to existing experimental data. The software developed in this study is used to compare with experimental and numerical results published by Zhang and Zou (2002). In their study, the risers are modeled through the spar moon-pool and frictional damping is considered between riser and riser guide frame. However, they did not consider gap between riser and riser guide frame. Thus, their spar modeling is very close to Case C herein. In the simulation, they use their own program DeepCAT. DeepCAT is the name of the simulation software jointly developed by ABS and ABB (Zhang and Zou, 2002). 0.05 is used for the frictional coefficients in the DeepCAT simulation. In Case C simulation, a 0.07 frictional damping coefficient is used. Due to different coefficients and location of guide frames, the results are different, but the reduction rate in pitch response is very close to result of this study.

Table 5.14 shows the comparison of natural periods from free decay test. The results show that Case C has 17seconds and 8 seconds larger surge periods than experiment and DeepCAT simulation, respectively. Heave natural periods shows that Case C result is

almost identical to the measured heave periods. Pitch natural periods show that Case C is stiffer than DeepCAT simulation and measurement results. However, the damping ratio is not compared due to information is not provided in the reference.

Table 5.15 shows the surge motion response results. The results show that Case C over estimates the surge motion due to larger surge natural periods. However like Case C, the DeepCAT result also show that the buoyancy-can effects are not significant for surge response.

Table 5.16 shows the heave motion response results. The mean and extreme values from Case C are slightly larger than DeepCAT simulation and measured results. It is hard to find the exact reason because the heave time series and spectrum are not available. One of the possible reasons is that larger surge motion in Case C, the heave motion from surge set down and set up can be overestimated in heave motion. However, the heave motion standard deviation from Case C is closer to measured result. The heave motion from DeepCAT shows that the Coulomb damping does not reduce the heave motion. On the other hand, Case C clearly shows the Coulomb damping effects on heave motion.

Table 5.17 shows the pitch motion response results. These results show larger mean and extreme values from Case C. However, the reduction rate in Table 5.18 is very similar to DeepCAT simulation. The comparisons show that buoyancy-can effects in both simulation results are comparable to each other.

**Table 5.14. Natural periods comparison.**

	Surge (sec)	Heave (sec)	Pitch (sec)
Measured	240	28	49
DeepCAT	245	29	50
Case C	257	27.8	45.5

**Table 5.15. Spar surge response comparison.**

Surge Response in 100 – year Hurricane simulation			
	MEAN (m)	STD (m)	EXE (m)
Measured	-19.30	2.10	-26.00
DeepCAT (truncated riser model)	-19.48	2.08	-25.18
DeepCAT (extended riser model)	-19.02	2.13	-25.14
CASE A	-21.97	2.02	-28.23
CASE C	-22.18	2.01	-28.42
<i>Notes:</i> STD = standard deviation; EXE = extreme			

**Table 5.16. Spar heave response comparison.**

Heave Response in 100 – year Hurricane simulation			
	MEAN (m)	STD (m)	EXE (m)
Measured	-0.20	0.11	-0.57
DeepCAT(truncated riser model)	-0.21	0.09	-0.51
DeepCAT(extended riser model)	-0.20	0.09	-0.50
CASE A	-0.24	0.14	-0.81
CASE C	-0.24	0.10	-0.71
<i>Notes:</i> STD = standard deviation; EXE = extreme			

**Table 5.17. Spar pitch response comparison.**

Pitch Response in 100 – year Hurricane simulation			
	MEAN (deg.)	STD (deg.)	EXE (deg.)
Measured	-1.20	0.80	-4.90
DeepCAT (truncated riser model)	-2.00	1.08	-6.37
DeepCAT (extended riser model)	-1.53	0.92	-5.02
CASE A	-2.32	1.05	-6.92
CASE C	-1.64	0.90	-5.51
<i>Notes:</i> STD = standard deviation; EXE = extreme			

**Table 5.18. Comparison of pitch motion reduction.**

% of Pitch motion Reduction (Truncated riser model Vs. Fully modeled riser)			
	MEAN (%)	STD (%)	EXE (%)
DeepCAT	23.5	14.8	21.2
WINPOST	29.2	13.5	24.1

## CHAPTER VI

### CASE STUDY 2: ALTERNATIVE RISER SUPPORT SYSTEM

#### 6.1. Introduction

In this chapter, the dynamic behavior of a classical spar platform is investigated with an alternate riser support system. As mentioned before, the spar platform generally uses buoyancy-cans for supporting risers in vertical direction, but as the water depth gets deeper the required buoyant force increases due to increasing riser weight. It has been reported that the dimensions of a buoyancy-can are 4-meter in diameter and 80-meter long in 1324-meter water depth. Due to large volume of buoyancy-can, it makes installation difficult, particularly from a safety point of view. Thus, the alternative system is to hang the risers off the spar platform using pneumatic cylinders rather than the buoyancy-cans. The pneumatic cylinder allows the riser to move relative to one another and the spar hull. In this chapter, the risers inside of the spar moon-pool are fully modeled with pneumatic cylinders, and the results are compared with buoyancy-can model (i.e. Case F in Chapter V).

#### 6.2. Description of the Spar Platform, Mooring System and Risers

The dimension, mooring lines configuration and risers configuration of the spar platform used in this study is exactly same as Chapter V (i.e. case study 1: buoyancy-can



effect on spar Platform) except the riser support system. The principle particulars of the spar platform and characteristics of mooring line and riser are summarized in Table 5.1 through Table 5.4 in Chapter V. Due to the risers are hanging off the spar platform, the additional riser pretensions on the spar platform are considered for the pneumatic riser support system. The arrangement of mooring lines and risers are shown in Fig. 6.1. Table 6.1 shows the mooring lines and risers pretension on the spar platform.

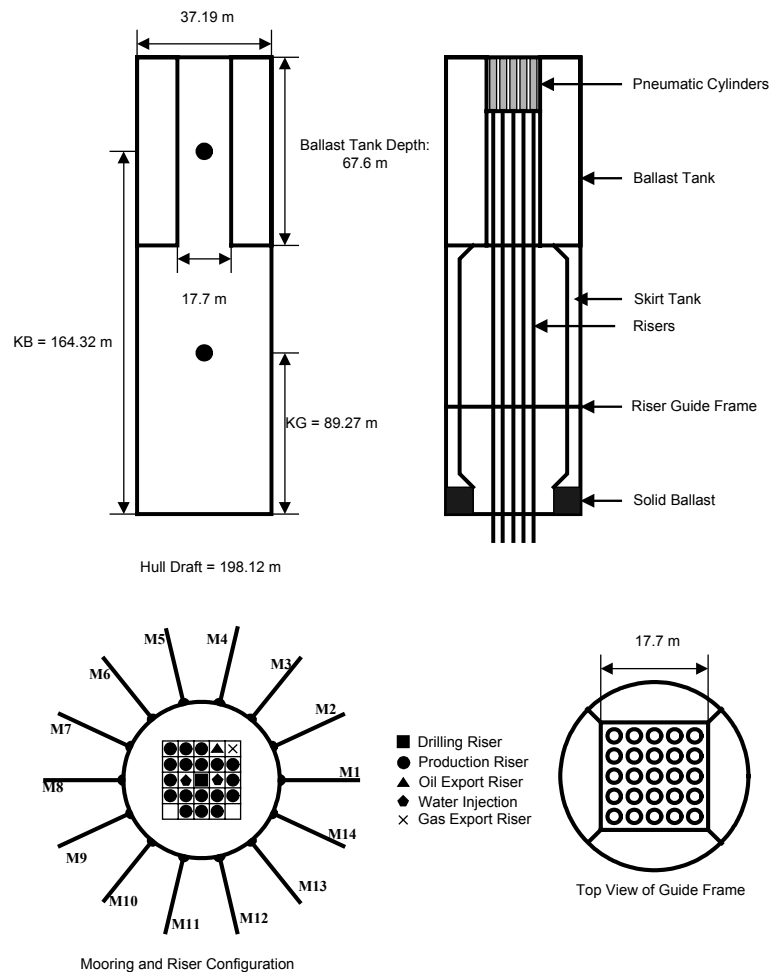


**Fig. 6.1. The illustration of the spar platform and mooring/riser configuration (not to scale).**

**Table 6.1. Pretension from mooring lines and risers.**

Pretension	Unit	Quantity
Vertical mooring tension	$N$	3.219E+07
Vertical riser tension (pneumatic riser support system)	$N$	5.034E+07

### 6.3. Description of Case Study and Design Environmental Conditions

As mentioned before, the simulation is conducted for two different spar platforms with free decay simulations and the 100-year hurricane condition for the Gulf of Mexico. The spar platforms used in the simulations are summarized in Table 6.2. The Case A Spar platform uses pneumatic cylinders for supporting riser. Thus, the risers are hanging off the topside of spar platform. In the Case A modeling, all the pneumatic cylinders are modeled as nonlinear spring rather than constant top tension (i.e. buoyancy-can) on top of the risers, and guide frames are modeled as cubic spring with a large spring constant (i.e. Case F in Chapter V). Due to absence of the buoyancy-can, rubber type centralizers protect the risers when it touches the guide frames. The rubber type centralizer is modeled as a cubic spring. The Case B Spar platform uses buoyancy-cans for the supporting risers, and the risers are modeled as a freely standing structure. In the Case B modeling, all the buoyancy-cans are modeled as constant top tension on top of the risers and uses the identical guide frame model (i.e. cubic spring) as Case A.

To evaluate damping ratio and natural period of the spar platform, free decay simulations are conducted. After free decay simulations, the 100-year hurricane simulations are conducted for both spar platforms. The environmental condition and direction of the 100-year hurricane conditions for the Gulf of Mexico are summarized in

Chapter V (Section 5.3). The time step used in time-domain hurricane condition simulation is 0.05 seconds and the total simulation time is 3 hours (216000 time steps).

**Table 6.2. Summary of the spar platform used in case study.**

	Riser	Guide Frame	Coulomb Damping	Riser Support Type
CASE A	Fully modeled	Cubic Spring	Considered	Pneumatic Cylinder (Dynamic Force)
CASE B	Fully modeled	Cubic Spring	Considered	Buoyancy-Can (Constant Force)

## 6.4. Results

### 6.4.1. Free Decay Simulation

Free decay simulation results are shown in Fig. 6.2 through Fig. 6.11. The results show that pneumatic cylinders do not change the surge and pitch motion significantly, but it is interesting to notice that heave motion is totally different due to additional heave restoring force from pneumatic cylinders. To see the pneumatic cylinder effect, in the heave free decay simulation, Coulomb damping effect is not considered. The Case A heave free decay time series shows that the first down crossing peak is larger than Case B. The reason is that large initial heave offset stiffens the pneumatic cylinders, and it makes springing-like phenomena in first down crossing peak. After first down crossing heave motion, the Case A Spar has smaller motion amplitudes and period than those of the Case B Spar platform. The heave natural period difference is clearly shown in the Fig. 6.4 and Fig. 6.5. Fig. 6.6 through Fig. 6.9 show the time series of the top tension on the drilling

riser and production riser in heave free decay simulation. Fig. 6.6 and Fig. 6.8 show the dynamic top tension from pneumatic cylinder. Both dynamic top tension time series show identical phase as heave motion. These results clearly show that the dynamic forces on the spar platform have 180-degree phase difference and give additional heave restoring force on the spar platform. Fig. 6.7 and Fig. 6.9 show that the constant buoyant force from buoyancy-can. The free decay simulation results are summarized in Table 6.3. The surge, pitch, and heave damping ratios are calculated by averaging first seven peaks from free decay simulations.

**Table 6.3. Summary of free decay simulation.**

	SURGE		HEAVE		PITCH	
	CASE A	CASE B	CASE A	CASE B	CASE A	CASE B
$T_N$ (sec)	257.2	257.2	20.9	27.8	45.5	45.5
$\zeta$ (%)	6.00	5.99	3.10	2.72	3.52	3.52

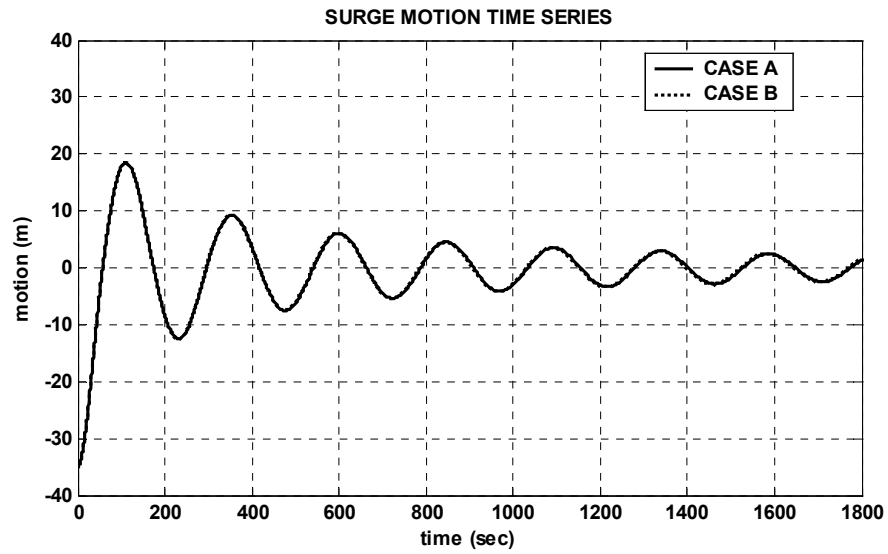


Fig. 6.2. Surge free decay time series.

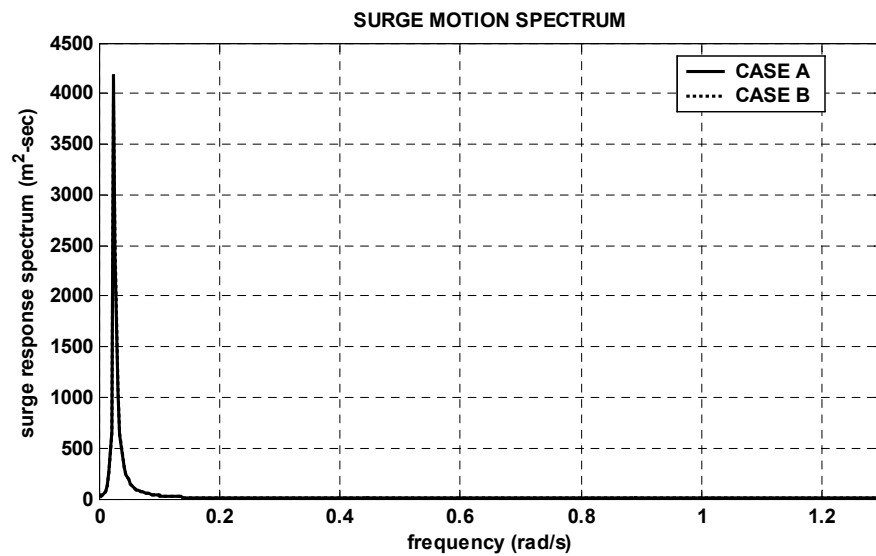


Fig. 6.3. Surge free decay spectrum.

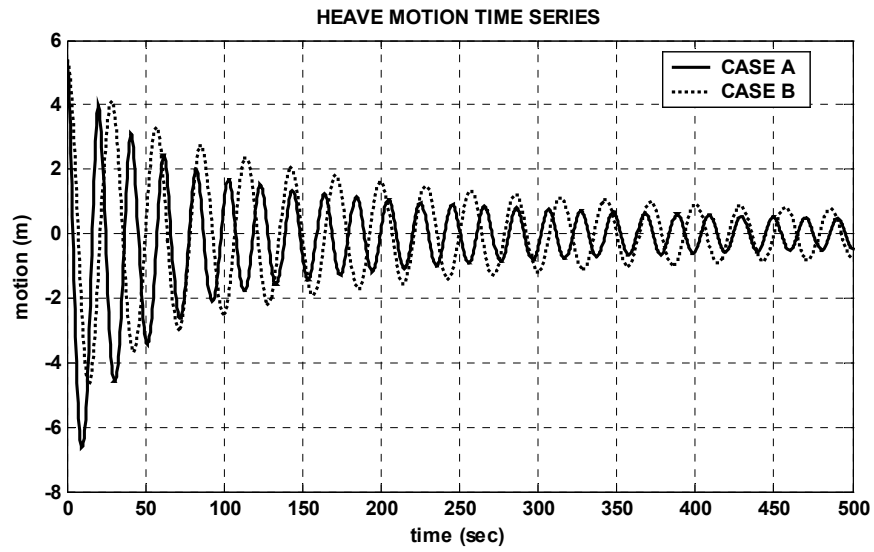


Fig. 6.4. Heave free decay time series.

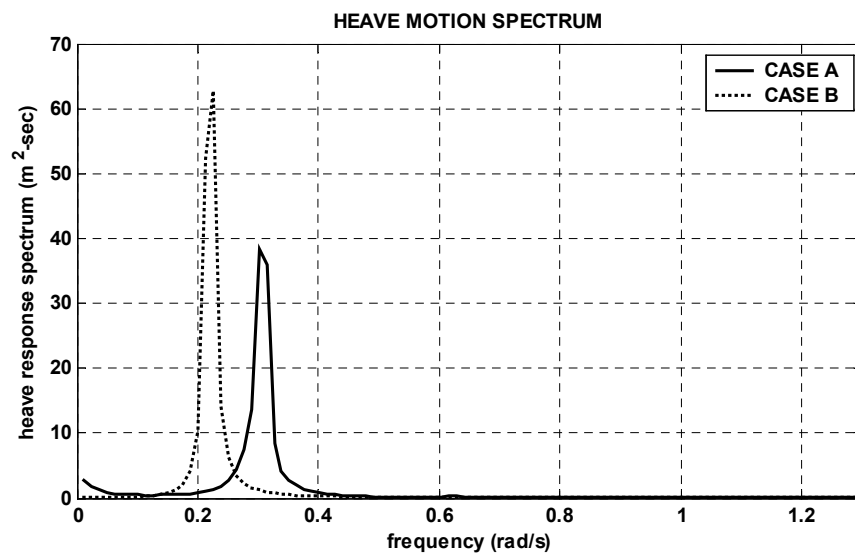
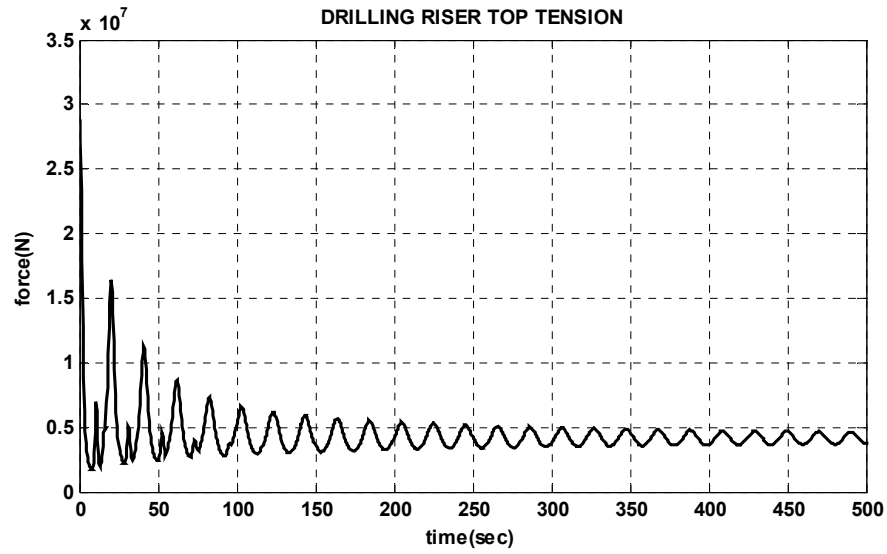
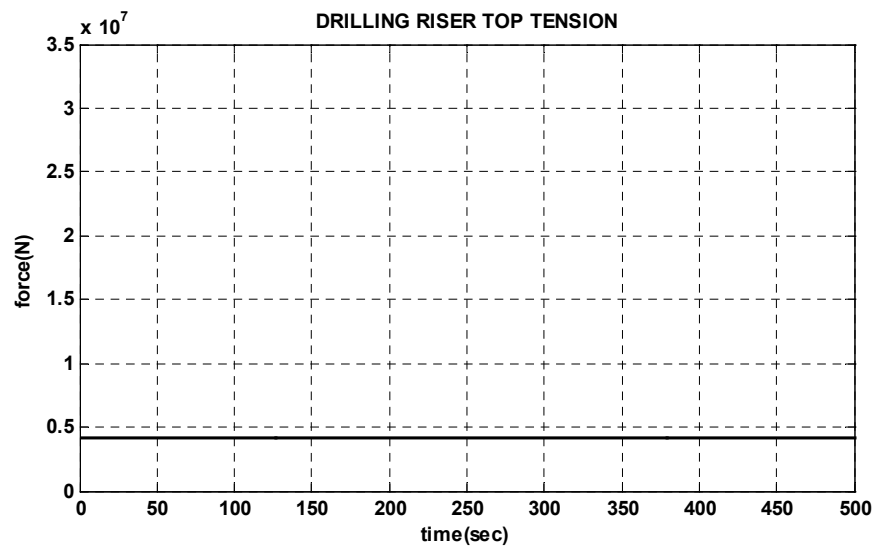


Fig. 6.5. Heave free decay spectrum.



**Fig. 6.6. Drilling riser top tension time series (CASE A).**



**Fig. 6.7. Drilling riser top tension time series (CASE B).**

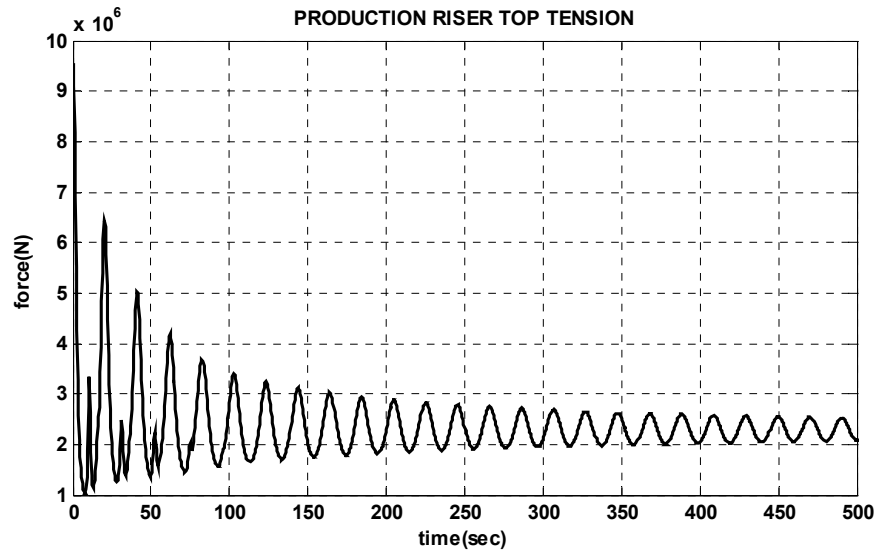


**Fig. 6.8. Production riser top tension time series (CASE A).**

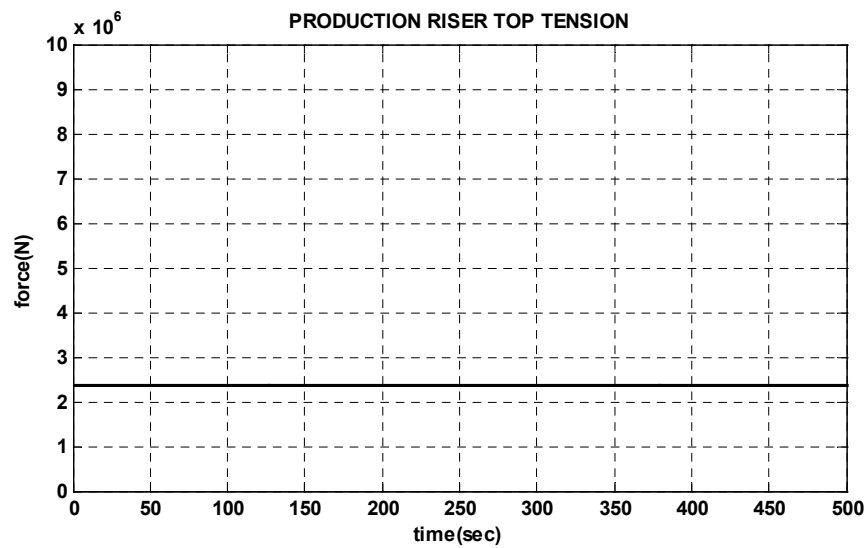


**Fig. 6.9. Production riser top tension time series (CASE B).**



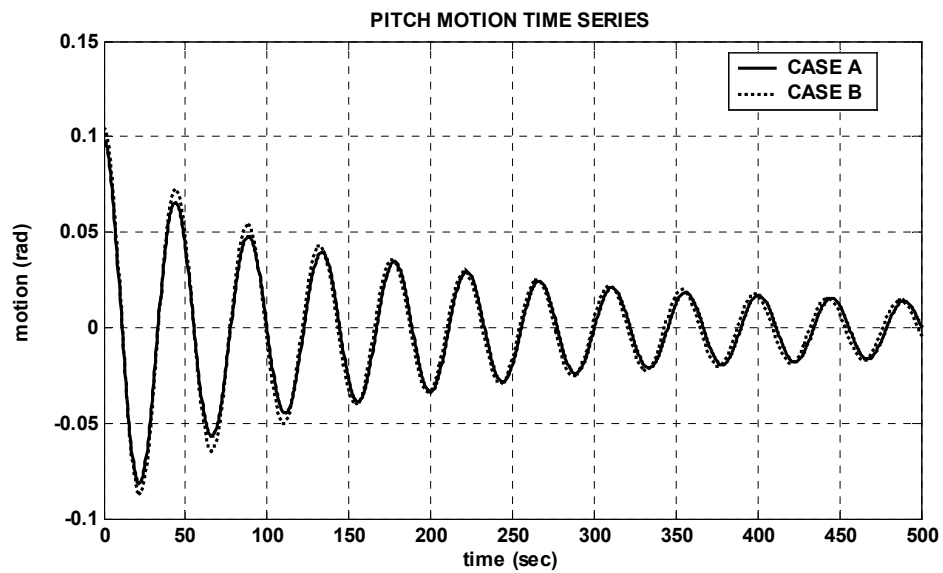


Fig. 6.10. Pitch free decay time series.

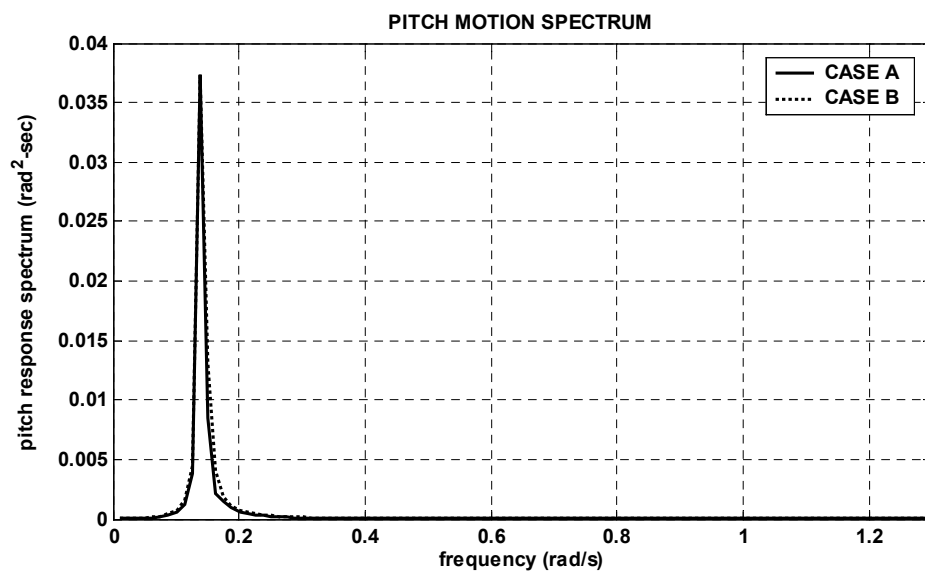


Fig. 6.11. Pitch free decay spectrum.

#### 6.4.2. 100-year Hurricane Simulation

Fig. 6.12, Fig. 6.13, and Fig. 6.14 show the wave spectrum, wave time series, and wind velocity spectrum which are used in simulations. The 100-year hurricane simulation results are shown in Fig. 6.15 through Fig. 6.23. The results show that the Case A Spar and Case B Spar have almost identical surge and pitch responses. This means that the contribution from pneumatic cylinders is not significant in surge and pitch motions. However, the heave response of Case A Spar is much larger than that of Case B Spar. Table 6.4 and Table 6.5 show that the Case A Spar and the Case B Spar have almost identical low frequency heave motion, but Case A Spar has 3.5 times larger wave frequency motion than Case B Spar platform. The larger wave frequency motion is caused by the additional heave restoring force from pneumatic cylinders that increases the heave natural frequency and therefore increases the heave wave frequency motion significantly. Due to the large wave frequency heave motion, the riser top tensions also show large standard deviation in Case A Spar platform. The summary of statistics, time series, and spectrum of riser top tension are shown in Table 6.6, Table 6.7 and Fig. 6.24 through Fig. 6.31. Comparison of top tension statistics of both cases show that the extreme top tension of production riser and drill riser of Case A Spar is slightly increased, but the standard deviation is increased significantly. The large standard deviation in axial tension may causes increased fatigue of riser system. The most loaded mooring line (i.e. M2 mooring in Fig. 6.1) top tension is shown in Fig. 6.32 through Fig. 6.34. Fig. 6.34 shows that Case A and Case B Spar have almost identical mooring top tension except for a small peak in heave natural period zone for Case A Spar. This means that the heave motion effect on the most loaded line is not

significant. A summary of the most loaded line statistic is shown in Table 6.8. Based on simulation results, the alternative riser support system results in larger heave motion as well as larger top tension on the riser compared with buoyancy-can riser support system. The pneumatic riser support system also increases the payload of a spar platform. Thus, buoyancy-can riser support system has better performance in spar hull motion and vertical riser system.

**Table 6.4. Summary of 100-year hurricane condition statistics (CASE A).**

CASE A						
	SURGE	SWAY	HEAVE	ROLL	PITCH	YEW
UNIT	m	m	m	deg.	deg.	deg.
MEAN	-2.23E+01	-4.17E+00	-3.43E-01	4.47E-01	-1.63E+00	-1.77E+00
STD	2.01E+00	1.16E+00	2.52E-01	3.49E-01	9.00E-01	2.60E-01
EXE	-2.84E+01	-7.79E+00	-1.31E+00	1.49E+00	-5.48E+00	-2.85E+00
LF	1.91E+00		7.07E-02		8.24E-02	
WF	6.31E-01		2.42E-01		8.51E-02	
<i>Notes:</i> STD = standard deviation; EXE = extreme; LF = low frequency; WF = wave frequency						

**Table 6.5. Summary of 100-year hurricane condition statistics (CASE B).**

CASE B						
	SURGE	SWAY	HEAVE	ROLL	PITCH	YEW
UNIT	m	m	m	deg.	deg.	deg.
MEAN	-2.22E+01	-4.16E+00	-2.39E-01	3.80E-01	-1.64E+00	2.26E+00
STD	2.02E+00	1.17E+00	1.02E-01	3.52E-01	9.04E-01	6.48E-01
EXE	-2.84E+01	-7.80E+00	-7.09E-01	1.51E+00	-5.52E+00	4.18E+00
LF	1.91E+00		7.18E-02		8.35E-02	
WF	6.31E-01		6.96E-02		8.48E-02	
<i>Notes:</i> STD = standard deviation; EXE = extreme; LF = low frequency; WF = wave frequency						

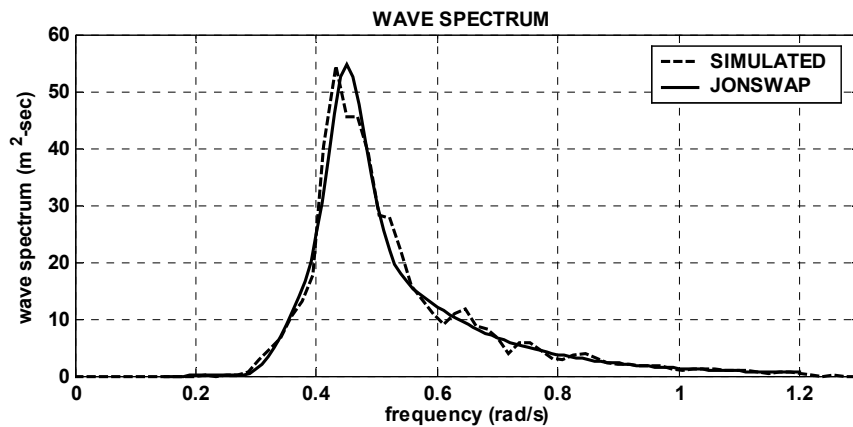


Fig. 6.12. 100-year hurricane wave spectrum.

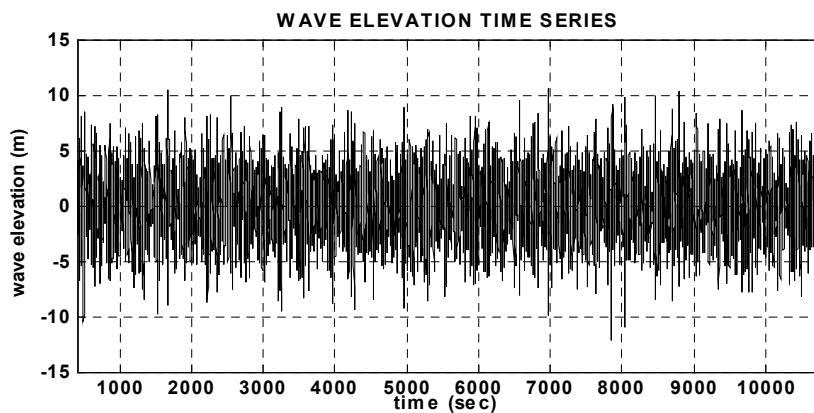


Fig. 6.13. 100-year hurricane wave time series.

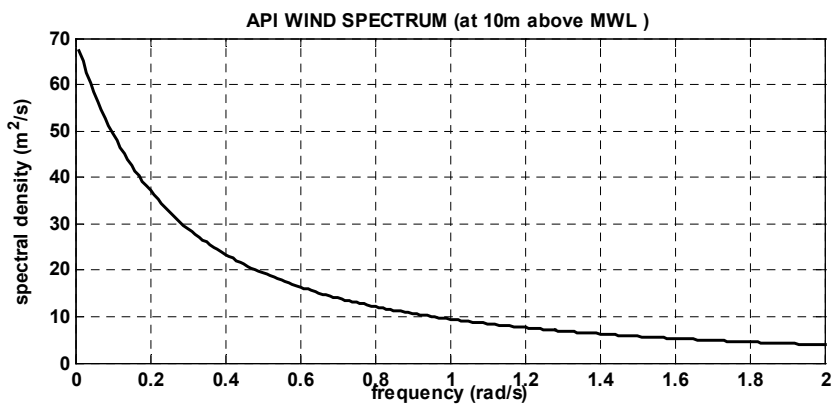


Fig. 6.14. 100-year hurricane wind velocity spectrum.

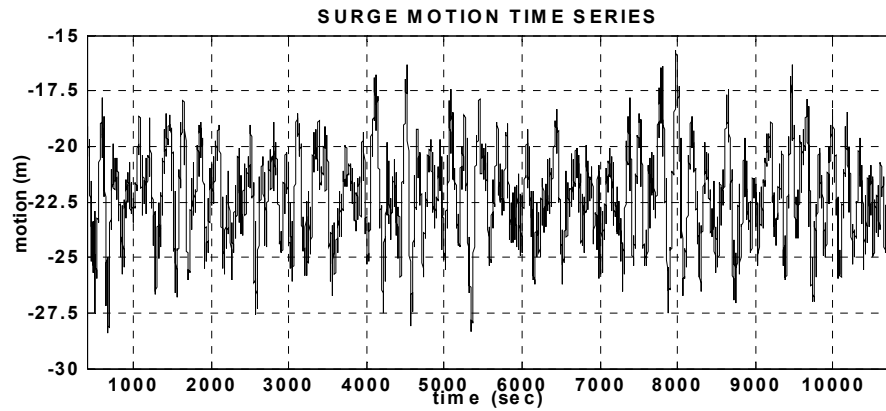


Fig. 6.15. Surge response time series (CASE A).

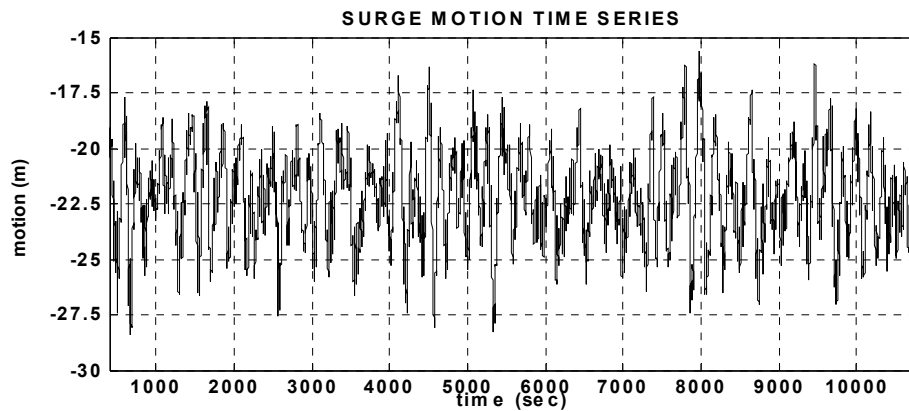


Fig. 6.16. Surge response time series (CASE B).

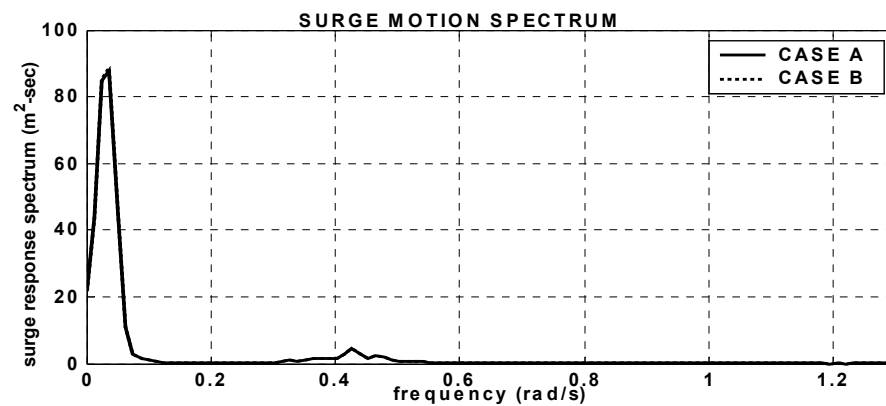


Fig. 6.17. Surge response spectrum.

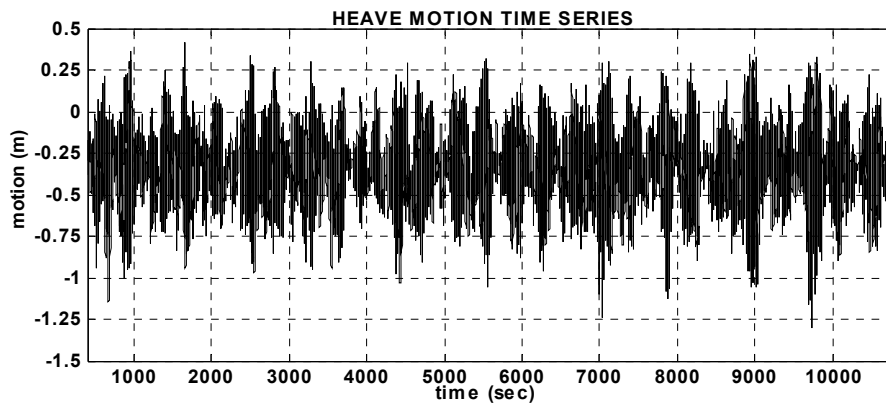


Fig. 6.18. Heave response time series (CASE A).

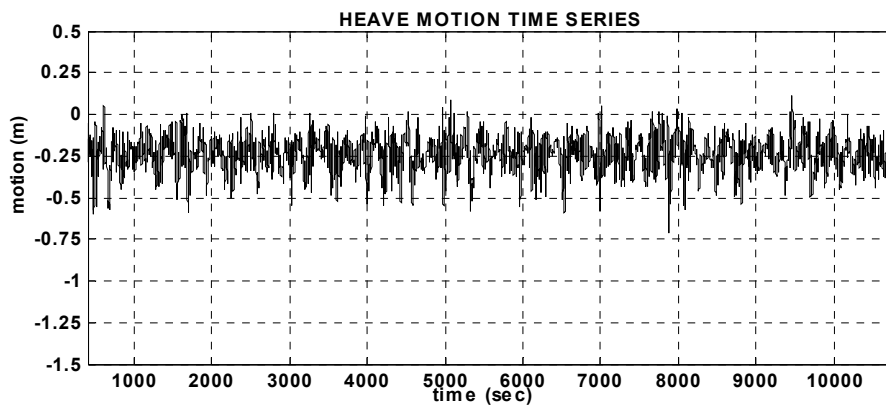


Fig. 6.19. Heave response time series (CASE B).

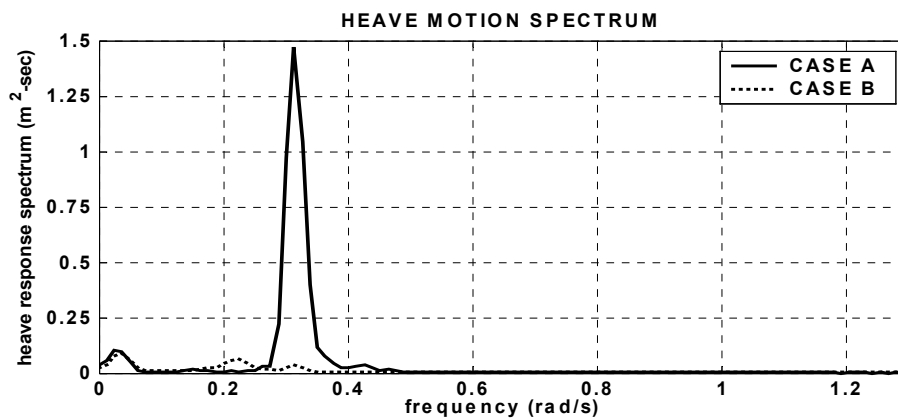


Fig. 6.20. Heave response Spectrum.

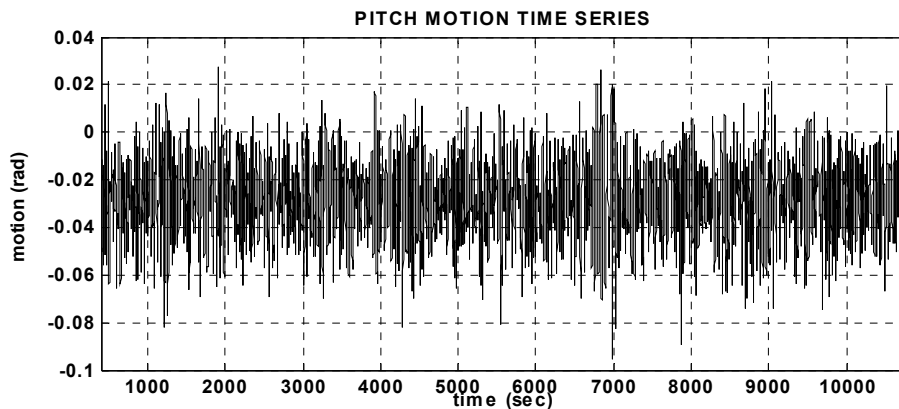


Fig. 6.21. Pitch response time series (CASE A).

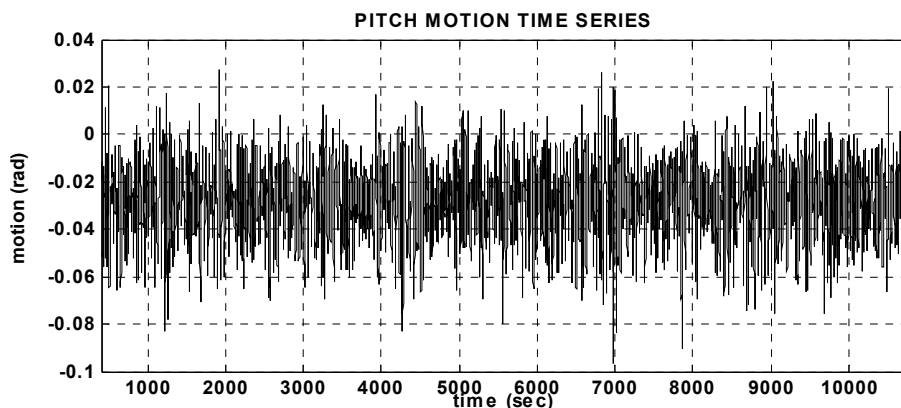


Fig. 6.22. Pitch response time series (CASE B).

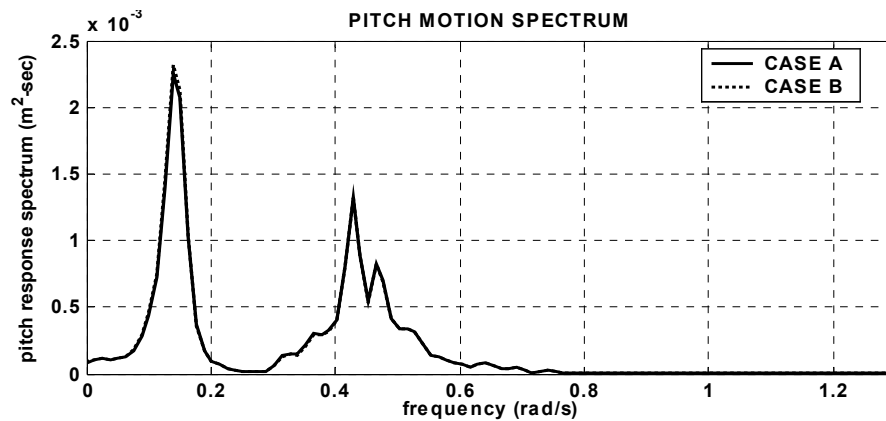
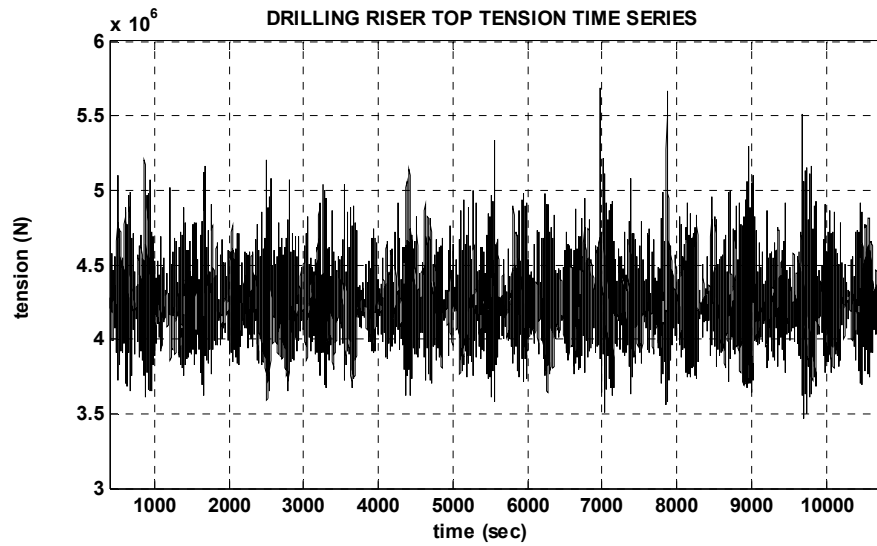
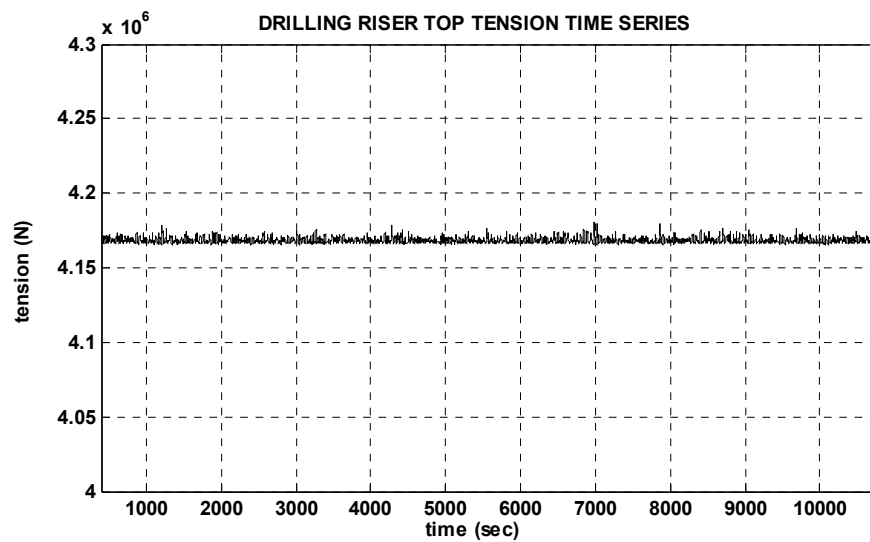


Fig. 6.23. Pitch response spectrum.



**Fig. 6.24. Drilling riser top tension time series (CASE A).**



**Fig. 6.25. Drilling riser top tension time series (CASE B).**



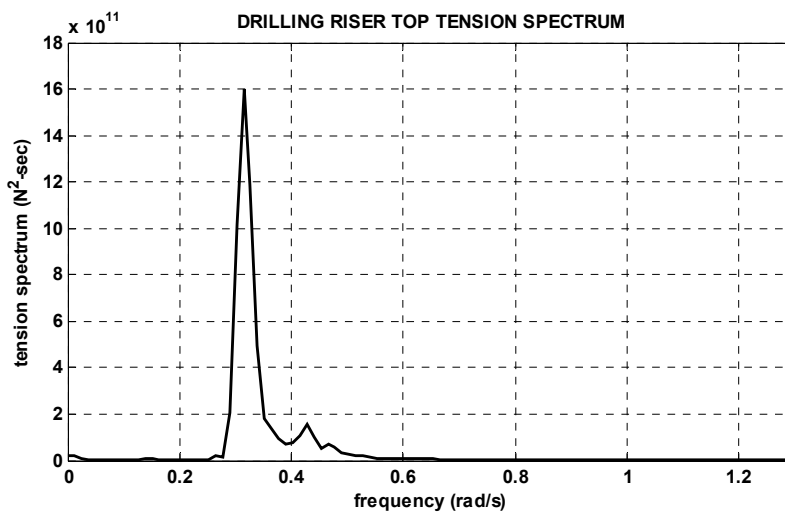


**Fig. 6.26. Drilling riser top tension spectrum (CASE A).**

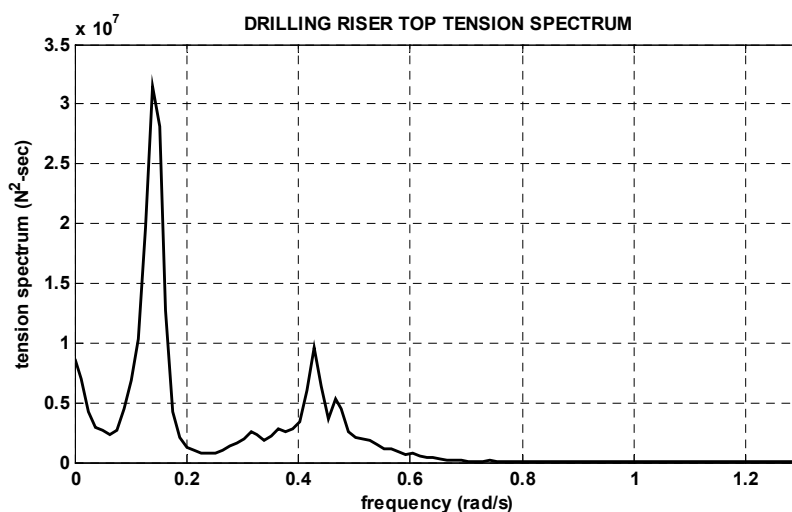


**Fig. 6.27. Drilling riser top tension spectrum (CASE B).**

**Table 6.6. Summary of drilling riser top tension statistics.**

	MEAN	STD	EXE	LF STD	WF STD
UNIT	N	N	N	N	N
CASE A	4.25E+06	2.75E+05	5.68E+06	3.52E+04	2.72E+05
CASE B	4.17E+06	1.72E+03	4.18E+06	1.35E+03	1.04E+03
<i>Notes:</i> STD = standard deviation; EXE = extreme; LF = low frequency; WF = wave frequency					

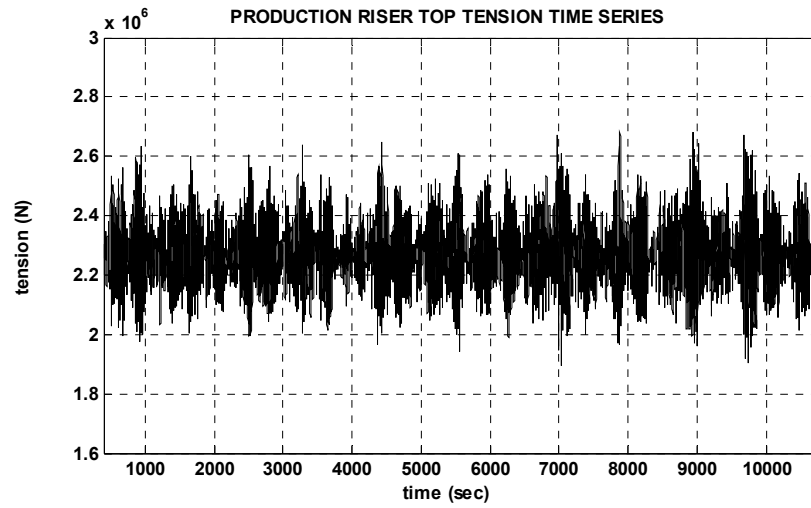


**Fig. 6.28. Production riser top tension time series (CASE A).**

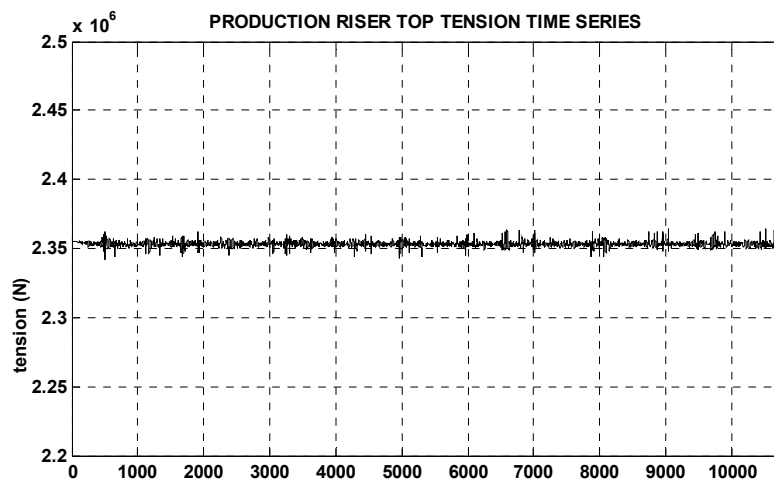


**Fig. 6.29. Production riser top tension time series (CASE B).**

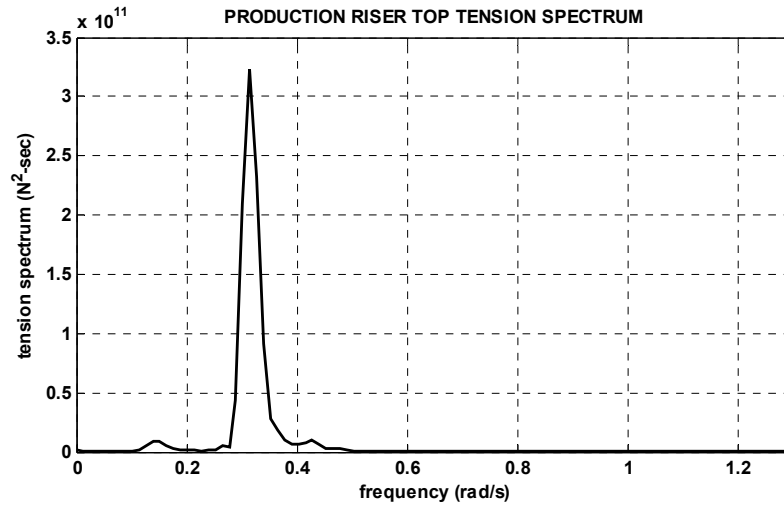


**Fig. 6.30. Production riser top tension spectrum with pneumatic cylinder (CASE A).**

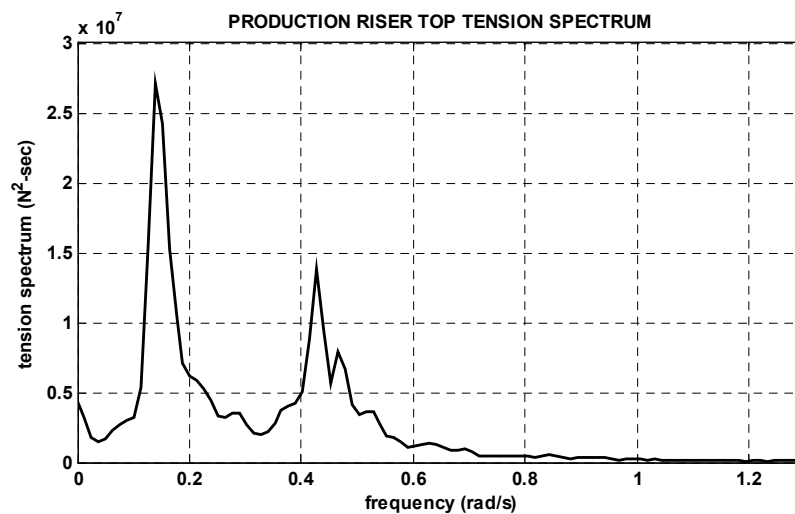


**Fig. 6.31. Production riser top tension spectrum with buoyancy-can (CASE B).**

**Table 6.7. Summary of drilling riser top tension statistics.**

	MEAN	STD	EXE	LF STD	WF STD
UNIT	N	N	N	N	N
CASE A	2.27E+06	1.17E+05	2.68E+06	2.34E+04	1.14E+05
CASE B	2.35E+06	1.94E+03	2.36E+06	1.24E+03	1.41E+03
<i>Notes:</i> STD = standard deviation; EXE = extreme; LF = low frequency; WF = wave frequency					

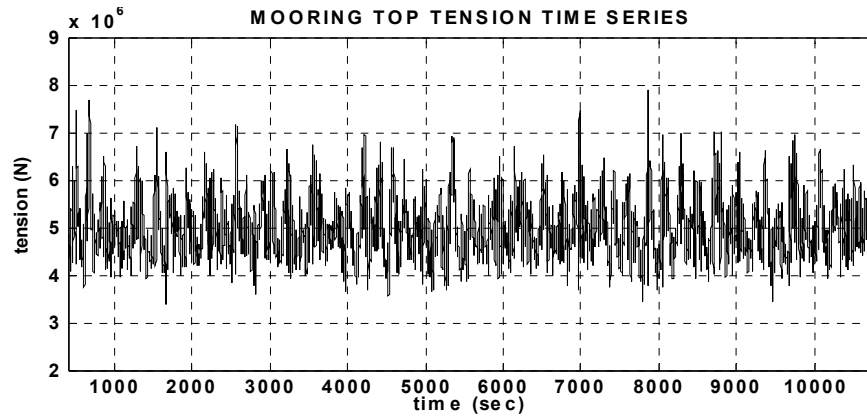


Fig. 6.32. Most loaded line top tension time series (CASE A).

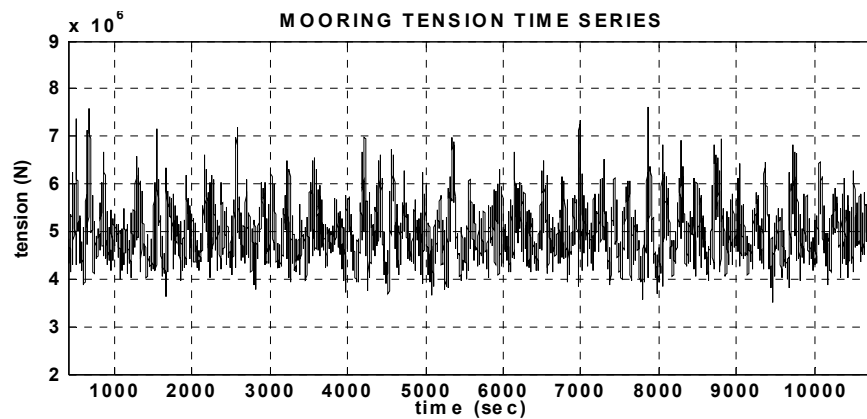


Fig. 6.33. Most loaded line top tension time series (CASE B).

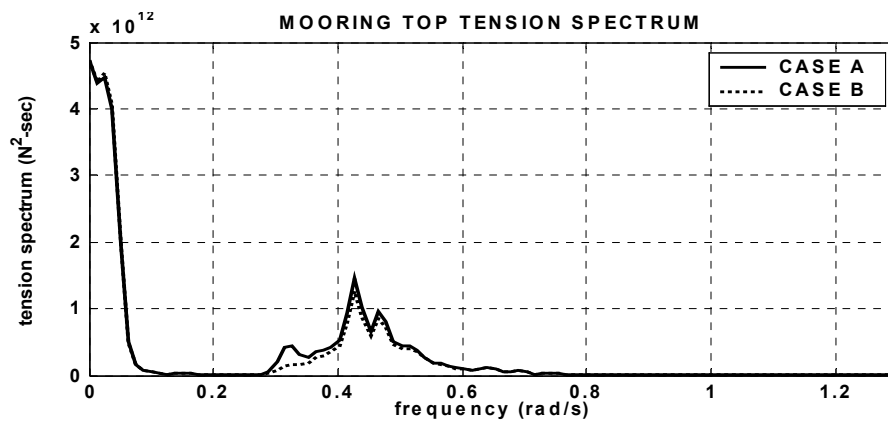


Fig. 6.34. Most loaded line top tension spectrum.

**Table 6.8. Summary of most loaded line top tension statistics.**

	MEAN	STD	EXE	LF	WF
UNIT	N	N	N	N	N
CASE A	4.96E+06	6.25E+05	7.90E+06	4.77E+05	4.03E+05
CASE B	4.96E+06	6.03E+05	7.62E+06	4.79E+05	3.67E+05
<i>Notes:</i> STD = standard deviation; EXE = extreme; LF = low frequency; WF = wave frequency					

## CHAPTER VII

### CASE STUDY 3: MATHIEU'S INSTABILITY

#### 7.1. Introduction

In this chapter, Mathieu's instability of a classical spar is investigated for a regular wave environment and the West Africa and North Sea swell conditions. Swell waves have been reported 25-second peak period swell waves offshore West Africa and North Sea. Generally, a spar platform has a 27~30-second heave natural period and a 45~60-second pitch natural period respectively. Due to heave and pitch motion characteristics of the spar platform, the spar heave natural period is near the peak period of swell waves and the pitch natural period twice the peak period of swell waves. As mentioned before, if there is no damping, the ratio between pitch natural frequency and heave motion frequency is near 0.5 ( $\alpha = 0.25$ ) then the Mathieu's instability occurs even  $\beta = 0$ , and as shown in Fig. 2.1 (i.e. principle unstable zone in Mathieu instability diagram), the first unstable zone, called as principle unstable zone, is not sensitive to damping compare with the secondary unstable zone. Due to these two reasons, the case studies are focused on the principle unstable zone.

The objective of this case study is to evaluate damping effects and hull/mooring/riser coupled effects on the principle instability. Five different spar platforms are simulated with five different wave environments to capture the damping effects and hull/mooring/riser coupled effects in principle instability. The Mathieu instability of a spar platform is carefully checked by systematic comparison of each simulation results.

## 7.2. Description of the Spar Platform, Mooring System and Risers

The dimension, mooring lines configuration and risers configuration of the spar platform used in this study is exactly same as Chapter V (i.e. case study 1: buoyancy-can effect on spar Platform) except the spar hull drag coefficient. The principle particulars of the spar platform and characteristics of mooring line and riser are summarized in Table 5.1 through Table 5.4 in Chapter V. As mentioned in section 7.1, four different spar hull drag coefficients are used to capture the pitch damping effects on the Mathieu instability. Table 7.1 summarizes the spar hull drag coefficient.

**Table 7.1. Drag coefficient of the spar platform.**

Designation	CASE	Quantities
Drag coefficient (with mooring lines and risers)	CASE D	1.5
	CASE E	
Drag coefficient (without mooring lines and risers)	CASE A	0 (pitch damping 0.03%)
	CASE B	0.5 (pitch damping 1.0%)
	CASE C	2.5 (pitch damping 3.0%)

## 7.3. Description of Case Study and Environmental Conditions

As mentioned in section 7.1, the simulation conducted for five different spar platforms with three regular wave environments and two swell wave environments. It is well known that pitch damping of a spar platform is around 1% ~ 4% of the pitch critical damping and depends on the pitch motion amplitude. Thus, simulations are conducted in 0.03% ~ 3.52% pitch damping ratio. The spar platforms used in the simulations are

summarized in Table 7.2. Table 7.3 summarizes the period and wave amplitude used in the regular wave simulation. In the regular wave simulation, the comparison can be divided into two categories. The first category is a comparison study for damping effects on Mathieu instability, and the second category is the comparison between no hull/mooring/riser coupling effects versus hull/mooring/riser effects on Mathieu instability. Because the mooring lines and risers are completely removed from Case A, Case B and Case C, the spar platform pitch damping ratios are artificially changed by using different drag coefficients for each spar platform. A zero drag coefficient is used in Case A, 0.5 drag coefficient is used in Case B, and 2.5 drag coefficient is used in Case C. Thus, Case A only considers radiation damping in the pitch direction. To simplify the comparison study, all the spar platforms use a heave plate with 1.5 drag coefficient. All mooring line and riser are considered in Case D and Case E Spar platform, and these cases use 1.5 drag coefficient for hull. The difference between the Case D and Case E Spar is the riser modeling. The Case D Spar uses a truncated riser and Case E uses fully modeled riser. Thus, buoyancy-can effect and Coulomb damping effects are considered in the Case E Spar platform. In the simulation, Case A, Case B and Case C Spar platforms are considered as a freely floating structure. Systematic comparisons between the five different spar platforms are used to show the damping effects and hull/mooring/riser coupled effects on Mathieu instability.

The swell wave conditions are summarized in Table 7.4. To generate the swell wave time series, a JONSWP spectrum is used in the simulation with a 6.0 over shooting parameter. CASE E Spar platform is used in swell environment conditions and the Mathieu instability is checked based on regular wave simulation results.



**Table 7.2. Summary of the spar platform used in case study.**

	Damping Ratio (%) Pitch/heave	Mooring	Riser	Coulomb Damping
CASE A	0.03 / 0.7	w/o	w/o	w/o
CASE B	1.0 / 0.7	w/o	w/o	w/o
CASE C	3.0 / 0.7	w/o	w/o	w/o
CASE D	3.3 / 2.72	w	w/t	w/o
CASE E	3.3 / 3.44	w	w/f	w
<i>Notes:</i> w/o = without consideration; w = with consideration w/t = consider riser as truncating modeled; w/f = consider riser as fully modeled				

**Table 7.3. Regular wave condition.**

	T (sec)	Wave amp.(m)
RW-A	26.0	6.00 ~7.00
RW-B	27.8	1.50 ~ 7.00
RW-C	22.7	7.00
<i>Notes:</i> RW = regular wave; amp. = amplitude		

**Table 7.4. Swell environment condition.**

	Hs (m)	Tp (sec)	$\gamma$
Swell-A	2.5	23	6.0
Swell-B	1.7	25	6.0

## 7.4. Results and Analysis

### 7.4.1. Free Decay Simulation

To evaluate the heave and pitch damping ratio and natural period of the spar platform, free decay simulations are conducted. Fig. 7.1 and Fig. 7.2 show the pitch free decay

simulation results for Case A, Case B, and Case C Spar platforms. To capture the different damping ratio, different drag coefficients are given for each spar hull. In Case A, the spar hull drag coefficient is 0.0 thus, only radiation damping is considered in this case. Case B and Case C use 0.5 and 2.5 drag coefficient to make the spar damping ratio as 1.0% and 3.0% respectively. Fig. 7.3 and Fig. 7.4 show pitch free decay simulation results for with mooring line and riser. As mentioned before, Case D and Case E use the same drag coefficient but different riser modeling. The fully modeled riser (Case E) has a small pitch natural period and slightly larger damping ratio compared with truncated riser model. Table 7.5 summarizes the pitch free decay simulation results. Fig. 7.5 and Fig. 7.6 show the heave free decay results for all cases. In the heave free decay simulations, one heave plate with a 1.5 drag coefficient is considered in all cases. In the Case E simulation, the spar platform initially tilted in pitch and roll directions, and it has additional damping from Coulomb friction. The results show that most of the heave damping in a classical spar platform comes from the mooring lines. Heave free decay simulation results are summarized in Table 7.6. From free decay simulation results, the heave natural period of the spar platform is half of the pitch natural period except for Case E, thus strong Mathieu instability is expected in the heave resonance zone.

Based on this free decay test, pitch and heave damping effects on the principle unstable zone in the Mathieu instability are investigated in the following regular wave simulation.

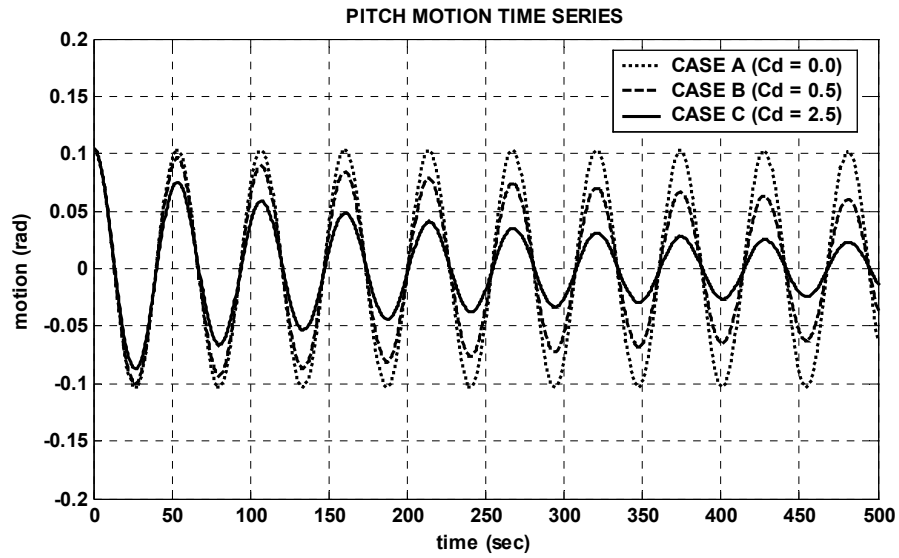


Fig. 7.1. Pitch free decay simulation time series (CASE A, CASE B, and CASE C).

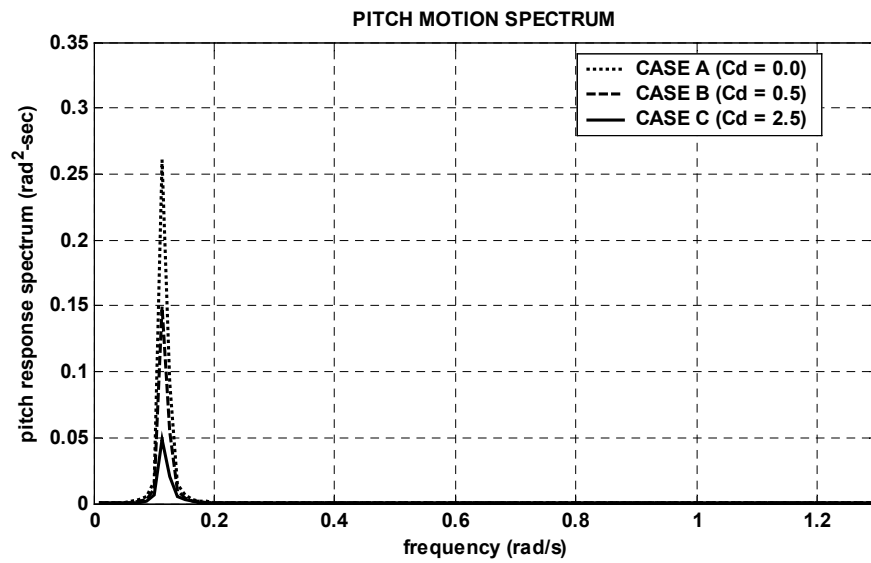


Fig. 7.2. Pitch free decay simulation spectrum (CASE A, CASE B, and CASE C).

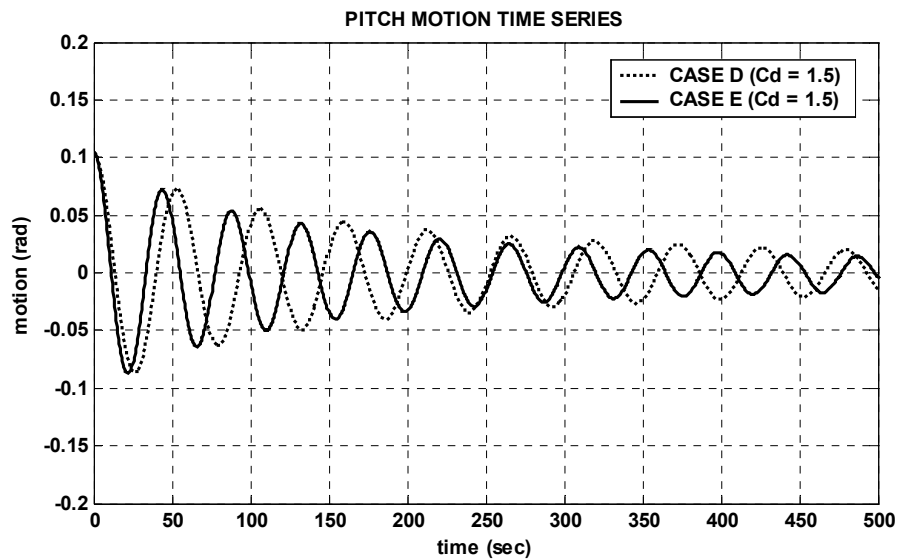


Fig. 7.3. Pitch free decay simulation time series (CASE D and CASE E).

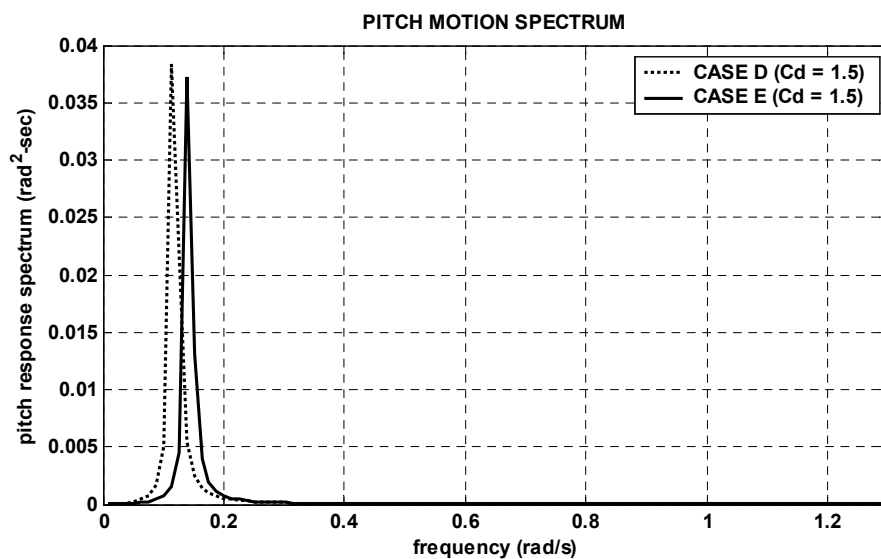


Fig. 7.4. Pitch free decay simulation spectrum (CASE D and CASE E).

Table 7.5. Pitch motion natural periods and damping ratios.

	CASE A	CASE B	CASE C	CASE D	CASE E
$T_N$ (sec)	57.6	57.6	57.6	57.6	45.5
$\zeta$ (%)	0.03	1.01	2.99	3.28	3.52

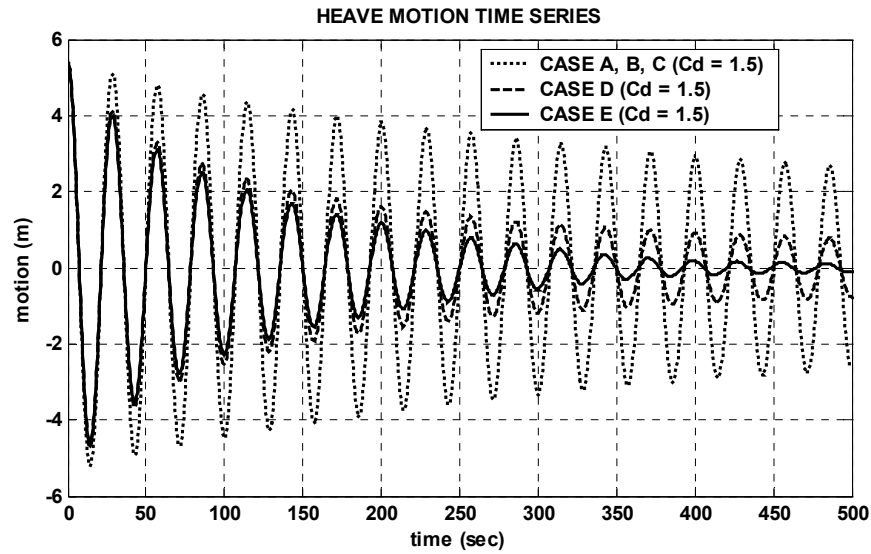


Fig. 7.5. Heave free decay time series.

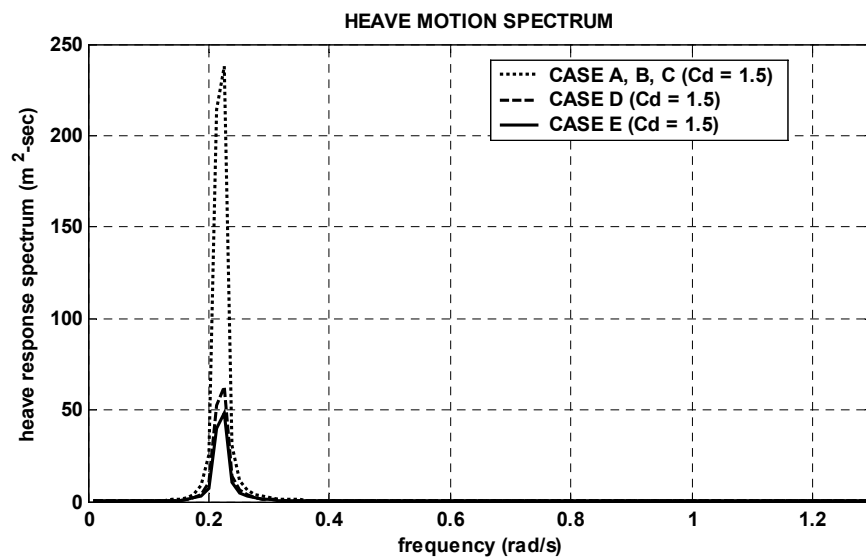


Fig. 7.6. Heave free decay spectrum.

Table 7.6. Heave motion natural periods and damping ratio.

	CASE A	CASE B	CASE C	CASE D	CASE E
$T_N$ (sec)	27.8	27.8	27.8	27.8	27.8
$\zeta$ (%)	0.77	0.77	0.77	2.72	3.44

#### 7.4.2. Mathieu's Instability in Regular Waves

The results of regular wave simulation A (RW-A) are shown in Table 7.7, Table 7.8, and Fig. 7.7 through Fig. 7.13. To capture the Mathieu instability, simulations are conducted with varying wave amplitudes. In 6.0-meter regular wave amplitude simulation, the Mathieu instability is triggered in Case A and Case B Spar. Fig. 7.7 shows the result from the Case A Spar platform. Fig. 7.7 clearly pitch motion drastically increased after 2000 seconds. The pitch response spectrum, Fig. 7.7, shows the largest peak exist in pitch natural period zone even in the 26.0 seconds long period wave environment. Table 7.7 summarizes the statistical results from the simulation. The comparison between Case A and Case B statistical results, in Table 7.7, show that the 1% pitch damping ratio is not enough to suppress the Mathieu instability. Thus, when the heave motion is larger than 8.0 meter the Mathieu instability is triggered in Case A and Case B Spar platform. However, 8.0 meter heave motion is not enough to trigger the Mathieu instability in Case C Spar. On the other hand, Fig. 7.9 shows spar heave and pitch motion without time varying pitch hydrostatic coefficient (i.e. constant pitch hydrostatic restoring coefficient), and this result shows that constant pitch hydrostatic restoring coefficient can not analyze the Mathieu instability and significantly underestimate the pitch motion of the spar platform. To clarify Mathieu instability, the detailed time series are shown in Fig. 7.8. The pitch motion time series shows that the pitch motion is stable up to 1000 seconds. The pitch time series in show that the pitch motion has same period as regular wave period (i.e. 26 second) in first 1000 seconds, but after 1000 seconds the pitch motion is disturbed. The reason is that the large heave motion changes the pitch restoring moment. Fig. 7.8 shows that the pitch

motion gradually increases by the superposition of two adjacent motion peaks and, it doubles the amplitude of pitch motion as well as period. After two pitch motion peaks are superposed, the pitch motion drastically increased because motion becomes the pitch natural period motion. When pitch motion is increased by Mathieu instability, the large pitch motion also disturbs the heave motion. Fig. 7.7 shows disturbed heave motion. Fig. 7.10 shows pitch response time series for Case B Spar platform. It is interesting to notice that Case B Spar has Mathieu instability in pitch motion, but the tendency of pitch motions are different from Case A Spar platform. The reason is because of the damping effect on pitch motion. As mentioned before, the Case B and Case C Spar platform have 1% and 3% damping ratio in pitch motion. When Mathieu instability occurs in Case B Spar platform, a 1% pitch damping maintains the pitch motion as stable rather than unstable. The results for Case D and Case E Spar platform are shown in Fig. 7.12 and Fig. 7.13 and summarized in Table 7.8. Due to Case D and Case E Spar platform include the mooring lines and risers, a larger wave amplitude is used in the simulation. Fig. 7.12 shows that the damping from mooring lines and risers, and the result from Case D Spar has the same tendency as Case C simulation. The Case C and Case D Spar have small disturbance in pitch motion. (i.e. 3000 sec – 6000 sec), but the pitch motion of the Case E Spar does not have disturbance in pitch motion. The reason is that the Case D Spar uses truncated riser model, thus the additional pitch restoring force from buoyancy-cans is not considered, but Case E Spar consider buoyancy-can effects. The buoyancy-can effects on the Mathieu instability are clearly shown in the following RW-B simulation.

**Table 7.7. Comparison of the statistics (Regular wave simulation A).**

RW A: T = 26 sec amp. = 6.0 m						
	CASE A		CASE B		CASE C	
	HEAVE	PITCH	HEAVE	PITCH	HEAVE	PITCH
UNIT	m	deg.	m	deg.	m	deg.
MEAN	7.03E-02	-5.94E-02	7.65E-02	-6.08E-02	7.92E-02	-6.55E-02
STD	5.05E+00	5.63E+00	5.49E+00	5.39E+00	5.61E+00	1.20E+00
EXE	8.23E+00	1.80E+01	8.23E+00	1.18E+01	8.23E+00	1.85E+00
<i>Notes:</i> STD = standard deviation; EXE = extreme						

**Table 7.8. Comparison of the statistics (Regular wave simulation A).**

RW A: T = 26 sec, amp. = 7.0 m				
	CASE D		CASE E	
	HEAVE	PITCH	HEAVE	PITCH
UNIT	m	deg.	m	deg.
MEAN	4.31E-02	-1.68E-01	-2.55E-02	-1.80E-01
STD	5.68E+00	1.43E+00	5.58E+00	1.65E+00
EXE	8.06E+00	-2.21E+00	7.94E+00	-2.51E+00
<i>Notes:</i> STD = standard deviation; EXE = extreme				



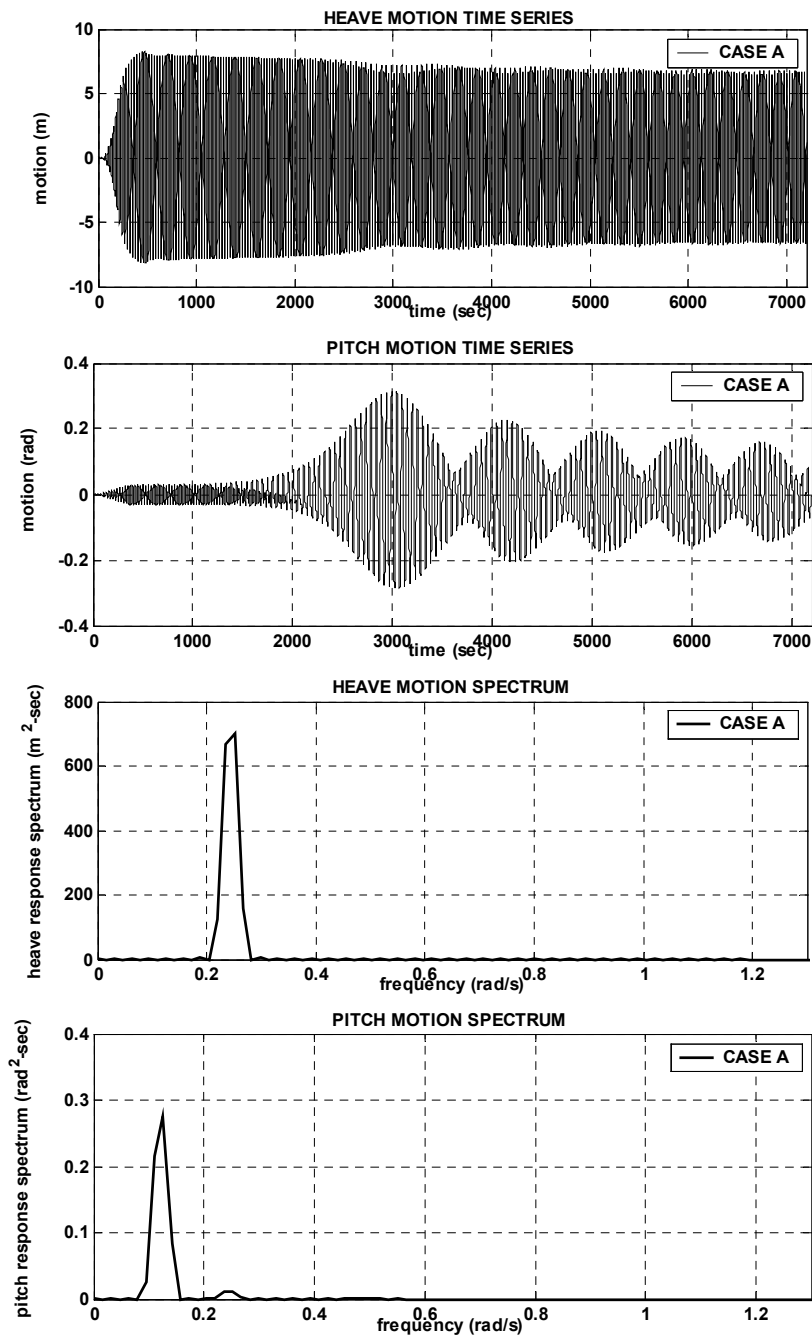
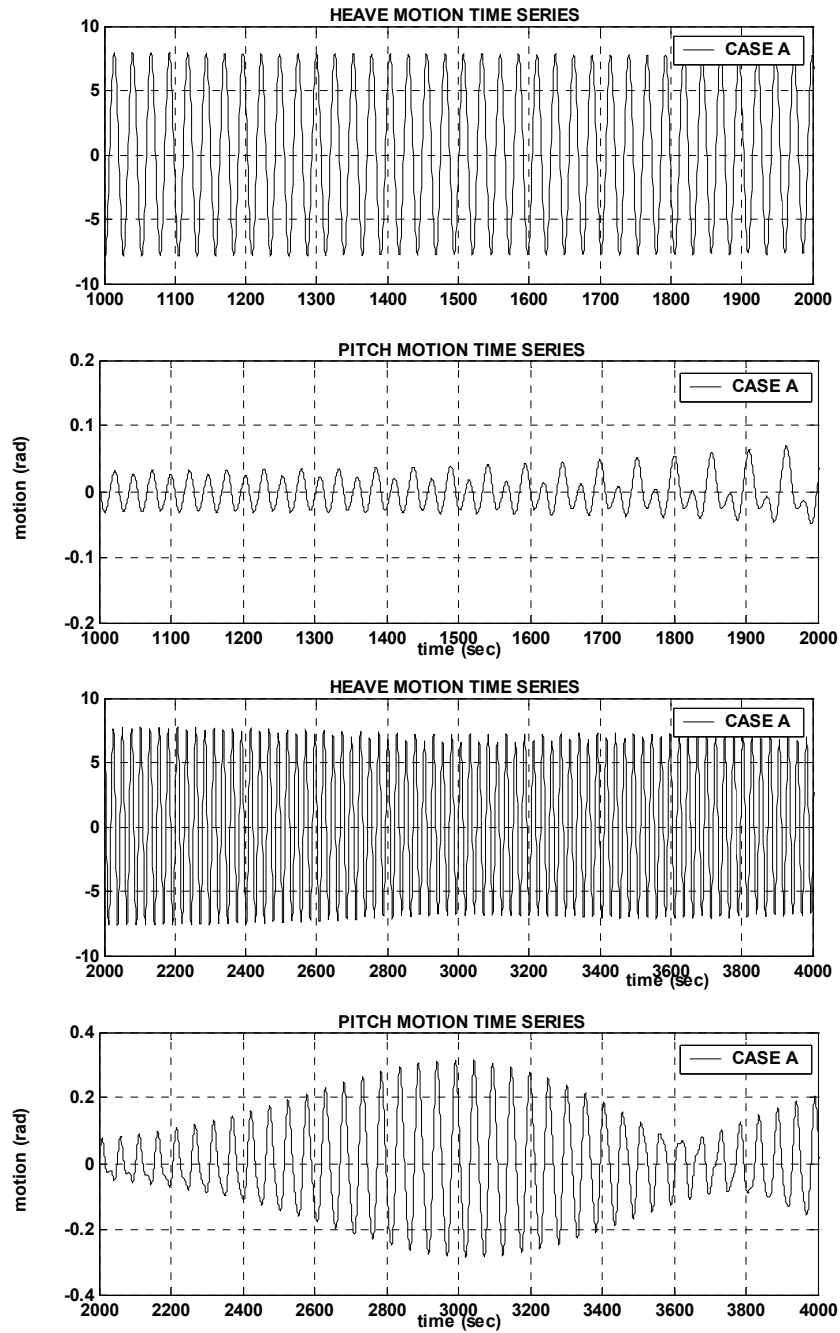
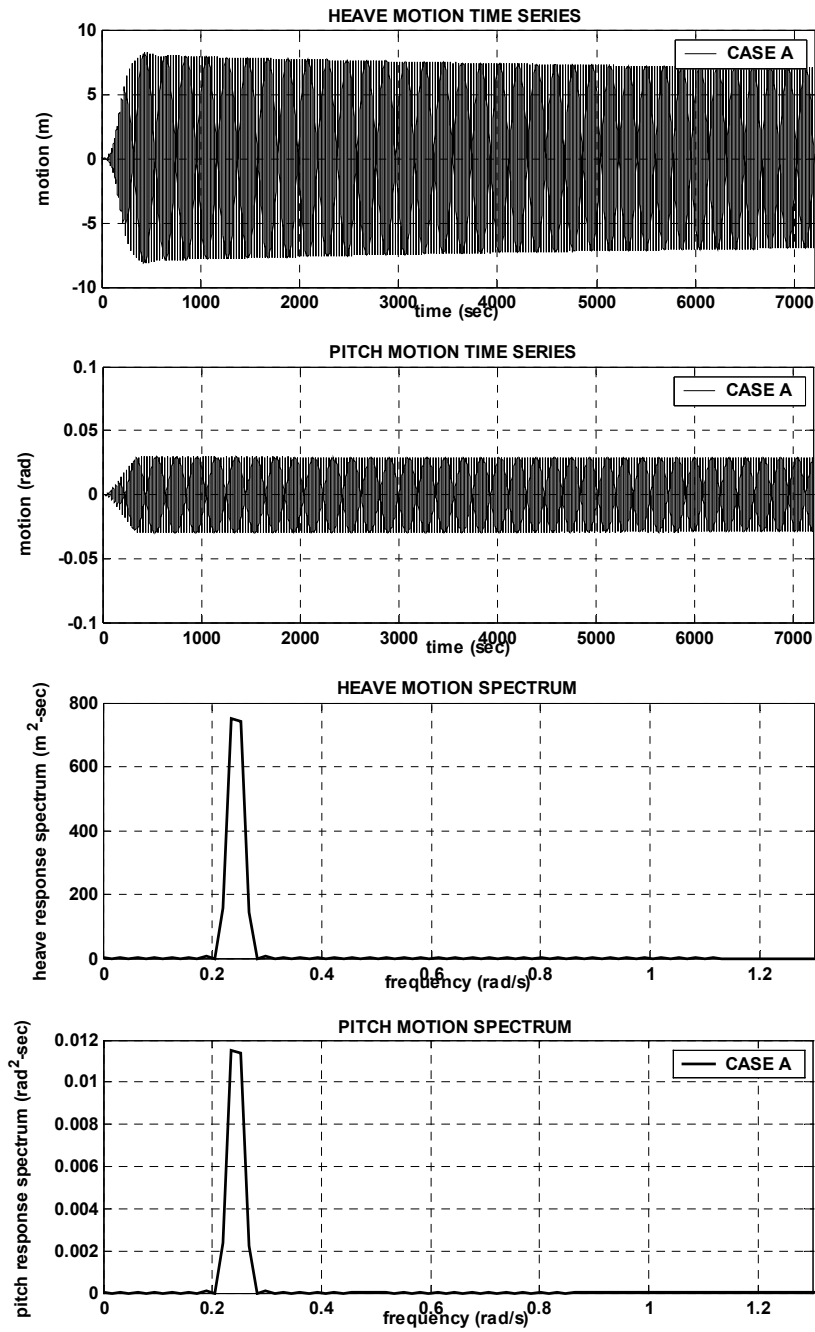


Fig. 7.7. Spar heave and pitch motions (CASE A:  $T_p = 26$  sec, amp. = 6.0 m).

CASE A:  $T = 26.0$  sec, amp. = 6.0 m



**Fig. 7.8.** Heave/Pitch response time series (1000 sec – 4000 sec).



**Fig. 7.9.** Spar heave and pitch motions without time varying pitch hydrostatic restoring coefficient (CASE A:  $T_p = 26$  sec, amp. = 6.0 m).

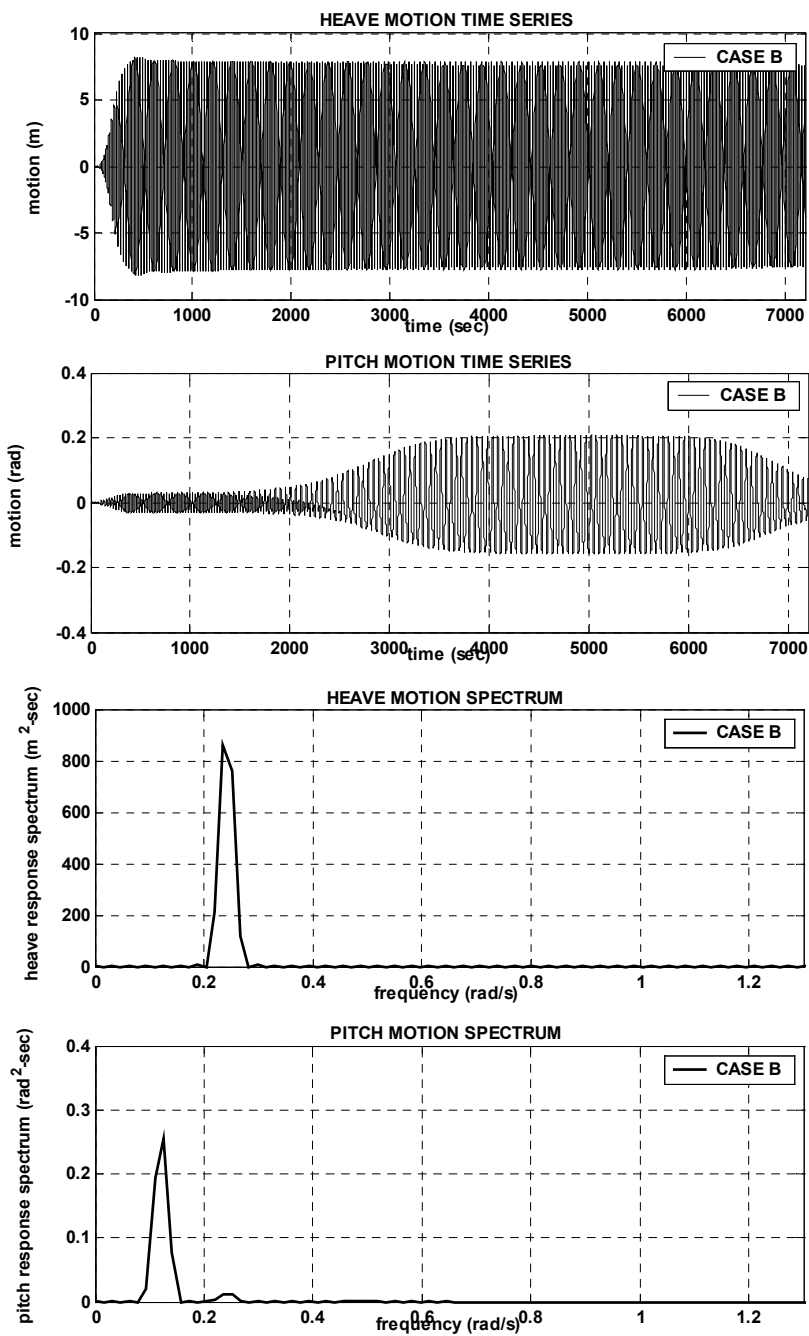


**Fig. 7.10. Spar heave and pitch motions (CASE B:  $T_p = 26$  sec, amp. = 6.0 m).**

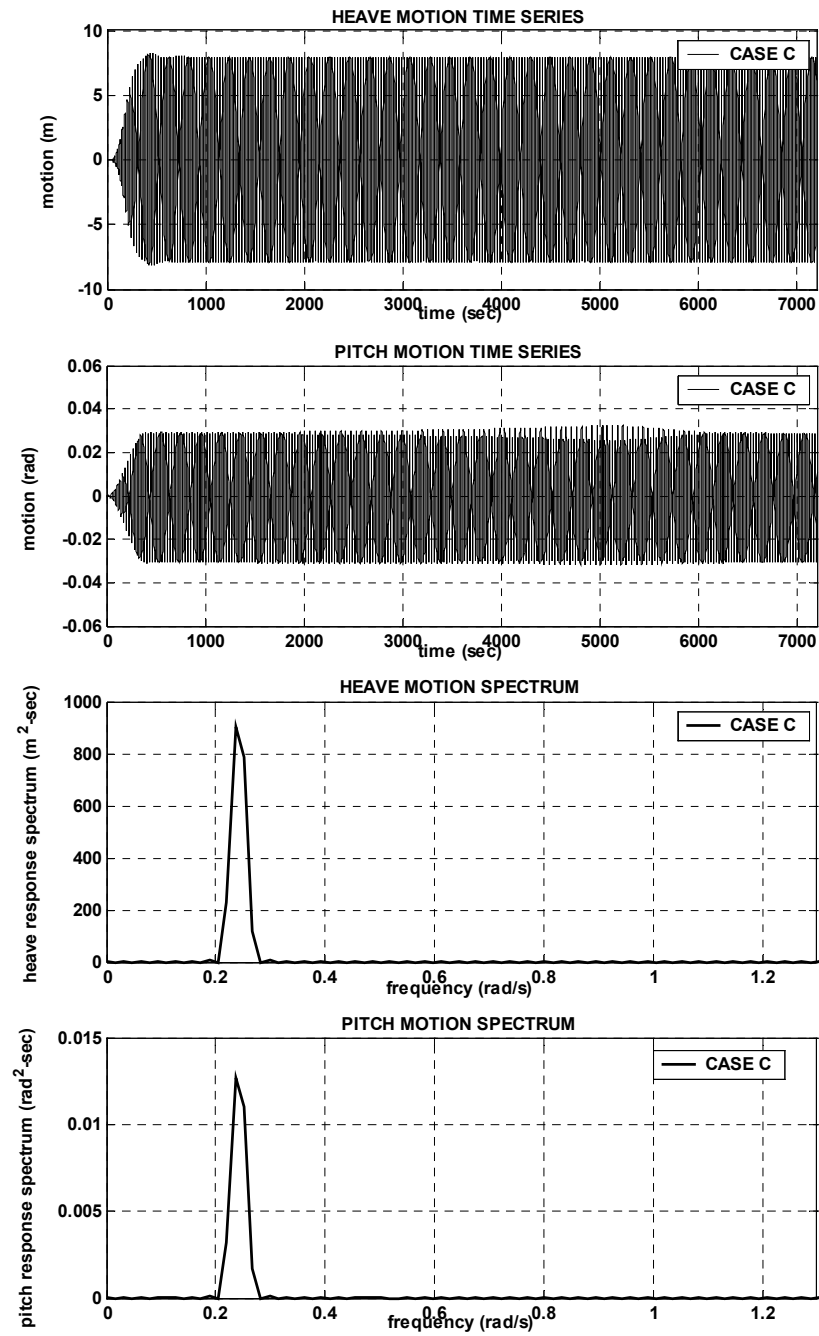


Fig. 7.11. Spar heave and pitch motions (CASE C:  $T_p = 26$  sec, amp. = 6.0 m).

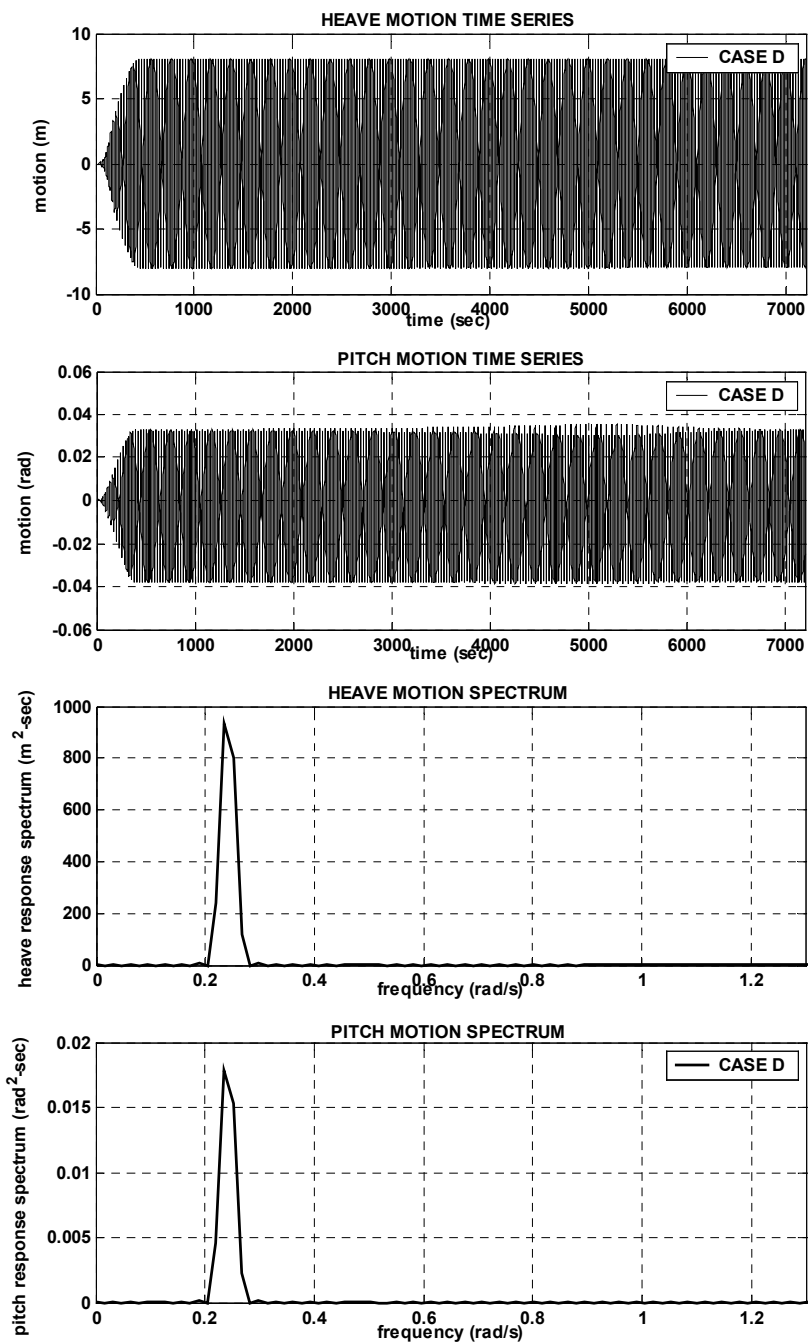


Fig. 7.12. Spar heave and pitch motions (CASE D:  $T_p = 26$  sec, amp. = 7.0 m).

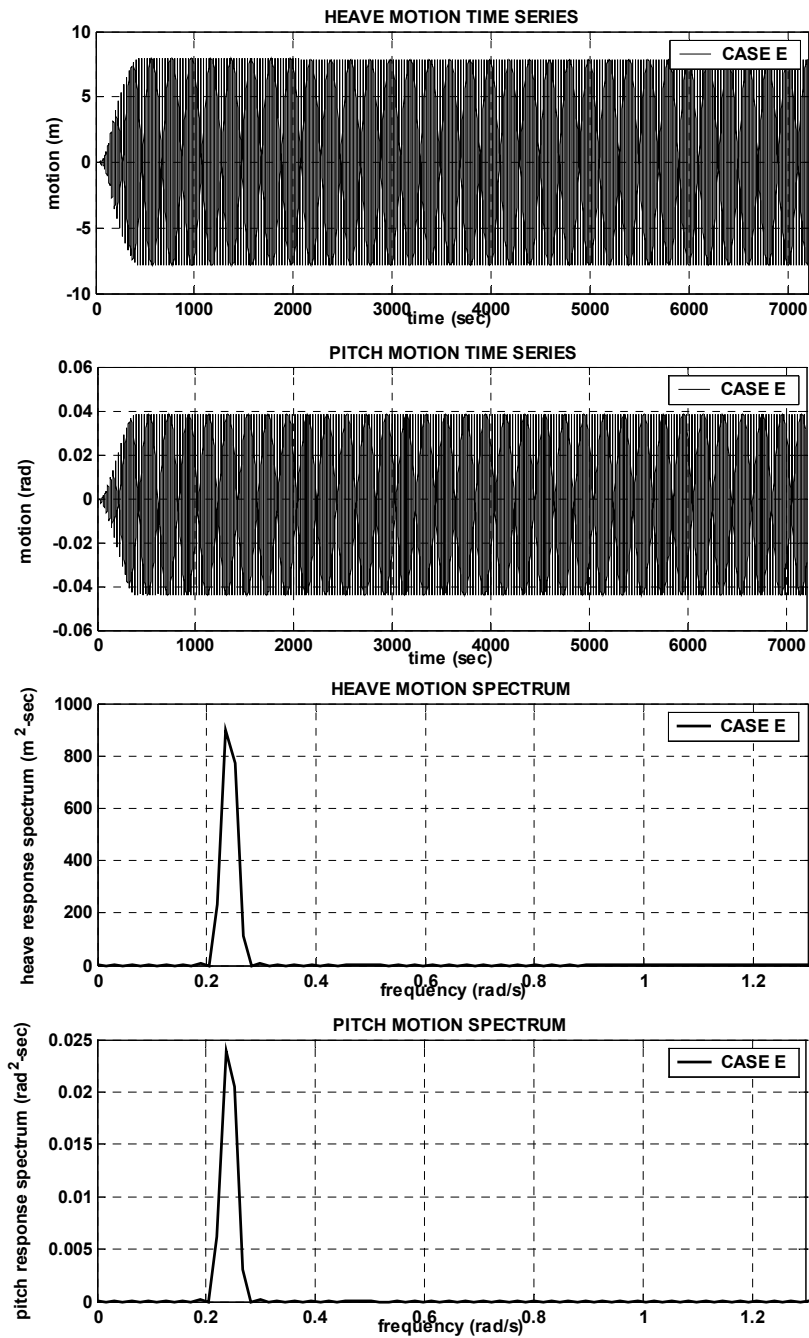


Fig. 7.13. Spar heave and pitch motions (CASE E:  $T_p = 26$  sec, amp. = 7.0 m).

To confirm the spar platform stability, the heave resonance zone is investigated in the RW-B simulation. As mentioned before, RW-B uses a 27.8 second wave period and this wave period is exactly same as the heave natural period as well as half of pitch natural period. The simulation results are shown in Fig. 7.14 through Fig. 7.19 and summarized in Table 7.9 and Table 7.10. In the simulation, the result from Case A Spar platform is not available due to the absence of damping from the drag force. The reason is that the Case A Spar platform is unrealistically modeled. When Mathieu instability is triggered in the Case A Spar platform the pitch motion is unrealistically large in small wave amplitudes due to the large heave resonance motion and almost zero pitch damping. Thus, in the RW-B simulation, the Case A Spar is not considered. The Case B simulation results are shown in Fig. 7.14. The results show that for heave motion larger than 8.0 meter the Case B Spar has Mathieu instability. This means that 1% pitch damping ratio is not enough to suppress the Mathieu instability. The CASE C Spar simulation results are shown in Fig. 7.15. The results show that the Case C Spar also has Mathieu instability when heave motion is larger than 8.0 meter. It is interesting to notice that, in RW-A case, the Case C Spar does not have Mathieu instability, but, in RW-B case, the Case C Spar has Mathieu instability. The reason is that, in RW-B case, the  $\alpha$  factor is 0.25 where the most severe Mathieu instability occurs. The Case C Spar in the 2.0 wave amplitudes is shown in Fig. 7.16. The results shows same tendency as RW-A Case B simulation results. This means that 3% pitch damping ratio can keep the pitch resonance motion stable even when the Mathieu instability is triggered.

The simulation results for the Case D and Case E Spar platforms are shown in Fig. 7.17 through Fig. 7.20. The Case D Spar results show Mathieu instability due to large heave motion and 0.25 alpha factors. However, the detailed time series for pitch motion



shows that Mathieu instability occurs after 2000 seconds, but, due to pitch damping effect, the superposition of two adjacent peaks cannot be fully developed as the pitch natural period of motion. It clearly shows that pitch damping dampened the pitch resonance from Mathieu instability. The Mathieu instability is not triggered in the Case E Spar even with a 11.3 meter heave motion. The reason is that additional restoring moment from buoyancy-can effect changes the pitch natural period of motion and it avoids the critical  $\alpha$  factor (i.e. 0.25) and also the additional restoring moment compensates for the heave motion disturbance in the pitch restoring moment. Fig. 7.19 clearly shows that the pitch motion of the Case E Spar platform only has wave frequency motion. This result clearly shows the buoyancy-can effects on Mathieu instability. It shows that in the same heave motion Case D has Mathieu instability but Case E does not have Mathieu instability. To ensure stability of CASE E Spar, a 22.7 second regular wave simulation is conducted. In the 22.7 second wave period, Case E Spar has 0.25  $\alpha$  factor. However, the results show that heave motion of the Case E Spar is not large even when a 7 meter wave amplitude is used.

The RW-A and RW-B simulation results show that buoyancy-can effects play very important role in Mathieu instability analysis for the spar platform. Thus, without proper modeling of risers and mooring lines in the simulation and experiment may lead to incorrect results under certain condition. The wave amplitudes and periods used in the simulation are not practical but only academic, still it is worthwhile to capture the Mathieu instability of a spar platform and to see the Mathieu instability mechanism is due to heave pitch coupling. Based on the regular wave simulation results, in the following section, Mathieu instability in a spar platform is checked for a Swell environment

**Table 7.9. Comparison of statistics (Regular wave simulation B).**

	RW B: T = 27.8 sec, amp. = 1.5				amp. = 2.0	
	CASE B		CASE C		CASE C	
	HEAVE	PITCH	HEAVE	PITCH	HEAVE	PITCH
UNIT	m	deg.	m	deg.	m	deg.
MEAN	7.40E-03	-2.11E-02	6.84E-03	-2.14E-02	1.24E-03	-2.65E-02
STD	4.82E+00	3.02E+00	4.82E+00	5.37E-01	6.11E+00	1.93E+00
EXE	-8.07E+00	-7.17E+00	-8.07E+00	-1.58E+00	9.83E+00	3.47E+00
<i>Notes:</i> STD = standard deviation; EXE = extreme						

**Table 7.10. Comparison of statistics (Regular wave simulation B and C).**

	RW B: T = 27.8 sec, amp. = 7.0				T = 22.7	
	CASE D		CASE E		CASE E	
	HEAVE	PITCH	HEAVE	PITCH	HEAVE	PITCH
UNIT	m	deg.	m	deg.	m	deg.
MEAN	-2.55E-02	-3.20E-01	-1.52E-02	-3.28E-01	1.05E-01	-7.83E-02
STD	8.12E+00	2.87E+00	7.96E+00	2.01E+00	1.59E+00	1.58E+00
EXE	1.15E+01	-6.36E+00	1.13E+01	-3.15E+00	2.38E+00	-2.31E+00
<i>Notes:</i> STD = standard deviation; EXE = extreme						

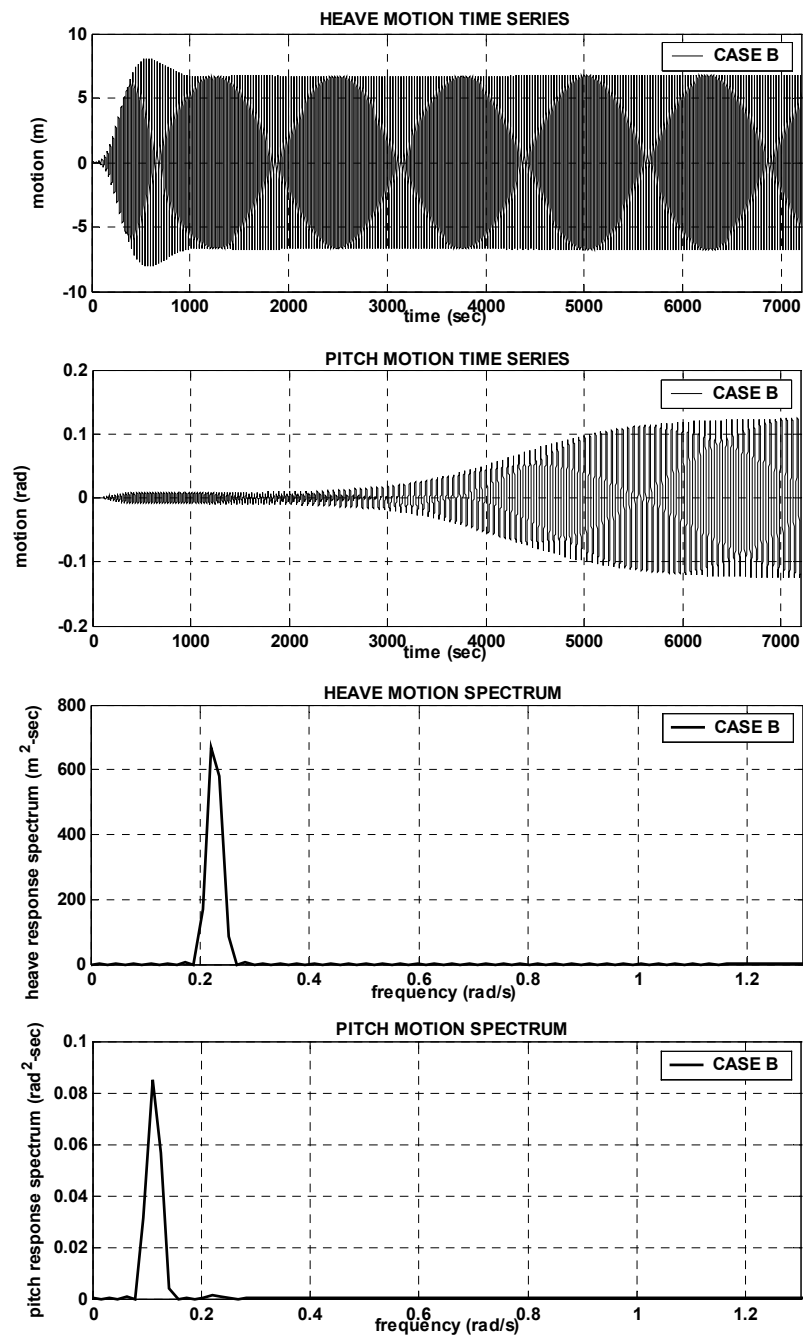


Fig. 7.14. Spar heave and pitch motions (CASE B:  $T_p = 27.8$  sec, amp. = 1.5 m).

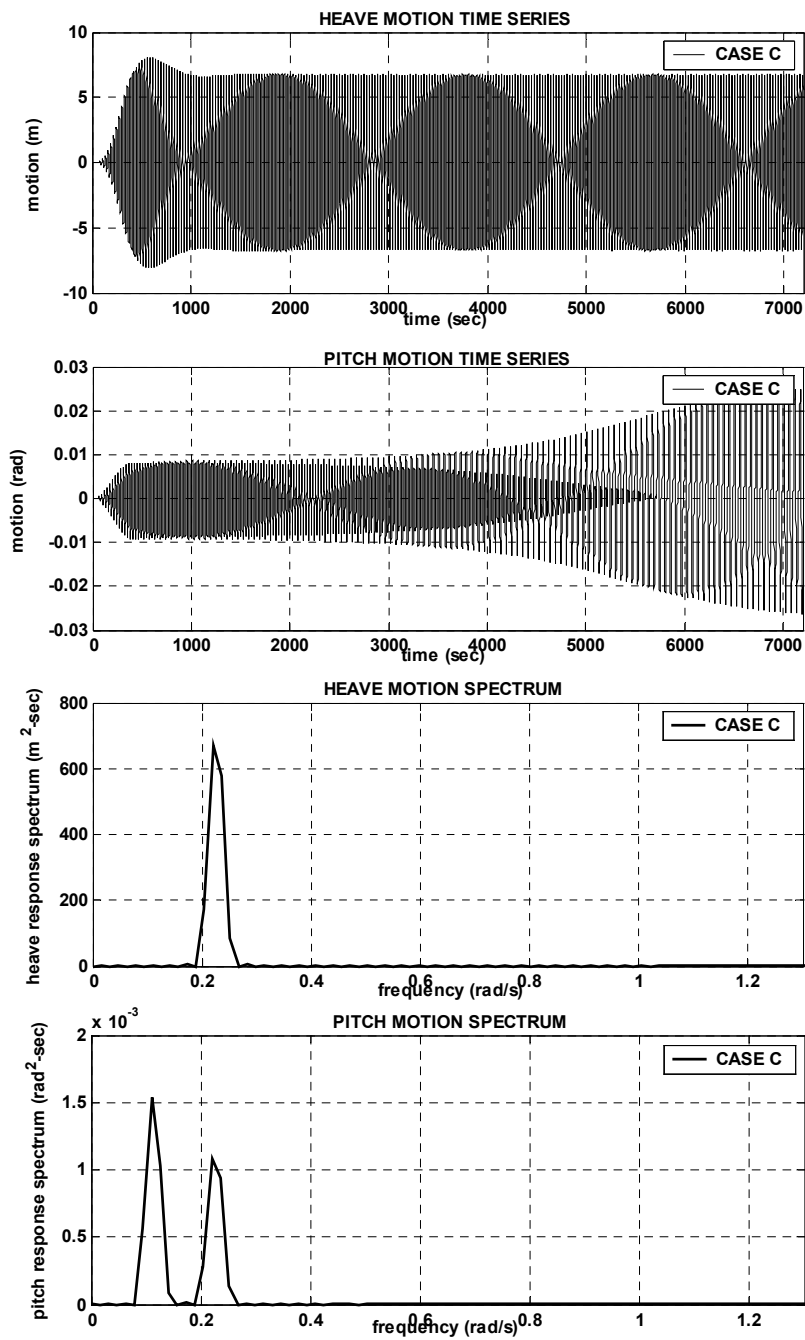


Fig. 7.15. Spar heave and pitch motions (CASE C:  $T_p = 27.8$  sec, amp. = 1.5 m).

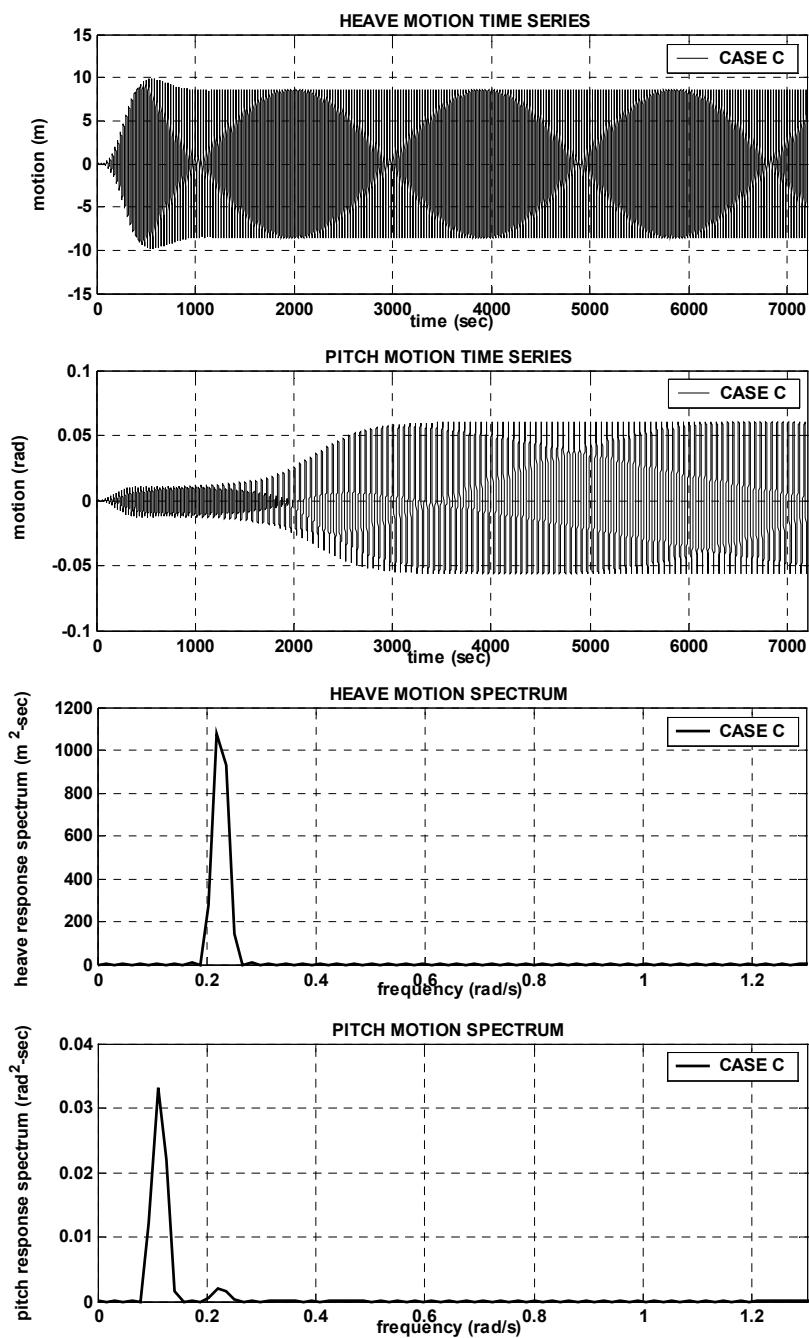


Fig. 7.16. Spar heave and pitch motions (CASE C:  $T_p = 27.8$  sec, amp. = 2.0 m).

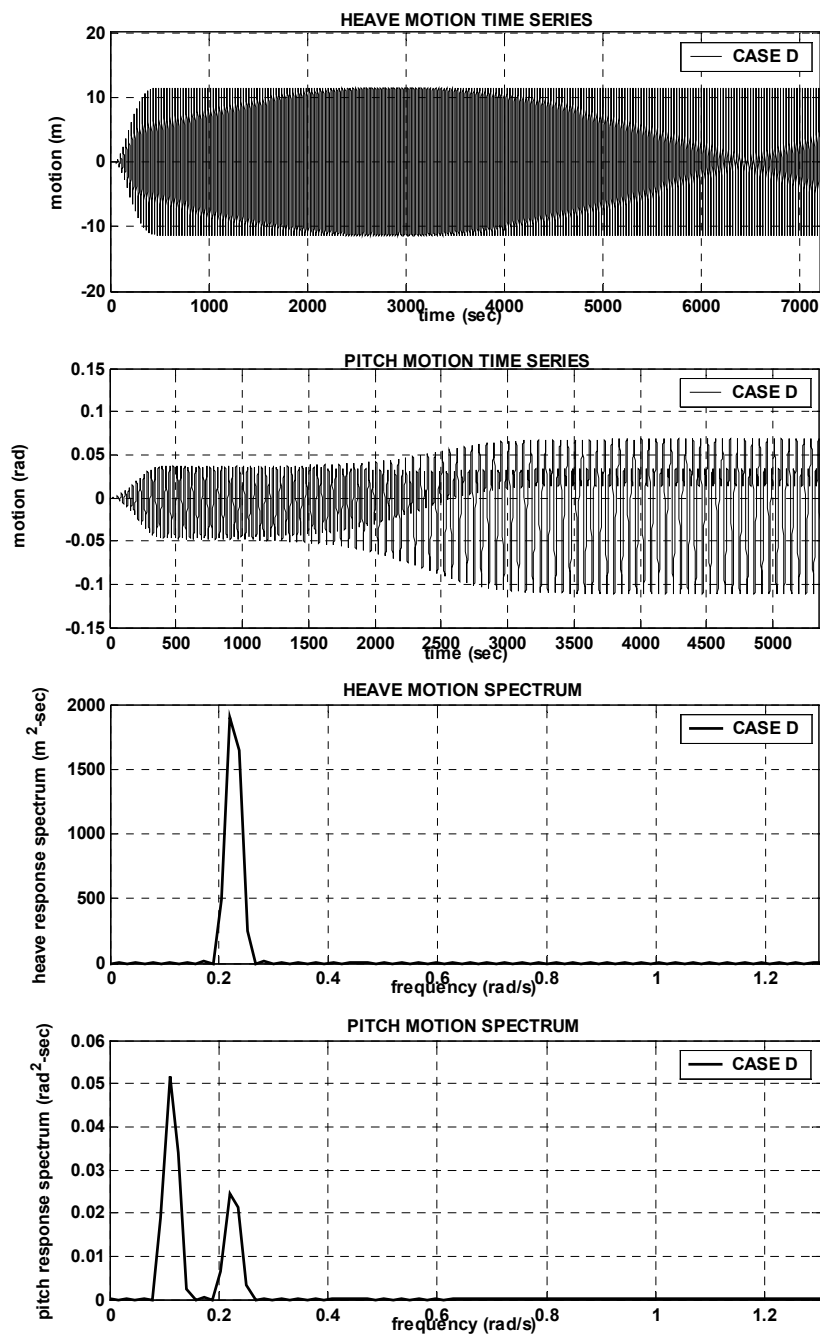
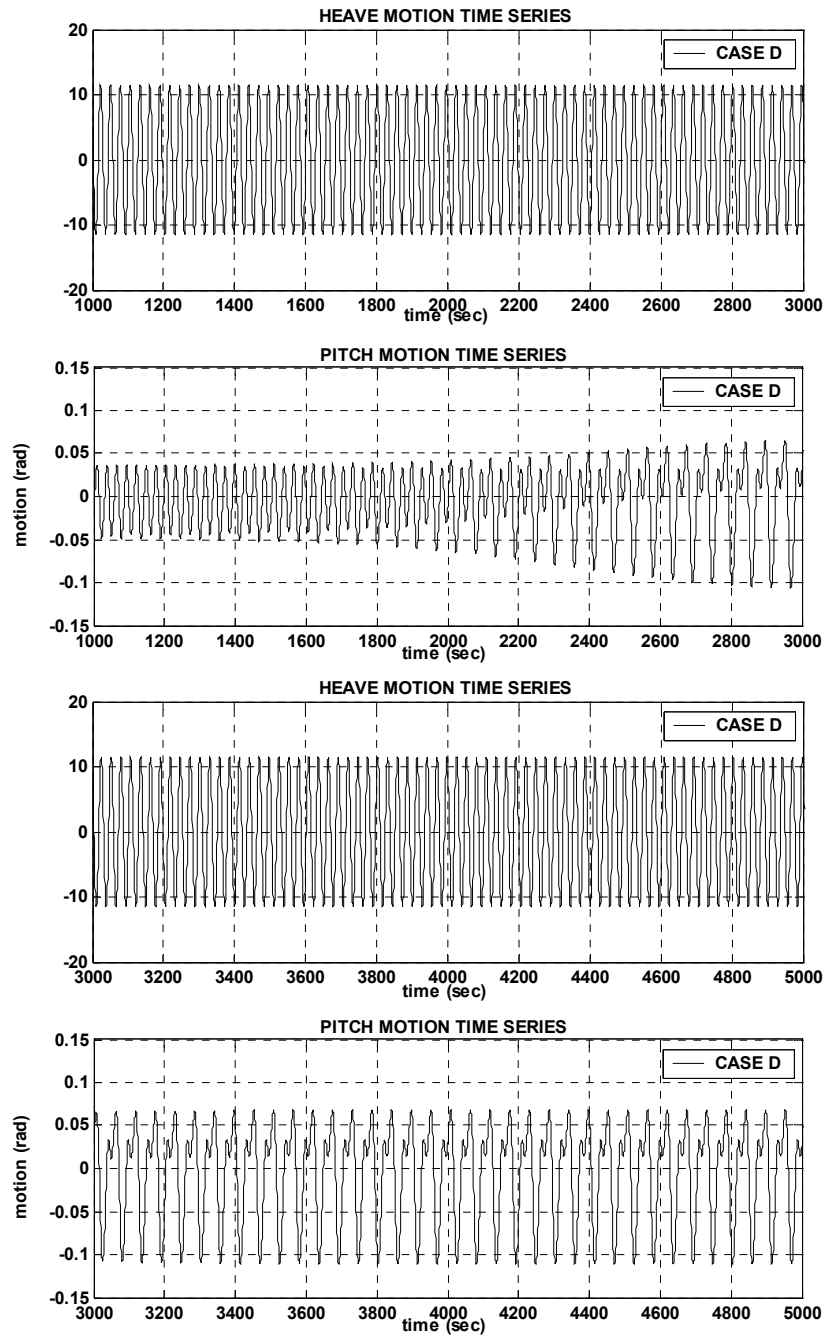


Fig. 7.17. Spar heave and pitch motions (CASE D:  $T_p = 27.8$  sec, amp. = 7.0 m).

CASE A:  $T = 27.8$  sec, amp. = 7.0 m



**Fig. 7.18. Heave/Pitch response time series (1000 sec – 5000 sec).**

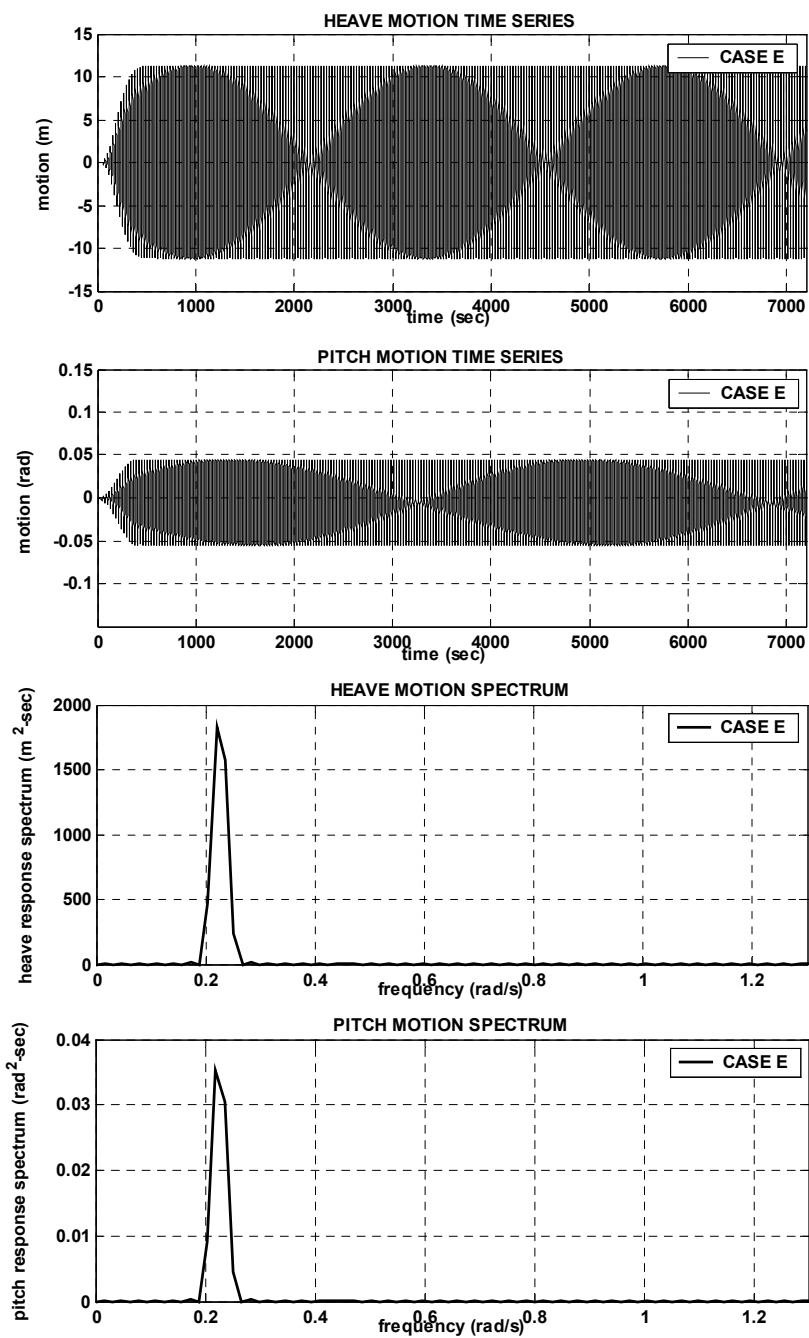


Fig. 7.19. Spar heave and pitch motions (CASE E:  $T_p = 27.8$  sec, amp. = 7.0 m).



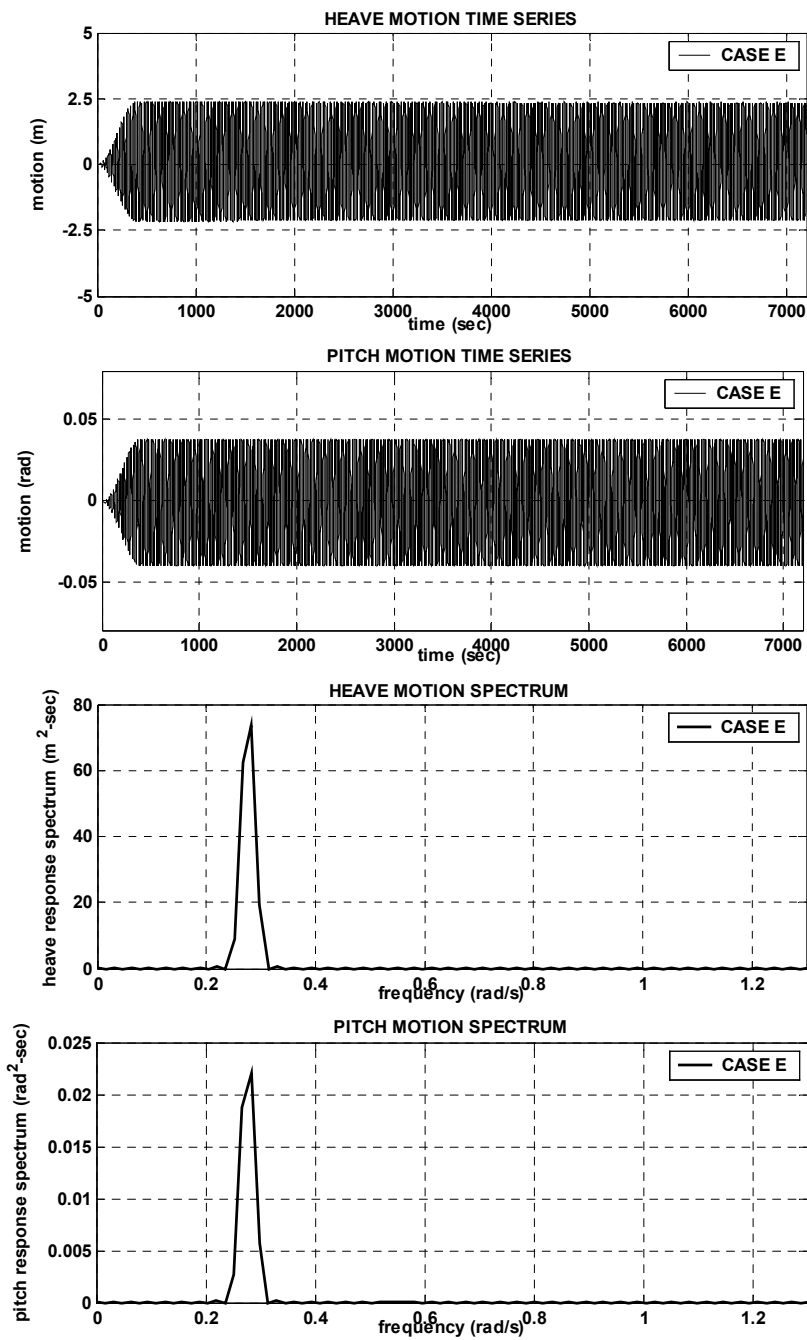


Fig. 7.20. Spar heave and pitch motions (CASE E:  $T_p = 22.7$  sec, amp. = 7.0 m).

### 7.4.3. Mathieu Instability in Swell Condition

Fig. 7.21 through Fig. 7.24 show the Swell wave spectrum and times series which are used in the simulation. The Swell-A and Swell- B simulation results are shown in Fig. 7.25 through Fig. 7.36 and summarized in Table 7.11 and Table 7.12. Based on the regular wave simulation (RW-A and RW-B), Mathieu instability is not triggered in CASE E Spar even in large heave motion. The Swell-A and Swell-B simulation results show that the maximum heave motion is around 1.7 ~ 1.9 meter and maximum pitch motion is around 0.6 ~ 0.7 degree. The ranges of heave and pitch motion in the regular wave simulation results show that the spar platform is very stable. It shows that the spar platform does not have Mathieu instability in the swell wave environment. However, the heave motion standard deviation in the swell condition is five times larger than in 100-year hurricane condition.

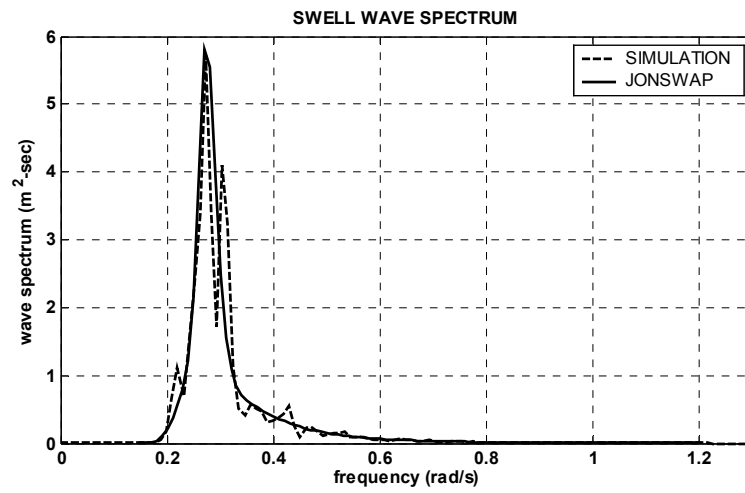


Fig. 7.21. Wave spectrum for Swell – A.

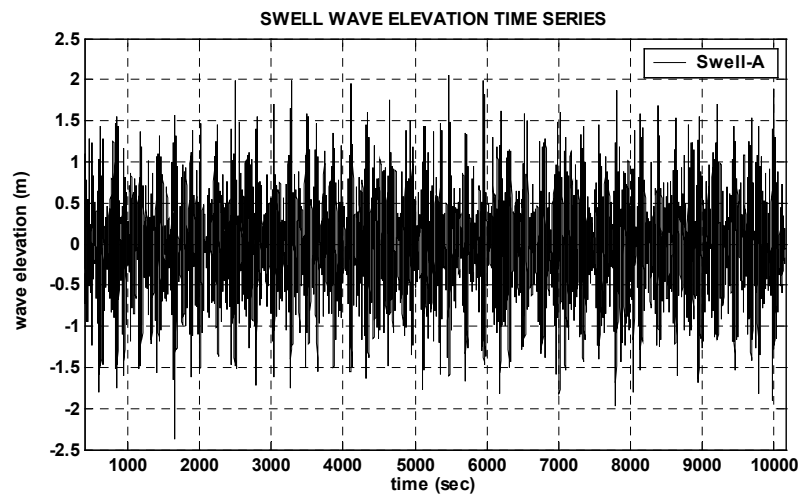


Fig. 7.22. Wave time series for Swell – A.

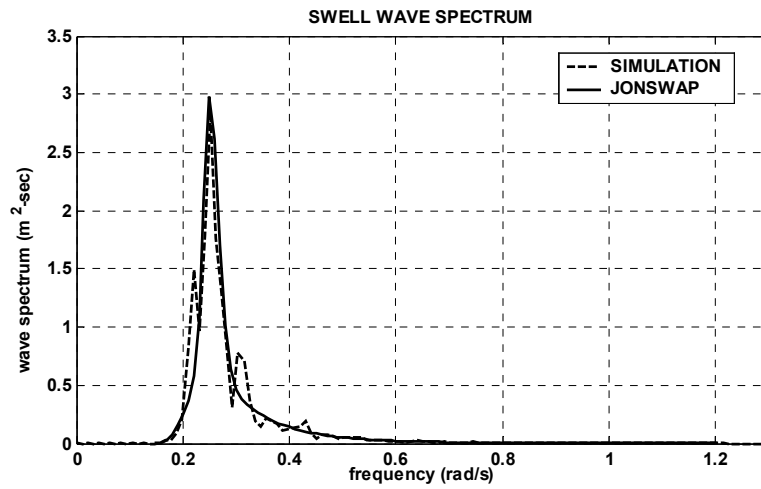


Fig. 7.23. Wave spectrum for Swell – B.

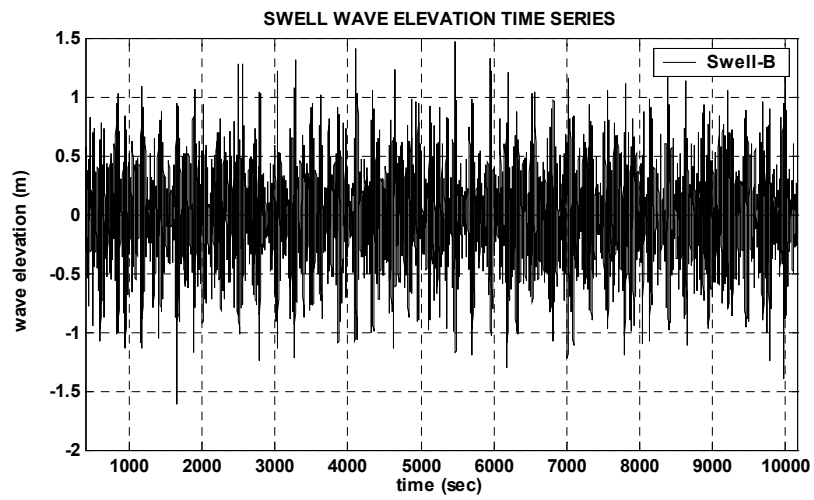


Fig. 7.24. Wave time series for Swell – B.

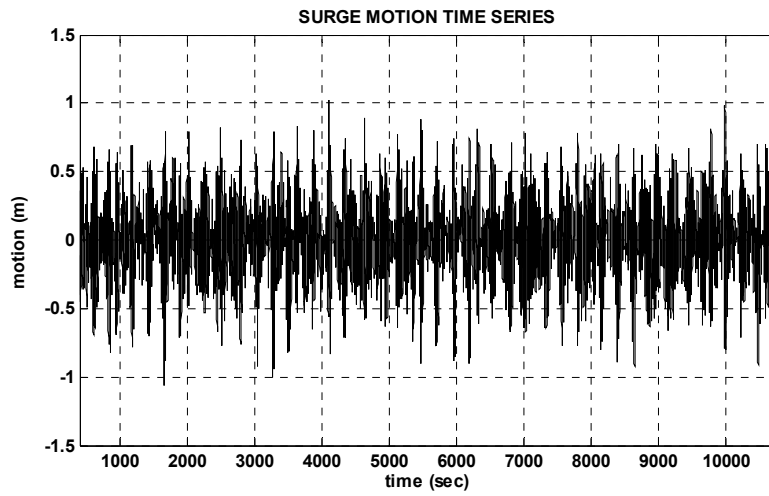


Fig. 7.25. Surge response time series ( $H_s = 2.5$  m,  $T_p = 23$  sec,  $\gamma = 6.0$ ).

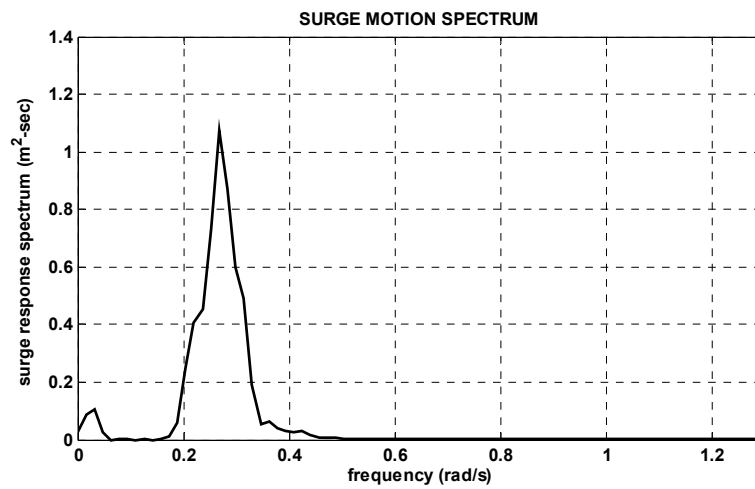
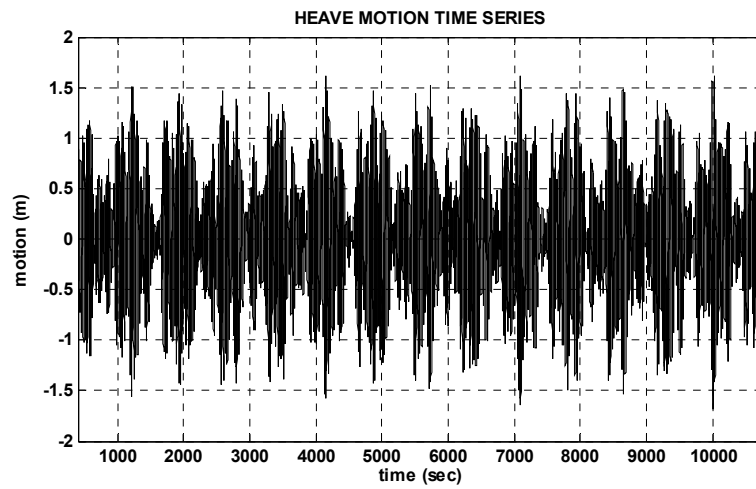
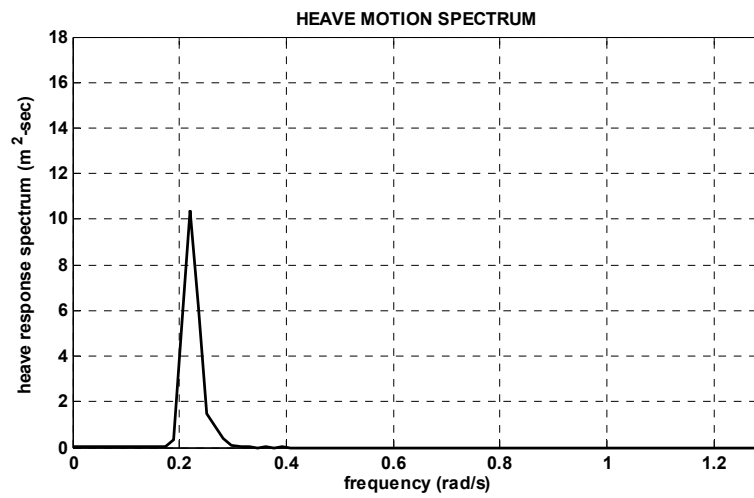


Fig. 7.26. Surge response spectrum ( $H_s = 2.5$  m,  $T_p = 23$  sec,  $\gamma = 6.0$ ).



**Fig. 7.27. Heave response time series ( $H_s = 2.5$  m,  $T_p = 23$  sec,  $\gamma = 6.0$ ).**



**Fig. 7.28. Heave response spectrum ( $H_s = 2.5$  m,  $T_p = 23$  sec,  $\gamma = 6.0$ ).**

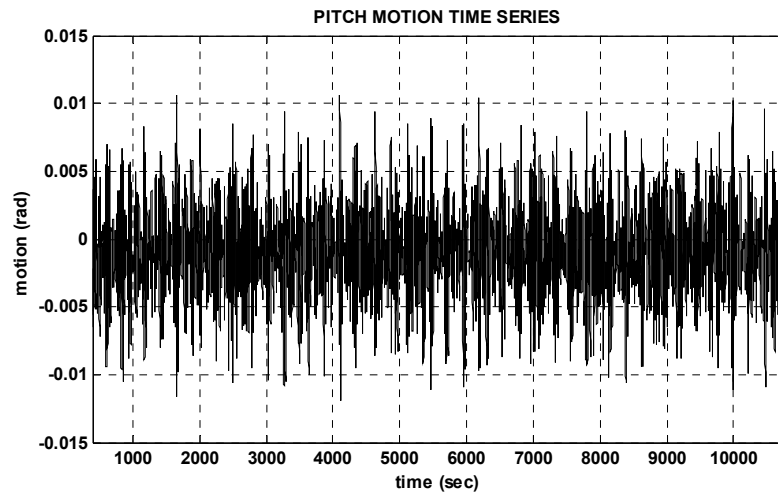


Fig. 7.29. Pitch response time series ( $H_s = 2.5$  m,  $T_p = 23$  sec,  $\gamma = 6.0$ ).

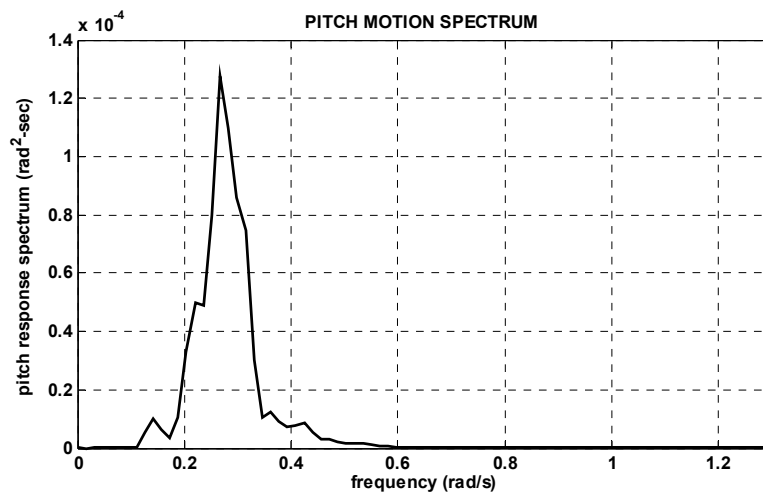


Fig. 7.30. Pitch response spectrum ( $H_s = 2.5$  m,  $T_p = 23$  sec,  $\gamma = 6.0$ ).

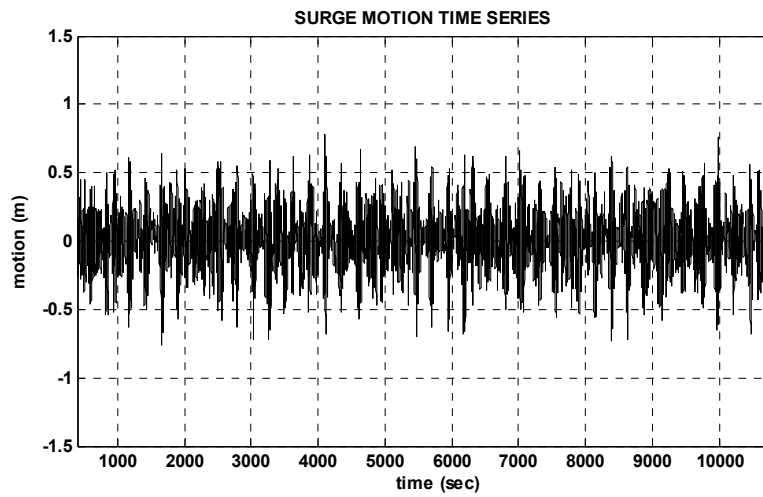


Fig. 7.31. Surge response time series ( $H_s = 1.7$  m,  $T_p = 25$  sec,  $\gamma = 6.0$ ).

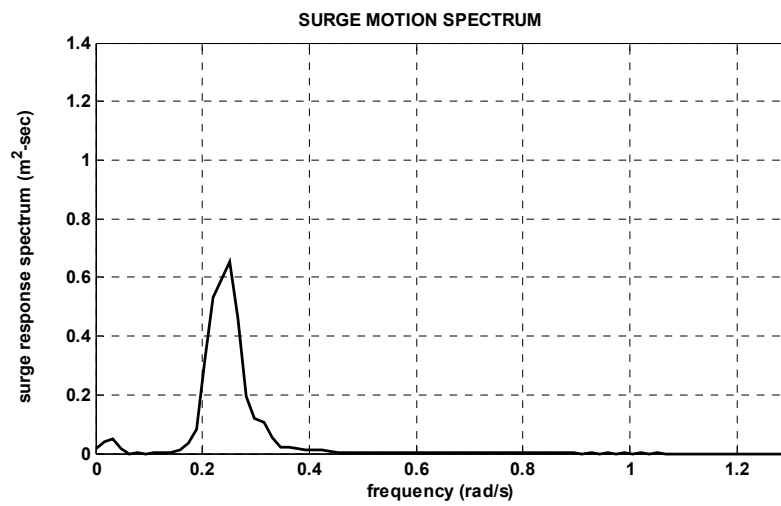
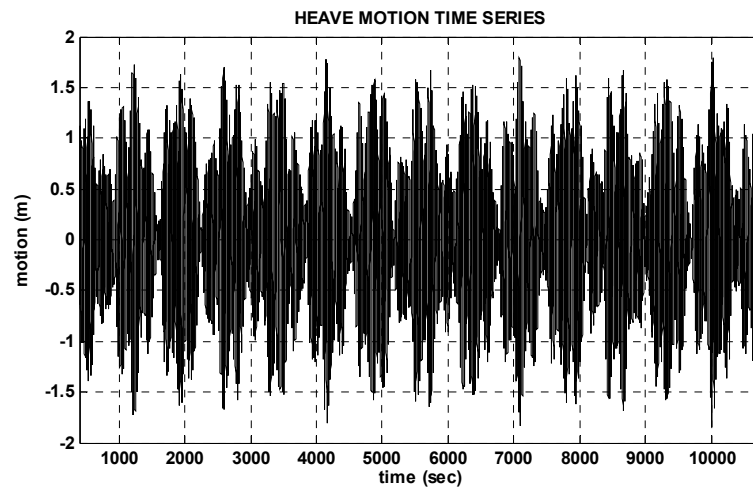
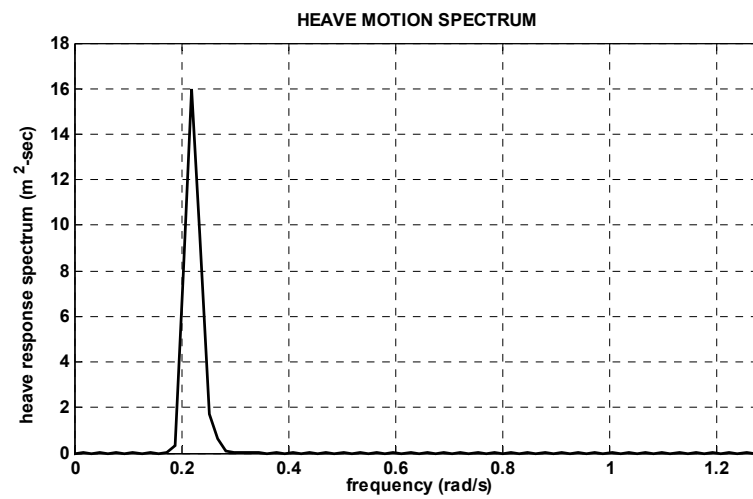


Fig. 7.32. Surge response spectrum ( $H_s = 1.7$  m,  $T_p = 25$  sec,  $\gamma = 6.0$ ).





**Fig. 7.33. Heave response time series ( $H_s = 1.7$  m,  $T_p = 25$  sec,  $\gamma = 6.0$ ).**



**Fig. 7.34. Heave response spectrum ( $H_s = 1.7$  m,  $T_p = 25$  sec,  $\gamma = 6.0$ ).**

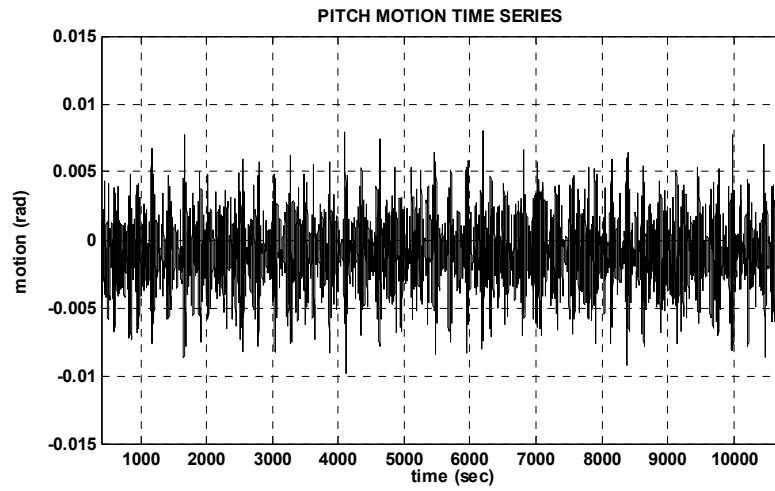


Fig. 7.35. Pitch response time series ( $H_s = 1.7$  m,  $T_p = 25$  sec,  $\gamma = 6.0$ ).

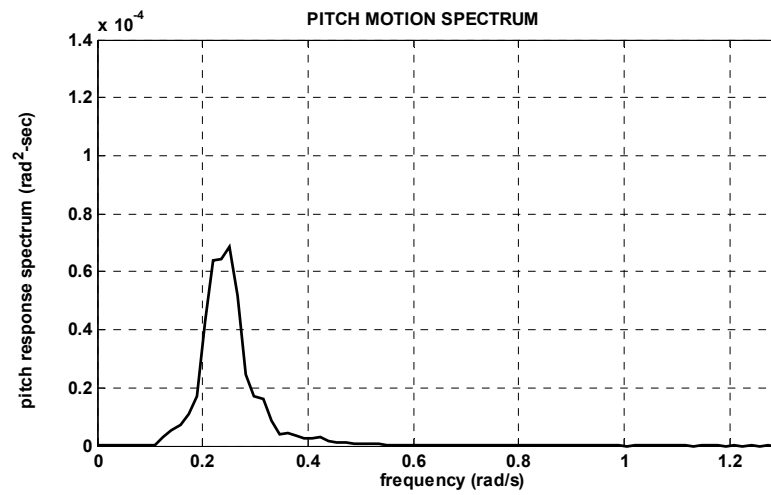


Fig. 7.36. Pitch response spectrum ( $H_s = 1.7$  m,  $T_p = 25$  sec,  $\gamma = 6.0$ ).

**Table 7.11. Summary of swell condition A statistics.**

SWELL CONDITION A			
	SURGE (m)	HEAVE (m)	PITCH (deg)
MEAN	-9.71E-04	-2.63E-03	-5.35E-01
STD	2.99E-01	6.30E-01	1.97E-01
EXE	-1.06E+00	-1.68E+00	-6.81E-01
LF STD	6.65E-02	5.31E-02	5.33E-03
WF STD	2.87E-01	5.91E-01	2.51E-02
<i>Notes:</i> STD = standard deviation; EXE = extreme; LF = low frequency; WF = wave frequency			

**Table 7.12. Summary of swell condition B statistics.**

SWELL CONDITION B			
	SURGE (m)	HEAVE (m)	PITCH (deg)
MEAN	-1.01E-02	-3.37E-03	-5.32E-02
STD	2.30E-01	7.55E-01	1.49E-01
EXE	7.86E-01	-1.84E+00	-5.61E-01
LF STD	5.88E-02	6.22E-02	6.02E-03
WF STD	2.18E-01	7.25E-01	1.82E-02
<i>Notes:</i> STD = standard deviation; EXE = extreme; LF = low frequency; WF = wave frequency			

## CHAPTER VIII

### CASE STUDY 4: LOOP CURRENT SIMULATION

#### 8.1. Introduction

In this chapter, the dynamic behavior of a spar platform in loop current environment is investigated. The clockwise flow that extends northward into the Gulf of Mexico and joins the Yucatan Current and the Florida Current is known as the Loop Current (Hofmann and Worley, 1986). Fig. 8.1 shows loop current for the Gulf of the Mexcio. Due to strong current and deep draft of a spar platform, the loop current can generate vortex-induced vibration for a classical spar platform. The pressure difference around a bluff body in current may experience flow separation. Due to velocity difference between the outermost boundary layers and innermost boundary layer, and if the velocity of flow is large enough, this causes the boundary layers to roll into the near wake and form periodic vortices. The interaction of the structure with these vortices causes it to vibrate transverse to the flow direction, and this phenomenon is called as vortex-induced vibration. The frequency of vortex shedding can be found from the Strouhal number that is a function of Reynolds number and body geometry. The spar Reynolds number is in the range of  $10^7$  in 1~2m/s current velocity. In this Reynolds number range, the Strouhal number is around 0.21 ~ 0.23 for circular cylinders (Lienhard, 1966). However, as noted by Roshko (1961), the Strouhal number for the circular cylinders appears to be proportional to the inverse of the drag coefficient. For Reynolds numbers between  $10^2$  and  $10^7$ , but excluding the transitional

regime  $R \cong 10^6$ , the Strouhal number is approximated closely by  $S = 0.23/C_D$ . Based on this approximated formulation, the Strouhal number can be 0.153 when  $C_D$  is 1.5. As mentioned before, the vortex-induced vibration is modeled as lift a force on a spar hull. Thus, in the case study, simulations are conducted for 0.4 lift coefficients with 0.153 and 0.23 Strouhal numbers.

The dimension, mooring lines configuration, and risers configuration of the spar platform used in this study is exactly same as Chapter V (i.e. case study 1: buoyancy-can effect on spar Platform) except the riser support system. The principle particulars of the spar platform and characteristics of mooring line and riser are summarized in Table 5.1 through Table 5.4 in Chapter V.

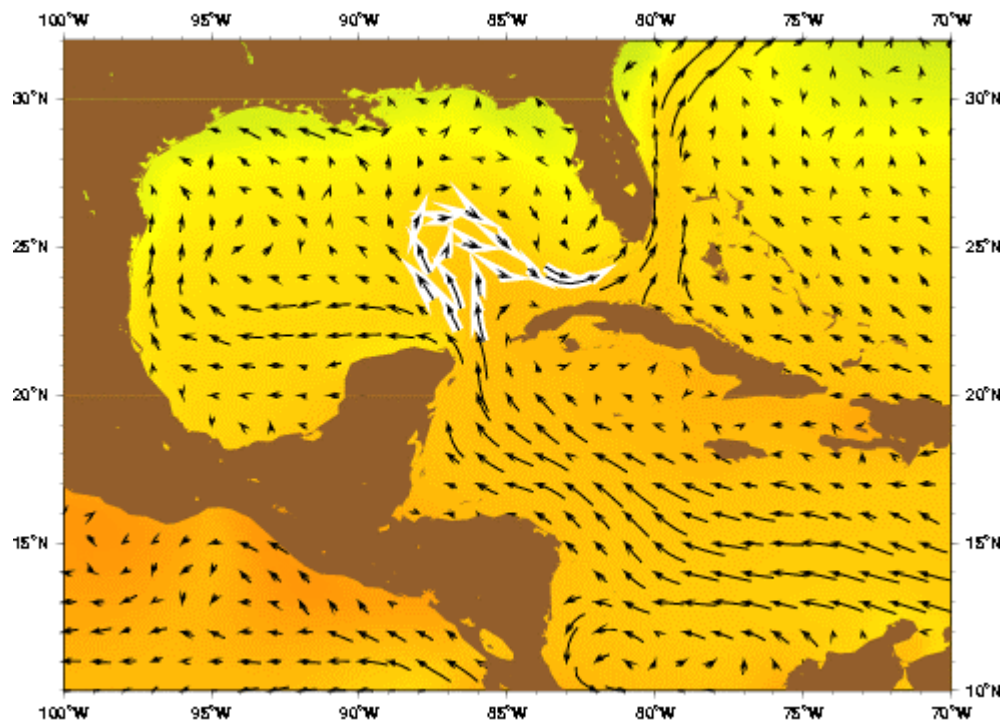


**Fig. 8.1.** Loop current for the Gulf of Mexico (Gyory et al., 2001).

## 8.2. Description of Case study and Design Environmental Conditions

As mentioned before, three simulations are conducted in the case study. The difference among the three spar platforms is the lift coefficient. The Case A Spar platform uses zero lift coefficient, thus Case A Spar ignores the vortex-induced vibration effects. Case B and Case C Spar platforms use a 0.4 lift coefficient. As mentioned before, the simulations are conducted at 0.153 and 0.23 Strouhal numbers.

In the loop current simulations, the current is assumed to be steady and the irregular wave is unidirectional. The wave heading is 180 degrees with respect to global axis. A JONSWAP spectrum of significant wave height,  $H_s = 6.1$  meter, peak period  $T_p = 8.87$  sec, and overshoot parameter  $\gamma = 2.0$  was selected to represent a typical loop current condition in the Gulf of Mexico. The current flows from 90 degree right of wave direction. This environmental direction causes the most severe vortex-induced vibration of the spar surge motion. The current velocity is assumed to be 2.13 m/sec from mean water level to 91.44 m water depths and is reduced to 0.91 m/sec at 243.84 m (300 ft) and zero at 914.4 m. The wind speed used is 22.35 m/sec at 10m above mean water level and wind direction is collinear to wave direction. The API wind spectrum is used for the generation of time varying wind forces. Fig. 8.2 and Fig. 8.3 show environment direction of the loop current condition and loop current profile, respectively. The time step used in simulation is 0.05 seconds and the total simulation time is 3 hours (216000 time steps).

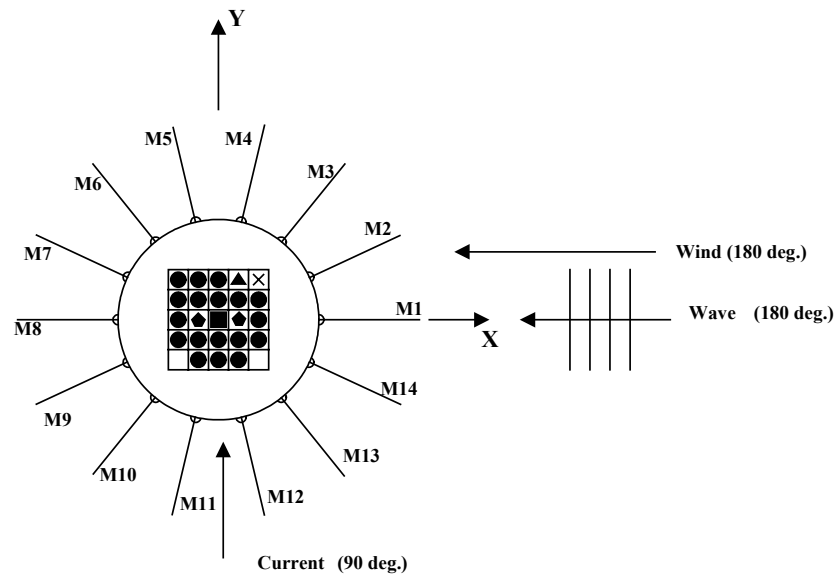


**Fig. 8.2. Environmental direction of loop current condition.**

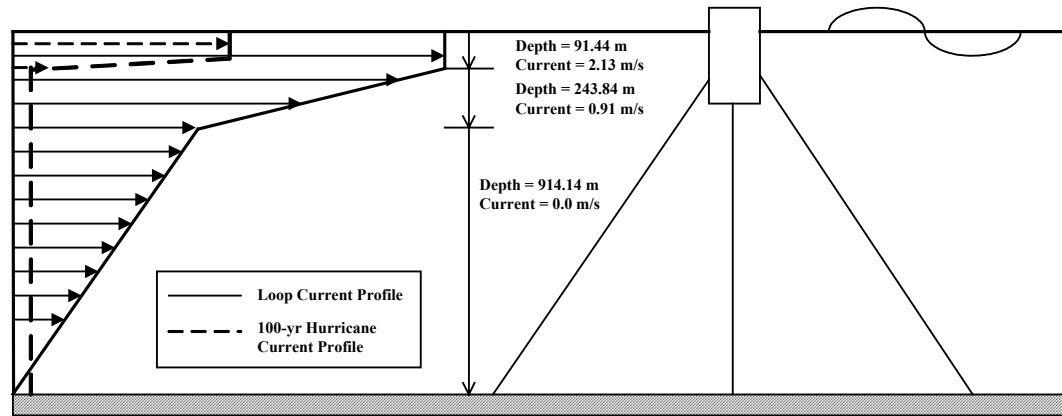


**Fig. 8.3. Loop current and 100-yr hurricane current profile.**

### 8.3. Results and Analysis

In the simulation, the loop current comes from 90 degree with respect to global axis, thus vortex-induced vibration effects are in the surge and pitch motion of the spar platform. Fig. 8.4 through Fig. 8.6 show the wind velocity spectrum, wave spectrum, and wave time series used in the simulations. The input wave spectrum is truncated at  $0.2 \text{ (rad/sec)} < \omega < 1.2 \text{ (rad/sec)}$  in this study, and wind spectrum is truncated at  $2 \text{ (rad/sec)}$ .

The simulated surge motion results are shown in Fig. 8.7 through Fig. 8.10. Comparisons of simulated surge time series clearly show the vortex-induced vibration effects in Case B and Case C Spar platforms. Comparison of the surge spectrum in Fig. 8.10 shows that the peak induced by vortex-induced vibration for Case B is in the range of 57 second through 125 seconds (peak period = 69 seconds) and 56 second through 251 seconds (peak period = 125 seconds) for Case C. The most severe vortex induced vibration event, called as synchronized or lock-in, occurs in the range of  $0.9 \sim 1.2$  times of the structure natural frequency. Case C simulation results show lock-in situation clearly. Strouhal frequencies of both cases (Case B and Case C) include the pitch natural periods, thus the large vortex-induced vibration effects on pitch motion are expected.



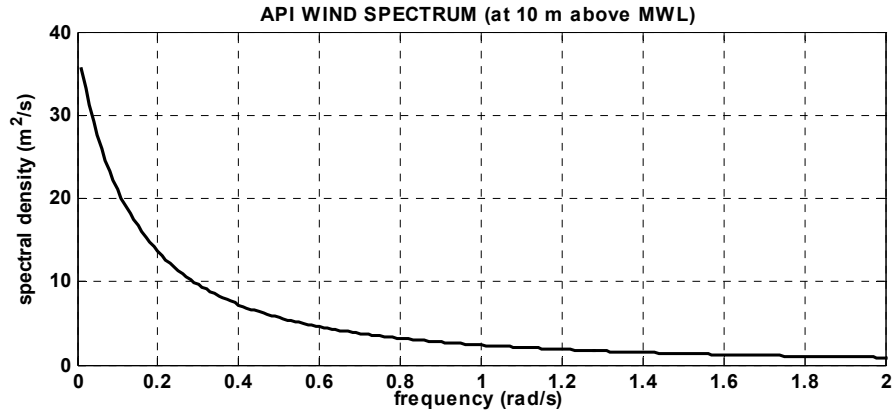


Fig. 8.4. Loop current condition wind velocity spectrum.

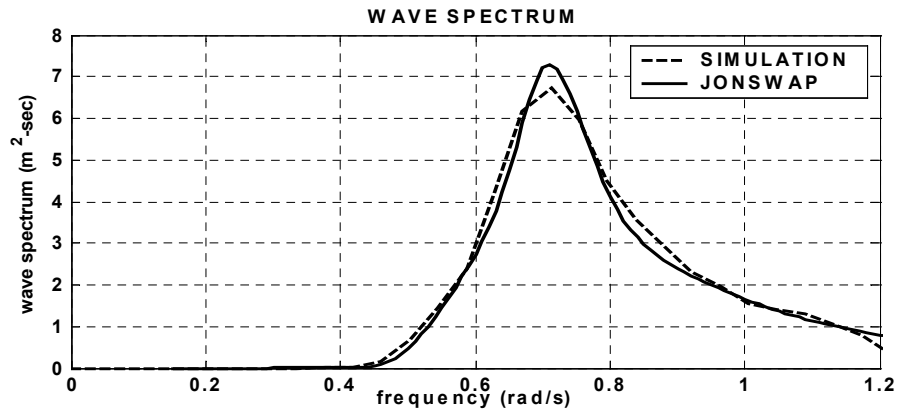


Fig. 8.5. Loop current condition wave spectrum.

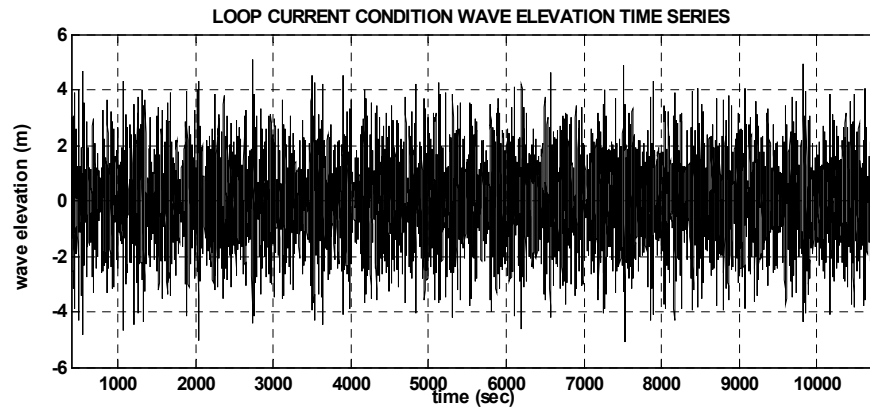


Fig. 8.6. Loop current condition wave time series.

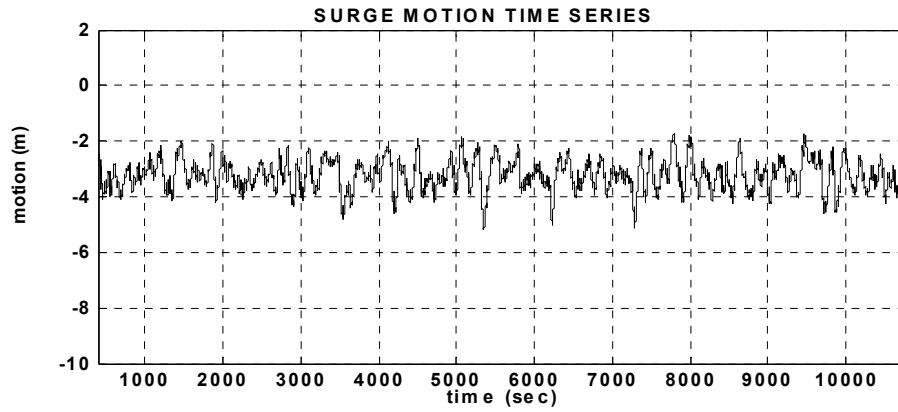


Fig. 8.7. Surge response time series (CASE A,  $C_L = 0.0$ ).

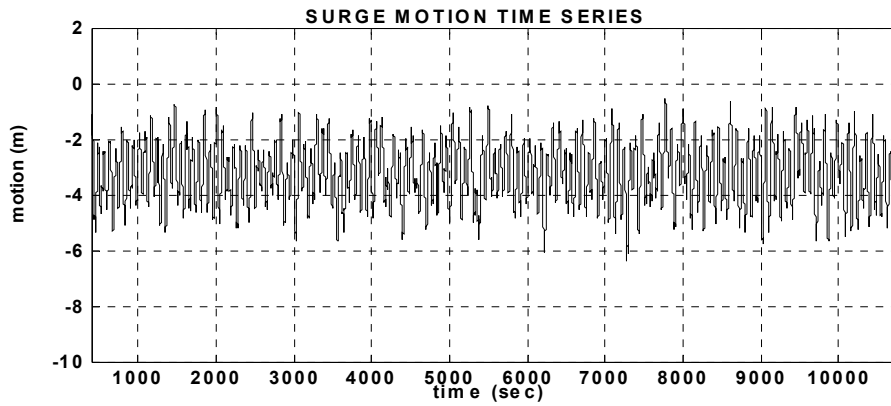


Fig. 8.8. Surge response time series (CASE B,  $St = 0.23$ ,  $C_L = 0.4$ ).

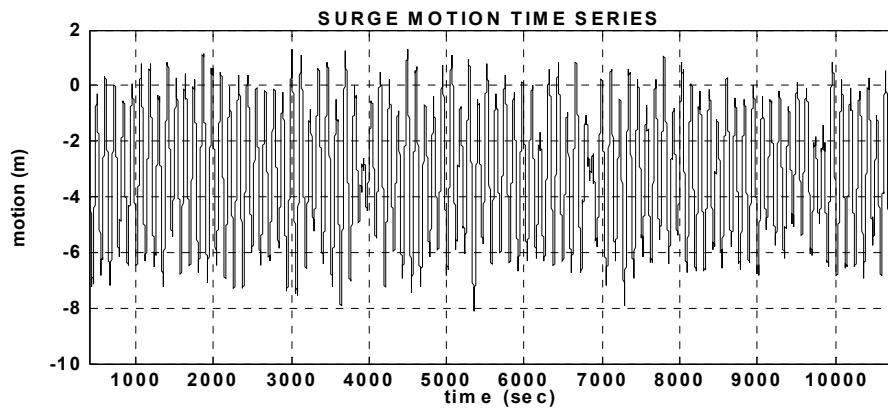
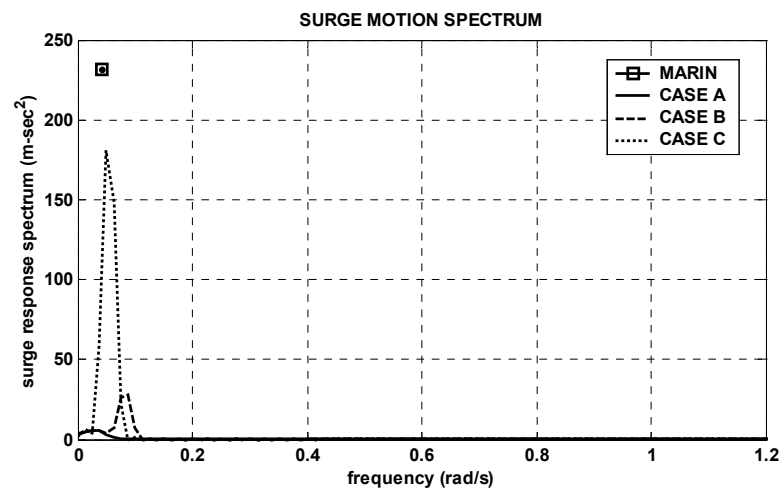
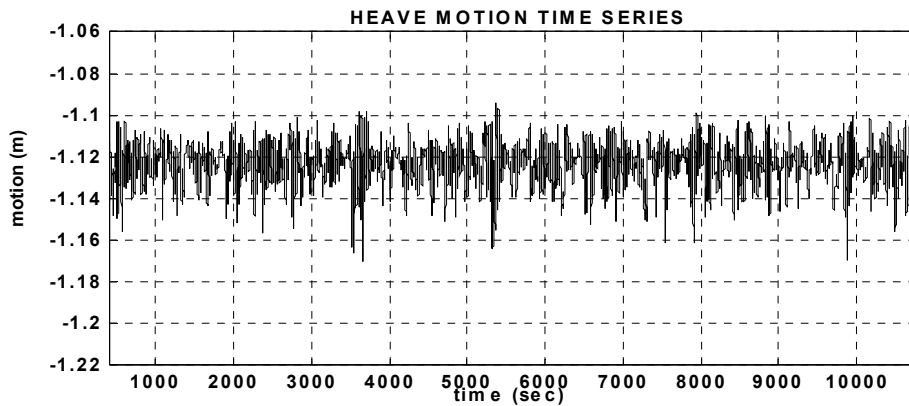


Fig. 8.9. Surge response time series (CASE C,  $St = 0.153$ ,  $C_L = 0.4$ ).



**Fig. 8.10. Comparison of surge response spectrum (□ shows the peak from experiment).**

Fig. 8.11 through Fig. 8.14 show the simulated heave motion results. Due to the large surge motion, heave is also affected by vortex-induced vibration. The set up and set down effects from the surge motion are clearly shown in the heave motion spectrum. Due to large surge motion in Case C, the heave motion is also larger in Case C compared to Case B.



**Fig. 8.11.** Heave response time series (CASE A,  $C_L = 0.0$ ).

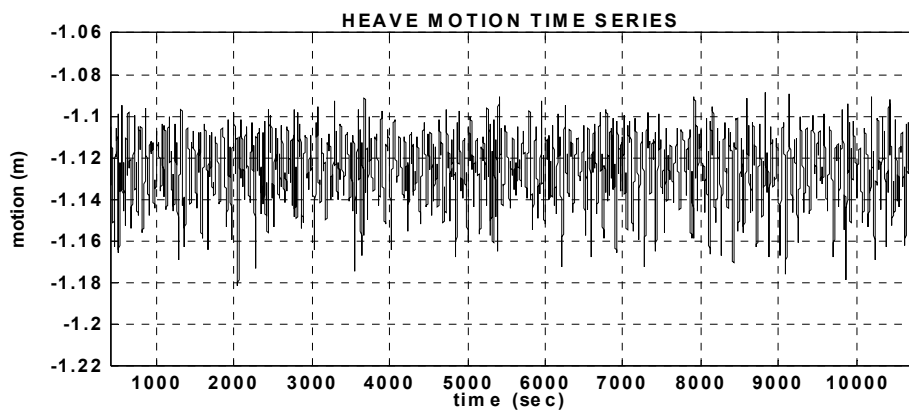


**Fig. 8.12.** Heave response time series (CASE B,  $St = 0.23$ ,  $C_L = 0.4$ ).

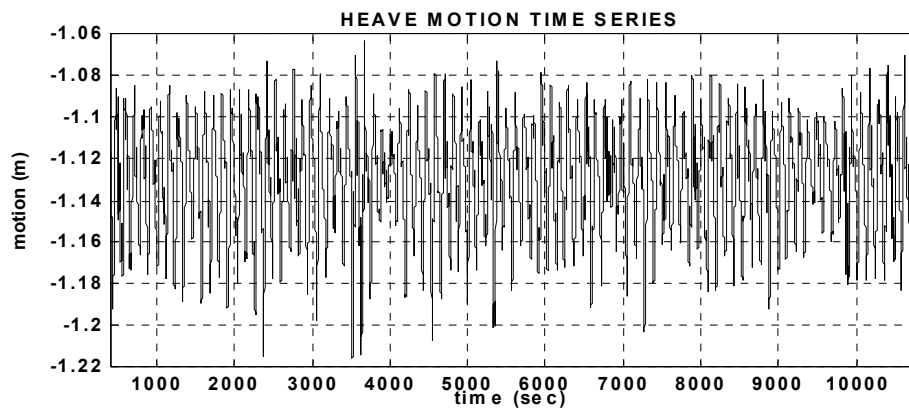


**Fig. 8.13.** Heave response time series (CASE C,  $St = 0.153$ ,  $C_L = 0.4$ ).

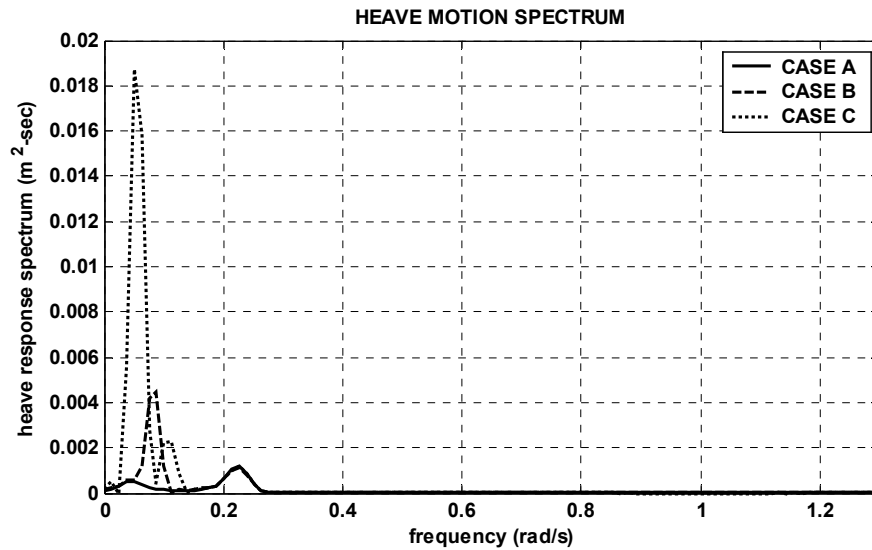


**Fig. 8.14. Comparison of heave response spectrum.**

Fig. 8.15 through Fig. 8.18 show the simulated pitch motion results. Due to the change in current velocity with depth, the lift force frequency are changed with depth in the simulation and these factor generate additional exciting moment for the spar pitch motion. As mentioned before, the Strouhal frequencies of both (Case B and Case C) simulations near the pitch natural period (i.e. 45.5 seconds). Due to additional exciting moment and Strouhal frequency, pitch motion is also increased significantly.

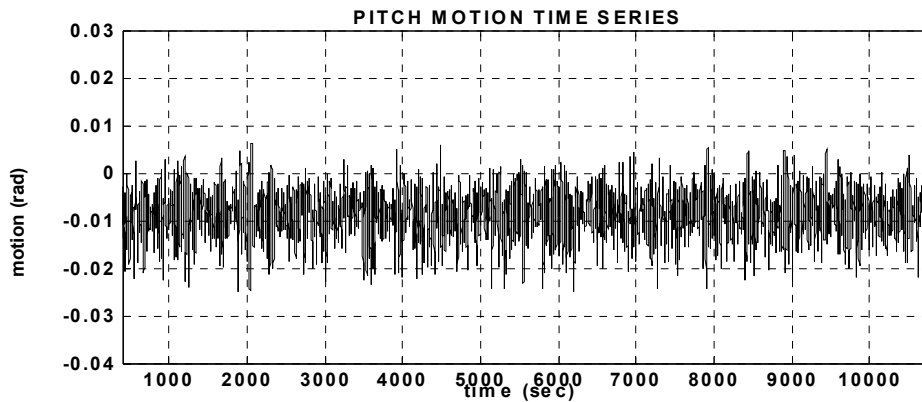


Fig. 8.15. Pitch response time series (CASE A,  $C_L = 0.0$ ).

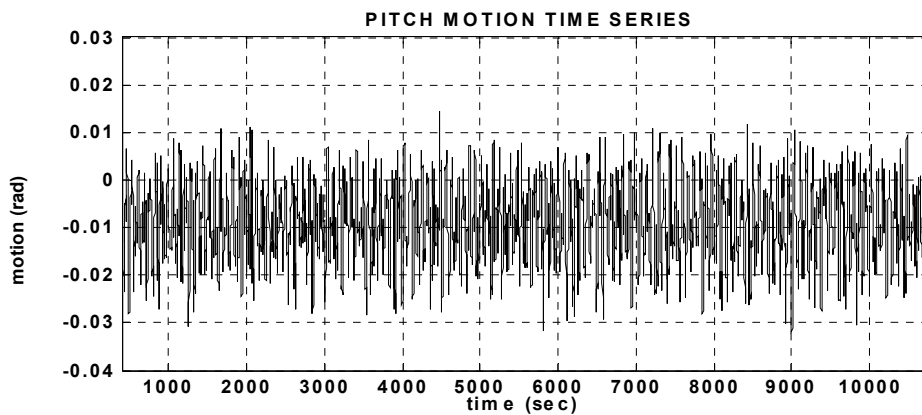


Fig. 8.16. Pitch response time series (CASE B,  $St = 0.23$ ,  $C_L = 0.4$ ).

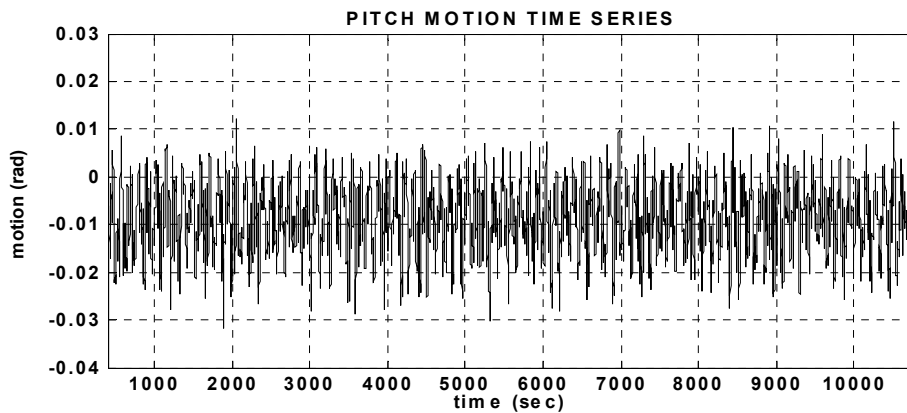
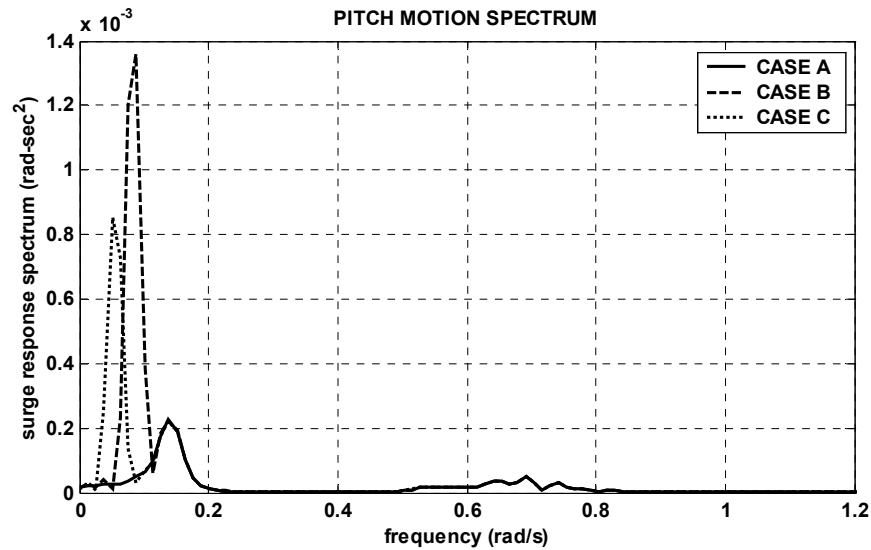


Fig. 8.17. Pitch response time series (CASE C,  $St = 0.153$ ,  $C_L = 0.4$ ).



**Fig. 8.18. Comparison of Pitch response spectrum.**

The statistical results are summarized in Table 8.1 through Table 8.3. Comparisons of statistics show that the surge standard deviation in Case B and Case C Spar is two times and four times larger than that of Case A, respectively. In pitch motion, Case B and Case C Spar is 1.7 and 1.4 times larger standard deviation compared with CASE A. Due to larger surge and pitch motion, the heave motion standard deviations is also increased by factor of 1.5 and 2.6 in Case B and Case C compared with Case A. Because vortex-induced vibration effects are considered as a harmonic lift force on a spar hull the spar motion (i.e. 6 degree of freedom of motions) mean values of Case A, Case B, and Case C is almost identical.

**Table 8.1. Summary of loop current condition statistics (CASE A).**

CASE A (CL = 0.0)						
	SURGE	SWAY	HEAVE	ROLL	PITCH	YEW
UNIT	m	m	m	deg.	deg.	deg.
MEAN	-3.22E+00	3.67E+01	-1.12E+00	-6.13E-01	-5.02E-01	9.32E-01
STD	5.44E-01	3.80E-02	1.01E-02	1.55E-02	2.66E-01	1.40E-01
EXE	-5.16E+00	3.68E+01	-1.17E+00	-6.80E-01	-1.43E+00	1.46E+00
LF STD	5.33E-01		6.68E-03		2.86E-02	
WF STD	1.08E-01		7.18E-03		2.02E-02	
<i>Notes:</i> STD = standard deviation; EXE = extreme; LF = low frequency, WF = wave frequency						

**Table 8.2. Summary of loop current condition statistics (CASE B).**

CASE B (St = 0.23, CL = 0.4)						
	SURGE	SWAY	HEAVE	ROLL	PITCH	YEW
UNIT	m	m	m	deg.	deg.	deg.
MEAN	-3.22E+00	3.67E+01	-1.13E+00	-6.11E-01	-5.01E-01	9.30E-01
STD	1.07E+00	4.87E-02	1.52E-02	1.59E-02	4.40E-01	1.93E-01
EXE	-6.38E+00	3.68E+01	1.18E+00	6.77E-01	1.84E+00	1.48E+00
LF STD	1.07E+00		1.33E-02		5.43E-02	
WF STD	1.10E-01		7.05E-03		2.02E-02	
<i>Notes:</i> STD = standard deviation; EXE = extreme; LF = low frequency, WF = wave frequency						

**Table 8.3. Summary of loop current condition statistics (CASE C).**

CASE C (St = 0.153, CL = 0.4)						
	SURGE	SWAY	HEAVE	ROLL	PITCH	YEW
UNIT	m	m	m	deg.	deg.	deg.
MEAN	-3.19E+00	3.67E+01	-1.13E+00	-6.11E-01	-5.02E-01	9.30E-01
STD	2.30E+00	1.42E-01	2.62E-02	1.66E-02	3.82E-01	3.47E-01
EXE	-8.13E+00	3.69E+01	-1.22E+00	-6.86E-01	-1.82E+00	1.83E+00
LF STD	2.31E+00		2.51E-02		4.61E-02	
WF STD	1.12E-01		7.08E-03		2.02E-02	
<i>Notes:</i> STD = standard deviation; EXE = extreme; LF = low frequency, WF = wave frequency						



Fig. 8.19 through Fig. 8.22 show a simulated most loaded mooring line tension time series and spectrum. It is obvious that large surge, heave and pitch motion standard deviations in Case B and Case C Spar platform both spar platforms also have larger standard deviation in mooring line tension compared with Case A Spar platform. Table 8.4 shows that standard deviation of mooring line tension increased by 20% and 102% in Case B and Case C Spar platform compared with Case A Spar platform respectively.

This case study has some limitations with current modeling as well as evaluating the vortex-shedding force. As mentioned before, the current is modeled as unidirectional with steady velocity and the vortex-shedding force is modeled as harmonic lift force in the numerical analysis program. However, the results show that neglecting vortex-induced vibration effects on a spar platform lead to significantly underestimating results in motion as well as mooring line tension in loop current condition.

**Table 8.4. Summary of statistics of most loaded line top tension statistics.**

	MEAN	STD	EXE	LF STD	WF STD
UNIT	N	N	N	N	N
CASE A	3.16E+06	5.42E+04	3.36E+06	2.77E+04	4.49E+04
CASE B	3.16E+06	6.52E+04	3.42E+06	4.56E+04	4.50E+04
CASE C	3.16E+06	1.10E+05	3.56E+06	1.00E+05	4.55E+04
<i>Notes:</i> STD = standard deviation; EXE = extreme; LF = low frequency, WF = wave frequency					

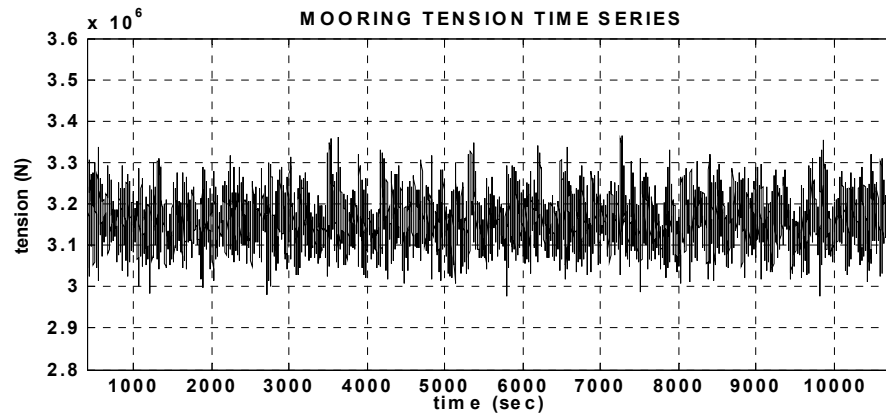


Fig. 8.19. Mooring top tension time series (CASE A,  $C_L = 0.0$ ).

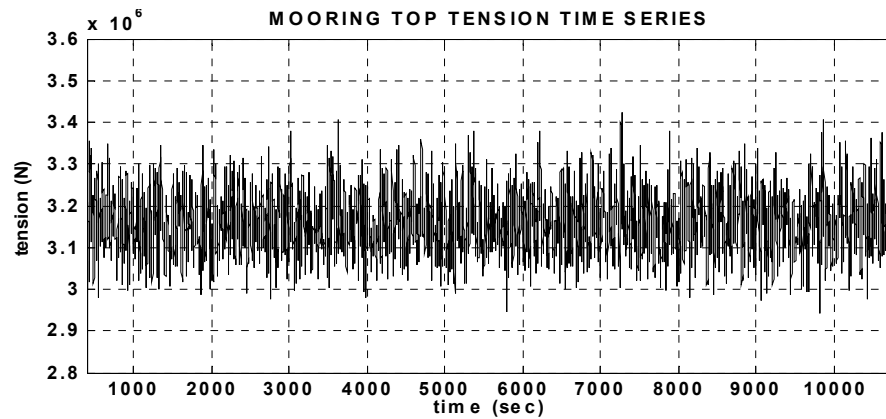


Fig. 8.20. Mooring top tension time series (CASE B,  $St = 0.23$ ,  $C_L = 0.4$ ).

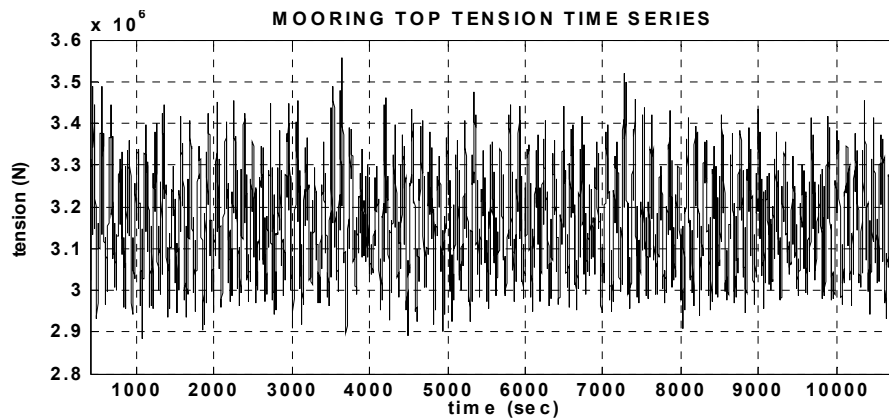
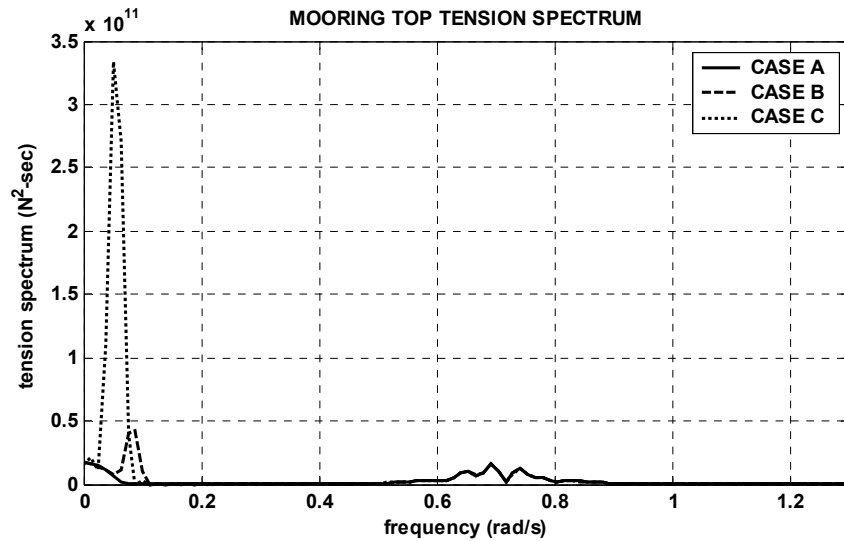


Fig. 8.21. Mooring top tension time series (CASE C,  $St = 0.153$ ,  $C_L = 0.4$ ).



**Fig. 8.22. Comparison of top tension spectrum.**

In the case study only considers loop current condition, but it has been reported that vortex-induced vibration with hurricane environment by Anam (2000). In his dissertation, the vortex-induced vibration event of the Neptune Spar with Hurricane George was studied. The field data show the vortex-induced vibration event following Hurricane George (early hours of September). Due to Hurricane is subsided, the environmental conditions were not severe (i.e. wave = 2 m, current = 0.45 m/s, and wind = 11.1 m/s) enough to make the spar dynamic motion and static offset, but the Neptune Spar experienced significant vortex-induced vibration event. The reason is that corresponding current velocity creates lock-in situation for the horizontal motion of the spar (Anam, 2000). His study also shows the vortex-induced vibration of the spar platform in strong wind, wave, and current from different direction. Thus, the vortex-induced vibration is important not only in loop current condition but also in hurricane condition. The vortex-induced vibration problem in offshore structure is still in progress, thus more research in this area is required.

## CHAPTER IX

### SUMMARY, CONCLUSIONS AND RECOMMENDATIONS

#### 9.1. Dynamics of a Spar Platform with Buoyancy-Can

The coupled dynamics of a classical spar designed for 914 m (3000 ft) water depth is investigated in the time domain using the analysis software WINPOST, that includes the newly developed numerical scheme for modeling the effects of the riser buoyancy-can. The buoyancy-cans inside of spar moon-pool are ignored or simplified in previous studies. Due to the fact that riser effects (i.e. buoyancy-can effects) are neglected, the spar heave and pitch motions are over estimated in simulations as well as in experiments. However, this study models the buoyancy-can effects by using multiple contact coupling and gap-contact between the riser buoyancy-can and guide frames by using one linear connected spring and three different nonlinear gap-contact springs.

Numerical simulations are conducted for the 100-yr hurricane condition with non-parallel wind, wave, and current. The coupling effects of riser buoyancy-cans and support guide frames on the global spar motions are determined using various riser buoyancy-can modeling techniques for evaluating multiple contact effects inside of the spar moon-pool. Conclusions are as follows:

- The results show that both predicted pitch and roll motions are reduced significantly when the effects of contact forces on the support guide frames

are considered.

- The multi-contact coupling forces between the riser buoyancy-cans and riser guide frames do not change the spar surge motion nor the most loaded line tension.
- The results from the gap contact effect between the riser buoyancy-cans and riser guide frames show that the gap effect does not change the global spar motion.
- The surge free decay simulation results show that the gap effect causes a periodic impact-like force on the buoyancy-can and this periodic force may produce fatigue in the buoyancy-can.
- The Coulomb (friction) damping between the riser buoyancy-cans and riser guide frames reduces the spar heave motion significantly in the spar heave natural period region.
- The heave free decay simulation clearly shows the Coulomb (friction) damping causes the heave amplitude to decay linearly, but it does not alter the natural period of the system.
- The new fully coupled analysis software that includes riser buoyancy-can effects inside of the spar moon-pool developed in this dissertation better predicts the spar motions.

## **9.2. Dynamics of a Spar Platform with Pneumatic Riser Support System**

An alternative spar riser support system is called that pneumatic riser support system. The pneumatic riser support system is compared with the buoyancy-can riser support system in the free decay test as well as the 100-year hurricane conditions of Gulf of Mexico.

The free decay simulation results show that pneumatic cylinders do not change the surge and pitch motion significantly, but the heave motion is totally different because there is additional heave restoring force from pneumatic cylinders. Due to the additional restoring force from pneumatic cylinders, the heave natural frequency of the spar platform is increased. The 100-year hurricane simulation results show that the pneumatic riser support system produces larger heave motion. The reason is that the pneumatic riser support system increases the spar natural period in heave direction, and thus the spar platform more exposed to wave energy. The pneumatic riser support system increases the riser top tension compared with the buoyancy-can riser support system. Because risers are hanging off the spar platform with the pneumatic cylinder, the pneumatic riser support system also increases the spar platform payload. Thus, the buoyancy-can riser support system produces smaller spar hull motions, and there is less top tension in the vertical riser system.

### 9.3. Mathieu's Instability in Spar Platform

Due to heave and pitch coupling of the spar platform, the pitch restoring coefficient is a function of heave motion, and this can be expressed by the Mathieu instability equation. When the spar experiences the Mathieu instability, the spar experiences large pitch motions. Thus, the Mathieu instability of a classical spar platform is investigated for various types of spar hull modeling. A damped Mathieu stability diagram is also developed.

First, the classical spar is modeled in a regular wave environment without considering the effects of the mooring lines and risers. The drag coefficient of the spar hull is changed to determine the pitch damping effects on Mathieu instability. The simulation results clearly show the Mathieu instability mechanism as well as the pitch damping effects on the Mathieu instability. The Mathieu stability diagram also shows that increasing pitch damping suppresses the Mathieu instability problem.

Second, the spar is modeled in regular waves, and the mooring lines and risers are considered. The results show that mooring line and riser buoyancy-can effects play an important role in the Mathieu instability analysis of a spar platform. Thus, the possibility of Mathieu instability is expected to be overestimated without proper modeling of riser buoyancy-cans and mooring lines in the computer simulations and in the model basin experiments.

Additional simulations are conducted for West Africa and North Sea swell environment conditions. The Swell-A and Swell-B simulation results show that for both cases the maximum heave motion is 1.7 ~ 1.9 meters (5.5 ~ 6.2 ft) and the maximum pitch motion is around 0.6 ~ 0.7 degrees. Based on the regular wave simulation results, the spar

platform is very stable in this range of heave and pitch response. It shows that the spar platform does not experience Mathieu instability in the typical swell environment condition. However, the heave motion standard deviation in the swell condition is five times larger than that for the 100-year hurricane condition. Thus, to reduce the Mathieu instability problem in a spar hull design, one may reduce the pitch natural period below 45 seconds. Increasing a spar heave natural period higher than 30 seconds also avoids the dominant swell wave energy as well as reduces the possibility of Mathieu instability in swell environment.

#### **9.4. Vortex Induced Vibration on Spar Hull**

The loop current condition in Gulf of Mexico is simulated for a classical spar platform. In this case study, the simplified vortex-induced vibration effects are added in the WINPOST computer simulation for the analysis. There are some limitations with current modeling as well as evaluating the vortex-shedding force. As mentioned before, the current is modeled as unidirectional with steady velocity and the vortex-shedding force is modeled as a harmonic lift force. The results show that neglecting vortex-induced vibration effects on a spar platform yield significantly underestimated results in surge or sway motion (i.e. 100 % in the Case B and 322% in the Case C) and mooring line tension.



## 9.5. Recommendations and Future Studies

Four main subjects are studied in this research; Buoyancy-can effect on the global spar motion, Alternative pneumatic riser support system, Mathieu instability in a spar platform, and vortex-induced vibration in a spar platform. The recommendations and future studies are as follows;

### Buoyancy-can effects on the global spar motion

- The multi-contact coupling numerical model including gap boundary condition is developed. However, the spring coefficient and friction coefficient between buoyancy-can and riser guide frames need to be further validated using structural experiment.
- The hydrodynamic coefficients (i.e. inertia, drag, and added mass coefficients) of the buoyancy-can inside of the spar moon-pool need be further validated with model basin experiment.
- In this research, the additional excitation force from sloshing inside of the spar moon-pool was not considered. More theoretical and experimental work is needed to consider the additional excitation force from sloshing.

### Mathieu instability

- The proper modeling of mooring lines, riser buoyancy-cans and spar moon-

pool is required to estimate the Mathieu instability in model basin experiment and computer simulation.

- Mathieu instability of a spar platform was investigated based on the stability chart in regular wave and regular wave simulation. However, more work is needed to develop the stability charts in irregular waves.

#### Vortex-induced vibration

- A more rigorous hull modeling effort using computational fluid dynamics using Navier-Stokes equation is needed.
- The computer simulation and experimental modeling of vortex-induced vibration needs to consider the effects of the mooring lines and risers.
- The lift and drag coefficient for the spar hull with helical strakes, risers and mooring lines needs to be further investigated.

## REFERENCES

- Anam, I., 2000. Evaluations of the dynamic response of spar platforms. Ph.D. Dissertation, Civil Engineering Department, Texas A&M University, College Station, TX.
- ANSI/API RP-2A WSD, 1994. Recommended practice for planning, designing and constructing fixed offshore platforms-working stress design. American Petroleum Institute, pp. 23.
- Cao, P., and Zhang, J., 1996. Slow motion responses of compliant offshore structures. Proceedings of the 6th International Offshore and Polar Engineering Conference, Los Angeles, vol. 1, pp. 296-303.
- Chen, X., Zhang, J., Johnson, P., and Irani, M. 2001. Dynamic analysis of mooring lines by using three different methods. Proceedings of the 11th International Offshore and Polar Engineering Conference, Stavanger, vol. 4, pp. 635-642.
- Donley, M. G., and Spanos, P. D., 1990. Dynamic Analysis of Nonlinear Structures by the Method of Quadraticization. Lecture Notes on Engineering, Springer-Verlag, New York.
- Garret, D. L., 1982. Dynamic analysis of slender rods. Journal Energy Resources Technology, vol. 104, pp. 302-307
- Günther, C., Eike, L., and Casten, Ö., 1988. Offshore Structures, Springer-Verlag, New York, vol. 1, pp. 132-135.
- Gupta, H., Finn, L. D., and Weaver, T. O., 2000. Effects of spar coupled analysis. Proceeding of the 32nd Offshore Technology Conference, Houston, pp. 629-638, OTC 12082.

- Gyory, J., Mariano, A. J., and Ryan, E. H., 2001. The loop Current, Rosenstiel School of Marine and Atmospheric Science, University of Miami, Miami, FL.
- Hagedorn, P., 1981. Non-linear Oscillations. Oxford University Press, Oxford, pp. 220-225.
- Haslum, H. A., and Faltinsen, O. M., 1999. Alternative shape of spar platforms for use in hostile areas. Proceeding of the 31st Offshore Technology Conference, Houston, pp. 217-228, OTC 10953.
- Hofmann, E. E., and Worley, S. J., 1986. An investigation of the circulation of the Gulf of Mexico, *Journal of Geophysical Research*, 91(C12), pp. 14221-14236.
- Inman, D.J., 1996. *Engineering Vibration*. Prentice Hall, Paramus, NJ, pp. 94.
- Johnson, C. P., Mekha, B. B., Matos, C., and Roesset, J. M., 1996. Analysis in the time domain of a deepwater spar platform. *Proceedings of Energy Week Conference and Exhibition*, Houston, vol.3, pp. 266-270.
- Jordan, D. W., and Smith, P., 1987. *Nonlinear Ordinary Differential Equation*. Clarendon Press, Oxford.
- Kim, C. H., Kim, M. H., Liu, Y. H., and Zhao, C. T., 1994. Time domain simulation of nonlinear response of a coupled TLP system. *International Journal of Offshore and Polar Engineering*, vol. 4, no. 4, pp. 281-291.
- Kim, M. H., 1997. *WINTCOL/WINPOST User's Manual*. Ocean Engineering Program, Civil Engineering Department, Texas A&M University, College Station, TX.
- Kim, M. H., and Yue, D. K. P., 1990. The complete second-order diffraction solution for an axisymmetric body: Part 2. Bichromatic incident waves and body motions. *Journal of Fluid Mechanics*, vol. 211, pp. 557-593.

- Kim, M. H., Tahar, A., and Kim, Y. B., 2001a. Variability of spar motion analysis against various design methodologies/parameters. Proceedings of the 20th Offshore Mechanics and Arctic Engineering, (OMAE), vol. 1, pp. 153-152.
- Kim, M. H., Tahar, A., and Kim, Y. B., 2001b. Variability of TLP motion analysis against various design methodologies/parameters. Proceedings of the 11th International Offshore and Polar Engineering, Stavanger, vol. 1, pp. 467-473.
- Kim, M.H., Mercier, R.S., Gu, G, Wu, C., and Botelho, D., 1993. PC-based wave load computation on large-volume multi-column structures. Proceedings of the 3rd International Offshore and Polar Engineering Conference, Singapore, vol. 1, pp. 334-340.
- Kim, M.H., Roesset, J.M., and Zhang, J., 1997. Nonlinear dynamic analysis methods for spar platforms. Proceedings of the Society of Naval Architects and Marine Engineers Conference (Gulf Section), Houston.
- Lee, C. H., 1995. WAMIT Theory Manual. Department of Ocean Engineering, Massachusetts Institute of Technology, Cambridge, MA.
- Lienhard, J. H., 1966. Synopsis of lift, drag, and vortex frequency data for rigid circular cylinders. Research Division Bulletin 300, College of Engineering, Washington State University, Pullman, WA.
- Ma, W., Lee, M. Y., Zou, J., and Huang, E. W., 2000. Deepwater nonlinear coupled analysis tool, Proceeding of the 32nd Offshore Technology Conference, Houston, pp. 655-665, OTC 12085.

- Magee, A. Sablok, A. Maher, J. Halkyard, J. Finn, L., and Datta, I., 2000. Heave plate effectiveness in the performance of Truss Spars. 19th Offshore Mechanics and Arctic Engineering, (OMAE), vol. 2, pp. 469-479.
- Mekha, B.B., Johnson, C.P., and Rosset, J.M., 1995. Nonlinear response of a Spar in deep water: Different hydrodynamic and structural models. Proceedings of the 5th International Offshore and Polar Engineering Conference, Los Angeles, vol. 1, pp.462-469.
- Mekha, B. B., Weggel, D. C., Johnson, C. P., and Roesset, J. M., 1996. Effects of second order diffraction forces on the global response of spars. Proceedings of the 6th International Offshore and Polar Engineering Conference, Los Angeles, vol. 1, pp. 273-280.
- Nordgren, R. P., 1974. On computation of the motions of elastic rods. Journal of Applied Mechanics, pp. 777-780
- Paulling, J.R., and Webster, W.C., 1986. A consistent large-amplitude analysis of the coupled response of a TLP and tendon system. Proceeding of the 5th Offshore Mechanics and Arctic Engineering, (OMAE), vol. 3, pp.126-133.
- Prislin, I., Halkyard, J. E., DeBord, F., Collins, J. I., and Lewis, J. M. 1999. Full-scale measurements of the Oryx Neptune production spar platform performance. Proceeding of the 31st Offshore Technology Conference, Houston, pp. 209-215, OTC 10952.
- Ran, Z., and Kim, M.H., 1997. Nonlinear coupled responses of a tethered Spar platform in waves. International Journal of Offshore and Polar Engineering, vol. 7, No. 2, pp. 111-118.

- Ran, Z., Kim, M.H., Niedzwecki, J.M., and Johnson, R.P., 1995. Response of s Spar platform in random waves and currents (Experiment Vs. Theory). *International Journal of Offshore and Polar Engineering*, vol. 6, No. 1, p 27-34.
- Ran, Z., Kim, M.H., and Zheng, W., 1999. Coupled dynamic analysis of a moored spar in random waves and current (Time-domain Vs. Frequency-domain Analysis). *Journal of Offshore Mechanics and Arctic Engineering*, vol. 121, pp.194-199.
- Rho, J. B., Choi, H. S., Lee, W. C., Shin, H. S., and Park, I. K., 2002. Heave and pitch motion of a spar platform with damping plate. *Proceedings of the 12th International Offshore and Polar Engineering Conference, Kitakyshu*, vol. 1, pp. 198-201.
- Roshko, A., 1961. Experiments on the flow past a circular cylinder at very high Reynolds number. *Journal of Fluid Mechanics*, vol. 10, pp. 345-356.
- Tahar, A., Ran, Z., and Kim, M.H., 2002, Hull/mooring/riser coupled spar motion analysis with buoyancy-can effect. *Proceedings of the 12th International Offshore and Polar Engineering Conference, Kitakyshu*, vol. 1, pp. 223-230.
- Ude, T. C., Kumar, S., and Winterstein, S. R., 1996. TFPOP 2.1: Stochastic response analysis of floating structures under wind, current and second-order wave loads. Rep. # RMS-18, RMS Program, Stanford University, CA.
- Weggel, D. C., and Roesset, J. M., 1996a. The behavior of spar platforms. COSU-96.
- Weggel, D. C., and Roesset, J. M., 1996b. Second order dynamic response of a large diameter spar platform: Numerical predictions versus experimental results. *Offshore Mechanics and Arctic Engineering, (OMAE)*, vol. 1, pp. 489-496.

- Zhang, J., Chen, L., Ye, M., and Randall, R. E., 1995. Hybrid wave model for unidirectional irregular waves, Part I: Theory and numerical scheme. *Applied Ocean Research*, vol. 18, pp. 77-92.
- Zhang, L., Zou, J., and Huang, E. W., 2002. Mathieu instability evaluation for DDCV/SPAR and TLP tendon design. *Proceeding of the 11th Offshore Symposium, Society of Naval Architect and Marine Engineer (SNAME), Houston*, pp. 41-49.
- Zhang, X., and Zou, J., 2002. Coupled effects of risers/supporting guide frame on spar responses. *Proceedings of the 12th International Offshore and Polar Engineering Conference, Kitakyshu*, vol. 1, pp. 231-236.



## APPENDIX A

### FLOW CHART OF WINPOST

This appendix provides a flow chart for the hull/mooring/riser coupled analysis in time domain by WINPOST. In a time domain analysis, the mooring/riser and platform dynamics are solved simultaneously as an integrated system. The hydrodynamic forces on the platform are evaluated by diffraction theory. The first- and second-order wave force, added mass and radiation damping are obtained by WAMIT. The viscous force on platform and the hydrodynamic forces on the mooring/riser are calculated in the WINPOST. After calculating the hydrodynamic force on the hull/mooring/riser, the hull/mooring/riser coupled equation of motion is solved simultaneously by WINPOST. Thus, there are two processes to develop the input data. The first process uses WAMIT to get the hydrodynamic coefficient from diffraction theory, and second process is to prepare input for the slender body (i.e. mooring lines and risers) and coupling between hull and mooring/risers. Due to WINPOST solving hull/mooring/riser simultaneously in time domain, output can be divided into three parts. The first part is wave elevation output, second part is output for hull motion, and the third part is output for mooring lines and risers. Fig.A.1 shows the process of coupled analysis by WINPOST.

The input and output of the WAMIT presented here are only the part for WINPOST input. The detailed explanation about input and output for WAMIT is described in the WAMIT user manual (Lee, 1995). Input and output of WAMIT are summarized in Table A.1 and Table A. 2.

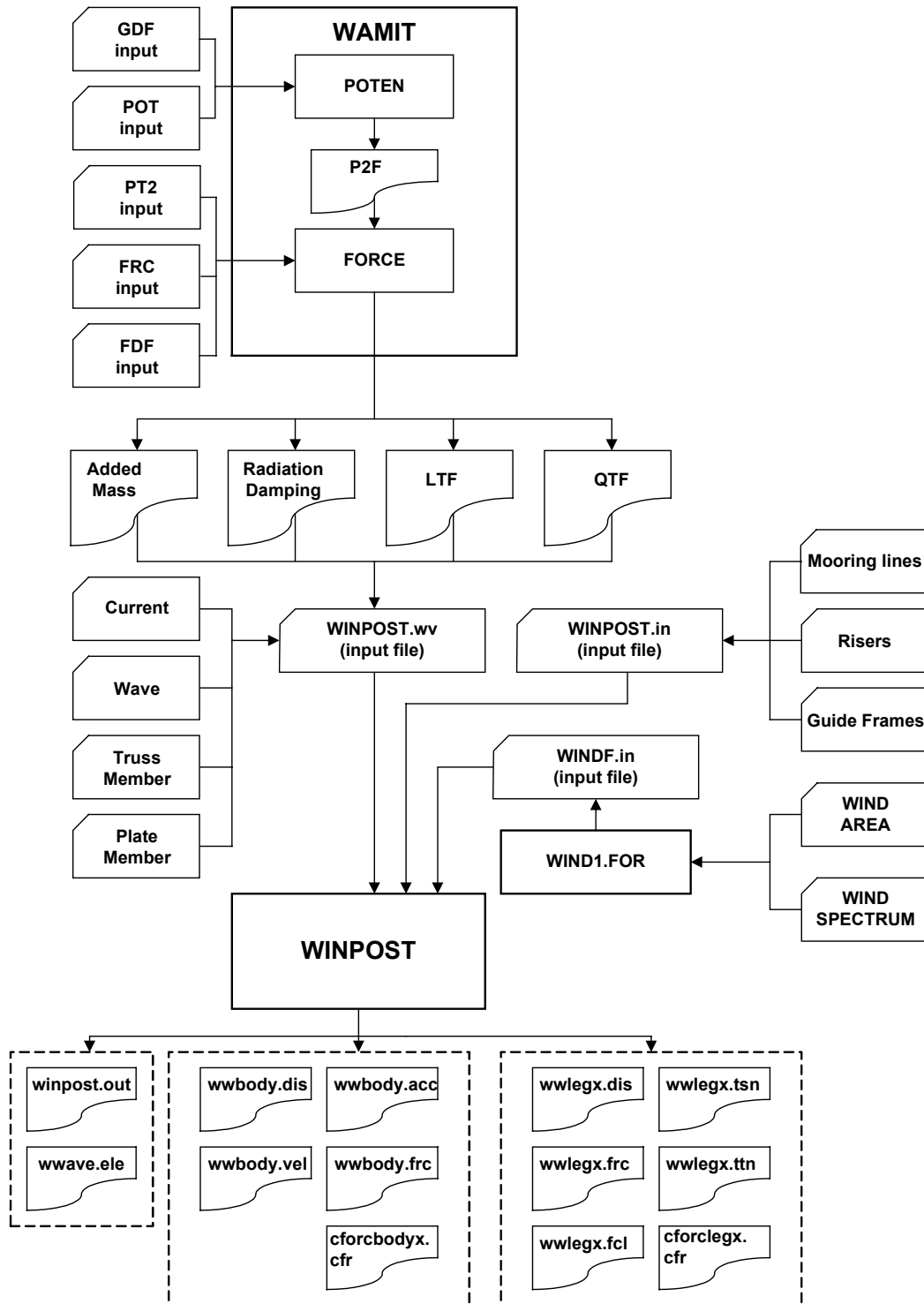


Fig.A.1 Flow chart of coupled analysis by WINPOST

## WAMIT Input and Output

**Table A.1 Input data for WAMIT**

Input	
<b>GDF</b>	is the geometric data file, which contains a description of discretized wetted surface of body, body length scale, gravity, symmetry indices, and total number of panel.
<b>POT</b>	is used to input various parameters to the <b>POTEN</b> subprogram.
<b>PT2</b>	contains two set of parameters. One specifies mode indices for which the second-order output is calculated. The other specifies period/wave heading pairs for which second-order output is calculated.
<b>FRC</b>	is used to input various parameters to the <b>FORCE</b> subprogram.
<b>FDF</b>	is contains all requisite data perform the integration of the quadratic forcing over the entire free surface exterior to the bodies.
<b>POTEN</b>	is subprogram, which solves for the radiation and diffraction velocity potential on the body surface for the specified mode.
<b>FORCE</b>	is subprogram, which computes global quantities including the hydrodynamic coefficients, motions, and first- and second-order forces.

**Table A. 2 Output from WAMIT**

Output	
P2F	is output from POTEN, which is used as input for FORCE.
<b>M<sup>a</sup></b>	is added-mass of the platform.
<b>C</b>	is radiation damping of the platform.
LTF	is linear force transfer function.
QTF	is quadratic force transfer function.

## **WINPOST Input and Output**

**WINPOST.IN** can be divided into four groups. The first group contains dimension, total number of leg (i.e. mooring lines and risers), maximum number of the iteration for static analysis, total number of time steps of calculation and output for time domain analysis, and position (in global coordinate system) of the origin of the rigid-body coordinate system. The second group contains all the material properties of the legs. The third group contains information about geometry of legs, spring coefficients of connection, location of guide frames, gap between buoyancy-cans and guide frames, and coulomb damping coefficient. The last group contains run-time commands.

**WINPOST.WV** consists of two groups of data. The first group is for the hydrodynamic information of a platform from WAMIT (i.e. number of frequency, added-mass, radiation damping, LTF, and QTF). The second group contains wave spectrum, current profile, and geometry and hydrodynamic coefficient (i.e.  $C_d$ ,  $C_m$ ,  $C_I$ , and  $C_L$ ) of truss and plate members.

**WINDF.IN** is the wind force time series, which is used for WINPOST. WIND1.FOR is subprogram, which generates the time series of wind force (i.e. WINDF.IN) on a rigid body (i.e. floating platform). The output files from WINPOST are summarized in Table A.

3.

**Table A. 3 Output from WINPOST**

Output for wave	
winpost.out	contains all the input data for rechecking.
wwave.ele	records wave elevation time series in the time domain analysis.
Output for platform	
wwbody.dis	contains the displacement of the platform.
wwbody.vel	contains the velocity of the platform.
wwbody.acc	contains the acceleration of the platform.
wwbody.frc	records external forces (e.g. diffraction forces, viscous forces).
cforcbodyx.cfr	contains the contact force on the platform from buoyancy-can.
Output for mooring lines and risers	
wwlegx.dis	contains the nodal position and slope of the leg x (e.g. wwleg01.dis).
wwlegx.frc	contains the nodal reaction forces (in global coordinate) of the leg x.
wwlegx.fcl	contains the nodal reaction forces (in local/element coordinate) of the leg x.
wwlegx.tsn	contains the nodal axial tension of the leg x.
wwlegx.ttn	contains the nodal axial tension of the last node, which connected to the platform.
cforclegx.cfr	contains the contact force on buoyancy-cans from platform (i.e. guide frame).

## APPENDIX B

### NOMENCLATURE

#### Hydrodynamics (CHAPTER II)

A	wave amplitude.
$\mathbf{F}_{\text{HS}}^{(1)}$	first-order hydrostatic restoring force.
$\mathbf{F}_{\text{R}}^{(1)}$	first-order radiation force.
$\mathbf{F}_{\text{EX}}^{(1)}$	first-order excitation force.
$\mathbf{F}_{\text{q}}^{(2)}$	quadratic product of first-order potential force.
$\mathbf{F}_{\text{P}}^{(2)}$	second-order potential force.
$\mathbf{F}_{\text{R}}^{(2)}$	second-order radiation potential
$\mathbf{F}_{\text{HS}}^{(2)}$	second-order hydrostatic force.
$f_{\text{jl}}^{\pm}$	complete sum- and difference-frequency exciting force quadratic transfer functions.
g	gravitational accelerations.
k	wave number.
$k^{\pm}$	sum- and difference-wave number.
$\mathbf{n}$	normal vector, $(n_1, n_2, n_3) = \mathbf{n}$ and $(n_4, n_5, n_6) = \mathbf{r} \times \mathbf{n}$ .
p	pressure.
$p_{\text{jl}}^{\pm}$	sum- and difference-frequency quadratic transfer functions for the pressure.
$Q^{\pm}$	sum- and difference- free surface forcing term.
u, v, w	particle velocity vectors with respect to x-, y-, and z- axis in Cartesian coordinate system.
$\mathbf{V}_{\mathbf{n}}$	normal velocity of the body at its surface.
$\Phi$	total velocity potential (real).
$\Phi^{(1)}$	first-order total velocity potential (real).
$\Phi^{(2)}$	second-order total velocity potential (real).

$\Phi_I$	incident wave velocity potential (real).
$\Phi_I^{(1)}$	first-order incident wave velocity potential (real).
$\Phi_I^{(2)}$	second-order incident wave velocity potential (real).
$\phi_I^{(1)}$	first-order incident wave velocity potential (complex).
$\phi_I^{(2)}$	second-order incident wave velocity potential (complex).
$\phi_I^\pm$	second-order sum- and difference-incident wave potential (complex).
$\Phi_D$	diffraction potential (real).
$\Phi_D^{(1)}$	first-order diffraction potential (real).
$\Phi_D^{(2)}$	second-order diffraction potential (real).
$\phi_D^{(1)}$	first-order diffraction potential (complex).
$\phi_D^{(2)}$	second-order diffraction potential (complex).
$\phi_D^\pm$	second-order sum- and difference-diffraction potential (complex).
$\Phi_R$	radiation potential (real).
$\Phi_R^{(1)}$	first-order radiation potential (real).
$\Phi_R^{(2)}$	second-order radiation potential (real).
$\phi_R^{(1)}$	first-order radiation potential (complex).
$\phi_R^{(2)}$	second-order radiation potential (complex).
$\phi_R^\pm$	second-order sum- and difference-radiation potential (complex).
$\phi_i^{(1)}$	velocity potential of the rigid body motion with unit amplitude in the $i$ -th mode in the absence of incident waves.
$\alpha$	rotational body motion vector.
$\Xi$	translational body motion vector.
$\nabla$	differential operator.
$\eta$	free surface elevation.
$\eta_r$	relative wave height.
$\rho$	fluid density and represent.

$\theta$	incident wave angle.
$\omega$	wave frequency.
$\omega^\pm$	sum- and difference-frequency.

### Platform Motion (CHAPTER II)

$C_a$	added mass coefficient.
$C_d$	drag coefficient.
$C_L$	lift coefficient.
$C_m (= 1 + C_a)$	inertia coefficient.
$\mathbf{C}$	potential damping coefficient matrix.
$\mathbf{C}(\omega)$	wave damping coefficients.
$D(\omega_j - \omega_l)$	difference- frequency forces quadratic transfer function.
$\overline{FG}$	horizontal distance between center of gravity and center of flotation.
$F_n$	Morison's force.
$F_L$	lift force on the structure.
$f_v$	Strouhal frequency.
$\overline{GM}_T$	metacentric height in the transverse direction (in calm water).
$\overline{GM}_L$	metacentric height in the longitudinal direction (in calm water)
$h_1(\tau), h_2(\tau_1\tau_2)$	linear and quadratic impulse response functions.
$\mathbf{K}$	hydrostatic restoring coefficient matrix.
$L(\omega_j)$	linear force transfer functions.
$\mathbf{M}$	body mass matrix.
$\mathbf{M}^a$	added mass coefficient matrix.
$m(\infty)$	added mass of the body at the infinite frequency.
$R(t)$	retardation function.
$S(\omega_j + \omega_l)$	sum- frequency forces quadratic transfer function.
$S_\eta(\omega)$	wave spectrum.



$S_F^{(1)}(\omega)$	linear wave spectrum.
$S_F^{(2)-}(\omega)$	second-order difference-wave spectrum.
$S_F^{(2)+}(\omega)$	second-order sum-wave spectrum.
$\dot{u}_n, u_n$	fluid acceleration and velocity normal to the body.
$U_\infty$	incident steady current velocity from far upstream.
$\ddot{x}_n, \dot{x}_n$	normal acceleration and velocity of the structure.
$\alpha$	phase angle.
$\delta_{ij}$	Kronecker delta function.
$\nabla$	displaced volume (in calm water).
*	complex conjugate of the quantities.

### Slender Rod Theory (CHAPTER III)

$A_1(s)$	interpolation functions.
<b>B</b>	buoyant force of the rod per unit length.
EA	axial stiffness.
EI	bending stiffness.
$F^s$	hydrostatic force on the rod per unit length.
$F^d$	hydrodynamic load per unit length.
$F'$	resultant force acting along the centerline.
$F_{il}$	static force.
H	torque.
$K_{ijkl}^1$	material stiffness that comes from the bending stiffness.
$K_{nijlk}^2$	stiffness from tension and the curvature.
$L = \{L_1, L_2, L_3\}^T$	nodal resultant moment.
<b>m</b>	applied moment per unit length.
$M'$	resultant moment acting along the centerline.
$M_{ijkl}$	structure mass.

$M_{ijkl}^a$	added mass.
$\hat{M}_{ijkl}$	virtual mass.
$N = \{N_1, N_2, N_3\}^T$	nodal resultant force.
$P_m(s)$	interpolation functions.
$\mathbf{q}$	applied force per unit length.
$\mathbf{r}$	position vector of the center line of the rod.
$\mathbf{r}'$	unit tangent vector to the space curve.
$\mathbf{r}''$	the principle normal vector.
$\mathbf{r}' \times \mathbf{r}''$	bi-normal vector.
$\ddot{\mathbf{r}}^n, \dot{\mathbf{r}}^n$	acceleration and velocity normal to its centerline.
$T$	tension.
$\tilde{T}$	effective tension.
$\mathbf{V}^n, \dot{\mathbf{V}}^n$	fluid velocity and acceleration normal to the rod centerline.
$\mathbf{w}$	weight of the rod per unit length.
$\tilde{\mathbf{w}}$	effective weight.
$\rho$	mass of the rod per unit length.
$\kappa$	the curvature of the line.
$\lambda$	Lagrangian multiplier.
$\lambda$	line tension at the end nodes and the midpoint.

#### **Coupling between Platform and Mooring lines and Risers (CHAPTER IV)**

$A$	cross sectional area of the pneumatic cylinder.
$D$	viscous damping coefficient.
$\mathbf{e}_i$	unit vector which denotes the direction of the spring reference.
$F$	tension from pneumatic cylinder.
$K^L$	translational spring constant.
$K^\theta$	rotational spring constant.
$K^M$	coefficient from mooring line.

$K^R$	coefficients from riser.
$K^C$	coupling coefficient matrix between line and platform.
$K^{Pf}$	coefficients from the platform.
$p_i$	position vector of the point on the platform where the springs are attached.
$P$	pressure inside of the pneumatic cylinder.
$r_i$	position vector of the end node of the line which is attached to the rigid body by spring.
$T_0$	initial tension.
$V$	volume inside of the pneumatic cylinder.
$X_i$	translational motion of the platform.
$Z$	stroke of the pneumatic cylinder.
$\theta_i$	rotational motion of the platform.
$\mu$	coulomb damping coefficient.

### **Buoyancy-can Effect on Spar Platform (CHAPTER V)**

$H_s$	significant wave height
$\omega_p$	peak frequency
$\gamma$	over shooting parameter
$f_p$	average factor derived from measured spectrum
$\sigma(z)$	standard deviation of wind speed and related to turbulence intensity
$V_w(z)$	one hour mean wind speed (m/s) z meters above water level

## VITA

Bon-Jun Koo was born in Seoul, Korea on January 21, 1972. He graduated from Inha University with a bachelor of science in naval architecture and ocean engineering in February, 1996. He entered the graduate school at Inha University in March, 1996 and received a master of science in naval architecture in February, 1998. After graduation, he entered the graduate program at Texas A&M University in January, 1999 and received a Ph.D. in ocean engineering in August, 2003. He is married to Ji-hee Kim and has a son Sean H. Koo.

His permanent address is:

Seoul-si, Young Deung Po-gu,

Youido-dong, Kwang-jang Apt 11-1203

Seoul, Korea 150-010

e-mail address: [bonjun@hotmail.com](mailto:bonjun@hotmail.com)